



ISSN 2518-7198 (Print)
ISSN 2663-5089 (Online)

BULLETIN

OF THE KARAGANDA UNIVERSITY

PHYSICS

Series

2025 • Volume 30 • Issue 3(119)

ISSN 2663-5089 (Online)
ISSN-L 2518-7198 (Print)
Индексі 74616
Индекс 74616

**ҚАРАҒАНДЫ
УНИВЕРСИТЕТІНІҢ
ХАБАРШЫСЫ**

ВЕСТНИК
КАРАГАНДИНСКОГО
УНИВЕРСИТЕТА

BULLETIN
OF THE KARAGANDA
UNIVERSITY

ФИЗИКА сериясы

Серия ФИЗИКА

PHYSICS Series

2025

30-том • 3(119)-шығарылым
Том 30 • Выпуск 3(119)
Volume 30 • Issue 3(119)

1996 жылдан бастап шығады
Издается с 1996 года
Founded in 1996

Жылына 4 рет шығады
Выходит 4 раза в год
Published 4 times a year

Қарағанды / Караганда / Karaganda
2025

Бас редакторы
PhD, проф. **Н.Қ. Танашева**

Жауапты хатшы
PhD, қауымд. проф. **Д.Ж. Қарабекова**

Редакция алқасы

Н.Х. Ибраев,	физ.-мат. ғыл. д-ры, проф., акад. Е.А. Бөкетов атындағы Қарағанды университеті (Қазақстан);
Б.Р. Нүсіпбеков,	техн. ғыл. канд., проф., Әбілқас Сағынов атындағы Қарағанды техникалық университеті, Қарағанды (Қазақстан);
А.О. Сәулебеков,	физ.-мат. ғыл. д-ры, проф., М.В. Ломоносов атындағы Мәскеу мемлекеттік университетінің Қазақстан филиалы, Астана (Қазақстан);
Б.Р. Ильясов,	PhD, қауымд. проф., Astana IT University, Астана (Қазақстан);
А.Д. Погребняк,	физ.-мат. ғыл. д-ры, проф., Сумы мемлекеттік университеті (Украина);
А.П. Суржиков,	физ.-мат. ғыл. д-ры, проф., Томск политехникалық университеті (Ресей);
И.П. Курытник,	техн. ғыл. д-ры, проф., Освенцимдегі В. Пилецкий атындағы Мемлекеттік жоғары кәсіптік мектебі (Польша);
М. Стоев,	PhD, инженерия д-ры, «Неофит Рильский» Оңтүстік-Батыс университеті, Благоевград (Болгария);
В.Ю. Кучерук,	техн. ғыл. д-ры, проф., Винница ұлттық техникалық университеті (Украина);
В.А. Кульбачинский,	физ.-мат. ғыл. д-ры, проф., М.В. Ломоносов атындағы Мәскеу мемлекеттік университеті (Ресей);
Bisquert Juan,	проф., физика проф., Хайме I университеті, Кастельо-де-ла-Плана (Испания);
Chun Li,	PhD, Чанчунь ғылым және технология университеті (Қытай);
Д.Т. Валиев,	физ.-мат. ғыл. канд., доц., Томск ұлттық политехникалық зерттеу университеті (Ресей)

Редакцияның мекенжайы: 100024, Қазақстан, Қарағанды қ., Университет к-сі, 28
E-mail: vestnikku@gmail.com; karabekova71@mail.ru
Сайты: physics-vestnik.ksu.kz

Атқарушы редактор
PhD **Г.Б. Саржанова**

Корректорлары
С.С. Балкеева, И.Н. Муртазина

Компьютерде беттеген
В.В. Бутякин

Қарағанды университетінің хабаршысы. «Физика» сериясы. — 2025. — 30-т., 3(119)-шығ. — 106 б. — ISSN-L 2518-7198 (Print). ISSN 2663-5089 (Online).

Меншік иесі: «Академик Е.А. Бөкетов атындағы Қарағанды университеті» КеАҚ.

Қазақстан Республикасы Ақпарат және қоғамдық даму министрлігімен тіркелген. 30.09.2020 ж. № KZ38VPY00027378 қайта есепке қою туралы куәлігі.

Басуға 30.09.2025 ж. қол қойылды. Пішімі 60×84 1/8. Қағазы офсеттік. Көлемі 13,25 б.т. Таралымы 200 дана. Бағасы келісім бойынша. Тапсырыс № 119.

«Акад. Е.А. Бөкетов ат. Қарағанды ун-ті» КеАҚ баспасының баспаханасында басылып шықты.
100024, Қазақстан, Қарағанды қ., Университет к-сі, 28. Тел. (7212) 35-63-16. E-mail: izd_karu@mail.kz

© Академик Е.А. Бөкетов атындағы Қарағанды университеті, 2025

Главный редактор
PhD, проф. **Н.К. Танашева**

Ответственный секретарь
PhD, ассоц. проф. **Д.Ж. Карабекова**

Редакционная коллегия

Н.Х. Ибраев,	д-р физ.-мат. наук, проф., Карагандинский университет им. акад. Е.А. Букетова (Казахстан);
Б.Р. Нусупбеков,	канд. техн. наук, проф., Карагандинский технический университет им. А. Сагинова, Караганда (Казахстан);
А.О. Саулебеков,	д-р физ.-мат. наук, проф., Казахстанский филиал Московского государственного университета им. М.В. Ломоносова, Астана (Казахстан);
Б.Р. Ильясов,	PhD, ассоц. проф., Astana IT University, Астана (Казахстан);
А.Д. Погребняк,	д-р физ.-мат. наук, проф., Сумской государственный университет (Украина);
А.П. Суржиков,	д-р физ.-мат. наук, проф., Томский политехнический университет (Россия);
И.П. Курытник,	д-р техн. наук, проф., Государственная высшая профессиональная школа им. В. Пилецкого в Освенциме (Польша);
М. Стоев,	PhD, д-р инженерии, Юго-Западный университет «Неофит Рильский», Благоевград (Болгария);
В.Ю. Кучерук,	д-р техн. наук, проф., Винницкий национальный технический университет (Украина);
В.А. Кульбачинский,	д-р физ.-мат. наук, проф., Московский государственный университет им. М.В. Ломоносова (Россия);
Bisquert Juan,	проф., проф. физики, Университет Хайме I, Кастельо-де-ла-Плана (Испания);
Chun Li,	PhD, Чанчуньский университет науки и технологии (Китай);
Д.Т. Валиев,	канд. физ.-мат. наук, доц., Национальный исследовательский Томский политехнический университет (Россия)

Адрес редакции: 100024, Казахстан, г. Караганда, ул. Университетская, 28
E-mail: vestnikku@gmail.com; karabekova71@mail.ru
Сайт: physics-vestnik.ksu.kz

Исполнительный редактор
PhD **Г.Б. Саржанова**

Корректоры
С.С. Балкеева, И.Н. Муртазина

Компьютерная верстка
В.В. Бутяйкин

Вестник Карагандинского университета. Серия «Физика». — 2025. — Т. 30, вып. 3(119). — 106 с. — ISSN-L 2518-7198 (Print). ISSN 2663-5089 (Online).

Собственник: НАО «Карагандинский университет имени академика Е.А. Букетова».

Зарегистрирован Министерством информации и общественного развития Республики Казахстан. Свидетельство о постановке на переучет № KZ38VPY00027378 от 30.09.2020 г.

Подписано в печать 30.09.2025 г. Формат 60×84 1/8. Бумага офсетная. Объем 13,25 п.л. Тираж 200 экз. Цена договорная. Заказ № 119.

Отпечатано в типографии издательства НАО «Карагандинский университет им. акад. Е.А. Букетова». 100024, Казахстан, г. Караганда, ул. Университетская, 28. Тел.(7212) 35-63-16. E-mail: izd_karu@mail.kz

© Карагандинский университет им. акад. Е.А. Букетова, 2025

Chief Editor

PhD, Professor **N.K. Tanasheva**

Responsible secretary

Associate Professor, PhD **D.Zh. Karabekova**

Editorial board

N.Kh. Ibrayev,	Prof., Doctor of phys.-math. sciences, Karagandy University of the name of acad. E.A. Buketov (Kazakhstan);
B.R. Nussupbekov,	Prof., Cand. of techn. sciences, Abylkas Saginov Karaganda Technical University, Karaganda (Kazakhstan);
A.O. Saulebekov,	Prof., Doctor of phys.-math. sciences, Kazakhstan branch of Lomonosov Moscow State University, Astana (Kazakhstan);
B.R. Ilyassov,	PhD, Assoc. Prof., Astana IT University (Kazakhstan);
A.D. Pogrebnjak,	Prof., Doctor of phys.-math. sciences, Sumy State University (Ukraine);
A.P. Surzhikov,	Prof., Doctor of phys.-math. sciences, Tomsk Polytechnic University (Russia);
I.P. Kurytnik,	Prof., Doctor of techn. sciences, The State School of Higher Education in Oświęcim (Auschwitz) (Poland);
M. Stoev,	PhD, Doctor of engineering, South-West University “Neofit Rilski”, Blagoevgrad (Bulgaria);
V.Yu. Kucheruk,	Prof., Doctor of techn. sciences, Vinnytsia National Technical University, Vinnitsia (Ukraine);
V.A. Kulbachinskii,	Prof., Doctor of phys.-math. sciences, Lomonosov Moscow State University (Russia);
Bisquert Juan,	Prof. of phys., Prof. (Full), Universitat Jaume I, Castellon de la Plana (Spain);
Chun Li,	PhD, Changchun University of Science and Technology (China);
D.T. Valiev,	Assoc. Prof., Cand. of phys.-math. sciences, National Research Tomsk Polytechnic University (Russia)

Postal address: 28, University Str., 100024, Karaganda, Kazakhstan

E-mail: vestnikku@gmail.com; karabekova71@mail.ru

Web-site: physics-vestnik.ksu.kz

Executive Editor

PhD **G.B. Sarzhanova**

Proofreaders

S.S. Balkeyeva, I.N. Murtazina

Computer layout

V.V. Butyaikin

Bulletin of the Karaganda University. “Physics” Series. — 2025. — Vol. 30, Iss. 3(119). — 106 p. — ISSN-L 2518-7198 (Print). ISSN 2663-5089 (Online).

Proprietary: NLC “Karagandy University of the name of academician E.A. Buketov”.

Registered by the Ministry of Information and Social Development of the Republic of Kazakhstan. Rediscount certificate No. KZ38VPY00027378 dated 30.09.2020.

Signed in print 30.09.2025. Format 60×84 1/8. Offset paper. Volume 13,25 p.sh. Circulation 200 copies. Price upon request. Order № 119.

Printed in the Publishing house of NLC “Karagandy University of the name of acad. E.A. Buketov”.
28, University Str., Karaganda, 100024, Kazakhstan. Tel. (7212) 35-63-16. E-mail: izd_karu@mail.kz

МАЗМҰНЫ – СОДЕРЖАНИЕ – CONTENTS

КОНДЕНСАЦИЯ ЛАНҒАН КҮЙДІҢ ФИЗИКАСЫ ФИЗИКА КОНДЕНСИРОВАННОГО СОСТОЯНИЯ PHYSICS OF THE CONDENSED MATTER

<i>Mussabekova A.K., Aimukhanov A.K., Zeinidenov A.K., Ziyat A.Z., Abdrakhman K.T., Alexeev A.M.</i> The Influence of Al ₂ O ₃ Nanoparticles on Electron Transport in a Polymer Solar Cell	6
<i>Adaikhan S., Bekmyrza K.Zh., Baratova A.A., Kabyshev A.M., Rajagopal P., Aidarbekov N.K., Kuterbekov K.K., Kubenova M.M., Kuanysh M.D.</i> Development and Characterization of Nanostructured Ni–ScSZ Composite Anodes for Solid Oxide Fuel Cells	16

ТЕХНИКАЛЫҚ ФИЗИКА ТЕХНИЧЕСКАЯ ФИЗИКА TECHNICAL PHYSICS

<i>Kurbanbekov Sh.R., Kizatov A., Musakhan N., Saidakhmetov P.A., Kambarbekov S.Kh., Kaldar B.</i> Effect of HVOF spraying parameters on the structural-phase composition and mechanical properties of ZrCN coating.....	31
<i>Kengesbekov A.B., Serikbaikyzy A., Baizhan D., Batanov Y.Y., Kairbaeva L.S.</i> Investigation of the Influence of Modes of Intensive Plastic Deformation on the Process of Grain Refinement of Titanium Alloy Ti-13Nb-13Zr at Equal-Channel Angular Pressing and Subsequent Rotary Forging Compression .	41
<i>Hasanov E.R., Khalilova Sh.G., Mustafayeva R.K.</i> Transverse and Longitudinal Thermomagnetic Waves in Conducting Media	51
<i>Rakhadilov B.K., Buitkenov D.B., Apsezhanova A.K., Magazov N.M., Bayandinova M.B.</i> Influence of Wire Type on the Structure and Properties of Coatings Obtained by Electric Arc Metallization.....	59

ЖЫЛУФИЗИКАСЫ ЖӘНЕ ТЕОРИЯЛЫҚ ЖЫЛУ ТЕХНИКАСЫ ТЕПЛОФИЗИКА И ТЕОРЕТИЧЕСКАЯ ТЕПЛОТЕХНИКА THERMOPHYSICS AND THEORETICAL THERMOENGINEERING

<i>Zhumanbayeva A.S., Jaichibekov N.Zh., Kurmanova D.Y.</i> Study of the Influence of Turbulence Models on Hydrodynamic and Thermal Parameters of Heat Carriers in Calculations of Heat Exchangers	68
<i>Adem Akkuş.</i> On the Analytical Determination of the Seebeck Coefficient Using the Fermi–Dirac Approximation.....	77
<i>Sulyubayeva L.G., Baizhan D.R., Bolatov S.D., Berdimuratov N.Ye., Bazarov N.Ye.</i> Investigation of the Influence of Technological Regimes of Thermocyclic Electrolyte-Plasma Treatment On The Structural-Phase State and Tribocorrosion Properties of 12Kh1MF Steel	84
<i>Hosseini Motlagh S.N., Zarei M.A., Shakeri A.</i> Control Method of Plasma Burning in Tokamak Fusion Reactor with Neutron-Free p ¹¹ B Fuel via Alpha-Proton-Alpha Avalanche Reaction Mechanism..	95

Article

UDC 538.9; 535.215; 539.23; 535.3

 <https://doi.org/10.31489/2025PH3/6-15>

Received: 21.04.2025

Accepted: 23.06.2025

A.K. Mussabekova^{1✉}, A.K. Aimukhanov¹, A.K. Zeinidenov¹,
A.Z. Ziyat¹, K.T. Abdrakhman¹, A.M. Alexeev²

¹*Buketov University, Scientific Center of nanotechnology and functional nanomaterials, Karaganda, Kazakhstan;*

²*Kazan Federal University, Kazan, Russia*

**The Influence of Al₂O₃ Nanoparticles on Electron Transport
in a Polymer Solar Cell**

The effect of Al₂O₃ nanoparticles on the electron transport of SnO₂-based electron transport layer (ETL) in polymer solar cells was studied. Comprehensive studies of the morphology, optical, electrophysical and photoelectric properties of the composite films were carried out. It was found that doping SnO₂ films with Al₂O₃ nanoparticles leads to a decrease in the surface roughness of the composite films. According to the absorption spectra, it was shown that an increase in the concentration of Al₂O₃ nanoparticles in SnO₂ films leads to a decrease in the optical bandgap. Analysis of the impedance spectra showed that there is a critical concentration of Al₂O₃ nanoparticles at which the maximum improvement in the electrotransport characteristics of SnO₂ films is observed. At high Al₂O₃ concentrations (over 15 %), a decrease in electron mobility and an increase in recombination in the studied composite film are observed. Photovoltaic measurements have demonstrated that the highest efficiency of 2.8 % polymer solar cells is achieved at an optimal concentration of Al₂O₃ nanoparticles equal to 15 %. Further increase in the content of Al₂O₃ nanoparticles leads to a decrease in the efficiency of polymer solar cells. Since localized negative charges in Al₂O₃ nanoparticles create a local electric field, they screen the recombination of minority charge carriers in ETL SnO₂. This suppresses the leakage current in devices. Therefore, it is important to investigate the charge transfer mechanism in SnO₂:Al₂O₃ films and evaluate their potential for application in polymer solar cells.

Keywords: SnO₂, Al₂O₃, morphology, absorption, band gap, Bode plots, impedance, current-voltage characteristics

✉ *Corresponding author:* Assel K. Mussabekova, assel50193@gmail.com

Introduction

The demand for transparent conductive oxides (TCO) materials that combine high optical transparency and good electrical conductivity is growing rapidly due to the development of optoelectronic technologies. Such materials are in demand in thin-film solar cells [1], charge storage devices [2], flat-panel displays [3], gas sensors [4] and other applications. The most studied TCOs are films based on TiO₂, ZnO, SnO₂ and others, research that has been ongoing for over 40 years. These materials are wide-bandgap n-type semiconductors. Among the known n-type TCOs, the best characteristics are demonstrated by In₂O₃:Sn, SnO₂:F and ZnO:Al composites [5], which have a transparency above 90 % and a specific resistance of about 10⁻⁴ Ohm·cm [6, 7].

SnO₂ and its composite materials are widely known for their pronounced structural and optical properties when scaled down to the nanoscale. The efficiency of devices based on them is largely determined by the electrical and optical properties of transparent electrodes, as well as the technology of their production [8]. It is known that the degree of improvement of these properties depends significantly on the chemical composition, particle size and specific surface area of SnO₂.

One of the major challenges in obtaining high-performance SnO₂-based organic solar cells (OSCs) is the presence of defects such as oxygen vacancy [9] and other surface-related defects [10, 11]. These can lead to poor charge transport and low power conversion efficiency (PCE) in devices [12]. In addition, oxygen-induced degradation of the photoactive layer can occur in the metal oxide layer, allowing atmospheric oxygen to diffuse into the cell, resulting in an increase in defects that adversely affect the performance of the device [13]. Minimizing defects and reducing carrier recombination in the SnO₂ film by passivating the ETL/photoactive layer interface is critical in the fabrication of high-performance OSCs.

Wu et al. reported that the defect states of ZnO were suppressed by modifying its surface with an ultrathin Al layer, which could be partially oxidized to AlO_x [14]. It is known that the ultrathin Al₂O₃ film is an effective surface passivation method in silicon-based solar cells by utilizing its unique ability to form a layer without point defects [15]. It not only provides good chemical passivation by reducing the defect density at the interface through the hydrogen passivation associated with the deposition process, but also leads to a decrease in the minority carrier concentration near the interface due to the built-in electric field, which is called field effect passivation [16, 17]. In this case, the negative charges localized in the Al₂O₃ layer create a local electric field that screens the recombination of minority carriers [18]. Moreover, it is reported that the Al₂O₃ layer can also suppress the leakage current in the device, which turns out to be another advantage of Al₂O₃ passivation [19]. Currently, Al₂O₃ composites are at the threshold of commercial solar cell production and large-scale photovoltaic cell production [20], while there are rare reports of their use for OSC passivation. Thus, the use of Al₂O₃ may have potential applications in the field of photovoltaics.

Despite the studies conducted on the synthesis of SnO₂ films doped with Al₂O₃ [21], their electro-transport properties are still poorly understood. Therefore, it is important to study the charge transfer mechanism in such films and evaluate their potential for use in optoelectronic devices. This paper presents the results of a study of the effect of Al₂O₃ nanoparticles on electron transport in ETL SnO₂ polymer solar cells.

Experimental

Thin films preparation

The preparation of FTO substrates was carried out according to the procedure detailed in reference [22]. Composite films based on SnO₂ were obtained by the sol-gel method. The scheme for preparing composite films is shown in Figure 1. The initial reagents were SnCl₂ (99.9 %, Sigma Aldrich) in an amount of 2.25 g and AlCl₃ (99.9 %, Sigma Aldrich) in an amount corresponding to Al₂O₃ concentrations of 5 % (0.0667 g), 10 % (0.1334 g), 15 % (0.2001 g), 20 % (0.2268 g) and 25 % (0.33335 g). SnCl₂ and Al₂O₃ were dissolved in 1 ml of ethyl alcohol (99.9 %, Sigma Aldrich).

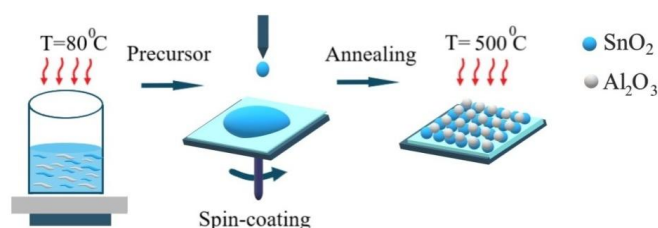


Figure 1. Scheme for preparing SnO₂:Al₂O₃ composite films

Afterwards, the prepared solutions were continuously stirred at 80 °C for 2 hours, followed by 24 hours at room temperature to complete the reactions and composition. Then, the obtained solution was applied to the surface of the substrates by centrifugation (on a SPIN150i centrifuge, Semiconductor Production System) at a rotation speed of 4000 rpm. The rotation time of the centrifuge at this rotation speed was 30 seconds. The obtained films were thermally annealed in air at a temperature of 500 °C for 1 hour.

To assemble the FTO/SnO₂:Al₂O₃/P3HT:PCBM/PEDOT:PSS/AgOSC, the photoactive material P3HT:PCBM was dissolved in chlorobenzene and stirred for 24 hours at room temperature. The photoactive layer was applied by centrifugation at a rotation speed of 2000 rpm on the FTO substrate, previously

deposited with the $\text{SnO}_2:\text{Al}_2\text{O}_3$ film. Afterwards, the obtained film was annealed in air at a temperature of 140 °C. The hole-transport layer of PEDOT:PSS was applied to the surface of the photoactive layer at a substrate rotation speed of 3000 rpm, after which the substrate was annealed at a temperature of 120 °C. At the final stage of OSC assembly, a silver electrode was applied to the surface of the hole-transport layer by vacuum-thermal deposition.

Analysis methods

Film surface morphology images were obtained using a MIRA 3LMU (TESCAN) electron microscope. A Co sample (9905-17, Micro-Analysis Consultants Ltd Unit 19, Edison Road, St Ives Cambridgeshire PE27 3 LF U.K.) was used as a standard for EDX analysis. The surface topography of the samples was studied using a JSPM-5400 atomic force microscope manufactured by JEOL Ltd. Probes manufactured by NT-MDT were used for scanning. Scanning was performed in a semi-contact mode with resonance frequency parameters of 140–390 kHz, cantilever stiffness of 3.1–37.6 N/m, and probe rounding radius of 10 nm; the scanning speed was 10 $\mu\text{m/s}$. Surface morphology parameters were calculated using the WinspmII Data Processing software package manufactured by JEOL Ltd.

The absorption spectra of the films were measured using the Avantes universal spectrometric complex based on the AvaSpec-ULS2048CL-EVO spectrometer and the AvaLight-DHc deuterium-halogen combined light source with a spectral emission range of 200–2500 nm.

The current-voltage characteristics of the solar cells were measured using the PVIV-1A setup (Newport, Canada). The Sol3A solar energy simulator (class AAA, Newport, Canada) with a radiation intensity of 100 mW/cm^2 was used as a light source.

The impedance spectra were measured using a P-45X potentiostat-galvanostat (Elins, Russia) with an additional FRA-24M frequency analyzer module installed to measure the electrophysical characteristics on alternating current.

Results and Discussion

Surface morphology

Figure 2 shows scanning electron microscope (SEM) images of the surface morphology of SnO_2 and $\text{SnO}_2:\text{Al}_2\text{O}_3$ (25 %) films, as well as a cross-section of the films. Analysis of the SEM images demonstrates the presence of micro-holes on the surface of the SnO_2 films, which is typical for thin-film structures [23]. Comparison of $\text{SnO}_2:\text{Al}_2\text{O}_3$ films with different concentrations of Al_2O_3 shows that the addition of 25 % Al_2O_3 to SnO_2 leads to the formation of a more uniform surface structure: the films become smoother and fine-grained, indicating a change in morphology when doped with Al_2O_3 nanoparticles.

Cross-section images of the studied films demonstrate that the film thickness increases with the addition of Al_2O_3 nanoparticles to SnO_2 from 79.69 nm to 93.73 nm.

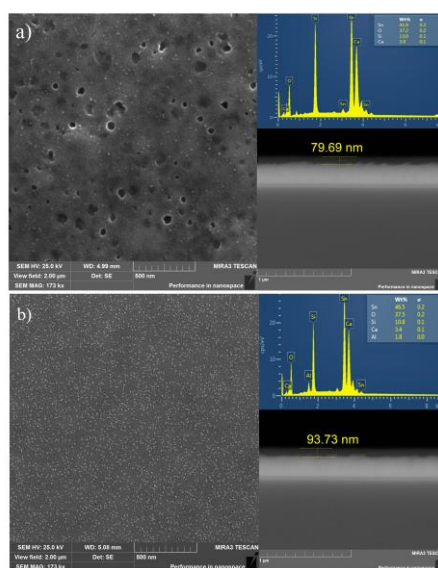


Figure 2. SEM images of the morphology of films and cross-section of SnO_2 , $\text{SnO}_2:\text{Al}_2\text{O}_3$ (25 %). Inset shows EDX spectra

Figure 3 shows atomic force microscope (AFM) images of SnO₂ and SnO₂:Al₂O₃ (25 %) films. The root mean square roughness (RMS) values for SnO₂ and SnO₂:Al₂O₃ (25 %) films are 2.4 and 1.83, respectively.

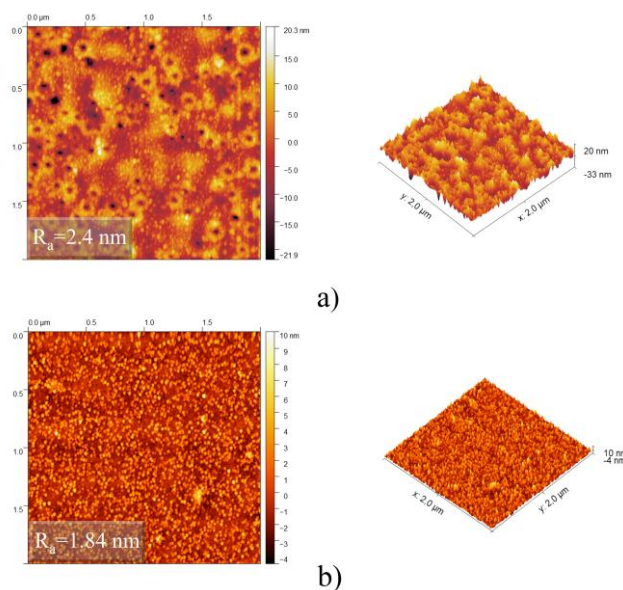


Figure 3. AFM images of SnO₂ and SnO₂:Al₂O₃ (25 %) films

From the analysis of the surface morphology it follows that the addition of Al₂O₃ helps to reduce the roughness of the films. This phenomenon can be explained by the fact that Al₂O₃ helps to reduce and fill the micro-holes present on the surface of SnO₂ films, thereby improving the texture and increasing the homogeneity of the surface.

Optical properties

Figure 4a shows the absorption spectra of SnO₂ films and SnO₂:Al₂O₃ composite films with different concentrations of Al₂O₃ nanoparticles (5 %, 10 %, 15 %, 20 %, 25 %). It follows from the analysis of the spectra that all the studied samples have a relatively high absorption coefficient in the region of $\lambda < 600$ nm, the value of which increases with an increase in the content of Al₂O₃ nanoparticles. In addition, the graph shows the wavelength of the optical absorption edge, determined by the method of linear extrapolation of the steeply increasing section of the spectrum. The dependence of the absorption edge position on the concentration of Al₂O₃ nanoparticles is presented in Table 1. The optical absorption edge corresponds to the energy threshold of the interband transition and reflects the fundamental width of the band gap [24].

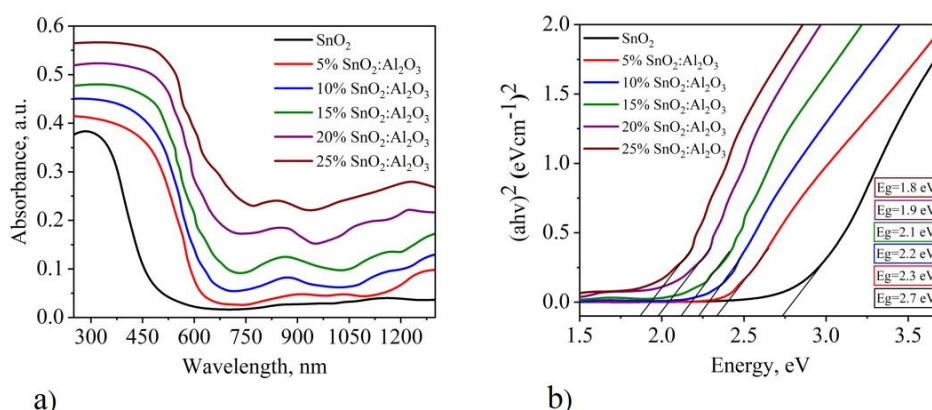


Figure 4. Absorption and Tauc plot of SnO₂ and SnO₂:Al₂O₃ (5 %, 10 %, 15 %, 20 %, 25 %)

With increasing concentration of Al₂O₃, a regular shift of the absorption edge to the region of longer wavelengths is observed, which indicates a change in the optical width of the forbidden material. In particular, for the SnO₂ film, the wavelength of the absorption edge is 320 nm, whereas for films with Al₂O₃ nano-

particles in concentrations of 5 %, 10 %, 15 %, 20 % and 25 %, this parameter increases to 419 nm, 451 nm, 482 nm, 498 nm and 506 nm.

Table 1

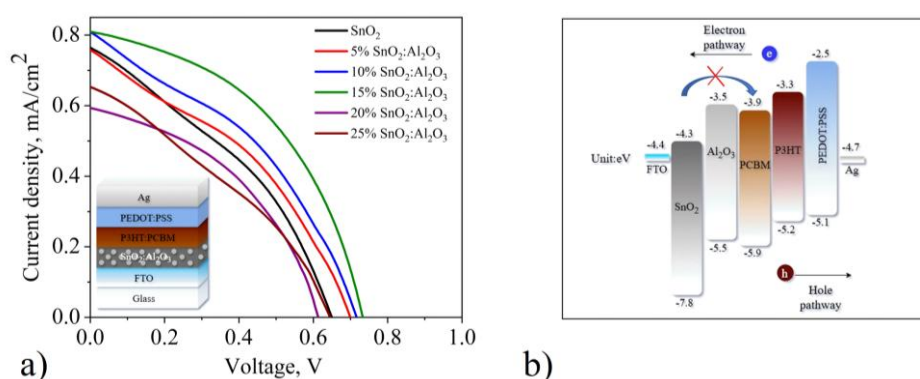
Optical parameters of SnO₂ and SnO₂:Al₂O₃ (5 %, 10 %, 15 %, 20 %, 25 %)

Samples	λ_{edge} , nm	D_i , optical density	Optical band gap (eV)
SnO ₂	320	0.37	2.83
5 % SnO ₂ :Al ₂ O ₃	419	0.41	2.33
10 % SnO ₂ :Al ₂ O ₃	451	0.44	2.24
15 % SnO ₂ :Al ₂ O ₃	482	0.47	2.12
20 % SnO ₂ :Al ₂ O ₃	498	0.51	1.98
25 % SnO ₂ :Al ₂ O ₃	506	0.56	1.87

Figure 4b shows the dependence of the optical band gap on the concentration of Al₂O₃ nanoparticles in SnO₂ and SnO₂:Al₂O₃ thin films with a content of 5 %, 10 %, 15 %, 20 % and 25 %. The optical band gap values of the films were calculated using the Tauc plot method [25]. The change in the optical band gap allows characterizing the electrical properties of the material, since it is directly related to the energy difference between the valence band and the conduction band. According to the data presented in Table 1, an increase in the concentration of Al₂O₃ nanoparticles leads to a consistent decrease in the optical band gap: for the SnO₂ film it is 2.83 eV, while for the composite films it decreases to 1.87 eV with an increase in the concentration of Al₂O₃ nanoparticles. It should be noted that reducing the optical band gap improves the transition of electrons from the valence band to the conduction band, resulting in an increase in the conductivity of the material [26].

Photoelectrical characterizations

Figure 5 shows the current-voltage characteristics of polymer solar cells with the FTO/SnO₂:Al₂O₃/P3HT:PCBM/PEDOT:PSS/Ag structure with ETL based on SnO₂ with different contents of Al₂O₃ nanoparticles. The current-voltage characteristics parameters are given in Table 2. Upon photoexcitation of the photoactive P3HT:PCBM layer, an electron-hole pair is formed, which then disintegrates into free charge carriers at the SnO₂/P3HT:PCBM and P3HT:PCBM/PEDOT:PSS interface. As a result, electrons are injected into the ETL layer of SnO₂, and holes into the hole transport layer (HTL) of PEDOT:PSS (Fig. 5b). As a result of this process, a photocurrent will flow in the circuit under study. Al₂O₃ nanoparticles in the ETL serve to block the process of reverse electron transfer from SnO₂ to the PCBM acceptor. Addition of Al₂O₃ nanoparticles to a concentration of 15 % in the SnO₂ film promotes an increase in the short-circuit current density by 32 %. A further increase in the concentration of Al₂O₃ nanoparticles leads to a decrease in the short-circuit current density. The efficiency of the cell with SnO₂ was 1.9 %, while it increased to 2.8 % with the addition of Al₂O₃ nanoparticles at a concentration of 15 %.

Figure 5. Current-voltage characteristics of SnO₂ and SnO₂:Al₂O₃ (5 %, 10 %, 15 %, 20 %, 25 %)

The increase in short-circuit current and cell efficiency with the addition of Al₂O₃ nanoparticles is associated with an increase in the concentration of free charge carriers in the composite film [27]. Additionally, Al₂O₃ nanoparticles reduce the number of surface defects, which decreases the probability of electron-hole recombination.

The decrease in efficiency with an increase in the content of Al₂O₃ nanoparticles above 15 % is obviously associated with the formation of structural and interphase defects that contribute to an increase in the recombination of charge carriers [28].

Table 2

Current-voltage parameters of SnO₂ and SnO₂:Al₂O₃ (5 %, 10 %, 15 %, 20 %, 25 %)

Samples	U_{oc} (V)	J_{sc} (mA/cm ²)	U_{max} (V)	J_{max} (mA/cm ²)	FF	PCE %
SnO ₂	0.65±0.01	7.65±0.05	0.41±0.01	4.4±0.05	0.37	1.9±0.05
5 % SnO ₂ :Al ₂ O ₃	0.7±0.01	7.55±0.05	0.43±0.01	4.6±0.05	0.38	2±0.05
10 % SnO ₂ :Al ₂ O ₃	0.72±0.01	8 ±0.05	0.46±0.01	4.9±0.05	0.39	2.3±0.05
15 % SnO ₂ :Al ₂ O ₃	0.73±0.01	8.1±0.05	0.51±0.01	5.4±0.05	0.46	2.8±0.05
20 % SnO ₂ :Al ₂ O ₃	0.64±0.01	6.55±0.05	0.37±0.01	3.9±0.05	0.35	1.5±0.05
25 % SnO ₂ :Al ₂ O ₃	0.61±0.01	5.9±0.05	0.38±0.01	4.1±0.05	0.43	1.6±0.05

To investigate the effect of Al₂O₃ nanoparticles on the electron transport of SnO₂ in polymer solar cells, electrical impedance spectra were measured (Fig. 6a).

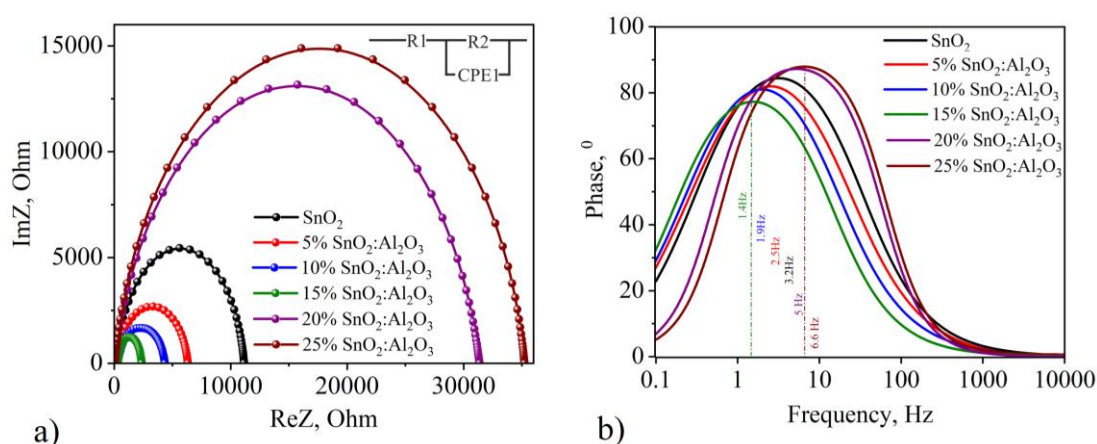
Figure 6. Impedance spectra and Bode plot SnO₂ and SnO₂:Al₂O₃ (5 %, 10 %, 15 %, 20 %, 25 %)

Figure 6(a) shows the impedance plots of the organic solar cells with the FTO/SnO₂:Al₂O₃/P3HT:PCBM/PEDOT:PSS/Ag structure. The electrical parameters were calculated based on the spectral data (Table 3) using the equivalent electrical circuit shown in the inset of Figure 6(a).

In this scheme, R_w denotes the equivalent resistance of the external electrodes (including R_{FTO}, R_{SnO₂:Al₂O₃}, PEDOT:PSS and Ag), and R_{tr} reflects the resistance associated with electron transfer at the interfaces between the P3HT:PCBM/SnO₂:Al₂O₃ and P3HT:PCBM/PEDOT:PSS layers. Table 3 shows the electrophysical parameters of the FTO/SnO₂:Al₂O₃/P3HT:PCBM/PEDOT:PSS/Ag structure. The organic solar cell is a multilayer structure. Since the photoactive layer and the electrodes were deposited under the same conditions, the R_w value is almost the same in all cases. Its slight change with an increase in the Al₂O₃ concentration is associated with an insignificant change in the film thickness. Changes in the R_{tr} value indicate the influence of the P3HT:PCBM/ETL interface on the electron transfer process. A decrease in R_{tr} indicates an improvement in electron transport at the interface. As can be seen from Table 1, the cells with ETL with a concentration of Al₂O₃ nanoparticles of 15 % have the lowest resistance R_{tr} , which indicates the formation of a film with improved conductivity and a lower degree of defectiveness. However, with an increase in the concentration of Al₂O₃ nanoparticles above 15 %, an increase in recombination at the P3HT:PCBM/SnO₂:Al₂O₃ interface is observed, which is associated with the formation of structural and interphase defects.

The mobility of charge carriers is one of the most important electrotransport parameters of thin films. There are a number of methods for its experimental determination [29], but each of them is characterized by certain limitations and disadvantages [30]. In this work, we used the impedance spectroscopy method to determine the conditional mobility of charge carriers μ , in the studied samples described in detail in [31].

The diffusion coefficient Dn was determined by the following formula:

$$Dn = \frac{L^2}{\tau D}. \quad (1)$$

Where L is the film thickness, τD is the effective time of charge passage through the OSC. The value of the conditional hole mobility μ was determined by the formula:

$$\mu = \frac{e * Dn}{k_B * T}. \quad (2)$$

Where e is the electron charge, k_B is the Boltzmann constant, T is the temperature.

As can be seen from Table 1, the conditional electron mobility increases and has a maximum value for OSC with ETL based on SnO_2 with a concentration of Al_2O_3 nanoparticles equal to 15 %. The minimum value of the conditional electron mobility in OSC is observed for OSC with ETL based on SnO_2 with Al_2O_3 nanoparticles with a concentration of 25 %. Obviously, the observed decrease in the values of the conditional electron mobility in OSC with exceeding the concentration of Al_2O_3 nanoparticles of 15 % is explained by the different degrees of probability of electron scattering on defects formed at the P3HT:PCBM/ SnO_2 : Al_2O_3 interface.

Figure 6(b) shows the Bode plot analysis, which allows estimating the carrier lifetime in OSC [32]. As can be seen from Figure 6(b), the phase angle maximum for the cell (with 15 % Al_2O_3 nanoparticles in ETL) is shifted to lower frequencies compared to pure SnO_2 -based ETL, indicating a longer carrier lifetime. This indicates a more effective suppression of charge recombination. Thus, the data clearly demonstrates the importance of the spatial separation of electron transport channels achieved by the incorporation of Al_2O_3 nanoparticles.

Table 3

Impedance parameters of SnO_2 and SnO_2 : Al_2O_3 (5 %, 10 %, 15 %, 20 %, 25 %)

Samples	R_{w_2} (Ohm)	R_{tr_2} (Ohm)	C , (pF)	τ_{D_2} (ps)	D_n , ($\text{cm}^2 \cdot \text{s}^{-1}$)	μ , ($\text{cm}^2 \text{V}^{-1} \cdot \text{s}^{-1}$)
SnO_2	68	11107	2.2517E-08	153	39.74	1.5
5 % SnO_2 : Al_2O_3	72	6247	1.8231E-08	131	46.35	1.8
10 % SnO_2 : Al_2O_3	81	4219	1.4762E-07	119	50.9	2
15 % SnO_2 : Al_2O_3	87	2694	1.0923E-07	95	64	2.5
20 % SnO_2 : Al_2O_3	64	31328	3.103E-08	198	30.64	1.2
25 % SnO_2 : Al_2O_3	59	33105	3.719E-08	219	27.73	1.1

Thus, the conducted study demonstrates how the use of Al_2O_3 nanoparticles in ETL affects the efficiency of polymer solar cells. The obtained data can be applied in the development of optoelectronic devices, including integrated circuits, microelectronic optical systems, as well as organic photoconverters, sensors and light-emitting diodes (OLEDs).

Conclusions

Composite SnO_2 films with different contents of Al_2O_3 nanoparticles were obtained by the sol-gel method. The effect of Al_2O_3 nanoparticles on the surface morphology of the films was studied using scanning electron microscopy and atomic force microscopy. It is shown that the addition of Al_2O_3 nanoparticles to SnO_2 promotes the formation of a more uniform and smooth surface. This may be due to the improvement of film formation conditions and a decrease in grain size due to the introduction of Al_2O_3 nanoparticles, which affect the growth of crystals in the film. The results of measuring the absorption spectra showed that an increase in the concentration of Al_2O_3 nanoparticles in the structure leads to a gradual decrease in the width of the optical bandgap of the material from 2.33 eV to 1.87 eV. This decrease indicates a change in the electronic structure, probably associated with the formation of new energy sublevels resulting from the interaction of Al_2O_3 nanoparticles with the SnO_2 matrix. Impedance spectroscopy revealed a reduction in recombination and an increase in charge carrier mobility at an Al_2O_3 nanoparticle concentration of 15 %, which contributes to the improvement of the material's transport properties. However, at high concentrations of Al_2O_3 nanoparticles (over 15 %), the opposite effect is observed — increased recombination and decreased mobility, which is associated with the formation of interphase defects that disrupt the continuity of the conductive paths. Photoelectric measurements showed that the maximum efficiency of solar cells was 2.5 % at

the optimal concentration of Al₂O₃. With a further increase in the content of Al₂O₃ nanoparticles (over 15 %), a decrease in efficiency is observed. This can be explained by an increase in the density of defects that impair the collection and transport of charges.

Funding

This research is funded by the Science Committee of the Ministry of Science and Higher Education of the Republic of Kazakhstan (Grant No. AP19679938).

References

- 1 Omura, K., Veluchamy, P., Tsuji, M., Nishio, T., & Murojono, D. (1999). Synthesis and Characterization of Nano-Crystalline Fluorine-Doped Tin Oxide Thin Films by Sol-Gel Method. *J. Electrochem. Soc.*, 146, 2113. <https://doi.org/10.1023/A:1025697322395>
- 2 Lavery, S.J., Feng, H., & Maguire, P. (1997). Adhesion of Copper Electroplated to Thin Film Tin Oxide for Electrodes in Flat Panel Displays. *J. Electrochem. Soc.*, 144, 2165; <https://doi.org/10.1149/1.1837758>
- 3 Tadeev, A.V., Delabouglise, G., & Labeau, M. (1998). Influence of Pd and Pt additives on the microstructural and electrical properties of SnO₂-based sensors. *Mater. Sci. Engg. B57*, 76; [https://doi.org/10.1016/S0921-5107\(98\)00251-7](https://doi.org/10.1016/S0921-5107(98)00251-7)
- 4 Chopra, K.L., Major, S., & Pandya, D.K. (1983). Transparent conductors-A status review. *Thin Solid Films*, 102, 1; [https://doi.org/10.1016/0040-6090\(83\)90256-0](https://doi.org/10.1016/0040-6090(83)90256-0)
- 5 Dawar, A.L., & Joshi, J.C. (1984). Semiconducting transparent thin films: their properties and applications. *J Mater Sci.*, 19, 1–23; <https://doi.org/10.1007/BF02403106>
- 6 Freeman, A.J., Poeppelmeier, K.R., Mason, T.O., Change, R.P.H., & Marks, T.J. (2000). Chemical and Thin-Film Strategies for New Transparent Conducting Oxides. *MRS Bull.* 25, 45; <https://doi.org/10.1557/mrs2000.150>
- 7 Ginley, D.S., & Bright, C. (2000). Transparent Conducting Oxides. *MRS Bull.* 25, 15–18; <https://doi.org/10.1557/mrs2000.256>
- 8 Rozati, S.M., & Akesteh, S. (2007). Influence of Air Flow Rate on Physical Properties of Zinc Oxide. *Mater. Charact.*, 58(4), 319; http://doi.org/10.1007/978-3-540-75997-3_270
- 9 Bohle, D.S., & Spina, C.J. (2007). The Relationship of Oxygen Binding and Peroxide Sites and the Fluorescent Properties of Zinc Oxide Semiconductor Nanocrystals. *J. Am. Chem. Soc.*, 129(41), 12380; <https://doi.org/10.1021/ja0747223>
- 10 Fonoberov, V.A., Alim, K.A., Balandin, A.A., Xiu, F.X., & Liu, J.L. (2006). Photoluminescence investigation of the carrier recombination processes in ZnO quantum dots and nanocrystals. *Phys. Rev. B.* 73(16), 165317–20; <https://doi.org/10.1103/PhysRevB.73.165317>
- 11 Klenk, R. (2001). Characterisation and modelling of chalcopyrite solar cells. *Thin Solid Films*, 387(1-2), 135–140; [https://doi.org/10.1016/S0040-6090\(00\)01736-3](https://doi.org/10.1016/S0040-6090(00)01736-3)
- 12 Cowan, S.R., Schulz, P., Giordano, A.J., Garcia, A., Macleod, B.A., Marder, S.R., Kahn, A., Ginley D.S., Ratcliff E.L., & Olsen, D.C. (2014). Chemically Controlled Reversible and Irreversible Extraction Barriers Via Stable Interface Modification of Zinc Oxide Electron Collection Layer in Polycarbazolebased Organic Solar Cells. *Adv. Funct. Mater.*, 24(29), 4671–4680; <https://doi.org/10.1002/adfm.201400158>
- 13 Wu, B., Wu, Zh., Yang, Q.Y., Zhu, F.R., Ng, T.W., Lee, C.S., Cheung, S.H. & So, S.K. (2016). Improvement of Charge Collection and Performance Reproducibility in Inverted Organic Solar Cells by Suppression of ZnOSubgap States. *ACS Appl. Mater. Inter.*, 8(23), 14717–14724; <https://doi.org/10.1021/acsami.6b03619>
- 14 Xu, T., Tian, Zh., Elmi, O., Krzeminski, C., Robbe, O., Lambert, Y., Yakeda, D., Okada, E., Wei, B., & Stiévenard, D. (2017). Optical and electrical properties of nanostructured implanted silicon n+ -p junction passivated by atomic layer deposited Al₂O₃. *Physica E.*, 93, 190; <https://doi.org/10.1016/j.physe.2017.06.017>
- 15 Wang, W.C., Lin, C.W., Chen, H.J., Chang, C.W., Huang, J.J., Yang, M.J., Tjahjono, B., Huang, J., Hsu, W.C., & Chen, M.J. (2013). Surface Passivation of Efficient Nanotextured Black Silicon Solar Cells Using Thermal Atomic Layer Deposition. *ACS Appl. Mater. Inter.*, 5(19), 9752–9759; <https://doi.org/10.1021/am402889k>
- 16 Lee, H., Tachibana, T., Ikeno, N., Hashiguchi, H., Arafune, K., Yoshida, H., Satoh, S., & Chikyow, T. (2012). Interface engineering for the passivation of c-Si with O-3-based atomic layer deposited AlO_x for solar cell application. *Appl. Phys. Lett.*, 100(14), 253504; <https://doi.org/10.1063/1.3701280>
- 17 Dingemans, G., & Kessels, W. (2012). Status and prospects of Al₂O₃-based surface passivation schemes for silicon solar cells. *Journal of Vacuum Science & Technology A.*, 30, 040802; <https://doi.org/10.1116/1.4728205>
- 18 Zhao, S.Y., Liu, X.K., Gu, W., Liang, X.Y., Ni, Z.Y., Tan, H., Huang, K., Yan, Y.C., Yu, X.G., Xu, M.C., Pi, X.D., & Yang, D.R. (2018). Al₂O₃-Interlayer-Enhanced Performance of All-Inorganic Silicon-QuantumDotNear-Infrared Light-Emitting Diodes. *IEEE Transactions on electron devices.* 65, 577; <https://doi.org/10.1109/TED.2017.2782772>
- 19 Poodt, P., Cameron, D.C., Dickey, E., George, S.M., Kuznetsov, V., Parsons, G.N., Roozeboom, F., Sundaram, G., & Vermeer, A.J. (2012). Spatial atomic layer deposition: A route towards further industrialization of atomic layer deposition. *Vac. Sci. Technol. A.*, 30, 010802; <https://doi.org/10.1116/1.3670745>

- 20 Xu, C., Tamaki, J., Miura, N., & Yamazoe, N. (1991). Promotion of tin oxide gas sensor by aluminum doping. *Talanta*, 38, 1169; [https://doi.org/10.1016/0039-9140\(91\)80239-V](https://doi.org/10.1016/0039-9140(91)80239-V)
- 21 Mohagheghi, M., & Saremi, M. (2004). Optical and Electrical Conductivity of SnO₂:Cu Nanoparticles. *J. Phys. D: Appl. Phys.* 37, 1248; <https://doi.org/10.23851/mjs.v32i3.944>
- 22 Chen, P., & Yin, X. (2017). Low temperature solution processed indium oxide thin films with reliable photoelectrochemical stability for efficient and stable planar perovskite solar cells, *J. Mater. Chem. A.*, 5 (20) 9641–9648; <https://doi.org/10.1039/c7ta00183e>
- 23 Marikkannan, M., Vishnukanthan, V., Vijayshankar, A., Mayandi, J., & Pearce, J.M. (2015). A novel synthesis of tin oxide thin films by the sol-gel process for optoelectronic applications. *AIP Advances*, 5, 027122; <https://doi.org/10.1063/1.4909542>
- 24 Qin, C., Kim, J.B., Gonome, H., & Lee, B.J. (2020). Absorption characteristics of nanoparticles with sharp edges for a direct-absorption solar collector. *Renew Energy*, 145, 21; <https://doi.org/10.1016/j.renene.2019.05.133>
- 25 Harynski, T., Olejnik, A., Grochowska, K., & Siuzdak, K., (2022). A facile method for Tauc exponent and corresponding electronic transitions determination in semiconductors directly from UV–Vis spectroscopy data. *Optical Materials. Vol. 127*, 112205; <https://doi.org/10.1016/j.optmat.2022.112205>
- 26 Kamarulzamanet. al. (2015). Band Gap Narrowing and Widening of ZnO Nanostructures and Doped Materials. *Nanoscale Research Letters*, 10, 346; <https://doi.org/10.1186/s11671-015-1034-9>
- 27 Gunasekar, K., Chakravarthi, N., Cho, W., Lee, J.W., Kim S.W., S.H., Kotov, Cha, N.A., & Jin, J.H. (2015). Optimization of polymer solar cells performance by incorporated scattering of ZnO nanoparticles with different particle geometry. *Synthetic Metals. Vol. 205*, 185–189; <https://doi.org/10.1016/j.synthmet.2015.04.009>
- 28 Kavanagh, S.R., Scanlon, D.O., & Walsh, A. (2022). Impact of metastable defect structures on carrier recombination in solar cells. *Faraday discussions*; <https://doi.org/10.1039/D2FD00043A>
- 29 Kar, A., Sain, S., Kundu, S., Bhattacharyya, A., Pradhan, S.K., & Patra, A. (2015). Influence of size and shape on the photocatalytic properties of SnO₂ nanocrystals. *Chem. Phys. Chem.*, 16, 1017–1025; <https://doi.org/10.1002/cphc.201402864>
- 30 Mahmoud, S.A., Alshomer, S., & Tarawnh, M.A. (2011). Structural and optical dispersion characterisation of sprayed nickel oxide thin films, *J. Mod. Phys.* 2, 1178–1186; <https://doi.org/10.4236/jmp.2011.210147>.
- 31 Rashad, M., Darwish, A.A., & Attia, A.A. (2017). Impact of film thickness on optical and electrical transport properties of noncrystalline GeSe_{1.4}Sn_{0.6} films, *J. Non-Cryst. Solids*, 470, 1–7; <https://doi.org/10.1016/j.jnoncrysol.2017.04.015>.
- 32 JunSeo, Y., Arunachalam, M., Ahn, K.-S., & Hyung Kang, S. (2021). Integrating heteromixed Cu₂O/CuO photocathode interface through a hydrogen treatment for photoelectrochemical hydrogen evolution reaction, *Appl. Surf. Sci.* 551, 149375; <https://doi.org/10.1016/j.apsusc.2021.149375>

Ә.Қ. Мұсабекова, А.К. Аймуханов, А.К. Зейниденов,
А.З. Зият, К.Т. Абдрахман, А.М. Алексеев

Al₂O₃ нанобөлшектерінің полимерлі күн элементіндегі электрондарды тасымалдауға әсері

Полимерлі күн элементтерінде SnO₂ негізінде алынған электрон тасымалдаушы қабатына (ETL) Al₂O₃ нанобөлшектерінің әсері зерттелді. Композиттік қабыршақтардың морфологиялық, оптикалық, электрофизикалық және фотоэлектрлік қасиеттерінің кешенді зерттеулері жүргізілді. SnO₂ қабыршақтарына Al₂O₃ нанобөлшектерін қосу арқылы композиттік қабыршақтар бетінің кедір-бұдырлығының төмендеуі анықталды. Жұтылу спектрлері арқылы SnO₂ қабыршақтарында Al₂O₃ нанобөлшектерінің концентрациясын арттыру оптикалық тыйым салу аймағы енінің азаюына алып келетіні айқындалды. Импеданс спектрлерін талдау арқылы SnO₂ қабыршақтарында Al₂O₃ нанобөлшектерінің электрондарды тасымалдаудың жоғары сипаттамалары анықталатын критикалық концентрациясы бар екені көрсетілді. Зерттелетін композиттік қабыршақтардың Al₂O₃ нанобөлшектерінің жоғары концентрациясында (15 %-дан жоғары) электрондардың қозғалғыштығының төмендеуі және рекомбинациясының жоғарылауы байқалады. Фотоэлектрлік өлшеулер арқылы ең жоғары пайдалы әсер коэффициенті (ПӘК) 2,8 % полимерлі күн элементтерінің Al₂O₃ нанобөлшектерінің оңтайлы концентрациясы 15 % екенін көрсетті. Al₂O₃ нанобөлшектерінің концентрациясының одан әрі артуы полимерлі күн элементтерінің ПӘК-нің төмендеуіне әкеледі. Al₂O₃ нанобөлшектеріндегі локализацияланған теріс зарядтар жергілікті электр өрісін тудыратындықтан, олар SnO₂ ETL-да негізгі емес заряд тасымалдаушылардың рекомбинациясын экрандайды. Бұл құрылғылардағы тоқтың ағып кетуін тежейді. Сондықтан SnO₂:Al₂O₃ қабыршақтарындағы зарядты тасымалдау механизмін зерттеу және олардың полимерлі күн элементтерінде қолдану потенциалын бағалау маңызды.

Кілт сөздер: SnO₂, Al₂O₃, морфология, жұтылу, тыйым салу аймағының ені, Боде графигі, импеданс, вольт-амперлік сипаттамалар

А.К. Мусабекова, А.К. Аймуханов, А.К. Зейниденов,
А.К. Зият, К.Т. Абдрахман, А.М. Алексеев

Влияние наночастиц Al₂O₃ на электронный транспорт в полимерном солнечном элементе

Изучено влияние наночастиц Al₂O₃ на электронный транспорт (ETL) на основе SnO₂ в полимерных солнечных элементах. Проведен комплексный исследования морфологических, оптических и электрофизических и фотоэлектрических свойств композитных пленок. Было выявлено, что допирование наночастицами Al₂O₃ пленок SnO₂ приводит к уменьшению шероховатости поверхности композитных пленок. По данным спектров поглощения показано, что увеличение концентрации наночастиц Al₂O₃ в пленках SnO₂ приводит к уменьшению оптической ширины запрещенной зоны. Анализ спектров импеданса показал, что существует критическая концентрация наночастиц Al₂O₃ при которой наблюдается максимальное улучшение электротранспортных характеристик пленок SnO₂. При высоких концентрациях Al₂O₃ (свыше 15 %) наблюдается снижение подвижности электронов и усиление рекомбинации в исследуемой композитной пленке. Фотоэлектрические измерения продемонстрировали, что наибольший коэффициент полезного действия (КПД) 2,8 % полимерных солнечных элементов достигается при оптимальной концентрации наночастиц Al₂O₃ равной 15 %. Дальнейшее увеличение содержания наночастиц Al₂O₃ приводит к снижению КПД полимерных солнечных элементов. Так как локализованные отрицательные заряды в наночастицах Al₂O₃ создают локальное электрическое поле, то они экранируют рекомбинацию неосновных носителей заряда в ETL SnO₂. Это подавляет утечку тока в устройствах. Поэтому важно исследовать механизм переноса зарядов в пленках SnO₂:Al₂O₃ и оценить их потенциал применения в полимерных солнечных элементах.

Ключевые слова: SnO₂, Al₂O₃, морфология, поглощение, ширина запрещенной зоны, график Боде, импеданс, вольт-амперные характеристики

Information about the authors

Mussabekova, Assel (*contact person*) — PhD student, Buketov University, Karaganda 100028, Kazakhstan; e-mail: assel50193@gmail.com; Scopus Author ID: 58429663700, ORCID ID: <https://orcid.org/0000-0003-3452-4622>

Aimukhanov, Aitbek — Candidate of Physical and Mathematical Sciences, Professor, Buketov University, Karaganda 100028, Kazakhstan, e-mail: a_k_aitbek@mail.ru; Scopus Author ID: 58493008700, ORCID ID: <https://orcid.org/0000-0002-4384-5164>

Zeinidenov, Assylbek — PhD, Professor, Buketov University, Karaganda 100028, Kazakhstan, e-mail: asyl-zeinidenov@mail.ru; Scopus Author ID: 56386144000; ORCID ID: <https://orcid.org/0000-0001-9232-8406>

Ziyat, Aizhuldyz — Master of Educational Sciences, Buketov University, Karaganda 100028, Kazakhstan, e-mail: aizhuldyz_12@mail.ru; ORCID ID: <https://orcid.org/0009-0005-3310-9058>

Abdrakhman, Kelbet — Master of Technical Sciences, Buketov University, Karaganda 100028, Kazakhstan, e-mail: kelbet.abdraxman@mail.ru

Alexeev, Alexandr — Candidate of Physical and Mathematical Sciences, Kazan Federal University, Kazan, Russia, e-mail: alalrus@mail.ru; Researcher ID: A-8526-2012, ORCID ID: <https://orcid.org/0000-0002-2800-6047>

S. Adaikhan, K.Zh. Bekmyrza, A.A. Baratova[✉], A.M. Kabyshev, P. Rajagopal,
N.K. Aidarbekov, K.K. Kuterbekov, M.M. Kubenova, M.D. Kuanysh

L.N. Gumilyov Eurasian National University, Astana, Kazakhstan

Development and Characterization of Nanostructured Ni–ScSZ Composite Anodes for Solid Oxide Fuel Cells

A thorough investigation was carried out on nickel-based anode composites with scandia-stabilized zirconia (Ni/ScSZ), fabricated using ceramic processing techniques from powders with varying particle sizes. The study emphasizes the role of initial component morphology and their ratios on sintering behavior, electrical conductivity, and polarization resistance under solid oxide fuel cell (SOFC) operating conditions. Samples incorporating nano-, submicron-, and micron-sized particles were comparatively analyzed to determine the most favorable parameters for constructing a percolative conductive network and reducing polarization losses. Experimental data obtained through dilatometry, electrical measurements, and electrochemical impedance spectroscopy confirmed that the use of nanoscale constituents leads to the formation of a dense and uniform microstructure with well-distributed porosity. Such features enhance both thermal stability and electrochemical performance. The findings highlight the potential of Ni/ScSZ-based materials as a viable alternative to conventional Ni/YSZ anodes, owing to their improved ionic conductivity and enhanced resistance to degradation, thus contributing to the advancement of more durable and efficient SOFC technologies.

Keywords: solid oxide fuel cell (SOFC), Ni/ScSZ composite anode, nanopowder dispersion, polarization resistance, triple-phase boundary, electrical conductivity, sintering kinetics, activation energy, impedance spectroscopy, fabrication method

[✉]Corresponding author: Baratova Aliya, aa.baratova@yandex.kz

Introduction

Solid oxide fuel cells (SOFCs) utilizing yttria-stabilized zirconia (YSZ) as the electrolyte represent one of the most promising technologies for converting chemical energy of fuels into electricity, owing to their high efficiency and environmental benefits. Currently, nickel-YSZ cermet (Ni/YSZ) is widely employed as the anode material in such systems due to its excellent electrocatalytic activity in hydrogen and syngas oxidation reactions [1, 2]. However, the stable and efficient operation of SOFCs with this type of anode typically requires elevated temperatures (above 800 °C), which imposes limitations on the selection of compatible materials for other cell components and increases the demands on the thermal and chemical durability of the overall structure [3, 4].

To reduce the operating temperature and enhance the durability of anodes, intensive research is being conducted to improve their catalytic and transport properties. Key strategies include tailoring the microstructure of anode materials and replacing the conventional YSZ electrolyte with solid electrolytes exhibiting higher ionic conductivity [5, 6]. Among the most promising alternatives is scandia-stabilized zirconia (ScSZ), which demonstrates oxygen ion conductivity that is two to three times higher than that of YSZ. Incorporating ScSZ into the anode cermet enhances the electrochemical performance by extending the active triple-phase boundary and reducing the tendency for carbon deposition during the operation with hydrocarbon fuels [7, 8].

This issue is particularly critical for cermet-based anodes employing scandia-stabilized zirconia (ScSZ), which lacks intrinsic electronic conductivity. In such systems, the electrochemical performance strongly depends on the quality of the interface between the electronic and ionic phases. When the chemical composition is fixed, the functional characteristics of the anode can be significantly enhanced by introducing nanostructured components. These materials increase the density of active triple-phase boundaries, facilitate charge transfer, and reduce polarization losses. Another promising strategy involves engineered macrostruc-

turing of the electrode architecture to optimize gas diffusion pathways and ensure long-term stability under extended operation [9–13].

Accordingly, the objective of this study is to develop and characterize nanostructured Ni–ScSZ composite anodes and to evaluate how particle size and phase ratio influence the microstructure, electrical conductivity, polarization resistance, and sintering kinetics of anodes intended for solid oxide fuel cells (SOFCs). The findings aim to identify optimal processing conditions for fabricating high-performance anodes and constructing a model fuel cell with elevated specific power output.

Materials and methods

Initial powders

Initial powders of NiO and ScSZ with nano- and submicron-scale particle sizes were employed in this study, differing in both chemical nature and synthesis technique. Nanopowders of NiO (Ni-n) and ScSZ (ScSZ-n, containing 10.5 mol% Sc₂O₃) were synthesized by the methods of wire electrical explosion [14] and laser evaporation [15], respectively. These synthesis routes are known to produce materials with high surface reactivity and a dense population of electrochemically active sites.

As submicron materials, a commercial NiO powder from the Ural Chemical Reagents Plant (Ni-m) and thermally treated ScSZ-n powder were used. The ScSZ-n powder was calcined at 1000 °C for 4 hours and then manually ground to obtain submicron-sized ScSZ (ScSZ-m). These materials exhibited lower specific surface areas (2.7 and 8.4 m²/g, respectively) and significantly larger particle sizes—up to 325 nm for Ni-m and 125 nm for ScSZ-m—suggesting pronounced aggregation and crystallite growth during the heat treatment process.

Table 1 summarizes the nomenclature and key physicochemical properties of the precursor powders used for the fabrication of the anode composites. The table includes chemical composition, specific surface area determined by the Brunauer–Emmett–Teller (BET) method (S_{BET}), equivalent particle diameter calculated from BET data (d_{BET}), and theoretical density (γ_{theor}). Analysis of these data reveals that the nanopowders Ni-n and ScSZ-n exhibit significantly higher surface areas (14.3 and 81.5 m²/g, respectively) and smaller equivalent particle sizes (56 and 13 nm, respectively) compared to their submicron counterparts, Ni-m and ScSZ-m. These characteristics confirm their nanoscale nature, reflecting a high degree of dispersion and a developed surface morphology that favors enhanced phase interaction in the composite anodes. In contrast, the submicron powders show signs of particle agglomeration and growth, particularly in the case of Ni-m ($d_{\text{BET}} = 325$ nm), which may adversely affect mass transport and reduce the density of electrochemically active regions in the final electrode structure. Despite these morphological and textural differences, the theoretical density remains constant for powders of identical chemical composition, as it is an intrinsic property of the bulk material.

Table 1

Nomenclature and properties of the initial powders

Designation	Composition	α	β (fm ³)	γ_{theor} , g/sm ³ γ
Ni-n	NiO	14.3	56	6.80
Ni-m	NiO	2.7	325	6.80
ScSZ-n	Zr _{0.81} Sc _{0.19} O _{1.905}	81.5	13	5.67
ScSZ-m	Zr _{0.81} Sc _{0.19} O _{1.905}	8.4	125	5.67

Figure 1 presents the morphology of the four powders studied, as observed using transmission electron microscopy (TEM) performed on a Jeol JEM-2100 instrument. Analysis of the micrographs in Figure 1 revealed that the ScSZ-n nanopowder (Fig. 1a) consists of uniformly distributed, near-spherical particles with a low degree of agglomeration. The particles appear well-dispersed, indicating the high efficiency of the laser evaporation technique employed in their synthesis.

In contrast, the ScSZ-m powder (Fig. 1b), obtained through calcination followed by mechanical grinding, exhibits irregularly shaped aggregates with a clumped morphology, indicating a strong tendency for particle agglomeration after thermal treatment.

The NiO nanopowder (Ni-n), shown in Figure 1c, consists of nearly spherical particles with minimal aggregation; the majority of the particles fall within the expected size range of 50–60 nm.

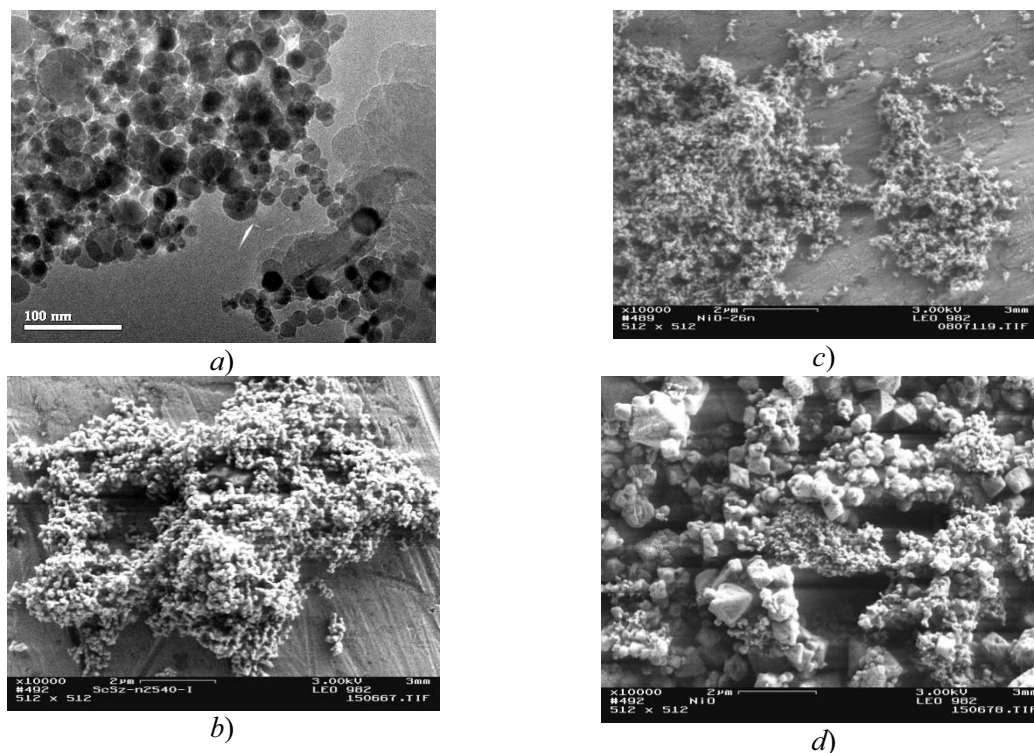


Figure 1. Microstructure of ScSZ and NiO powders with different particle sizes, obtained by transmission electron microscopy (Jeol JEM-2100): (a) ScSZ-n; (b) ScSZ-m; (c) Ni-n; (d) Ni-m

Meanwhile, the submicron NiO powder (Ni-m) presented in Figure 1d reveals a pronounced bimodal particle size distribution: along with fine fractions (~ 200 nm), large, well-faceted crystallites up to $1\text{--}1.5$ μm are also observed. Such morphology may adversely affect the homogeneity and electrical conductivity of the resulting anode composites.

Sample preparation

Three types of samples were prepared from the synthesized composite powders for studying sintering kinetics, electrical conductivity, and polarization resistance. To investigate sintering behavior, disk-shaped specimens with a diameter of 8 mm and a thickness of approximately 2 mm were fabricated using magnetic impulse pressing, achieving a relative density of 0.65–0.68. The sintering measurements were conducted in air within a temperature range of $20\text{--}1500$ $^{\circ}\text{C}$ using a Dil 402C dilatometer.

To measure electrical conductivity, the composite powders were statically pressed into rectangular bars measuring $3\times 2\times 30$ mm, with a relative density of 0.65. The optimal mass and pressing pressure were selected to ensure sample reproducibility. The Ni-n/ScSZ-n and Ni-n/ScSZ-m composites were sintered at 1200 $^{\circ}\text{C}$, while the Ni-m/ScSZ-m composition was sintered at 1400 $^{\circ}\text{C}$, with a dwell time of 4 hours in each case. After sintering, platinum probes with a diameter of 0.2 mm were attached to the samples. The specimens were then reduced in a hydrogen atmosphere at 900 $^{\circ}\text{C}$ for 1 hour. Electrical measurements were carried out using the four-probe DC method in humidified hydrogen (3 % H_2O) in the temperature range of $700\text{--}900$ $^{\circ}\text{C}$ in 50 $^{\circ}\text{C}$ increments using a Solartron SI-1260/1287 system. The density of the reduced samples was determined by hydrostatic weighing.

Polarization resistance of the anodes was measured using impedance spectroscopy on symmetrical cells with a solid-state ScSZ electrolyte in the form of a disk. The electrolyte was fabricated from a green tape composed of 87.2 wt.% ScSZ-n, 10 wt.% polyvinyl butyral (PVB), and 2.8 wt.% triethylene glycol dimethacrylate (TEGDMA). Circular disks with a diameter of 15 mm were cut from the tape, uniaxially pressed at 300 MPa, and sintered at 1250 $^{\circ}\text{C}$ for 4 hours. The resulting dense electrolyte pellets had a diameter of approximately 12 mm and a thickness of about 0.3 mm. Anode layers were applied by a painting technique using an ink composed of isopropanol, 82.1 wt.% Ni/ScSZ powder, 14 wt.% PVB, and 3.9 wt.% TEGDMA. The thickness of the deposited layers ranged from 20 to 30 μm . Firing of the anode layers was carried out in air at 1200 $^{\circ}\text{C}$ for Ni-n/ScSZ-n, 1250 $^{\circ}\text{C}$ for Ni-n/ScSZ-m, and 1300 $^{\circ}\text{C}$ for Ni-m/ScSZ-m composites, with a uniform dwell time of 4 hours. Prior to measurements, the electrodes were reduced in a

hydrogen atmosphere at 900 °C for 1 hour. Impedance measurements were performed in the frequency range from 0.1 Hz to 1 MHz, with an input signal amplitude of 10 mV, in the temperature range of 700–900 °C with 50 °C increments.

Results and discussion

Sintering kinetics

Figure 2 presents the temperature-dependent relative shrinkage curves for the initial powders and the composite materials derived from them.

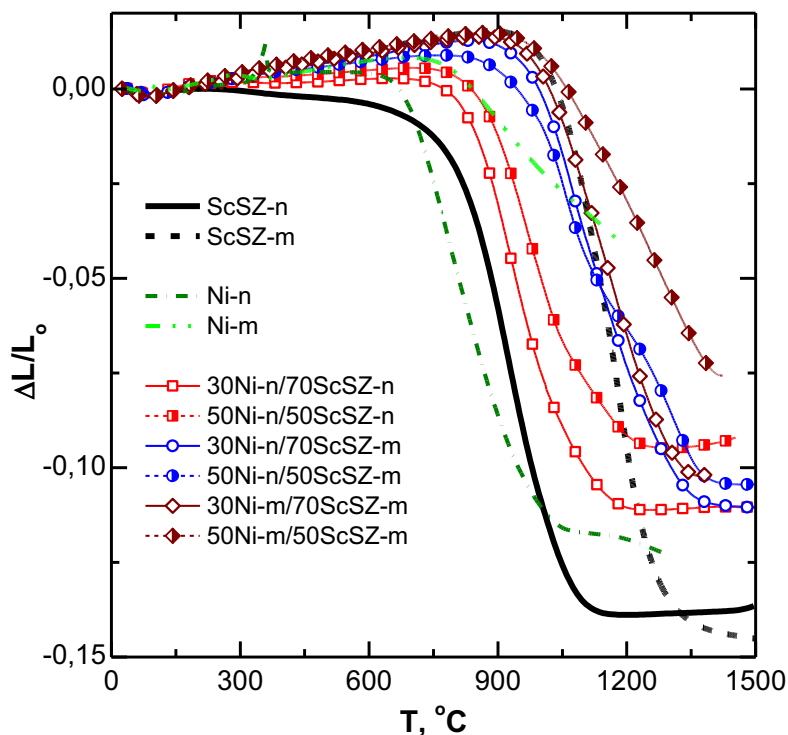


Figure 2. Linear shrinkage curves of compacted samples made from the initial powders and their corresponding composite materials

Analysis of the data reveals that samples prepared from nanoscale NiO (Ni-n) and ScSZ (ScSZ-n) powders complete the sintering process at temperatures below 1200 °C, with a divergence of no more than 2.5 % between their respective shrinkage curves. In contrast, samples formed from submicron powders (Ni-m and ScSZ-m) exhibit a shift in the onset of intensive shrinkage by 200–250 °C toward higher temperatures. Furthermore, the divergence between their shrinkage curves at 1200 °C reaches 5.4 %.

Composites incorporating the nanosized NiO component (Ni-n), specifically 30Ni-n/70ScSZ-n, 50Ni-n/50ScSZ-n, 30Ni-n/70ScSZ-m, and 50Ni-n/50ScSZ-m, exhibit a shift in the sintering temperature range to higher values—by approximately 50–80 °C—compared to their individual constituents. It was found that increasing the volume fraction of NiO in the composite leads to a higher sintering temperature and a reduction in total shrinkage. For Ni-n/ScSZ-n composites containing 30 and 50 vol.% Ni, the mismatch in shrinkage with the ScSZ-n electrolyte was approximately 3 % and 4.5 %, respectively. Similar trends were observed in the Ni-n/ScSZ-m and Ni-m/ScSZ-m systems, although the effect was less pronounced in the Ni-n/ScSZ-m series. This is likely attributed to the slower sintering kinetics of the coarser ScSZ-m powder, which plays a dominant role in the overall densification behavior of the composite.

Electrical conductivity of cermet composites

Figure 3 presents the dependence of electrical conductivity on the nickel volume fraction for three types of Ni/ScSZ anode composites measured at 900 °C. Analysis of these curves reveals several important insights into the nature of charge transport and the structural characteristics of the studied materials. According to the data presented in Figure 3, a sharp increase in electrical conductivity is observed when the nickel content exceeds 30 vol.%. This phenomenon is attributed to reaching the percolation threshold, beyond which a

continuous electron-conducting network formed by metallic nickel is established throughout the material. Below this threshold, conductivity is predominantly ionic in nature, governed solely by the solid electrolyte ScSZ.

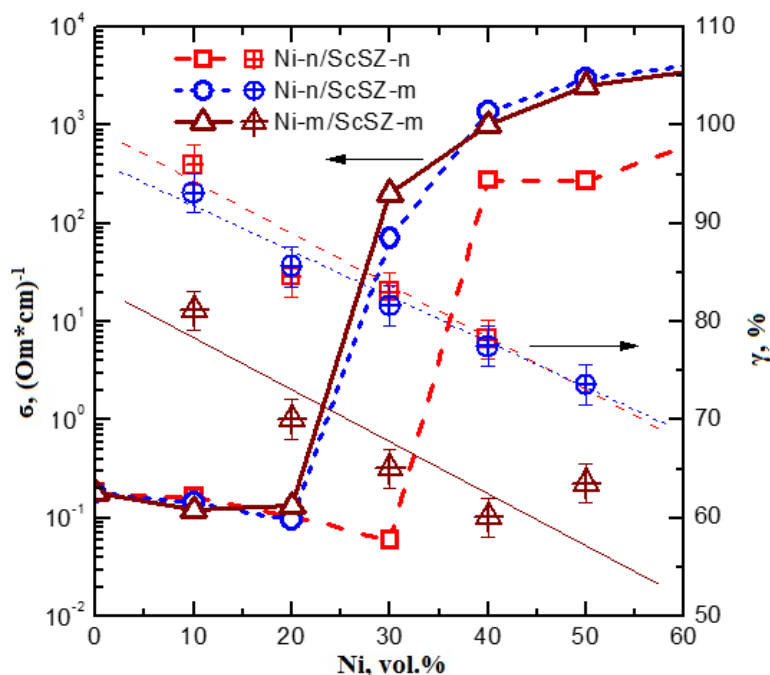


Figure 3. Electrical conductivity of three types of Ni/ScSZ anode composites at 900 °C as a function of nickel volume content (cross symbols indicate the relative density of the samples after reduction in hydrogen—right axis)

A comparative analysis of the three types of composites—Ni-n/ScSZ-n, Ni-n/ScSZ-m, and Ni-m/ScSZ-m—reveals distinct features in the transition from ionic to electronic conductivity (Fig. 3). In the Ni-n/ScSZ-n composite, this transition occurs more abruptly and is shifted toward higher nickel concentrations (~35 vol.%), which is likely due to the mismatch in particle sizes between the Ni-n nanoparticles (dBET = 56 nm) and the nano-sized ScSZ electrolyte (dBET = 13 nm). During composite preparation, the smaller ScSZ particles tend to envelop the larger Ni particles, thereby hindering the formation of continuous electronic pathways.

In the Ni-n/ScSZ-m composite, which incorporates nanostructured nickel (Ni-n) and submicron-sized electrolyte (ScSZ-m), the transition to electronic conductivity appears more gradual (Fig. 3). This behavior may be attributed to the lower surface area of ScSZ-m, which results in less extensive coverage of Ni particles and, consequently, an earlier formation of a continuous electronic network. Such morphological characteristics promote a more uniform distribution of nickel and improved interparticle contact, reflected in a steady increase in overall conductivity.

For the Ni-m/ScSZ-m composite, composed of submicron components, the conductivity increases more gradually, with the transition from ionic to electronic conduction occurring near 30 vol.% Ni. This behavior is attributed to the lower active surface area and coarser structure of the powders, which hinder the formation of continuous conductive pathways. Additionally, the increase in NiO content leads to a reduction in the sample density due to its reduction to metallic Ni—an effect associated with a significant volumetric expansion (~41 %) during the reduction process [16].

Figure 3 also presents the values of relative density after reduction (indicated by cross-marked symbols on the right axis). It can be observed that an increase in Ni content leads to a decrease in density due to increased porosity, which also affects the overall conductivity behavior.

Polarization resistance

Figure 4 displays the temperature-dependent electrical conductivity of various anode composites based on nanoscale nickel (Ni-n) and submicron electrolyte ScSZ-m. In part (a) of the figure, it is evident that the

conductivity of the 30Ni-n/70ScSZ-m and 40Ni-n/60ScSZ-m composites decreases with increasing temperature, indicating the predominance of metallic (electronic) conduction.

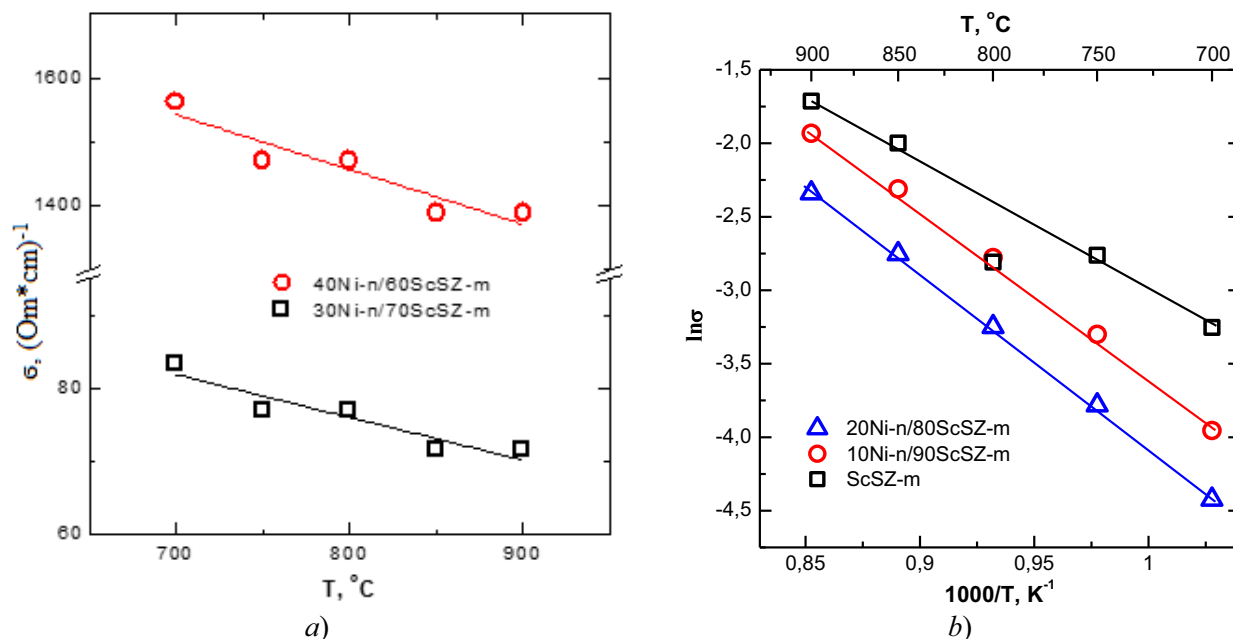


Figure 4. Temperature dependences of conductivity for composite mixtures: *a)* 40Ni-n/60ScSZ-m, 30Ni-n/70ScSZ-m, *b)* 20Ni-n/80ScSZ-m, 10Ni-n/90ScSZ-m, ScSZ-m

Such behavior is characteristic of composites containing more than 30 vol.% of nickel, where a continuous electronically conductive network is formed.

Part (b) of Figure 4 displays the conductivity behavior of compositions with lower nickel content — 10 and 20 vol.%. These composites exhibit an increase in conductivity with rising temperature, indicating an ionic conduction mechanism, which is characteristic of the ScSZ-based electrolyte matrix. The pure ScSZ composition, without any Ni addition, serves as a reference sample and shows the lowest conductivity values across the entire temperature range, further confirming its purely ionic conductivity nature.

The analysis of the impedance spectra presented in Figure 5 highlights the influence of the gas atmosphere on the impedance response of a symmetric cell featuring a 50Ni-n/50ScSZ-m anode composition at 900 $^{\circ}\text{C}$. The impedance plots are shown in the complex plane format ($\text{Re}(Z)$, $-\text{Im}(Z)$), with the real part of the impedance (Ohm) on the x-axis and the negative imaginary component (Ohm) on the y-axis, oriented downward—consistent with the standard representation of Nyquist plots.

Figure 5 presents three impedance spectra corresponding to different gas compositions: 100 %, 50 %, and 25 % hydrogen diluted with argon.

Each spectrum exhibits the shape of two overlapping semicircles, with each arc representing a distinct electrochemical process occurring at the anode. The high-frequency arc, located on the left side of the Nyquist plot, is associated with charge transfer across the electrode–electrolyte interface and is characterized by the resistance $R_{\eta\text{-HF}}$. In contrast, the low-frequency arc on the right side is attributed to diffusion and surface-related phenomena such as hydrogen adsorption, transport, and electrochemical conversion. This arc is described by the resistance $R_{\eta\text{-LF}}$.

The equivalent circuit shown in the inset of Figure 5 consists of a series resistance R_s (ohmic resistance) and two parallel RC elements (or constant phase elements, CPEs), representing the polarization resistances $R_{\eta\text{-HF}}$ and $R_{\eta\text{-LF}}$.

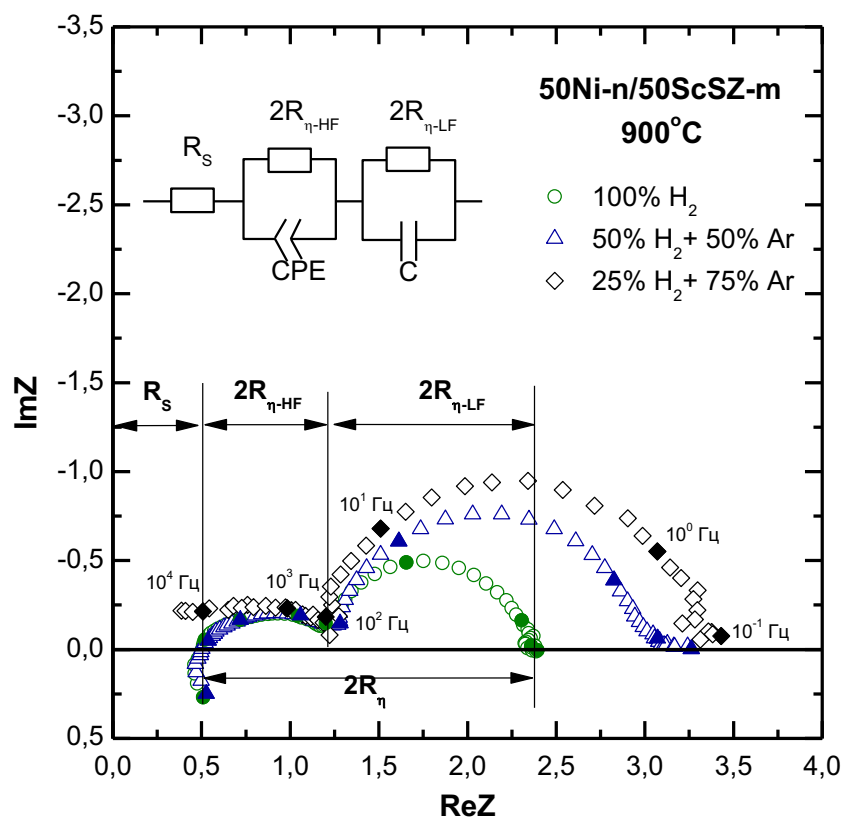


Figure 5. Impedance spectra of the 50Ni-n/50ScSZ-m electrode measured at 900 °C in hydrogen atmospheres of varying concentration (inset—equivalent circuit diagram)

The duplication of these resistances in the model stems from the symmetrical configuration of the cell, where identical anodes on both sides contribute equally to the overall impedance.

Analysis of the arc shapes and sizes indicates that as hydrogen concentration decreases, the most significant changes occur in the low-frequency region: the radius of the low-frequency arc ($R_{\eta-LF}$) increases markedly when transitioning from 100 % to 25 % H_2 . This trend reflects a deterioration in surface activity and increased difficulty of hydrogen diffusion, particularly along the triple-phase boundary. Thus, lowering the hydrogen partial pressure reduces the efficiency of the anodic processes, as evidenced by the rise in polarization resistance. Meanwhile, the high-frequency component ($R_{\eta-HF}$), associated with charge transfer across the anode/electrolyte interface, remains virtually unchanged, indicating stable interfacial contact and minimal influence of gas composition on this mechanism [17].

Thus, the total polarization resistance of the anode ($R = R_{\eta-HF} + R_{\eta-LF}$) increases with decreasing hydrogen concentration, primarily due to the rise in $R_{\eta-LF}$. These findings confirm the high sensitivity of the 50Ni-n/50ScSZ-m composite to the composition of the reducing atmosphere and emphasize the critical role of gas environment control in the operation of SOFC anodes.

Figure 6 illustrates the temperature-dependent behavior of the total polarization resistance of Ni/ScSZ anode composites, as well as its high-frequency and low-frequency components.

Analysis of the data shows that the high-frequency contribution ($R_{\eta-HF}$) exhibits typical thermally activated behavior and follows an Arrhenius-type dependence. This indicates that charge transfer across the interface between the ionically and electronically conductive phases is an energetically driven process. The observed trend reflects temperature-sensitive kinetics and underscores the effectiveness of interfacial interactions near the triple-phase boundary.

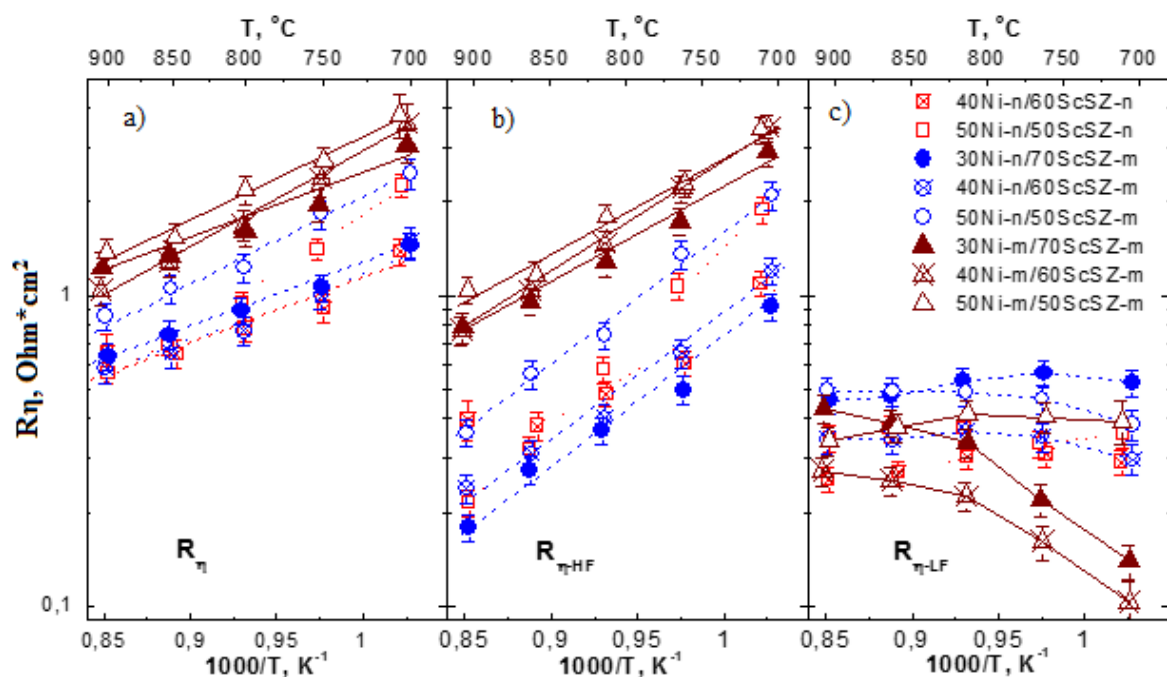


Figure 6. Temperature dependence of the polarization resistance of Ni/ScSZ composite anodes: (a) total polarization resistance as a function of temperature; (b) temperature dependence of the high-frequency component; (c) temperature dependence of the low-frequency component

Analysis of graph (b) in Figure 6, which illustrates the temperature dependence of the high-frequency component of polarization resistance ($R_{\eta\text{-HF}}$), clearly highlights the effect of particle size on charge transfer efficiency at the electrode–electrolyte interface. The lowest resistance values (ranging from 0.2 to 0.3 $\text{Ohm}\cdot\text{cm}^2$ at 900 °C) were observed for the anode composed of nano-sized nickel and nano-structured electrolyte (50Ni-n/50ScSZ-n). The second-best performance was demonstrated by the anode based on nano-nickel and submicron electrolyte (50Ni-n/50ScSZ-m), which exhibited a slightly higher resistance in the range of 0.4–0.6 $\text{Ohm}\cdot\text{cm}^2$. Despite the reduced dispersion of one phase, the composite based on nano-nickel and submicron electrolyte still maintains favorable electrochemical performance, underscoring the predominant role of the metallic component’s dispersion. The highest $R_{\eta\text{-HF}}$ values (approximately 0.8–1.0 $\text{Ohm}\cdot\text{cm}^2$) were observed for the anode entirely composed of submicron powders (50Ni-m/50ScSZ-m). This increased resistance is attributed to the less developed microstructure and the limited number of effective contacts between the conducting and ionic phases, resulting in a lower density of active triple-phase boundaries. All the presented curves follow an Arrhenius-type trend, confirming the thermally activated nature of the high-frequency process and its sensitivity to temperature. Part (c) of Figure 6 presents the temperature dependence of the low-frequency component of the polarization resistance ($R_{\eta\text{-LF}}$), which is primarily associated with surface and diffusion-related processes. Unlike the high-frequency contribution, the temperature dependence of $R_{\eta\text{-LF}}$ is relatively weak. The resistance values remain nearly constant, averaging around $0.3 \pm 0.2 \text{ Ohm}\cdot\text{cm}^2$. This indicates that mass transport and adsorption phenomena at the anode surface are not significantly influenced by temperature within the studied range. The similarity of $R_{\eta\text{-LF}}$ values across all anode types can be attributed to their comparable porosity ($\sim 55 \pm 10 \%$), as confirmed by water absorption measurements.

Figure 7 presents SEM images of fracture cross-sections of symmetrical cells with an “electrode–electrolyte–electrode” architecture, incorporating different types of anodes: 50Ni-n/50ScSZ-n, 40Ni-n/60ScSZ-m, and 40Ni-m/60ScSZ-m.

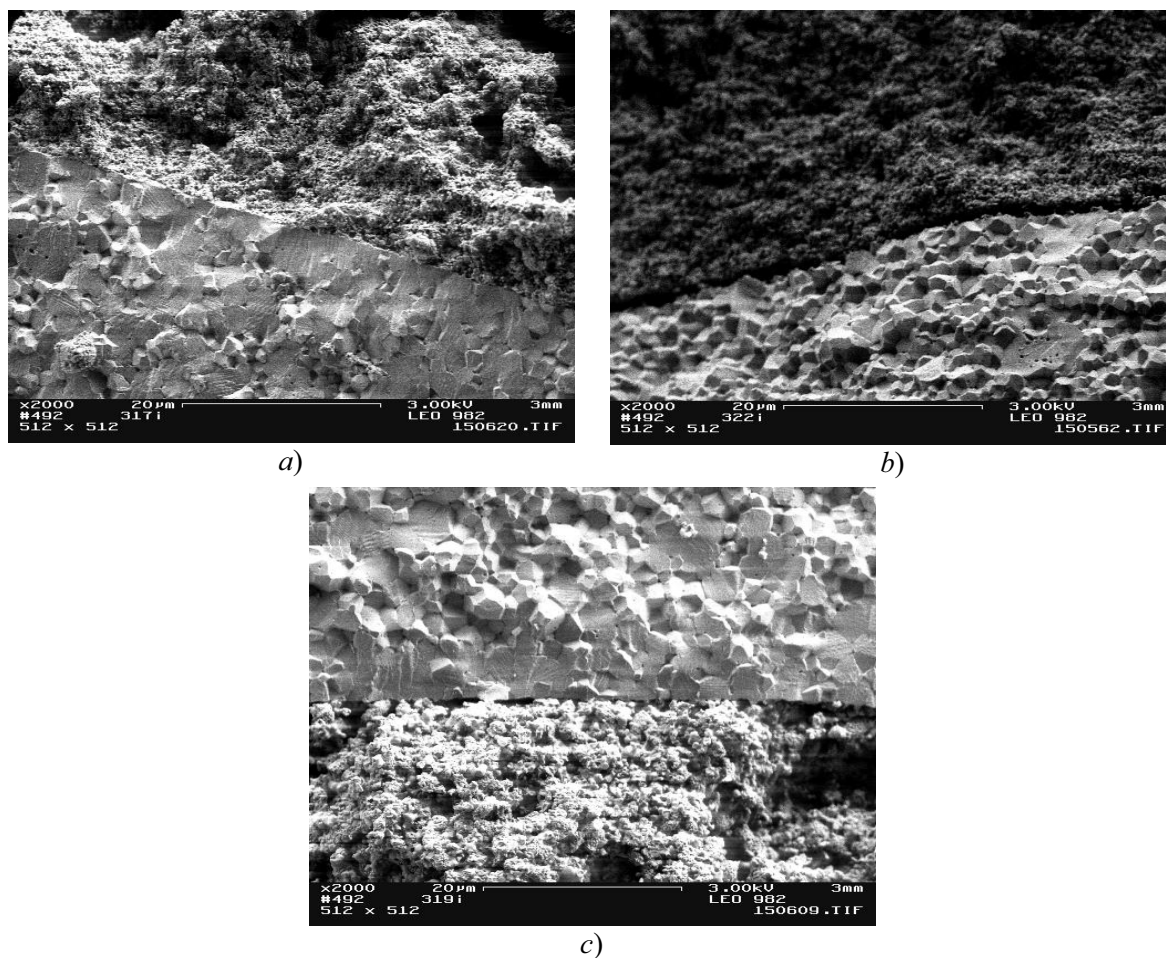


Figure 7. SEM images of fracture cross-sections of “electrode–electrolyte–electrode” structures with different types of electrodes: (a) electrode type—50Ni-n/50ScSZ-n; (b) electrode type—40Ni-n/60ScSZ-m; (c) electrode type—40Ni-m/60ScSZ-m

The analysis of these micrographs shows that, in all samples, the solid electrolyte layer is densely sintered and free of visible structural defects such as cracks or voids, indicating high sintering quality. The electrodes are firmly bonded to the electrolyte, with clearly defined interfaces and no signs of delamination or poor adhesion, confirming the mechanical integrity and suitability of the fabricated composite structures for high-temperature SOFC operation.

Furthermore, a strong visual cohesion between the electrode and electrolyte is evident, with no detectable separation or interface discontinuity—an essential criterion for maintaining long-term electrochemical stability under thermal cycling conditions. In all three cases, the porosity within the electrode layer appears uniformly distributed, with pore sizes predominantly in the submicron range. This morphology is beneficial for gas permeability and enhances the effective area of the triple-phase boundary, which is critical for efficient electrochemical reactions in SOFC anodes.

Additionally, the interface between the nickel-based anode and the electrolyte was examined using energy-dispersive spectroscopy (EDS), the results of which confirmed a homogeneous distribution of nickel within the near-surface region and the absence of diffusion zones depleted in conductive phases (Fig. 8). This effect was particularly evident in the anodes containing nanostructured nickel (50Ni-n/50ScSZ-n and 40Ni-n/60ScSZ-m), where the high dispersity of the metallic phase ensured closer phase contact and a higher density of conductive pathways.

Figure 8 presents the results of energy-dispersive spectroscopy (EDS) conducted at the electrode–electrolyte interface for symmetrical cells incorporating different types of anodes: 50Ni-n/50ScSZ-n, 40Ni-n/60ScSZ-m, and 40Ni-m/60ScSZ-m.

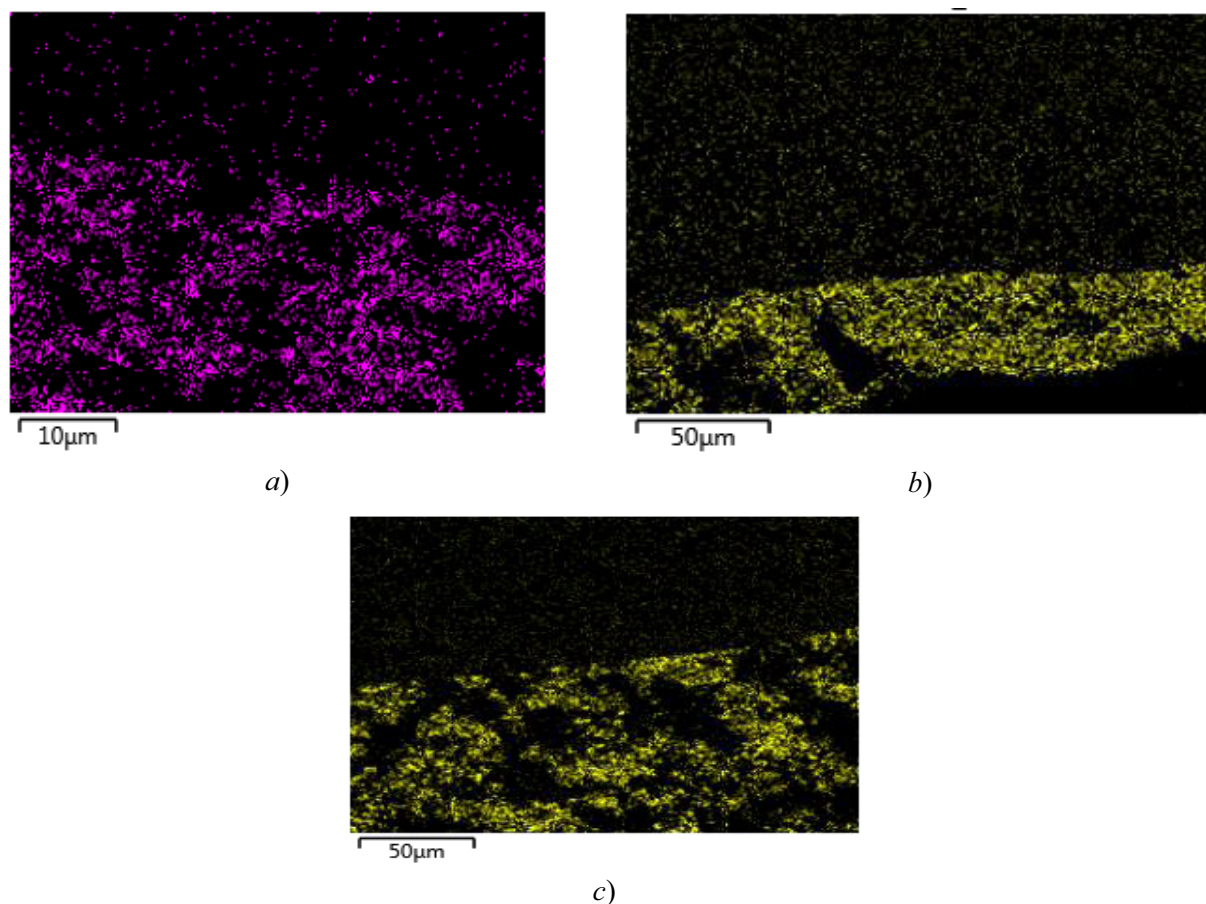


Figure 8. EDS analysis of Ni distribution at the electrode–electrolyte interface for different electrode types:
 (a) electrode type—50Ni-n/50ScSZ-n; (b) electrode type—40Ni-n/60ScSZ-m;
 (c) electrode type—40Ni-m/60ScSZ-m

The data in Figure 8 reveal that the degree of continuity and uniformity in nickel distribution across the electrode–electrolyte interface varies depending on the morphology and dispersity of the composite constituents. In particular, the sample with the 40Ni-n/60ScSZ-m composition (Fig. 8b) demonstrates the most uniform and compact contact with the electrolyte. This is attributed to the synergistic effect of nanostructured nickel and submicron-scale ScSZ, which promotes the development of an extended three-phase boundary. The presence of a high density of triple-phase contact points (Ni–ScSZ–gas) in this configuration facilitates enhanced charge transfer and more efficient initiation of electrochemical reactions.

The 50Ni-n/50ScSZ-n sample (Fig. 8a), despite containing nanostructured components in both phases, exhibits a less continuous interfacial contact. This may be attributed to an imbalance in particle size distribution and potential phase overlap during suspension mixing, which could hinder the formation of a well-integrated composite structure.

The composite 40Ni-m/60ScSZ-m (Fig. 8c), composed of submicron powders, exhibits the sparsest distribution of nickel at the electrode–electrolyte interface, indicating a lower density of effective active zones. Accordingly, based on the composition and dispersity of the components, a trend can be established in the increasing density of the interfacial contact zone—and, consequently, the concentration of active triple-phase boundaries—as follows: m–m < n–n < n–m. These findings align well with previously obtained polarization resistance data, where samples with more developed interfacial microstructures displayed lower R_{η} values, thereby confirming the critical role of microstructural architecture in determining anode performance efficiency.

Figure 9 presents the concentration-dependent behavior of the total polarization resistance (R_{η}) for four different types of Ni/ScSZ-based anodes: Ni-n/ScSZ-n, Ni-n/ScSZ-m, Ni-m/ScSZ-m, and Ni-n/ScSZ-n-film, measured at 800 °C and 900 °C. The analysis of these trends provides insight into the influence of both the

dispersion of the component powders and the method of anode structure formation on the electrochemical performance of the composites.

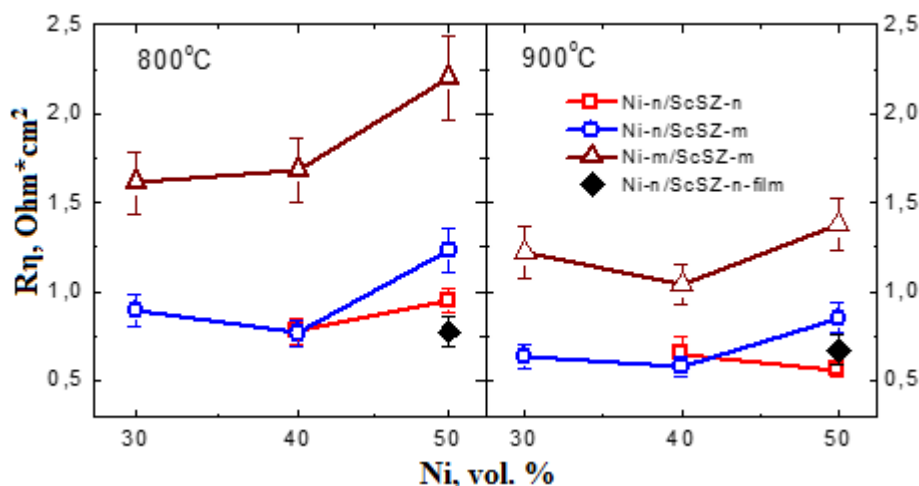


Figure 9. Dependence of the total polarization resistance R_{η} of three types of composite anodes on Ni content in the composite at 800 and 900 °C

The most significant reduction in polarization resistance is achieved when nanostructured nickel is combined with a submicron electrolyte (Ni-n/ScSZ-m), particularly at a Ni content of approximately 40 vol.%, where a distinct minimum in R_{η} is observed. This improvement is attributed to the formation of an optimal triple-phase boundary and a more efficient distribution of conductive pathways. A similar minimum is also evident for Ni-m/ScSZ-m anodes; however, their polarization resistance values are higher due to a lower active surface area and a coarser microstructure. These findings are consistent with the results reported in [18], which examined a Ni/YSZ anode prepared via co-precipitation.

The Ni-n/ScSZ-n anode exhibits the lowest polarization resistance at 900 °C ($\sim 0.56 \text{ Ohm}\cdot\text{cm}^2$), with only a slight increase to $\sim 0.9 \text{ Ohm}\cdot\text{cm}^2$ when the temperature is reduced to 800 °C, indicating excellent thermal stability. The Ni-n/50ScSZ-n-film anode, prepared via tape casting and co-sintering, also shows consistently low polarization resistance across the investigated temperature range. At 800 °C, its resistance is approximately $0.85 \text{ Ohm}\cdot\text{cm}^2$, decreasing to around $0.75 \text{ Ohm}\cdot\text{cm}^2$ at 900 °C, which is characteristic of thermally activated charge transfer processes. Despite its denser structure and lower porosity compared to samples fabricated via screen-printing, the film-based anode maintains high electrochemical performance. This highlights the effectiveness of interface formation during the casting process, as well as the presence of a sufficiently developed triple-phase boundary that supports favorable conditions for electrochemical reactions.

Table 2 summarizes the activation energy (E_a) values for Ni/ScSZ anode composites with varying particle size distributions at nickel volume concentrations of 30 %, 40 %, and 50 %. Analysis of the data reveals a pronounced impact of microstructural parameters on the kinetics of electrode processes. For the Ni-n/ScSZ-n composition—where both components are nanostructured—the activation energy reaches $65.5 \pm 5.1 \text{ kJ/mol}$, which is significantly higher compared to the other formulations. This value notably exceeds the typical activation energy associated with surface reactions, suggesting a more complex or energy-intensive charge transfer mechanism in this microstructure.



This surface reaction exhibits an activation energy of 42.7 kJ/mol and is likely the dominant contributor to the polarization resistance observed in the electrodes studied in this work. It represents a model anodic electrochemical process in solid oxide fuel cells (SOFCs), describing the surface interaction between adsorbed hydroxyl (OH) and hydrogen (H) species on the nickel surface, leading to the formation of water and the concomitant reduction of nickel. This reaction can be considered a simplified depiction of one of the elementary steps involved in the electrochemical oxidation of hydrogen at the anode.

Table 2

Activation energy of the electrode process

Composite Type Ni / ScSZ	E_a , kJ/mol		
	$C_{Ni} = 30$ vol. %	$C_{Ni} = 40$ vol. %	$C_{Ni} = 50$ vol. %
n/n	–	36.5 ± 9.8	65.5 ± 5.1
n/m	33.3 ± 2.8	43.3 ± 4.9	42.9 ± 4.6
m/m	32.1 ± 4.8	48.9 ± 2.8	44.4 ± 6.8
n/n-film	–	–	40.0 ± 6.0

This increase in the activation energy barrier is likely associated with the specific microstructural features of the composite formed during bulk pressing and sintering. In particular, excessive overlapping of the ScSZ-n nanoparticles—lacking electronic conductivity—may reduce the effectiveness of the interfacial contact between phases, thereby hindering charge transfer across the triple-phase boundaries.

Support for this microstructural influence hypothesis comes from the results obtained for the Ni-n/ScSZ-n-film sample, fabricated using a lamination technique. Despite having an identical chemical composition and particle dispersion, this film-type anode exhibited a significantly lower activation energy of 40.0 ± 6.0 kJ/mol compared to its bulk-pressed counterpart. This observation underscores the critical importance of controlled microstructure formation, which enables more favorable conditions for interfacial interaction and efficient charge transfer between phases.

An analysis of the impedance spectra for cells with 50Ni-n/50ScSZ-n electrodes, based on the data presented in Figure 10, highlights the influence of electrode fabrication techniques on the electrochemical characteristics of the cells.

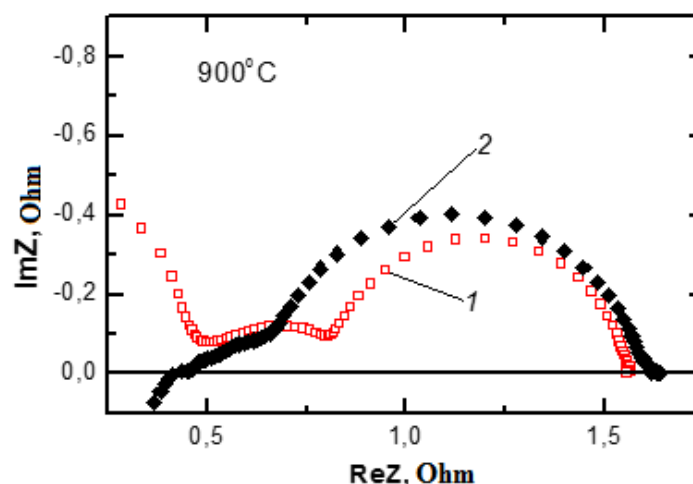


Figure 10. Impedance spectra of cells with 50Ni-n/50ScSZ-n electrodes:
(1)—cells with electrodes applied by painting; (2)—cells with electrodes applied by co-sintering

The spectra allow for a comparison between two types of electrodes prepared by different methods: the first sample (curve 1) was produced using the traditional ink-based painting technique to apply the anode layer, while the second (curve 2) involved co-sintering of pre-formed film laminates.

The impedance spectra shown in Figure 10 provide insight into the effect of electrode fabrication methods on the polarization behavior of the anodes. A comparison of the two samples, represented by curves (1) and (2), reveals that the second electrode (curve 2) exhibits a lower high-frequency component of the polarization resistance ($R_{\eta-HF}$), indicating more efficient charge transfer at the electrode–electrolyte interface. This reduction in resistance is likely attributed to the formation of a denser and more uniform interface achieved through the co-sintering method, which reduces defects commonly associated with electrodes applied via painting techniques.

At the same time, the low-frequency component ($R_{\eta-LF}$) shown in Figure 10, which is associated with diffusion processes within the porous anode structure, is higher for the second sample. This is likely due to reduced porosity, which limits the transport of gaseous species. Nevertheless, the total polarization resistance of the anode corresponding to curve (2) remains comparable to or even lower than that of the anode fabricat-

ed by the conventional painting method. These findings highlight the potential of alternative electrode fabrication techniques for enhancing the electrochemical performance of solid oxide fuel cells (SOFCs) [19, 20].

Conclusion

This study presents a comprehensive investigation into the effects of particle size distribution and volume ratio of components in Ni/ScSZ-based cermet composites—comprising nickel and scandia-stabilized zirconia (Sc_2O_3 -stabilized ZrO_2)—on their sintering behavior, electrical properties, and electrochemical performance as anodes for solid oxide fuel cells (SOFCs). The composites were synthesized using nano- and submicron-sized powders of NiO and ScSZ (10.5 mol% Sc_2O_3), with particle sizes ranging from 20 to 330 nm. Three types of composites differing in phase dispersity were examined: “nano–nano”, “nano–micro”, and “micro–micro”, with the nickel volume fraction varied between 10 and 50 vol%.

It was established that the percolation threshold, marking the transition from purely ionic to mixed ionic-electronic conductivity, is influenced by the particle size ratio of the composite constituents: for the “nano–nano” system, the threshold occurs at approximately 35 vol% Ni, while in other systems it is reached around 30 vol%. The lowest polarization resistance ($\sim 0.55 \Omega \cdot \text{cm}^2$ at 900 °C) was observed in anodes containing about 40 vol% nickel, attributed to the optimal development of the triple-phase boundary. The incorporation of nanoscale components—either one or both phases—led to a significant enhancement in the electrochemical performance of the anodes compared to their submicron counterparts.

It was found that the percolation threshold, which governs the transition from ionic to mixed conductivity, strongly depends on the particle size ratio of the composite components. For the “nano–nano” systems, this threshold is reached at approximately 35 vol% Ni, whereas in other types of composites it occurs near 30 vol%. The lowest polarization resistance ($\sim 0.55 \Omega \cdot \text{cm}^2$ at 900 °C) was observed for anodes containing around 40 vol% Ni, which correlates with the optimal development of the triple-phase boundary. Incorporating nanostructured components—either partially or entirely—led to a marked improvement in the electrochemical performance of the anodes compared to those composed of submicron powders.

These results validate the effectiveness of an integrated strategy for optimizing the morphology and phase composition of Ni/ScSZ-based anodes and highlight the practical potential of such composites for use in high-performance, energy-efficient solid oxide fuel cell technologies.

Acknowledgments

This research has been funded by the Science Committee of the Ministry of Science and Higher Education of the Republic of Kazakhstan (Grant No. AP19680484).

References

- 1 Vafaenezhad, S., Hanifi, A.R., Laguna-Bercero, M.A., & Sarkar, P. (2022). Microstructure and long-term stability of Ni–YSZ anode supported fuel cells: A review. *Journal of Power Sources*, 541, 231–244. <https://doi.org/10.1016/j.jpowsour.2022.231944>.
- 2 Wang, X., Zhang, Y., Zhang, H., & Han, M. (2024). Mechanism analysis of the reduction process of the NiO–YSZ anode of a solid oxide fuel cell by hydrogen. *Journal of The Electrochemical Society*, 171(9), 091501. <https://doi.org/10.1149/1945-7111/ad1649>.
- 3 Rao, M., Sun, X., & Hagen, A. (2020). Durability of solid oxide electrolysis stack under dynamic load cycling for syngas production. *arXiv preprint, arXiv:2002.02169*. <https://arxiv.org/abs/2002.02169>.
- 4 Omeiza, L.A., Kabyshev, A., Bekmyrza, K., Kubenova, M., Kuterbekov, K.A., Baratova, A., Adaikhan, S., Bakar, S.A., Azad, A.K. (2024). Strontium-Doped $\text{BaZr}_{0.8}\text{Ni}_{0.2}\text{O}_{3-\delta}$ Cobalt-Free Cathode Materials for Solid Oxide Fuel Cell. *International Journal of Precision Engineering and Manufacturing-Green Technology*, 12(4), 1295–1307. <https://doi.org/10.1007/s40684-024-00667-z>.
- 5 Drosakis, C., Douvartzides, S., Athanasiou, C., & Skodras, G. (2024). Recent Progress on the Materials of Oxygen Ion-Conducting Solid Oxide Fuel Cells and Experimental Analysis of Biogas-Assisted Electrolysis over a LSC Anode. *Energies*, 17(22), 5526. <https://doi.org/10.3390/en17225526>.
- 6 Arifin, N., Afifi, A.A., Samreen, A., Hafriz, R.S., & Muchtar A. (2023). Characteristic and challenges of scandia stabilized zirconia as solid oxide fuel cell material — In depth review. *Solid State Ionics*. 399, 116302. <http://dx.doi.org/10.2139/ssrn.4419870>.
- 7 Kuterbekov, K.A., Bekmyrza, K.Zh., Kabyshev, A.M., Kubenova, M.M., Aidarbekov, N.K., & Nurkenov, S.A. (2022). Investigation of the Characteristics of Materials with the Ruddlesden-Popper Structure for Solid Oxide Fuel Cells. *Bulletin of the Karaganda University, Physics Series*, 108(4), 32–47. <https://doi.org/10.31489/2022ph4/32-47>.
- 8 Feng, Z., Hansen, K., Bhandari, H.B., & Vohs, J. (2024). Stabilization of Ni–Ysz Anodes Using an Ald-Grown Aluminum Titanate Interlayer. *ECS Advances*, 3(2), 024502. <https://ssrn.com/abstract=4625745> or <http://dx.doi.org/10.2139/ssrn.4625745>.

- 9 Helal, H., Ahrouch, M., Rabehi, A., Zappa, D., & Comini, E. (2024). Nanostructured Materials for Enhanced Performance of Solid Oxide Fuel Cells: A Comprehensive Review. *Crystals*, 14, 306. <https://doi.org/10.3390/cryst14040306>.
- 10 Liang, F., Su, Y., Zhou, P., Pan, Z., Yao, P., Bian, L., Jiao, Z., Yan, Z., Yuan, Q., & Wu, J. (2025). Realizing a Robust High-Performance Ni–GDC Nanocomposite Anode for SOFCs by Self-Assembly of Reactive Cosputtered Nanolayers, *Nano Letters*, 25(11), 4276–4283. <https://doi.org/10.1021/acs.nanolett.4c05909>.
- 11 Arifin, N.A., Afifi, A.A., Kumar, N., Roslan, N.N., & Muchtar A. (2024). Influence of Metal Dopant (Cu, Co, Sm, Sn) on Ni/ScSZ Thin Film Anode in Solid Oxide Fuel Cell. *Journal of Regional Development and Technology Initiatives*, 2(2), 103–117. <https://doi.org/10.58764/j.rdti.2024.2.81>.
- 12 Timurkutluk, B., Ari, A., Altan T., & Genc O. (2024). Evaluation of anode support microstructure in solid oxide fuel cells using virtual 3D reconstruction: A simulation study. *International Journal of Hydrogen Energy*, 82, 1157–1170, <https://doi.org/10.1016/j.ijhydene.2024.08.066>.
- 13 Nikonov, A.V., Pavzderin, N.B., Khrustov, V.R., Semenova, I.V., Demidova, K.I., Kuterbekov, K.A., Bekmyrza, K.Zh., Nurakov, S.N., Koketay, T.A., & Gyrdasova, O.I. (2021). Investigation of thermal, electrical, and electrochemical properties of $\text{Pr}_{1-x}\text{Sr}_x\text{Fe}_{1-y}\text{Co}_y\text{O}_3$ ($0 < x < 0.4$; $y = 0.2, 0.5$) cathode materials for SOFC. *Journal of Alloys and Compounds*, 865, 158898, <https://doi.org/10.1016/j.jallcom.2021.158898>.
- 14 Rakhadilov, B.K., Berdimuratov, N.E., Zhurerova, L.G., Bayatanova, L.B., Kurbanbekov, Sh.R., & Satbayeva, Z.A. (2023). Study of the VAC of the EPCTT process with varying electrode parameters. *Bulletin of the Karaganda University «Physics Series»*, 111(3), 13632–142. <https://doi.org/10.31489/2023ph3/136-142>.
- 15 Auner, A. W., Burton, M. A., Nagel, L. A., Crowhurst, J. C., Weisz, D.G., & Knight, K. B. (2024). A comparative study of cerium oxides formed by pulsed laser ablation and continuous wave laser heating. *Journal of the American Ceramic Society*, 107(3), 514–521. <https://doi.org/10.1111/jace.19429>.
- 16 Prakash, B.S., Kumar, S.S., & Aruna, S.T. (2014). Properties and development of Ni/YSZ as an anode material in solid oxide fuel cell: A review. *Renewable and Sustainable Energy Reviews*, 36, 149–179. <https://doi.org/10.1016/j.rser.2014.04.043>.
- 17 Develos-Bagarinao, K., Yamaguchi, T., & Kishimoto, H. (2023). Elucidating the performance benefits enabled by YSZ/Ni–YSZ bilayer thin films in a porous anode-supported cell architecture. *Nanoscale*, 15(27), 11569–11581, <https://doi.org/10.1039/D3NR01604H>.
- 18 Xi, X., Abe, H., & Naito, M. (2014). Effect of composition on microstructure and polarization resistance of solid oxide fuel cell anode Ni–YSZ composites made by co-precipitation. *Ceramics International*, 40(10), 16549–16555. <https://doi.org/10.1016/j.ceramint.2014.08.009>.
- 19 Fernandez Visentini, A., de Anna, P., Jougnot, D., & Lehmann, P. (2023). Electrical Signatures of Diffusion-Limited Mixing: Insights from a Milli-fluidic Tracer Experiment. *Transp Porous Med*, 146, 435–461. <https://doi.org/10.1007/s11242-021-01607-0>.
- 20 Asenbauer, J., Eisenmann, T., Kuenzel, M., Kazzazi, A., Chen, Z., & Bresser, D. (2020). The success story of graphite as a lithium-ion anode material — fundamentals, remaining challenges, and recent developments including silicon (oxide) composites. *Sustainable Energy & Fuels*, 4(12), 5387–5416. <https://doi.org/10.1039/D0SE00175A>.

С. Адайхан, К.Ж. Бекмырза, А.А. Баратова, А.М. Кабышев, П. Раджагопал,
Н.К. Айдарбеков, К.К. Кутербеков, М.М. Кубенова, М.Д. Қуаныш

Қатты оксидты отын элементтері үшін Ni–ScSZ наноқұрылымды композиттің анодтарын әзірлеу және сипаттау

Мақалада никель және скандий оксидімен тұрақтандырылған цирконий диоксидіне (Ni/ScSZ) негізделген анодты композиттер қасиеттерінің жан-жақты зерттелуі ұсынылған. Композиттер әртүрлі дисперстік ұнтақтардан керамикалық технология арқылы дайындалды. Зерттеу барысында компоненттердің морфологиясы мен олардың көлемдік қатынасының қыздырғанда тығыздалу, электрөткізгіштік және поляризациялық кедергіге әсері қарастырылды. Нано-, субмикрон- және микроөлшемді бөлшектері бар үлгілер салыстырмалы түрде зерттеліп, тиімді өткізгіштік тор құрылуын және кедергілерді азайтатын онтайлы параметрлер анықталды. Дилатометрия, электрлік өлшеулер және импеданстық спектроскопия нәтижелері бойынша, нанодисперстік компоненттерді қолдану біртекті құрылым мен жақсы таратылған кеуектілік қалыптастырып, жылулық тұрақтылық пен электрохимиялық тиімділікті арттырады. Ni/ScSZ негізіндегі материалдар дәстүрлі Ni/YSZ анодтарының орнына қолдануға жарамды, себебі олар жоғары ионөткізгіштікке және деградацияға төзімділікке ие. Бұл оларды жоғары тиімді және ұзақ қызмет ететін ҚООЭ жүйелерін дамытуға болашағы зор етеді.

Кілт сөздер: қатты оксидты отын элементі (ҚООЭ), Ni/YSZ аноды, наноқұрам, поляризациялық кедергі, үш фазалы шекара, электрөткізгіштік, тығыздалу кинетикасы, белсендіру энергиясы, импеданстық спектроскопия, дайындалу әдісі

С. Адайхан, К.Ж. Бекмырза, А.А. Баратова, А.М. Кабышев, П. Раджагопал,
Н.К. Айдарбеков, К.К. Кутербеков, М.М. Кубенова, М.Д. Куаныш

Разработка и характеристика наноструктурированных композитных анодов Ni-ScSZ для твердооксидных топливных элементов

В статье представлено всестороннее исследование анодных композитов на основе никеля и стабилизированного оксида циркония с добавкой оксида скандия (Ni/ScSZ), полученных методом керамической технологии из порошков с различной дисперсностью. Основное внимание уделено влиянию морфологии исходных компонентов и их соотношений на процессы спекания, электрическую проводимость и сопротивление поляризации в условиях работы твердооксидных топливных элементов (ТОТЭ). В ходе исследования сравнивались образцы, содержащие нано-, субмикро- и микрочастицы, с целью определения оптимальных параметров, обеспечивающих формирование эффективной проводящей сети и снижение потерь. Согласно данным дилатометрии, измерений проводимости и импедансной спектроскопии, использование нанокomпонентов способствует образованию однородной и плотной микроструктуры с равномерной пористостью, что обеспечивает высокую термическую стабильность и улучшенные электрохимические характеристики. Установлено, что композиты Ni/ScSZ могут стать перспективной заменой традиционным анодам на основе Ni/YSZ благодаря лучшей ионной проводимости и устойчивости к деградации, что делает их привлекательными для разработки более долговечных и эффективных систем ТОТЭ.

Ключевые слова: твердооксидный топливный элемент (ТОТЭ), анод Ni/ScSZ, нанопорошки, сопротивление поляризации, тройная фазная граница, электрическая проводимость, кинетика спекания, энергия активации, импедансная спектроскопия, метод получения

Information about the authors

Adaikhan, Saule — PhD student, L.N. Gumilyov Eurasian National University, Astana, Kazakhstan; e-mail: adaikhansaule@gmail.com.

Bekmyrza, Kenzhebatyr — PhD, Teacher-Researcher, Associated professor, L.N. Gumilyov Eurasian National University, Astana, Kazakhstan; SCOPUS Author ID: 55227303800; ORCID ID: 0000-0001-8902-8736; e-mail: kbekmyrza@yandex.kz.

Baratova, Aliya (*contact person*) — Candidate of Physical and Mathematical Sciences, Senior Teacher, L.N. Gumilyov Eurasian National University, Astana, Kazakhstan; SCOPUS Author ID 55221822500; ORCID ID: 0000-0002-7015-3657; e-mail: aa.baratova@yandex.kz.

Kabyshev, Asset — PhD, Teacher-Researcher, L.N. Gumilyov Eurasian National University, Astana, Kazakhstan; SCOPUS Author ID: 56177620700; ORCID ID: 0000-0003-1472-4045; e-mail: asetenu@gmail.com.

Rajagopal, Packiaraj — PhD, Postdoc, L.N. Gumilyov Eurasian National University, Astana, Kazakhstan; SCOPUS Author ID: 57202507376; ORCID ID: 0000-0001-6336-9524; e-mail: drpackiaraj93@gmail.com.

Aidarbekov, Nursultan — PhD, Senior Teacher, L.N. Gumilyov Eurasian National University, Astana, Kazakhstan; SCOPUS Author ID: 57222254501; ORCID ID 0000-0002-1981-5416; e-mail: nursultan02_22.10.92@mail.ru.

Kuterbekov, Kairat — Doctor of Physical and Mathematical Sciences, Professor, Teacher-Researcher, L.N. Gumilyov Eurasian National University, Astana, Kazakhstan; SCOPUS Author ID: 6603440057; ORCID ID: 0000-0001-5421-271X; e-mail: kkuterbekov@gmail.com.

Kubenova, Marzhan — PhD, Teacher-Researcher, L.N. Gumilyov Eurasian National University, Astana, Kazakhstan; SCOPUS Author ID 57197744698; ORCID ID: 0000-0002-7015-3657; e-mail: kubenova.m@yandex.kz.

Kuanysh, Maral — Master student, L.N. Gumilyov Eurasian National University, Astana, Kazakhstan; e-mail: markamellyy@mail.ru.


Article

UDC 620.18

 <https://doi.org/10.31489/2025PH3/31-40>

Received: 19.03.2025

Accepted: 07.06.2025

Sh.R. Kurbanbekov¹, A. Kizatov², N. Musakhan¹,
P.A. Saidakhmetov³, S.Kh. Kambarbekov¹, B. Kaldar⁴

¹Research Institute Natural Sciences, Nanotechnologies and New materials,
Khoja Akhmet Yassawi International Kazakh-Turkish University, Turkestan, Kazakhstan;

²Researcher of Scientific Research Center "Veritas",

D. Serikbayev East Kazakhstan Technical University, Ust-Kamenogorsk, Kazakhstan;


³Researcher Department of Physics, M. Auezov South Kazakhstan University, Shymkent, Kazakhstan;

⁴Yasavi International Kazakh-Turkish University, Turkestan, Kazakhstan

Effect of HVOF spraying parameters on the structural-phase composition and mechanical properties of ZrCN coating

The article presents the results of a study on the influence of HVOF spraying parameters on the phase composition, mechanical properties, and adhesion characteristics of zirconium carbonitride (ZrCN) coatings. X-ray diffraction analysis of the ZrCN coatings revealed the presence of ZrCN, ZrC, ZrN, ZrO, Fe, and FeN phases, indicating a complex coating structure and possible oxidation and elemental diffusion processes. The formation of ZrC and ZrN is attributed to the thermal decomposition of ZrCN powder during the coating process, while the presence of the oxide phase ZrO is explained by the use of an oxygen-containing gas mixture during HVOF spraying. The microhardness of the ZrCN coatings reaches values in the range of 1500–1800 HV, depending on the spraying parameters. Adhesion test results showed that the maximum coating bond strength under tensile load was 7.49 MPa. Optimal coating characteristics were achieved at the following spraying parameters: substrate distance of 35–40 cm, propane pressure of 1.7 bar, air pressure of 2.6 bar, and oxygen pressure of 2.8 bar. These conditions allow the formation of a dense, wear-resistant coating structure with enhanced performance characteristics.

Keywords: HVOF, microhardness, adhesion, structure, phase composition, ZrCN coating, X-ray diffraction

 *Corresponding author:* Kambarbekov, Sardor, sardor.kambarbekov@mail.ru

Introduction

Currently, ensuring high wear resistance and durability of cutting tools of technological equipment is one of the key tasks in mechanical engineering and metalworking. Cutting tools and parts operating under conditions of intensive wear and high mechanical loads require the use of wear-resistant protective coatings [1]. Both physical and chemical deposition methods are actively used to form protective and functional coatings. Physical processing methods include physical vapor deposition, plasma spraying, and magnetron sputtering, which provide dense, wear-resistant coatings with high adhesion to the substrate [2–6]. Additionally, to increase wear resistance and corrosion resistance of materials, sol-gel technologies and laser coating methods are actively used, ensuring control over the composition and structure of the formed layers [7, 8].

Among the above methods, the most promising is the HVOF technology, which allows obtaining nanostructured coatings. HVOF technology has become widespread in many industries due to its flexibility and cost-effectiveness in obtaining high-quality coatings [9–11]. The physical and mechanical properties of HVOF sprayed coatings largely depend on the nano- or microstructure of the coating, which in turn largely depends on the physical and chemical state of the particles at the point of impact on the substrate, such as speed, temperature, degree of melting and oxidizer content [12–14]. In particular, coatings that can withstand wear, high mechanical loads and chemically aggressive influences are of particular importance. In this regard, ZrCN coatings demonstrate excellent characteristics under such conditions [15, 16]. It has been proven that ZrCN-based ceramics have high thermal stability and resistance to physical and chemical environments, which makes them an excellent candidate for protective coatings of cutting tools and metal parts operating in extreme conditions [17–19]. It was found that the grains of ZrN/ZrCN coatings were denser, finer and more compact than those of Zr/ZrN coatings. Accordingly, higher values of hardness, modulus and H/E were demonstrated by ZrN/ZrCN coatings [20].

The aim of this study is to investigate the influence of HVOF spraying mode parameters on the phase composition and mechanical properties of ZrCN coating.

Materials and methods

The ZrCN coatings were deposited using the HVOF method on a Termika-3 system [21], which is equipped with a control panel that allows precise adjustment of the gas supply pressures. Figure 1 presents both a visual and schematic illustration of the equipment used. As the pressure increases, the gas components are mixed inside the chamber, after which the powder material with a metered feed enters the burner, where it is transported by compressed air supplied by the compressor.

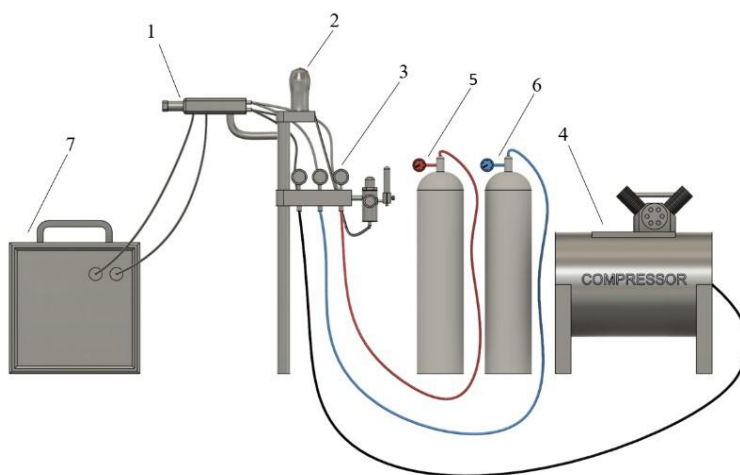


Figure 1. External view and structural diagram of the HVOF spraying system: 1—torch; 2— powder feeder; 3—gas control panel; 4—compressor; 5—gas cylinder (C_3H_8); 6—gas cylinder (O_2); and 7—chiller

At the outlet of the burner, the powder particles enter the flame zone, where they are heated to a state that ensures their plastic deformation. Then the molten particles are directed to the pre-prepared surface of the substrate, forming a uniform protective coating. The ZrCN powder with a particle size range of 20–100 μm exhibits an irregular polyhedral fragmented morphology, which is known to have lower flowability compared to spherical particles. The main spraying parameters are given in Table 1. Steel grade 65G [22], which belongs to the group of high-carbon, alloyed steels, was used as a substrate.

Table 1

Coating application parameters

№	Distance	Propane	Air Pressure	Oxygen	Powder
Sample a	35–40 cm	1.7 bar	2.6 bar	2.8 bar	ZrCN
Sample b			2.8 bar		
Sample c			3 bar		

Table 2 shows the chemical composition of 65G steel. Before spraying, the substrate surface was mechanically processed (grinded) to remove oxide films, and then sandblasted to improve coating adhesion.

Table 2

Chemical composition of steel 65G [22]

Steelgrade	Mass fraction of elements, %			
	Carbon	Silicon	Manganese	Chromium
65G	0.62–0.70	0.17–0.37	0.90–1.20	0.25

The phase composition of the obtained ZrCN-based coatings was studied using an X'Pert PRO X-ray diffractometer with Cu-K α radiation ($\lambda = 1.5406 \text{ \AA}$), a voltage of 40 kV and a current of 30 mA. The scanning angle range was from 20.01° to 89.99° with a step of 0.02° and a data accumulation time of 2 s. The diffraction patterns were processed using High Score Plus software.

Microhardness was investigated using the Vickers method in accordance with GOST 9450-76 on the HLV-1DT microhardness tester. A diamond tetrahedral pyramid with angles of 136° was used as an indenter in the study. During the measurement, a load of HV_{0.5} was applied to the surface of the sample, and the indenter was held for 10 seconds. Then the diagonal dimensions of the input traces (d1 and d2) were determined with accuracy [24].

To study the adhesive properties of the coatings, tests were carried out in accordance with ASTM D4541-22. Using an Elcometer 510 hydraulic adhesion meter (Elcometer Instruments, Manchester, UK). The strength of the adhesive coatings was determined under the following conditions: hold time 0.50 s; target speed 1.00 MPa/s; backing size 20 mm.

Results and discussion

To study the phase composition of the ZrCN powder intended for spraying, X-ray phase analysis was carried out, the diffraction pattern of which is shown in Figure 2. It can be seen from the figure that the presence of the ZrCN peak next to the ZrC, ZrN peaks indicates its partial preservation [23] and confirms its decomposition with the formation of zirconium nitride. Zirconium carbonitride combines high hardness with good plasticity, which contributes to the increased resistance of the material to the formation and propagation of cracks.

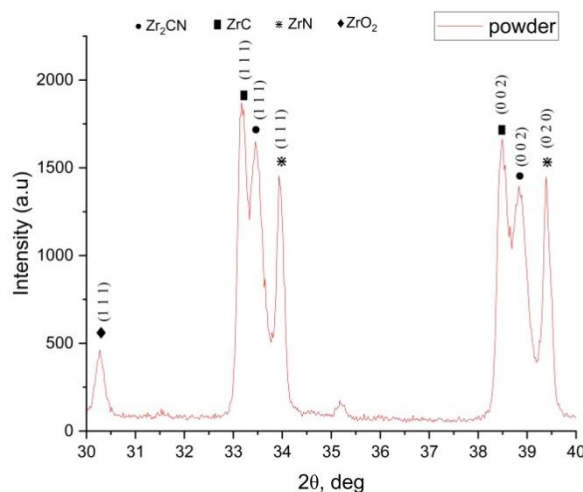


Figure 2. X-ray diffraction pattern of ZrCN powder

X-ray diffraction patterns of three coating samples are shown in Figure 3. The study of the phase composition of the sprayed coatings by the HVOF method showed the presence of the following phases: ZrCN, ZrC, ZrN, ZrO, Fe and FeN. The X-ray diffraction results confirmed that ZrC_{1-x}N_x crystallizes in a face-centered cubic (FCC) structure, and its diffraction peak is located between the control peaks of ZrC and ZrN, which indicates complete mutual solubility of these phases [24], the parameters of the ZrCN crystal lattice are cubic system, space group Fm-3m. Compared to titanium and hafnium carbonitrides, ZrCN has greater plasticity, which has a positive effect on the crack resistance of ceramics made on its basis [25]. In

works [26, 27], high values of hardness and critical intensity factors were revealed. In addition to high hardness, an important advantage of the coating is its relatively high thermal conductivity, which reduces the risk of thermal damage [28]. The formation of ZrC and ZrN phases is associated with thermal decomposition of ZrCN powder. Addition of large amounts of oxygen to the ZrN structure can distort its crystal structure, introduce defects and promote the formation of an amorphous structure. A decrease in grain size and an increase in the lattice constant are associated with the presence of oxygen in the coatings. These effects will manifest themselves as a broadening of peaks in X-ray diffraction patterns [29]. Many nitrides such as ZrN crystallize in sodium chloride type structures, and in an ideal perfect crystal first order Raman scattering is forbidden. However, it is known that deposited coatings contain vacancies which cause distortion of the structure [30], and as a consequence the Raman spectrum consists of broadened bands due to disorder and second order processes.

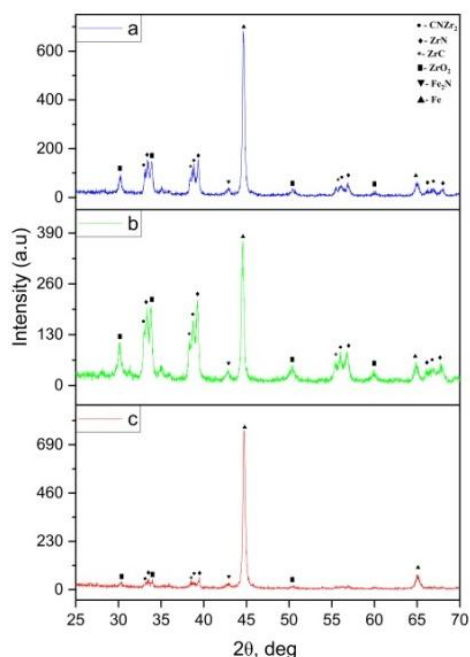


Figure 3. X-ray diffraction pattern after ZrCN coating HVOF modes:
sample *a* distance 35–40 cm, fuel pressure 1.7 bar, air pressure 2.6 bar, oxygen pressure 2.8 bar;
sample *b* 35–40 cm, fuel pressure 1.7 bar, air pressure 2.8 bar, oxygen pressure 2.8 bar
and sample *c* 35–40 cm, fuel pressure 1.7 bar, air pressure 3 bar, oxygen pressure 2.8 bar

It is known [31] that zirconium oxide can be found in mainly different phases: tetragonal ZrO₂, monoclinic ZrO₂ and cubic ZrO₂. Usually pure t-ZrO₂ in the tetragonal phase exists if Y₂O₃ yttrium oxide is present in the coatings [32]. HVOF promotes the formation of a mixture of c-ZrO₂ and t-ZrO₂, but if the cooling is very fast, more of the cubic phase remains. The formation of the ZrO phase, which possesses a similar cubic lattice structure with the space group Fm-3m, is attributed to the use of an oxygen–propane mixture as the oxidizing environment during high-velocity oxy-fuel spraying. This led to an active interaction of ZrCN with oxygen and a partial loss of carbon. Excess carbon released during the decomposition of ZrCN diffused into the metal matrix, promoting the formation of carbide (ZrC) and oxide (ZrO) phases. All samples exhibit low Zr/(C+N) ratio, $0.3 \leq \text{Zr}/(\text{C}+\text{N}) \leq 0.6$, which suggests the presence of an additional amorphous phase, most likely amorphous C or CN_x. Indeed, these phases were also observed in the TiCN system [33]. The Fe phase was detected at an angle of 44.62°, its main parameters are: cubic system, space group—Im-3m. In addition, the FeN phase, space group P-3m1, with a cubic lattice was identified. At the same time, the main lines of this phase coincide in positions with the shifted lines of the (ZrC)(ZrN) type phases with cubic lattice parameters mentioned earlier. The peaks of the phase lines in sample 3 at angles of 38.76° have characteristic broadenings, indicating the presence of phases of transformed compositions. The microhardness of the coatings and the substrate is an important parameter determining their mechanical properties and performance characteristics. Figure 4 shows the obtained microhardness values for the substrate and ZrCN coatings. The initial microhardness values of the substrate are 400–500 HV, which corresponds to the typical characteris-

tics of hardened steel 65G. This indicates a relatively low hardness of the base material compared to the applied coatings and emphasizes the need to use protective layers to improve wear resistance.

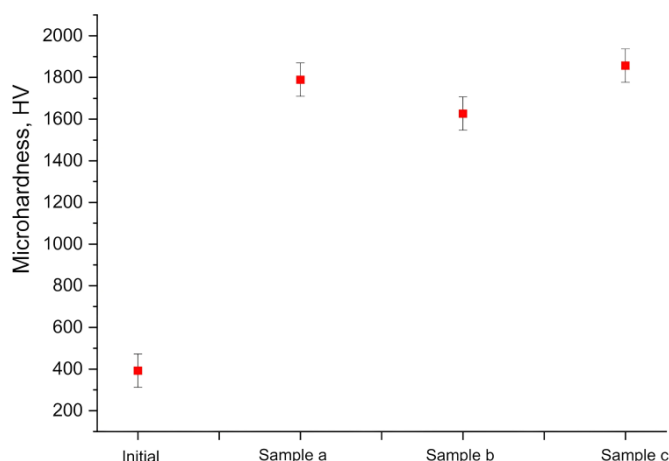


Figure 4. Microhardness values of 65G steel. HVOF modes:

sample *a* distance 35–40 cm, fuel pressure 1.7 bar, air pressure 2.6 bar, oxygen pressure 2.8 bar;

sample *b* 35–40 cm, fuel pressure 1.7 bar, air pressure 2.8 bar, oxygen pressure 2.8 bar

and sample *c* 35–40 cm, fuel pressure 1.7 bar, air pressure 3 bar, oxygen pressure 2.8 bar

After deposition of ZrCN coatings, a significant increase in microhardness is observed, with values varying depending on the sample. Sample *a* shows an increase in microhardness to 1600 HV, indicating the formation of a dense coating with a good degree of particle compaction. Sample *b* reaches a maximum hardness of 1800 HV, which can be associated with the optimal particle size of the coating, uniform phase distribution and minimal porosity. Sample *c* shows microhardness in the range of 1500–1600 HV, which is slightly lower than the second sample, but still indicates high coating strength. A smooth change in microhardness is observed at the coating-base interface, indicating possible diffusion of alloying elements and temperature effects during the spraying process.

Coating adhesion tests were carried out using the pull-off method in accordance with GOST 32299-2013 (ISO 4624: 2002) at a temperature of 20 ± 5 °C no earlier than three days after coating application. To improve the adhesive bond, the coating surface at the gluing point of the “mushroom” was treated with sandpaper, provided and degreased with ethyl alcohol. The adhesive was applied according to the manufacturer’s instructions. Epoxy Adhesive 2214 was applied in an even layer to the surface of the “mushroom”, then the “mushroom” was pressed against the coating and kept until the adhesive hardened, ensuring the centering of the surfaces to be glued. If necessary, excess glue was removed. Using a cutting tool (annular cutter), the coating was cut to the metal around the “mushroom”. Saw cuts were made across the entire coating thickness until the metal appeared, with the cut width being at least 1 mm. Tests were conducted at least 24 hours after gluing the “mushrooms”. To measure adhesion, the “mushroom” was placed in a special adhesion meter device. The adhesion meter’s stop mechanism was hooked onto the “mushroom” and by pressing the handle, a normal tear-off force was applied, the value of which was recorded on the device scale. It should be noted that non-compliance of the coating with the operating conditions of its application (e.g., climatic conditions), insufficient quality of surface preparation and other violations of the application technology lead not only to a decrease in its efficiency and reliability, but also to defective coating.

In Figure 5, the final result was a maximum bond strength at break of 7.49 MPa per square centimeter. But even with such a break, the surface of the sample was not damaged. In sample *b*, we can see distinct places that were attached to the “mushrooms” and it is clear that the surface of the sample was not deformed during the break. When breaking, it was obvious that we only tore off the adhesive, not the surface of the sample. With such indicators, the surface of the sample was not affected in any way and no visual deformations were visible.

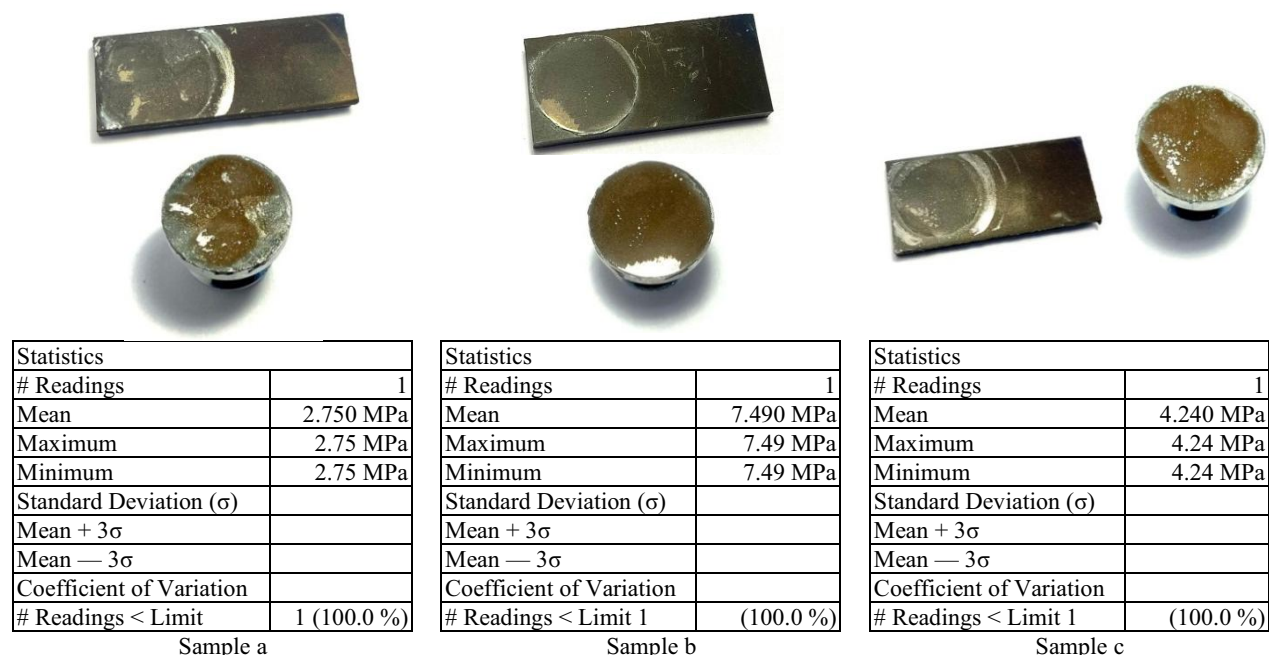


Figure 5. Image of the sample surface and the results obtained after the adhesion test

Conclusion

This research paper presents the results of structural-phase, microhardness and adhesion of ZrCN coatings applied by the HVOF method on 65G steel. The study showed that ZrCN coatings applied by the HVOF method form a complex phase structure including ZrCN, ZrC, ZrN, ZrO phases. The best formation of ZrCN and ZrC phases is achieved at moderate values of atmospheric pressure, which minimizes oxidation and increases the coating density. Sample (b) demonstrates the most favorable phase composition, which confirms its best mechanical properties, such as high hardness, wear resistance and chemical resistance. ZrCN-based coatings have significantly higher microhardness compared to the substrate, which is largely due to the formation of ZrC, ZrN. Sample (b) demonstrates the greatest strength, having a microhardness of 1800 HV, which makes it the most suitable for use under high loads. In addition, the maximum adhesion at adhesion failure is 7.49 MPa per square centimeter, which shows that sample (b) of the coating has high adhesion and has a layered structure characteristic of thermal spraying. The results obtained confirm that HVOF spraying can form coatings with high wear resistance and heat resistance, ensuring reliable operation under extreme conditions.

Acknowledgments

This research is funded by the Committee of Science of the Ministry of Science and Higher Education of the Republic of Kazakhstan (grant No. AP22787358).

References

- 1 Исламкулов К.М. Разработка инновационной технологии упрочнения дисковых пил хлопкоочистительных машин / К.М. Исламкулов // Международный журнал прикладных и фундаментальных исследований. — 2015. — 6-1. — 25–30.
- 2 Тулина А.А. Исследование свойств оксидных покрытий, полученных методом вакуумно-дугового осаждения / А.А. Тулина, А.Ю. Назаров, В.Р. Мухамедеев // Вестник УГАТУ. — 2023. — Т. 27. — № 4 (102). — С. 144–151.
- 3 Компаниец Д.Ю. Разработка оборудования для формирования ИМ-покрытий на оконных стёклах магнетронным методом. Магистерская диссертация / Д.Ю. Компаниец. — Минск, 2024. — 77 с.
- 4 Rakhadilov B.K. Obtaining functional gradient coatings based on Al₂O₃ by detonation spraying / B.K. Rakhadilov, A.B. Nugumanova, P. Kowalewski, M.K. Kylyshkanov, L.B. Bayatanova, D.N. Kakimzhanov // Bulletin of the University of Karaganda–Physics. — 2020. — 100(4). — 22–27. <https://doi.org/10.31489/2020Ph4/22-27>
- 5 Vorobyova M. PVD for decorative applications: A review / M. Vorobyova, F. Biffoli, W. Giurlani, S. M. Martinuzzi, M. Linser, A. Caneschi, M. Innocenti // Materials. — 2023. — 16(14). — 4919. <https://doi.org/10.3390/ma16144919>

- 6 Frank F. ZrN-based hard coatings deposited by chemical and physical vapor deposition [Doctoral dissertation, Technical University of Leoben] / F. Frank. — 2022.
- 7 Нургазина Г.М. Синтез металлосодержащих нанокмпозитов и их применение в катализе: дис. ... д-ра философии (PhD). Спец. 6D060600 — Химия. / Г.М. Нургазина. — Астана, 2013. — 300 с.
- 8 Ahmed T. Tribology Behaviour in High-performance Coatings for Bike Chains Deposited by PVD. Master's thesis / T. Ahmed. — Coimbra, July 2024.
- 9 Rakhadilov B. Preparation and characterization of NiCr/NiCr-Al₂O₃/Al₂O₃ multilayer gradient coatings by gas detonation spraying / B. Rakhadilov, D. Buitkenov, Z. Sagdoldina, Z. Idrisheva, M. Zhamanbayeva, D. Kakimzhanov // Coatings. — 2021. — 11(12). — 1524. <https://doi.org/10.3390/coatings11121524>
- 10 Kantay N. Influence of detonation-spraying parameters on the phase composition and tribological properties of Al₂O₃ coatings / N. Kantay, B. Rakhadilov, S. Kurbanbekov, D. Yeskermessov, G. Yerbolatova, A. Apsezhanova // Coatings. — 2021. — 11(7). — 793. <https://doi.org/10.3390/coatings11070793>
- 11 Rakhadilov B.K. Effect of HVOF method spraying parameters on phase composition and mechanical and tribological properties of 86WC-10Co-4Cr coating / B.K. Rakhadilov, N. Muktanova, D.N. Kakimzhanov, P. Kowalewski // Bulletin of the University of Karaganda-Physics. — 2024. — 11529(3). — 71–83. <https://doi.org/10.31489/2024ph3/71-83>
- 12 Skakov M. Development and Studying of the Technology for Thermal Spraying of Coatings Made from Ultra-High-Molecular-Weight Polyethylene / M. Skakov, I. Ocheredko, B. Tuyakbayev, M. Bayandinova, M. Nurizinova // Coatings. — 2023. — 13. — 698. <https://doi.org/10.3390/coatings13040698>
- 13 Рахадиллов Б.К. Теоретические исследования и решения оптимальных режимов процесса термического напыления HVOF для покрытия Cr₃C₂-NiCr. / Б.К. Рахадиллов, Ш. Р. Курбанбеков, Б. Сейтов, Н. Муктанова, Д.Э. Балтабаева, К. Катпаева // Вестник НЯЦ РК. — 2023. — № 4. — С. 22–31. <https://doi.org/10.52676/1729-7885-2023-4-22-31>
- 14 Рахадиллов Б.К. Влияние варьирования расстояния напыления на структурно-фазовое состояние и механотрибологические свойства покрытий на основе 86WC-10Co-4Cr, полученных методом HVOF / Б.К. Рахадиллов, Н. Муктанова, Д.Н. Какимжанов // Вестник НЯЦ РК. — 2024. — № 3. — С. 91–104. <https://doi.org/10.52676/1729-7885-2024-3-91-104>
- 15 Larijani M.M. The effect of carbon fraction in Zr(C, N) films on the nano-structure properties and hardness / M.M. Larijani, M.B. Zanjibar, A. Majdabadi // Journal of Alloys and Compounds. — 2010. — 492. — 735–738. <https://doi.org/10.1016/j.jallcom.2009.12.035>
- 16 Kolchev S. Structure and mechanical properties of TiCN-ZrCN multilayer coatings / S. Kolchev, T. Cholakova, L. Kolaklieva, R. Kakanakov, G. Bahchedjiev, V. Chitanov, E. Zlatareva // Journal of Physics: Conference Series. — 2024. — 2710(1). — 012025. IOP Publishing.
- 17 Silva E. Structure-property relations in ZrCN coatings for tribological applications / E. Silva, M.R. de Figueriredo, R. Franz, R.E. Galindo, C. Palacio, A. Espinosa, V.S. Calderon, C. Mitterer, S. Carvalho // Surface and Coatings Technology. — 2010. — 205. — 2134–2141. <https://doi.org/10.1016/j.surfcoat.2010.08.126>
- 18 Fominov E.V. The influence of zirconium and titanium nitride based coatings on tribodeformation processes of friction while cutting with carbide inserts / E.V. Fominov, M.M. Aliev, K.G. Shuchev, A.V. Fomenko // Journal of Friction and Wear. — 2024. — 45(1). — 18–23. <https://doi.org/10.3103/S106836662470003X>
- 19 Dorkar N.V. Friction and wear mechanisms of hot-pressed SiC – in situ Zr₂CN composites in extreme conditions of humidity and temperature / N.V. Dorkar, Y.W. Kim, B.V.M. Kumar // Wear. — 2025. — 564. — 205718.
- 20 Ul-Hamid, A. Deposition, microstructure and nanoindentation of multilayer Zr nitride and carbonitride nanostructured coatings / A. Ul-Hamid // Scientific Reports. — 2022. — 12. — 5591. <https://doi.org/10.1038/s41598-022-09449-6>
- 21 Kurbanbekov S. Research on the structural–phase and physical–mechanical characteristics of the Cr₃C₂–NiCr composite coating deposited by the HVOF method on E110 zirconium alloy / S. Kurbanbekov, B. Rakhadilov, D. Kakimzhanov, B. Seitov, K. Katpaeva, A. Kurmantayev, ... A. Kengesbekov // Coatings. — 2024. — 14(8). — 1030. <https://doi.org/10.3390/coatings14081030>
- 22 Прокат из рессорно-пружинной углеродистой и легированной стали. Технические условия. ГОСТ 14959-79. — Введ. 01.01.1981. — Москва: Изд-во Стандартиформ, 2006. — 21 с.
- 23 Löbel M. Microstructure and corrosion properties of AlCrFeCoNi high-entropy alloy coatings prepared by HVAF and HVOF / M. Löbel, T. Lindner, T. Mehner, L.M. Rymer, S. Björklund, S. Joshi, T. Lampke // Journal of Thermal Spray Technology. — 2022. <https://doi.org/10.1007/s11666-021-01255-2>
- 24 Harrison R. Processing and characterisation of ZrC_xN_y ceramics as a function of stoichiometry via carbothermic reduction-nitridation (Doctoral dissertation, Imperial College London) / R. Harrison. — 2015.
- 25 Jonda E. Microstructure and selected properties of Cr₃C₂–NiCr coatings obtained by HVOF on magnesium alloy substrates / E. Jonda, L. Łatka, W. Pakielat // Materials. — 2020. — 13(12). — 2775. <https://doi.org/10.3390/ma13122775>
- 26 Марков Ю.М. Получение карбонитрида циркония в режиме CBC-Aз / Ю.М. Марков // Современные материалы, техника и технологии. — 2017. — 6(14). — С. 88–93.
- 27 Матренин С.В. Структура и физико-механические свойства керамики на основе ZrCN / С.В. Матренин, Е.Д. Кузьменко // В Инновационные технологии в машиностроении: Сборник трудов XV Международной научно-практической конференции. — Томский политехнический университет. — 2024. — С. 13–15.
- 28 Кузьменко Е.Д. Исследование механических свойств керамики на основе ZrCN / Е.Д. Кузьменко // Исследования и разработки в области машиностроения, энергетики и управления : материалы XXIV Междунар. науч.-техн. конф. студентов, аспирантов и молодых ученых [в 2-х ч.] (25-26 апреля 2024). — Гомель, 2024. — Часть 1. — С. 76–78.

- 29 Крутский Ю.Л. Карбиды некоторых переходных металлов: Свойства, области применения и методы получения. Часть 2. Карбиды хрома и циркония (обзор) / Ю.Л. Крутский, Т.С. Гудыма, Т.М. Крутская, А.О. Семенов, А.В. Уткин // Известия вузов. Черная металлургия. — 2023. — 66(4). — 445–458. <https://doi.org/10.17073/0368-0797-2023-4-445-458>
- 30 Ul-Hamid A. Synthesis, microstructural characterization and nanoindentation of Zr, Zr-nitride and Zr-carbonitride coatings deposited using magnetron sputtering / A. Ul-Hamid // Journal of Advanced Research. — 2021. — 29. — 107–119. <https://doi.org/10.1016/j.jare.2020.11.010>
- 31 Vaz F. Property change in ZrN_xO_y thin films: effect of the oxygen fraction and bias voltage / F. Vaz, P. Carvalho, L. Cunha, L. Rebouta, C. Moura, E. Alves, A.R. Ramos, A. Cavaleiro, Ph. Goudeau, J.P. Rivi re // Thin Solid Films. — 2004. — 469–470. — 11–17.
- 32 Kim D.J. Effect of Ta_2O_5 , Nb_2O_5 , and HfO_2 alloying on the transformability of Y_2O_3 -stabilized tetragonal ZrO_2 / D.J. Kim // Journal of the American Ceramic Society. — 1990. — 73(1). — 115–120. <https://doi.org/10.1111/j.1151-2916.1990.tb05100.x>
- 33 Manninen N.K. Ag–Ti(C, N)-based coatings for biomedical applications: Influence of silver content on the structural properties / N. K. Manninen, R. E. Galindo, N. Benito, N. M. Figueiredo, A. Cavaleiro, C. Palacio, S. Carvalho // Journal of Physics D: Applied Physics. — 2011. — 44(37). — 375501. <https://doi.org/10.1088/0022-3727/44/37/375501>

Ш.Р. Курбанбеков, А. Кизатов, Н. Мусахан,
П.А. Саидахметов, С.Х. Камбарбеков, Б. Қалдар

HVOF б рку параметрлерінің ZrCN жабындарының құрылымдық-фазалық құрамына және механикалық қасиеттеріне әсері

Мақалада HVOF б рку параметрлерінің цирконий карбонитриді (ZrCN) жабынының фазалық құрамына, механикалық қасиеттеріне және адгезиялық сипаттамаларына әсерін зерттеу нәтижелері берілген. ZrCN жабындарының рентгендік дифракциялық талдауы ZrCN, ZrC, ZrN, ZrO, Fe және FeN фазаларының болуын анықтады, б л к рделі жабын құрылымын және элементтердің ықтимал тотығу және диффузиялық процестерін к рсетеді. ZrC және ZrN т зілуі жабу процесінде ZrCN  нтағының термиялық ыдырауымен байланысты, ал ZrO оксид фазасының пайда болуы HVOF шашу кезінде оттегі қоспасы қолданылғанымен т сіндіріледі. ZrCN жабындарының микроаттылығы б рку параметрлеріне байланысты 1500–1800 HV диапазонындағы м ндерге жетеді. Адгезия сынауларының нәтижелері  зілу кезінде жабынның максималды байланыс беріктігі 7,49 МПа болғанын к рсетті. Оңтайлы сипаттамаларға келесі б рку параметрлері арқылы қол жеткізілді: субстратқа дейінгі қашықтық 35–40 см, пропан қысымы 1,7 бар, ауа — 2,6 бар, оттегі 2,8 бар. Белгіленген шарттар  німділік қасиеттері жақсартылған тығыз, тозуға т зімді жабын құрылымын қалыптастыруға м мкіндік береді.

Кілт с здер: HVOF, микроаттылық, адгезия, құрылым, фазалық құрамы, ZrCN жабындары, рентгендік дифракция

Ш.Р. Курбанбеков, А. Кизатов, Н. Мусахан,
П.А. Саидахметов, С.Х. Камбарбеков, Б. Қалдар

Влияние параметров напыления HVOF на структурно-фазовый состав и механические свойства покрытий ZrCN

В статье представлены результаты исследования влияния параметров высокоскоростного газопламенного напыления (HVOF) на фазовый состав, механические свойства и адгезионные характеристики покрытия карбонитрида циркония (ZrCN). Рентгеноструктурный анализ покрытий ZrCN выявил присутствие ZrCN, ZrC, ZrN, ZrO, Fe и FeN фаз, что свидетельствует о сложной структуре покрытия и возможных процессах окисления и диффузии элементов. Формирование ZrC и ZrN связано с термическим разложением порошка ZrCN в процессе получения покрытия, а образование оксидной фазы ZrO объясняется тем, что при HVOF напылении использовалась смесь кислорода. Микротвердость ZrCN покрытий достигает значений в диапазоне 1500–1800 HV в зависимости от параметров напыления. Результаты испытаний на адгезию показали, что максимальная прочность сцепления покрытия при разрыве составила 7,49 МПа. Оптимальные характеристики достигнуты при параметрах напыления: расстояние до подложки 35–40 см, давление пропана 1,7 бар, воздуха — 2,6 бар, кислорода 2,8 бар. Установленные условия позволяют сформировать плотную, износостойкую структуру покрытия с улучшенными эксплуатационными свойствами.

Ключевые слова: HVOF, микротвёрдость, адгезия, структура, фазовый состав, покрытия ZrCN, рентгеновская дифракция.

References

- 1 Islamkulov, K.M. (2015). Razrabotka innovatsionnoi tekhnologii uprochneniia diskovykh pil khlopkoochistitelnykh mashin [Development of an innovative technology for hardening circular saws of cotton gins]. *Mezhdunarodnyi zhurnal prikladnykh i fundamentalnykh issledovaniy — International Journal of Applied and Fundamental Research*, (6-1), 25–30 [in Russian].
- 2 Tulina, A.A., Nazarov, A.Yu., & Mukhamadeev, V.R. (2023). Issledovanie svoystv oksidnykh pokrytii, poluchennykh metodom vakuumno-dugovogo osazhdeniia [Investigation of the properties of oxide coatings obtained by vacuum-arc deposition]. *Vestnik Ufimskogo gosudarstvennogo aviatsionnogo tekhnicheskogo universiteta — Bulletin of Ufa State Aviation Technical University*, 27, 4(102), 144–151 [in Russian].
- 3 Kompaniets, D.Yu. (2024). Razrabotka oborudovaniia dlia formirovaniia IM-pokrytii na okonnykh steklakh magnetronnym metodom [Development of equipment for the formation of IM coatings on window panes by the magnetron method]. *Master's thesis*. Minsk [in Russian].
- 4 Rakhadilov, B.K., Nugumanova, A.B., Kowalewski, P., Kylyshkanov, M.K., Bayatanova, L.B., & Kakimzhanov, D.N. (2020). Obtaining functional gradient coatings based on Al_2O_3 by detonation spraying. *Bulletin of the University of Karaganda – Physics*, 100(4), 22–27. <https://doi.org/10.31489/2020Ph4/22-27>
- 5 Vorobyova, M., Biffoli, F., Giurlani, W., Martinuzzi, S.M., Linser, M., Caneschi, A., & Innocenti, M. (2023). PVD for decorative applications: A review. *Materials*, 16(14), 4919. <https://doi.org/10.3390/ma16144919>
- 6 Frank, F. (2022). ZrN-based hard coatings deposited by chemical and physical vapor deposition. *Doctor's thesis*.
- 7 Nurgazina, G.M. Sintez metallsoderzhashchikh nanokompozitov i ikh primeneniye v katalize [Synthesis of metal nanocomposites and their application in catalysis]. *Doctor's thesis*. Astana [in Russian].
- 8 Ahmed, T. (2024). Tribology Behaviour in High-performance Coatings for Bike Chains Deposited by PVD. *Master's thesis*. Coimbra.
- 9 Rakhadilov, B., Buitkenov, D., Sagdoldina, Z., Idrisheva, Z., Zhamanbayeva, M., & Kakimzhanov, D. (2021). Preparation and characterization of NiCr/NiCr- Al_2O_3 / Al_2O_3 multilayer gradient coatings by gas detonation spraying. *Coatings*, 11(12), 1524. <https://doi.org/10.3390/coatings11121524>
- 10 Kantay, N., Rakhadilov, B., Kurbanbekov, S., Yeskermessov, D., Yerbolatova, G., & Apsezhanova, A. (2021). Influence of detonation-spraying parameters on the phase composition and tribological properties of Al_2O_3 coatings. *Coatings*, 11(7), 793. <https://doi.org/10.3390/coatings11070793>
- 11 Rakhadilov, B.K., Muktanova, N., Kakimzhanov, D.N., & Kowalewski, P. (2024). Effect of HVOF method spraying parameters on phase composition and mechanical and tribological properties of 86WC-10Co-4Cr coating. *Bulletin of the University of Karaganda – Physics*, 29, 3(115), 71–83. <https://doi.org/10.31489/2024ph3/71-83>
- 12 Skakov, M., Ocheredko, I., Tuyakbayev, B., Bayandinova, M., & Nurizina, M. (2023). Development and studying of the technology for thermal spraying of coatings made from ultra-high-molecular-weight polyethylene. *Coatings*, 13(4), 698. <https://doi.org/10.3390/coatings13040698>
- 13 Rakhadilov, B.K., Kurbanbekov, Sh.R., Seitov, B., Muktanova, N., Baltabaeva, D.E., & Katpaeva, K. (2023). Teoreticheskie issledovaniia i resheniia optimalnykh rezhimov protsessa termicheskogo napyleniia HVOF dlia pokrytii Cr_3C_2 -NiCr [Spraying Process for Cr_3C_2 -NiCr Coating]. *Vestnik Natsionalnogo Yadernogo Tsentra Respubliki Kazakhstan — Bulletin National Nuclear center of the Republic of Kazakhstan*, 4, 22–31. <https://doi.org/10.52676/1729-7885-2023-4-22-31> [in Russian]
- 14 Rakhadilov, B.K., Muktanova, N., & Kakimzhanov, D.N. (2024). Vliianie varirovaniia rasstoianiia napyleniia na strukturno-fazovoe sostoianie i mekhanotribologicheskie svoystva pokrytii na osnove 86WC-10Co-4Cr, poluchennykh metodom HVOF [Influence of Varying the Spraying Distance on the Structural-phase State and Mechanotribological Properties of 86WC-10Co-4Cr-based Coatings Obtained by the hvof Method]. *Vestnik Natsionalnogo Yadernogo Tsentra Respubliki Kazakhstan — Bulletin National Nuclear center of the Republic of Kazakhstan*, 3, 91–104. <https://doi.org/10.52676/1729-7885-2024-3-91-104> [in Russian]
- 15 Larijani, M.M., Zanjbar, M.B., & Majdabadi, A. (2010). The effect of carbon fraction in Zr(C, N) films on the nanostructure properties and hardness. *Journal of Alloys and Compounds*, 492, 735–738. <https://doi.org/10.1016/j.jallcom.2009.12.035>
- 16 Kolchev, S., Cholakova, T., Kolaklieva, L., Kakanakov, R., Bahchedjiev, C., Chitanov, V., & Zlatareva, E. (2024). Structure and mechanical properties of TiCN-ZrCN multilayer coatings. In *Journal of Physics: Conference Series* (Vol. 2710, No. 1, p. 012025). IOP Publishing.
- 17 Silva, E., de Figueiredo, M.R., Franz, R., Galindo, R.E., Palacio, C., Espinosa, A., Calderon, V.S., Mitterer, C., & Carvalho, S. (2010). Structure-property relations in ZrCN coatings for tribological applications. *Surface and Coatings Technology*, 205, 2134–2141. <https://doi.org/10.1016/j.surfcoat.2010.08.126>
- 18 Fominov, E.V., Aliev, M.M., Shuchev, K.G., & Fomenko, A.V. (2024). The influence of zirconium and titanium nitride based coatings on tribodeformation processes of friction while cutting with carbide inserts. *Journal of Friction and Wear*, 45(1), 18–23. <https://doi.org/10.3103/S106836662470003X>
- 19 Dorkar, N.V., Kim, Y.W., & Kumar, B.V.M. (2025). Friction and wear mechanisms of hot-pressed SiC-in situ Zr_2CN composites in extreme conditions of humidity and temperature. *Wear*, 564, 205718.
- 20 Ul-Hamid, A. (2022). Deposition, microstructure and nanoindentation of multilayer Zr nitride and carbonitride nanostructured coatings. *Scientific Reports*, 12, 5591. <https://doi.org/10.1038/s41598-022-09449-6>
- 21 Kurbanbekov, S., Rakhadilov, B., Kakimzhanov, D., Seitov, B., Katpaeva, K., Kurmantayev, A., ... & Kengesbekov, A. (2024). Research on the structural–phase and physical–mechanical characteristics of the Cr_3C_2 -NiCr composite coating deposited by the HVOF method on E110 zirconium alloy. *Coatings*, 14(8), 1030. <https://doi.org/10.3390/coatings14081030>

- 22 (2006). Prokat iz resorno-pruzhinnoi uglerodistoi i legirovannoi stali. Tekhnicheskie usloviia [Rolled products made of spring-loaded carbon steel and alloy steel. Technical specifications]. GOST 14959-79. From: 01.01.1981. Moscow: Izdatelstvo Standartinform [in Russian].
- 23 Löbel, M., Lindner, T., Mehner, T., Rymer, L.M., Björklund, S., Joshi, S., & Lampke, T. (2022). Microstructure and corrosion properties of AlCrFeCoNi high-entropy alloy coatings prepared by HVOF and HVOF. *Journal of Thermal Spray Technology*. <https://doi.org/10.1007/s11666-021-01255-2>
- 24 Harrison, R. (2015). Processing and characterisation of ZrC_xN_y ceramics as a function of stoichiometry via carbothermic reduction-nitridation (Doctoral dissertation, Imperial College London).
- 25 Jonda, E., Łatka, L., & Pakieła, W. (2020). Microstructure and Selected Properties of Cr₃C₂-NiCr Coatings Obtained by HVOF on Magnesium Alloy Substrates. *Materials*, 13(12), 2775. <https://doi.org/10.3390/ma13122775>
- 26 Markov, Yu.M. (2017). Poluchenie karbonitrida tsirkoniia v rezhime SVS-Az [Production of zirconium carbonitride in the SHS-Az mode]. *Sovremennye materialy, tekhnika i tekhnologii — Modern materials, machinery and technologies*, 6(14), 88–93 [in Russian].
- 27 Matrenin, S.V., & Kuzmenko, E.D. (2024). Struktura i fiziko-mekhanicheskie svoistva keramiki na osnove ZrCN [Structure and physico-mechanical properties of ceramics based on ZrCN]. *Innovatsionnye tekhnologii v mashinostroenii: sbornik trudov XV Mezhdunarodnoi nauchno-prakticheskoi konferentsii — Innovative technologies in mechanical engineering: Proceedings of the 15th International Scientific and Practical Conference* (pp. 13–15). Tomskii politekhnicheskii universitet [in Russian].
- 28 Kuzmenko, E.D. (2024). Issledovanie mekhanicheskikh svoistv keramiki na osnove ZrCN [Investigation of the mechanical properties of ceramics based on ZrCN]. *Issledovaniia i razrabotki v oblasti mashinostroeniia, energetiki i upravleniia: materialy XXIV Mezhdunarodnoi nauchno-tekhnicheskoi konferentsii studentov, aspirantov i molodykh uchenykh — Research and development in the field of mechanical engineering, energy and management: proceedings of the 24th International Scientific and Technical Conference of Students, Postgraduates and Young Scientists* (pp. 76–78). In two parts. Part 1 [in Russian].
- 29 Krutskii, Yu.L., Gudyma, T.S., Krutskaya, T.M., Semenov, A.O., & Utkin, A.V. (2023). Karbidy nekotorykh perekhodnykh metallov: Svoistva, oblasti primeneniia i metody polucheniia. Chast 2. Karbidy khroma i tsirkoniia (obzor) [Carbides of transition metals: Properties, application and production. Review. Part 2. Chromium and zirconium carbides]. *Izvestiia vuzov. Chernaia metallurgiiia — News. Ferrous Metallurgy*, 66(4), 445–458. <https://doi.org/10.17073/0368-0797-2023-4-445-458> [in Russian].
- 30 Ul-Hamid, A. (2021). Synthesis, microstructural characterization and nanoindentation of Zr, Zr-nitride and Zr-carbonitride coatings deposited using magnetron sputtering. *Journal of Advanced Research*, 29, 107–119. <https://doi.org/10.1016/j.jare.2020.11.010>
- 31 Vaz, F., Carvalho, P., Cunha, L., Rebouta, L., Moura, C., Alves, E., ... & Rivière, J.P. (2004). Property change in ZrN_xO_y thin films: effect of the oxygen fraction and bias voltage. *Thin Solid Films*, 469–470, 11–17.
- 32 Kim, D.J. (1990). Effect of Ta₂O₅, Nb₂O₅, and HfO₂ alloying on the transformability of Y₂O₃-stabilized tetragonal ZrO₂. *Journal of the American Ceramic Society*, 73(1), 115–120. <https://doi.org/10.1111/j.1151-2916.1990.tb05100.x>
- 33 Manninen, N.K., Galindo, R.E., Benito, N., Figueiredo, N.M., Cavaleiro, A., Palacio, C., & Carvalho, S. (2011). Ag–Ti(C, N)-based coatings for biomedical applications: Influence of silver content on the structural properties. *Journal of Physics D: Applied Physics*, 44(37), 375501. <https://doi.org/10.1088/0022-3727/44/37/375501>

Information about the authors

Kurbanbekov, Sherzod — PhD, Associate Professor, Director of the Research Institute Natural Sciences, Nanotechnologies and New materials, Khoja Akhmet Yassawi International Kazakh-Turkish University, Turkestan, Kazakhstan; e-mail: sherzod.kurbanbekov@ayu.edu.kz; ORCID ID: <https://orcid.org/0000-0001-5510-0568>

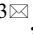
Kizatov, Aibar — Researcher of Scientific Research Center “Veritas”, D. Serikbayev East Kazakhstan Technical University, Ust-Kamenogorsk, Kazakhstan; e-mail: AKizatov@ektu.kz; ORCID ID: <https://orcid.org/0009-0004-6627-9742>

Musakhan, Nurken — Research Institute Natural Sciences, Nanotechnologies and New materials, Khoja Akhmet Yassawi International Kazakh-Turkish University, Turkestan, Kazakhstan; e-mail: nurken.mussakhan@ayu.edu.kz; ORCID ID: <https://orcid.org/0000-0003-4154-0356>

Saidakhmetov, Polat — Candidate of Science (Physics), Assistant professor, Department of Physics, M. Auezov South Kazakhstan University, Shymkent, Kazakhstan; e-mail: timpf_ukgu@mail.ru

Kambarbekov, Sardor (contact person) — Research Institute Natural Sciences, Nanotechnologies and New materials, Khoja Akhmet Yassawi International Kazakh-Turkish University, Turkestan, Kazakhstan; e-mail: sardor.kambarbekov@mail.ru; ORCID ID: <https://orcid.org/0009-0001-6794-1281>

Kaldar, Berik — Bachelor student, Yasavi International Kazakh-Turkish University, Turkestan, Kazakhstan; e-mail: Berik2002Berik@gmail.com; ORCID ID: <https://orcid.org/0009-0002-9267-7029>

A.B. Kengesbekov^{1, 2}, A. Serikbaikyzy¹, D. Baizhan³, Y.Y. Batanov¹, L.S. Kairbaeva^{1, 2}

¹ D. Serikbayev East Kazakhstan Technical University, Kazakhstan, Ust-Kamenogorsk;


² Institute of Composite Materials LLP, Ust-Kamenogorsk, Kazakhstan;

³ S. Amanzholov East Kazakhstan University, Kazakhstan, Ust-Kamenogorsk

Investigation of the Influence of Modes of Intensive Plastic Deformation on the Process of Grain Refinement of Titanium Alloy Ti-13Nb-13Zr at Equal-Channel Angular Pressing and Subsequent Rotary Forging Compression

Ultrafine-grained materials are currently of great interest due to their excellent mechanical and functional properties. One of the most effective methods to obtain such materials with a unique combination of microstructure and properties is intense plastic deformation (IPD). This paper deals with the development of an efficient IPD method for Ti-13Nb-13Zr titanium alloy based on a combined approach involving equal channel angular pressing (ECAP) and subsequent rotational forging compression ("RFC"). Ti-13Nb-13Zr titanium alloy was pressed at different temperatures using an equal channel angular pressing (ECAP) process through a channel angle of 130° for several passes, followed by rotational forging compression ("RFC"). Microstructural analysis showed that the application of combined processing (RCUP + RFC) transformed the coarse-grained (CG) structure into an ultrafine-grained structure (UFGS). In addition, the results of mechanical tests indicate that the application of combined processing method significantly increases the hardness and modulus of elasticity of titanium alloy Ti-13Nb-13Zr. These changes in the complex of properties allow us to consider this alloy as a highly effective alternative to traditional metallic materials used in biomedical implantology.

Keywords: Intense plastic deformation, ultrafine-grained structure, equal-channel angular pressing, rotary forging compression, titanium alloys.

 *Corresponding author:* Daryn, Baizhan, daryn.baizhan@mail.ru

Introduction

In recent decades, there has been a steady increase in interest in the use of titanium alloys in medicine, particularly in orthopedics, traumatology, dentistry and cardiac surgery. This is due to the unique properties of titanium and its alloys, such as high corrosion resistance, excellent biocompatibility, low specific weight, and a favorable combination of strength and elastic properties [1]. However, with the ever-increasing requirements for the durability and reliability of medical devices, especially implants, the need to improve the mechanical properties of materials without compromising their biocompatibility becomes obvious. Therefore, it is highly desirable to develop new materials for implants made of titanium and titanium alloys with higher tensile strength and elasticity modulus equivalent to the bone elasticity modulus.

One of the most urgent and promising directions in the field of improving the performance characteristics of titanium alloys is the formation of ultrafine grain structure ("UFGS"). Reduction of the average grain size to submicron level (less than 1 micron) provides a significant increase in strength, hardness and fatigue resistance due to intensification of the grain boundary hardening mechanism [2]. The strength of metallic materials increases with decreasing grain size, which is well known as the Hall-Petch relationship [3]. Grain refinement can induce hardening without the addition of any alloying elements and can potentially achieve the desired strength. Intense plastic deformation (IPD) is known as a new method to produce UMP structures and a large number of studies have been conducted on IPD and UMP structures. Equi-channel angular pressing, multilayer torsion, rotary forging and others are commonly used to fabricate IPD [4].

Nevertheless, most of the existing IPD methods require further optimization in terms of manufacturability, reproducibility and scalability for practical application in the medical industry. In addition, it is important to take into account the influence of deformation parameters on the phase composition, texture and, ultimately, on the biomechanical properties of the finished products. Thus, the actual scientific task is the develop-

ment of such a method of IPD, which will make it possible to obtain titanium alloys with UMP structure, possessing high strength, stability and suitability for the manufacture of medical implants.

Equal channel angular pressing (ECAP) is one of the most effective methods of severe plastic deformation, which is used to obtain ultrafine-grained and nanostructured materials. This process involves repeatedly pushing a sample through a system of channels with equal cross-sections connected at a certain angle. The main advantage of ECAP is the ability to achieve significant plastic deformation without changing the shape of the specimen, which makes this method attractive for improving the mechanical properties of metals and alloys such as strength, ductility and hardness. And also equal channel angular pressing is one of the most effective methods of intense plastic deformation (IPD), designed to produce ultrafine grained or nanostructured structure in metals and alloys without changing the external shape of the specimen. One of the key factors affecting the efficiency of the ECAP process is the geometry of the matrix channels, including the joint angle and corner rounding radius. Optimization of these parameters allows minimizing deformation inhomogeneities, reducing friction and lowering pressing forces, which is especially important for ensuring microstructure uniformity and improving the quality of the processed material.

Currently, scientists have proposed various variants of mechanical and thermomechanical treatments of Ti-13Nb-13Zr alloy [5]. For example, Majumdar et al. [6] have tried several combinations of hot working, ST and cooling conditions to optimize the mechanical performance. Park et al. [7] introduced warm cross rolling to obtain ultrafine grain structure in Ti-13Nb-13Zr alloy. Li et al. [8–12] first proposed to improve the mechanical properties of this alloy by multi-pass gauge rolling. Recently, he was able to improve this process and obtained the lowest Young's modulus ever reported for Ti-13Nb-13Zr [13]. In [14], the effect of thermomechanical treatment by equal-channel angular flattening on the structures and phase composition of Ti-13Nb-13Zr (TNZ) was investigated. In [15] the peculiarities of microstructure evolution and properties of Ti-13Nb-13Zr alloy under combined processing including ECAP and subsequent rotational forging compression (RFC) were investigated. Due to RCUP + RFC, the tensile strength increased to 1167.7 MPa and the elongation was 8.6 %. The excellent mechanical properties were mainly due to hardening by α -phase precipitation, dislocation hardening and grain refinement.

In this regard, the aim of this work is to develop an efficient IPD method for Ti-13Nb-13Zr titanium alloy based on a combined approach involving equal-channel angular pressing (ECAP) and subsequent rotational forging compression (RFC).

Materials and methods of experiments

Ti-13Nb-13Zr titanium alloy was chosen as the material for the study. The chemical composition of the main alloying elements is: 13.0 wt.% Nb, 13 wt.% Zr, 0.086 wt.% O, 0.009 wt.% N, 0.0012 wt.% H, the rest — Ti. The choice of this alloy is due to its wide application in the production of medical implants due to its high biocompatibility, corrosion resistance and low modulus of elasticity.

The study of structure and properties of samples after different treatment modes was carried out using optical and electron microscopy. Surface microstructure and cross-sectional morphology of the coatings were studied by scanning electron microscopy (SEM) on Vega 4 (Tescan, Czech Republic). Hardness and modulus of elasticity of the samples were measured by the Martens method according to ASTM E 2546 on a hardness tester FISCHERScope HM2000S ("Fischerscope", Germany), at indenter load $F = 245.2\text{ mN}$ and dwell time of 20s. Surface roughness was determined according to GOST 25142-82 using a profilometer model 130 [16].

A combined approach involving equal-channel angular pressing (ECAP) followed by rotational forging compression ("RFC") was used to obtain an ultrafine grained (UFG) structure.

Figure 1 shows the complete simulation of the equal-channel angular pressing process, including the punch path (a), channel geometry (b, c), finite element mesh (d), Mises stress distribution (e), and force versus displacement plot (f). The punch motion exhibits linear descent and return, which sets the initial conditions for deformation. The channel geometry and grid structure provide high detail of the calculation in the stress concentration zones. The stress distribution shows that the maximum stresses are concentrated in the corners of the channel, confirming the need for shape optimization to reduce peak values ($\sim 14 \times 10^8 \text{ N/m}^2$). The force-displacement plot illustrates the stability of the process with a peak force of $\sim 9 \times 10^6 \text{ N}$, which is associated with overcoming the material resistance. This model demonstrates a comprehensive approach to the analysis of ECAP, which allows us to evaluate the influence of process parameters and suggest optimal conditions for uniform formation of ultrafine-grained structure.

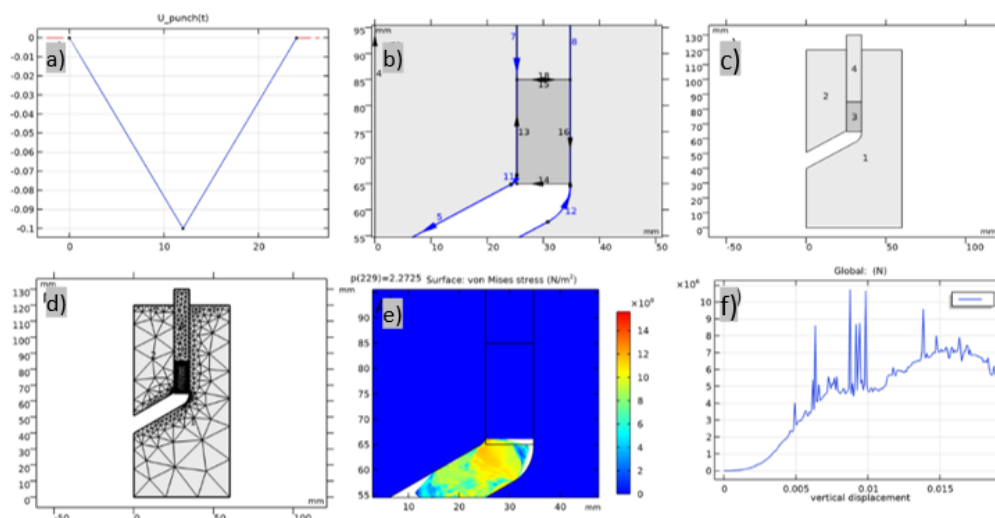


Figure 1. Modeling of ECAP process: (a) punch trajectory, (b, c) channel geometry, (d) finite element mesh, (e) Mises stress distribution, (f) force dependence on vertical displacement

The computational mesh used is characterized by high density in critical areas, which ensures the accuracy of the analysis and allows for a detailed study of the plastic behavior of the material. Thus, this model serves as an important tool for the study and optimization of the ECAP process, allowing the consideration of various geometrical and technological parameters. This, in turn, contributes to the improvement of material characteristics, reduction of production costs and expansion of the application of the ECAP method in industry.

Based on the theoretical calculations carried out using the finite element method, the design of the matrix for ECAP was developed and optimized. The main design criterion was to ensure uniform distribution of plastic deformation of the material while minimizing stress concentrations and pressing forces. Calculations showed that the optimal angle of channel connection is 130 degrees, which provides effective strain redistribution without significant increase in force.

High-strength tool steel of 9XΓCA grade, which has high wear resistance and deformation resistance, was used for manufacturing the matrix. The design includes an internal channel with an angle of 130 degrees, which allows minimizing the friction of the material against the walls and preventing local fractures during the passage of the sample. The actual design was fabricated with the calculated loads and contact conditions [17, 18].

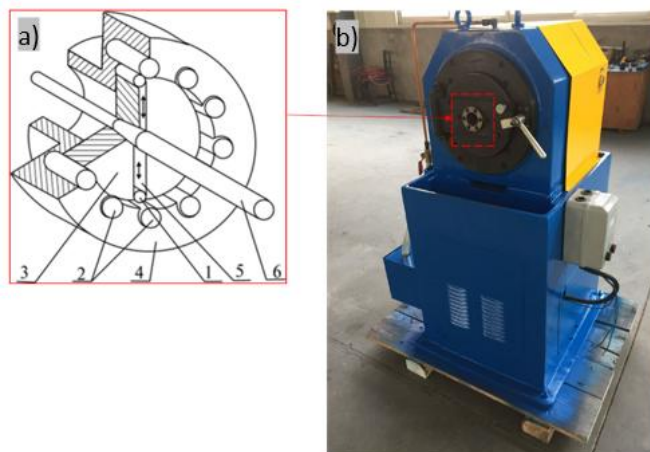
This matrix (Fig. 2) is designed for experiments to improve the mechanical properties of the material by intense plastic deformation.



Figure 2. Matrix for ECAP

The samples were prepared in the form of cylinders with a diameter of 10 mm and a height of 20 mm, which meets the requirements of a matrix fabricated with a channel angle of 130 degrees.

After equal channel angle pressing (ECAP), the material is subjected to an intermediate heat treatment to relieve residual stresses and stabilize the structure. This step is critical to prepare the material for the next processing step, rotational forging compression (RFC) (Fig. 3).



1, 2 — rollers; 3 — spindle; 4 — cage; 5 — strikers; 6 — workpiece

Figure 3. Rotary forging scheme (a) and rotary forging machine (b)

RFS complements ECAP by providing additional grain refinement through a complex combination of rotational and axial deformations, which contributes to microstructure equalization and increased uniformity of mechanical properties. Figure 4 shows a scheme of stages of combined ECAP and RFS processing with intermediate heat treatment, where each stage plays a key role in achieving ultrafine grain structure. The first stage of ECAP provides an intense plastic deformation initiating grain refinement and substructure formation. The material is then subjected to intermediate heat treatment, which relieves residual stresses, activates recrystallization processes and prepares the material for the next stage. The final stage of RFS (rotary forging compression) completes the process by creating complex deformation modes to eliminate structural inhomogeneities and additional grain refinement.

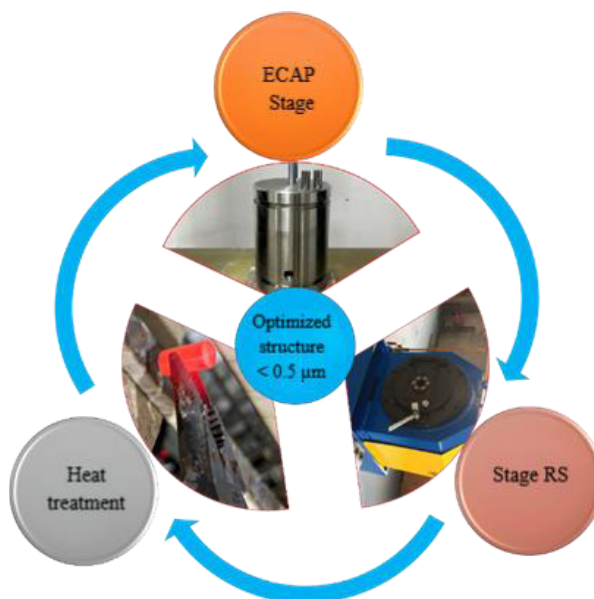


Figure 4. Schematic diagram of stages of combined processing of ECAP and RFS with intermediate heat treatment

Table summarizes the combined severe plastic deformation (SPD) regimes applied to titanium, involving equal-channel angular pressing (ECAP) and rotary forging compression (RFC), with varying numbers of cycles and processing temperatures. All processing was conducted in air.

Table

Modes of combined severe plastic deformation

Mode	Processing method	Processing temperature (°C)	Number of cycles	Processing method	Processing temperature (°C)	Number of cycles
Ti 1	ECAP	700	1	—	—	—
Ti 2	ECAP	700	1	RFC	800	2
Ti 3	ECAP	700	2	RFC	800	3
Ti 4	ECAP	Room temperature (25)	1	—	—	—

Results and Discussions

Room temperature the study of titanium microstructure after intense plastic deformation (IPD) with different number of cycles and application of heat treatment showed a significant influence of processing modes on the material structure (Fig. 5). In the initial state (*a*) titanium had a coarse-grained structure without defects. After 2 cycles with heat treatment (*b*), grain refinement and the beginning of recrystallization were observed, but the structure remained heterogeneous. Three cycles with heat treatment (*c*) promoted the formation of a fine-grained and homogeneous structure, practically devoid of defects. The maximum uniform ultrafine-grained structure was achieved after 5 cycles with heat treatment (*d*), which provided material stability and improved mechanical properties. In the case of 1 cycle without heat treatment (*e*), significant defects such as microcracks and inhomogeneous structure were found, which limits the strength properties. Thus, heat treatment after IPD plays a key role in improving the structure and properties of titanium.

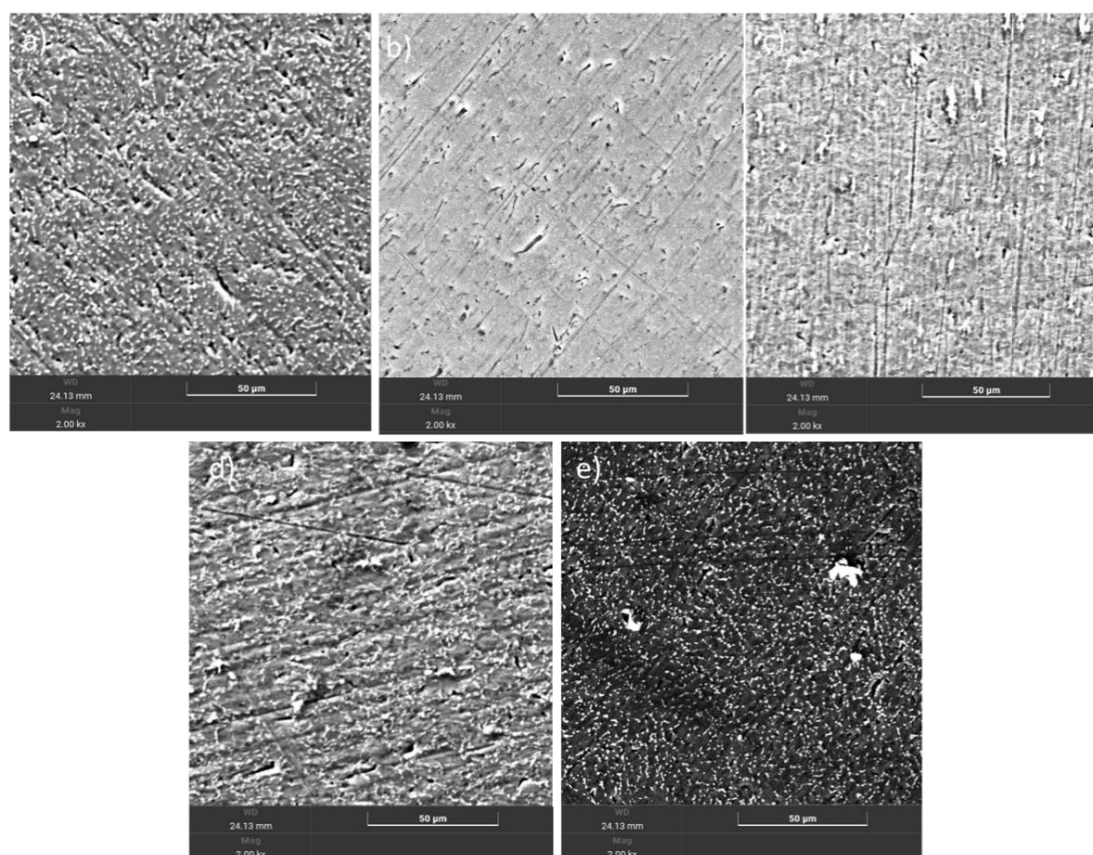


Figure 5. Microstructures of titanium alloy samples after various processing modes:
Ti_orig. (*a*); Ti_1 (*b*); Ti_2 (*c*); Ti_3 (*d*); Ti_4 (*e*)

Figure 6 shows the dependence of hardness (H) and modulus of elasticity (E) of titanium alloy samples on processing modes. The source material has low hardness and modulus of elasticity. After ECAP processing in Ti_1 mode, there is a slight increase in these parameters. A significant increase in hardness and elastic modulus is observed in the Ti_2 and Ti_3 modes, where combined ECAP + RFC treatment was applied. The maximum values are reached in the Ti_3 mode, which is associated with an increase in the number of cycles and more intensive grinding of grains. However, in the Ti_4 mode, when using ECAP at room temperature, the hardness and modulus of elasticity are significantly reduced, due to insufficient deformation of the material and a low degree of grain grinding.

Thus, combined ECAP + RFC treatment with an optimal number of cycles demonstrates the greatest efficiency in improving the mechanical characteristics of a titanium alloy.

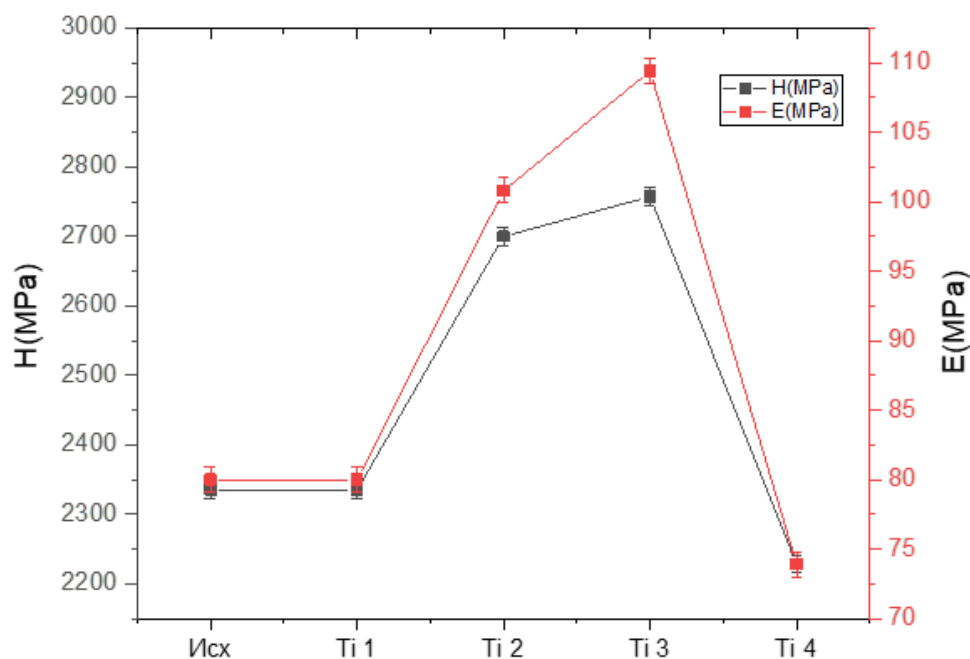


Figure 6. Hardness (H) and modulus of elasticity (E) of the samples

Conclusion

In the course of the study, an effective technology for intensive plastic deformation of Ti-13Nb-13Zr titanium alloy for medical purposes using equal-channel angular compression (ECAP) and rotational forging compression (RFC) was developed and experimentally substantiated.

The results of numerical finite element modeling have confirmed the importance of optimizing matrix geometry for ECAP. It has been shown that the channel connection angle of 130° ensures uniform distribution of plastic deformation and minimizes peak stresses in the material, which helps to prevent the destruction of samples during pressing.

The combined treatment, including the sequential use of ECAP and RFC with intermediate heat treatment, made it possible to achieve the formation of an ultra-fine-grained structure of the material and a significant increase in its mechanical characteristics. Experimental studies of the structure and properties of the titanium alloy have shown that the best results are achieved after five cycles of combined ECAP + RFC treatment at a temperature of $700\text{--}800^\circ\text{C}$. At the same time, the formation of a uniform ultrafine-grained structure with a minimum number of defects was observed, as well as a significant increase in the hardness and modulus of elasticity of the material compared with the initial state.

The developed technology of plastic deformation intensification opens up new prospects for the creation of a new generation of medical implants with improved performance, increased reliability and durability. The results obtained can be used to scale the process into industrial production and for further research aimed at optimizing deformation and heat treatment modes depending on the requirements for specific medical devices.

Acknowledgments

This research has been funded by the Committee of Science of the Ministry of Science and Higher Education of the Republic of Kazakhstan. (Grant No. BR24992862).

References

- 1 Shao L. β -Ti Alloys for Orthopedic and Dental Applications: A Review of Progress on Improvement of Properties through Surface Modification / L. Shao, Y. Du, K. Dai, H. Wu, Q. Wang, J. Liu, Y. Tang, L. Wang // *Coatings*. — 2021. — Vol. 11. — P. 1446. — DOI: <https://doi.org/10.3390/coatings11121446>.
- 2 Zhang X. Effect of Grain Size on Mechanical Properties and Deformation Mechanism of Nano-Polycrystalline Pure Ti Simulated by Molecular Dynamics / X. Zhang, A. I. A. Alduma, F. Zhan, W. Zhang, J. Ren, X. Lu // *Metals*. — 2025. — Vol. 15. — P. 271. — DOI: <https://doi.org/10.3390/met15030271>.
- 3 Regev M. A Study of the Metallurgical and Mechanical Properties of Friction-Stir-Processed Cu / M. Regev, S. Spigarelli // *Metals*. — 2021. — Vol. 11. — P. 656. — DOI: <https://doi.org/10.3390/met11040656>.
- 4 Baysal E. An Overview of Deformation Path Shapes on Equal Channel Angular Pressing / E. Baysal, O. Koçar, E. Kocaman, U. Köklü // *Metals*. — 2022. — Vol. 12. — P. 1800. — DOI: <https://doi.org/10.3390/met12111800>.
- 5 Семенова И.П. Ультрамелкозернистый двухфазный альфа-бета титановый сплав и способ его получения / И. П. Семенова, Г. И. Рааб, В. В. Полякова, Р. З. Валиев. — Пат. WO2013137765A1. — Международная заявка. — 2013-09-19. — Режим доступа: <https://patents.google.com/patent/WO2013137765A1/ru>.
- 6 Cvijović-Alagić I. Damage behavior of orthopedic titanium alloys with martensitic microstructure during sliding wear in physiological solution / I. Cvijović-Alagić, Z. Cvijović, M. Rakin // *Int. J. Damage Mech.* — 2019.
- 7 Majumdar P. The role of heat treatment on microstructure and mechanical properties of Ti-13Zr-13Nb alloy for biomedical load bearing applications / P. Majumdar, S. B. Singh, M. Chakraborty // *J. Mech. Behav. Biomed. Mater.* — 2011. — Vol. 4(7). — P. 1132–1144. — DOI: 10.1016/j.jmbbm.2011.03.023.
- 8 Park C.H. Improved pre-osteoblast response and mechanical compatibility of ultrafine-grained Ti-13Nb-13Zr alloy / C. H. Park, C. S. Lee, Y.-J. Shin, Je.-H. Jang, Jo.-Y. Suh, J.-W. Park // *Clin. Oral Implants Res.* — 2010. — Vol. 22. — P. 735–742.
- 9 Lee T. Microstructure tailoring to enhance strength and ductility in Ti-13Nb-13Zr for biomedical applications / T. Lee, Y.-Uk. Heo, C.S. Lee // *Scripta Mater.* — 2013. — Vol. 69(11–12). — P. 785–788. — DOI: 10.1016/j.scriptamat.2013.08.028.
- 10 Lee T. Microstructural evolution and strain-hardening behavior of multi-pass caliber-rolled Ti-13Nb-13Zr / T. Lee, K.-T. Park, D.J. Lee, J. Jeong, S. Oh, H. Kim, C. H. Park, C. S. Lee // *Mater. Sci. Eng. A.* — 2015. — Vol. 648. — P. 359–366. — DOI: 10.1016/j.msea.2015.09.062.
- 11 Lee T. Breaking the limit of Young's modulus in low-cost Ti-Nb-Zr alloy for biomedical implant applications / T. Lee, S. Lee, I.-S. Kim, Y. H. Moon, H. Kim, C. H. Park // *J. Alloys Compd.* — 2020. — Vol. 828. — P. 154401. — DOI: 10.1016/j.jallcom.2020.154401.
- 12 Klinge L. Nanostructured Ti-13Nb-13Zr alloy for implant application—material scientific, technological, and biological aspects / L. Klinge, L. Kluy, C. Spiegel, C. Siemers, P. Groche, D. Coraça-Huber // *Front. Bioeng. Biotechnol.* — 2023. — Vol. 11. — Art. 1255947. — DOI: 10.3389/fbioe.2023.1255947.
- 13 Xu H. Microstructure and mechanical properties evolution of Ti-13Nb-13Zr alloy processed by ECAP-Conform and rotary swaging / H. Xu, K. Wei, W. Wei, J. Džugan, I. Alexandrov, X. An, D. Wang, X. Liu, M. Daniel, D. Hradil, Q. Chen // *J. Alloys Compd.* — 2023. — Vol. 969. — P. 172351. — DOI: 10.1016/j.jallcom.2023.172351.
- 14 Godoy D. Severe plastic deformation and different surface treatments on the biocompatible Ti13Nb13Zr and Ti35Nb7Zr5Ta alloys: Microstructural and phase evolutions, mechanical properties, and bioactivity analysis / D. Godoy, A. Jr. Jorge, V. Roche, J.-C. Leprêtre, C. Afonso, D. Travessa, G. Asato, C. Bolfarini, W. Botta // *J. Alloys Compd.* — 2019. — Vol. 812. — P. 152116. — DOI: 10.1016/j.jallcom.2019.152116.
- 15 Gunderov D.V. et al. The Influence of Equal Channel Angular Pressing on Structure and Mechanical Properties of New β -Ti Alloy Ti-10Mo-8Nb-6Zr / D.V. Gunderov, A.A. Churakova, A.V. Polyakov, et al. // *Russ. J. Non-ferrous Metals*. — 2022. — Vol. 63. — P. 664–670. — DOI: 10.3103/S1067821222060086.
- 16 Rakhadilov B.K. Structure and phase composition of high-speed steels / B.K. Rakhadilov, W. Wieleba, M.K. Kylyshkanov, A.B. Kenesbekov, M. Maulet // *Bulletin of the University of Karaganda – Physics*. — 2020. — Vol. 98(2). — P. 83–92.
- 17 Kengesbekov A.B. Investigation of the characteristics of an indirect plasma torch / A.B. Kengesbekov, Z.B. Sagdoldin, D.B. Buitkenov, I.A. Ocheredko, S.A. Abdulina, K. Torebek // *Bulletin of the University of Karaganda – Physics*. — 2022. — Vol. 107(3). — P. 80–89.
- 18 Kengesbekov A.B. Formation of TiN coatings by air plasma spraying / A.B. Kengesbekov, B.K. Rakhadilov, L.G. Zhurerova, G.K. Uazyrkhanova, Y.Y. Kambarov // *Bulletin of the University of Karaganda – Physics*. — 2022. — Vol. 108(4). — P. 22–31.

А.Б. Кеңесбеков, А. Серікбайқызы, Д. Байжан, Е.Е. Батанов, Л.С. Каирбаева

Қарқынды пластикалық деформация режимдерінің Ti-13Nb-13Zr титан қорытпасының дәнін тең арналы бұрыштық престеу және одан кейінгі айналмалы-соғу сығымдау кезінде ұнтақтау процесіне әсерін зерттеу

Ультраұсақтүйіршікті (УҰТ) материалдар қазіргі кезде өздерінің жоғары механикалық және функционалдық қасиеттеріне байланысты үлкен қызығушылық тудыруда. Мұндай материалдарды ерекше микроқұрылымы мен қасиеттер үйлесімінде алудың ең тиімді әдістерінің бірі — интенсивті пластикалық деформация (ИПД). Осы жұмыста Ti-13Nb-13Zr титан қоспасына арналған тиімді ИПД әдісін әзірлеу қарастырылған. Бұл әдіс теңарналы бұрыштық престеу (ТБП) және одан кейінгі айналмалы-қысу соққысын (АҚС) қамтитын біріктірілген тәсілді қолдануға негізделген. Ti-13Nb-13Zr титан қоспасына бірнеше өту арқылы 130° бұрышты арнадан өтетін теңарналы бұрыштық престеу (ТБП) процесі әртүрлі температураларда жүргізілді, одан кейін айналмалы-қысу соққысы (АҚС) қолданылды. Микроқұрылымдық талдау нәтижелері көрсеткендей, ТБП мен АҚС-ты біріктіріп өңдеу арқылы бастапқы ірі түйіршікті (IT) құрылым ультратұсақтүйіршікке айналады. Сонымен қатар, механикалық сынақ нәтижелері аталған біріктірілген өңдеу әдісінің Ti-13Nb-13Zr титан қоспасының қаттылығы мен серпімділік модулін едәуір арттыратынын көрсетеді. Қалыптасқан қасиеттер кешеніндегі бұл өзгерістер бұл қоспаны биомедициналық имплантологияда қолданылатын дәстүрлі металл материалдарына жоғары тиімді балама ретінде қарастыруға мүмкіндік береді.

Кілт сөздер: интенсивті пластикалық деформация, ультратұсақтүйіршікті құрылым, теңарналы бұрыштық престеу, айналмалы-қысу соққысы, титан қорытпасы

А.Б. Кеңесбеков, А.Серікбайқызы, Д.Байжан, Е.Е. Батанов, Л.С. Каирбаева

Исследование влияния режимов интенсивной пластической деформации на процесс измельчения зерна титанового сплава Ti-13Nb-13Zr при равноканальном угловом прессовании и последующем вращательно-ковочном сжатии

Ультрамелкозернистые материалы в настоящее время представляют большой интерес благодаря своим превосходным механическим и функциональным свойствам. Одним из наиболее эффективных методов получения таких материалов с уникальным сочетанием микроструктуры и свойств является интенсивная пластическая деформация (ИПД). В настоящей работе рассматривается разработка эффективного метода ИПД для титанового сплава Ti-13Nb-13Zr, основанного на применении комбинированного подхода, включающего равноканальное угловое прессование (РКУП) и последующее вращательно-ковочное сжатие (ВКС). Титановый сплав Ti-13Nb-13Zr подвергался прессованию при различных температурах с использованием процесса равноканального углового прессования (РКУП) через угол канала 130° в течение нескольких проходов, с последующим вращательно-ковочным сжатием (ВКС). Микроструктурный анализ показал, что при применении комбинированной обработки (РКУП + ВКС) крупнозернистая (КЗ) структура трансформируется в ультрамелкозернистую (УМЗ) структуру. Кроме того, результаты механических испытаний свидетельствуют о том, что применение комбинированного метода обработки существенно повышает показатели твердости и модуля упругости титанового сплава Ti-13Nb-13Zr. Указанные изменения в комплексе свойств позволяют рассматривать данный сплав в качестве высокоэффективной альтернативы традиционным металлическим материалам, используемым в биомедицинской имплантологии.

Ключевые слова: интенсивная пластическая деформация, ультрамелкозернистая структура, равноканальное угловое прессование, вращательно-ковочное сжатие, титановые сплавы

References

- 1 Shao, L., Du, Y., Dai, K., Wu, H., Wang, Q., Liu, J., Tang, Y., & Wang, L. (2021). β -Ti Alloys for Orthopedic and Dental Applications: A Review of Progress on Improvement of Properties through Surface Modification. *Coatings*, 11, 1446. <https://doi.org/10.3390/coatings11121446>
- 2 Zhang, X., Alduma, A. I. A., Zhan, F., Zhang, W., Ren, J., & Lu, X. (2025). Effect of Grain Size on Mechanical Properties and Deformation Mechanism of Nano-Polycrystalline Pure Ti Simulated by Molecular Dynamics. *Metals*, 15, 271. <https://doi.org/10.3390/met15030271>

- 3 Regev, M. & Spigarelli, S.A. (2021). Study of the Metallurgical and Mechanical Properties of Friction-Stir-Processed Cu. *Metals*, 11, 656. <https://doi.org/10.3390/met11040656>
- 4 Baysal, E., Koçar, O., Kocaman, E., & Köklü, U. (2022). An Overview of Deformation Path Shapes on Equal Channel Angular Pressing. *Metals*, 12, 1800. <https://doi.org/10.3390/met12111800>
- 5 Semenova, I.P., Raab, G.I., Polyakova, V.V., & Valiev R.Z. Ultramelkozernistyi dvukhfaznyi alfa-beta titanovyi splav i sposob yego polucheniia [Ultrafine-grained two-phase alpha-beta titanium alloy and method of its preparation Ultrafine-grained two-phase alpha-beta titanium alloy and method of its preparation]. Patent №WO2013137765A1 International application— 2013-09-19 [in Russian].
- 6 Cvijović-Alagic', I., Cvijovic', Z., & Rakin, M. (2019). Damage behavior of orthopedic titanium alloys with martensitic microstructure during sliding wear in physiological solution. *Int. J. Damage Mech.*
- 7 Majumdar P., Singh S.B., & Chakraborty M. (2011). The role of heat treatment on microstructure and mechanical properties of Ti-13Zr-13Nb alloy for biomedical load bearing applications. *J. Mech. Behav. Biomed. Mater.*, 4(7), 1132–44. DOI: 10.1016/j.jmbbm.2011.03.023. Epub 2011 Mar 25. PMID: 21783122.
- 8 Park, C.H., Lee, C. S., Shin, Y.-J., Jang, Je.-H., Suh, Jo.-Y., & Park, J.-W. (2010). Improved pre-osteoblast response and mechanical compatibility of ultrafine-grained Ti-13Nb-13Zr alloy. *Clinical oral implants research*, 22, 735–742. DOI: 10.1111/j.1600-0501.2010.02053.x.
- 9 Lee, T., Heo, Y.-Uk, & Lee, C.S. (2013). Microstructure tailoring to enhance strength and ductility in Ti–13Nb–13Zr for biomedical applications. *Scripta Materialia*, 69(11–12), 785–788. DOI: 10.1016/j.scriptamat.2013.08.028.
- 10 Lee, Taekyung & Park, Kyung-Tae & Lee, Dong Jun & Jeong, Jiwon & Oh, Sang & Kim, Hyoung & Park, Chan Hee & Lee, Chong Soo. (2015). Microstructural evolution and strain-hardening behavior of multi-pass caliber-rolled Ti-13Nb-13Zr. *Materials Science and Engineering A*, 648, 359–366. DOI: 10.1016/j.msea.2015.09.062.
- 11 Lee, Taekyung & Lee, Sangwon & Kim, In-Su & Moon, Young Hoon & Kim, Hyoung & Park, Chan. (2020). Breaking the limit of Young's modulus in low-cost Ti–Nb–Zr alloy for biomedical implant applications. *Journal of Alloys and Compounds*, 828, 154401. DOI: 10.1016/j.jallcom.2020.154401.
- 12 Klinge, Lina & Kluy, Lukas & Spiegel, Christopher & Siemers, Carsten & Groche, Peter & Coraça-Huber, Débora (2023). Nanostructured Ti-13Nb-13Zr alloy for implant application—material scientific, technological, and biological aspects. *Frontiers in Bioengineering and Biotechnology*, 11, 1255947. DOI: 10.3389/fbioe.2023.1255947.
- 13 Xu, Hui & Wei, Kun & Wei, Wei & Džugan, Jan & Alexandrov, Igor & An, Xu & Wang, Dan & Liu, Xiang & Daniel, Matej & Hradil, David & Chen, Qiang. (2023). Microstructure and mechanical properties evolution of Ti-13Nb-13Zr alloy processed by ECAP-Conform and rotary swaging. *Journal of Alloys and Compounds*, 969, 172351. DOI: 10.1016/j.jallcom.2023.172351.
- 14 Godoy, DiegoJorgeJunior, Alberto & Roche, Virginie & Leprêtre, Jean-Claude & Afonso, Conrado & Travessa, Dilermando & Asato, Gabriel & Bolfarini, C. & Botta, Walter. (2019). Severe plastic deformation and different surface treatments on the bio-compatible Ti13Nb13Zr and Ti35Nb7Zr5Ta alloys: Microstructural and phase evolutions, mechanical properties, and bioactivity analysis. *Journal of Alloys and Compounds*, 812, 152116. 10.1016/j.jallcom.2019.152116
- 15 Gunderov, D.V., Churakova, A.A., & Polyakov, A.V. (2022). The Influence of Equal Channel Angular Pressing on Structure and Mechanical Properties of New β -Ti Alloy Ti–10Mo–8Nb–6Zr. *Russ. J. Non-ferrous Metals*, 63, 664–670. <https://doi.org/10.3103/S1067821222060086>
- 16 Rakhadilov, B.K., Wieleba, W., Kylyshkanov, M.K., Kenesbekov, A.B., & Maulet, M. (2020). Structure and phase composition of high-speed steels. *Bulletin of the University of Karaganda – Physics*, 98(2), 83–92.
- 17 Kengesbekov, A.B., Sagdoldin, Z.B., Buitkenov, D.B., Ocheredko, I.A., Abdulina, S.A., & Torebek, K. (2022). Investigation of the characteristics of an indirect plasma torch. *Bulletin of the University of Karaganda – Physics*, 107(3), 80–89.
- 18 Kengesbekov, A.B., Rakhadilov, B.K., Zhureroova, L.G., Uazyrkhanova, G.K., & Kambarov, Y.Y. (2022). Formation of TiN coatings by air plasma spraying. *Bulletin of the University of Karaganda – Physics*, 108(4), 22–31.

Information about the authors

Kengesbekov, Aidar — Leading researcher of the Research center “Protective and functional coatings” of East Kazakhstan Technical University named after D. Serikbayev, Ust-Kamenogorsk, Kazakhstan; e-mail: aidar.94.01@mail.ru; ORCID ID: <https://orcid.org/0000-0002-5630-9467>

Serikbaikyzy, Ainur — Doctoral student of the East Kazakhstan Technical University named after D. Serikbaev, Ust-Kamenogorsk, Ust-Kamenogorsk, Kazakhstan; e-mail: Serikbaikyzy.ainura@gmail.com; ORCID ID: <https://orcid.org/0009-0005-7734-9512>

Baizhan, Daryn (contact person) — Senior Researcher at the Scientific Research Center “Surface Engineering and Tribology”, S. Amanzholov East Kazakhstan University, Ust-Kamenogorsk, Kazakhstan; e-mail: daryn.baizhan@mail.ru; ORCID ID: <https://orcid.org/0000-0002-9105-3129>

Batanov, Yelaman — Engineer of the scientific center “Protective and functional coatings” of VKTU named after D. Serikbaev, Ust-Kamenogorsk, Kazakhstan; e-mail: — batanovelman1234@gmail.com; ORCID ID: <https://orcid.org/0009-0003-2593-6665>

Kairbayeva, Limara — Student of the EKTU named after D. Serikbaev, Ust-Kamenogorsk, Kazakhstan; e-mail: limaralkairbaeva52@gmail.com; ORCID ID: <https://orcid.org/0009-0001-6091-1071>

E.R. Hasanov^{1, 2}, Sh.G. Khalilova^{2, 1✉}, R.K. Mustafayeva¹¹Baku State University, Baku, Azerbaijan Republic;²Institute of Physics, Baku, Azerbaijan Republic**Transverse and Longitudinal Thermomagnetic Waves in Conducting Media**

The excited thermomagnetic wave in anisotropic conducting media is analyzed theoretically at different directions of the gradient of the temperature $\vec{\nabla}T$, relative to the wave vector \vec{k} . It is shown that at $\vec{k} \perp \vec{\nabla}T$ (transverse wave) and at $\vec{k} \parallel \vec{\nabla}T$ (longitudinal wave) the oscillation frequency has different values. In these two cases, the excited thermomagnetic waves are increasing. The increment of the increase in each case has different values. It is shown that the values in different directions of electrical conductivity for the excitation and for the increase of thermomagnetic waves play a major role. Depending on the selected conditions, the frequency of thermomagnetic waves changes significantly. In both cases (i.e. $\vec{k} \perp \vec{\nabla}T$ and $\vec{k} \parallel \vec{\nabla}T$), the choice of coordinate systems does not affect the theoretical calculation at all. The frequency and increment of thermomagnetic waves do not depend on the choice of coordinate systems. However, the choice of coordinate systems significantly affects the choice of the direction of the magnetic field and the temperature gradient. The velocity of hydrodynamic motions of charge carriers turns towards the temperature gradient. The excited magnetic field upon excitation of charge carriers (electrons) depends very much on the direction of the temperature gradient. The oscillation frequency of excitation of thermomagnetic waves depends linearly on the value of the temperature gradient. The increment of growth of excited thermomagnetic waves has different values for different values of the tensor of electrical conductivity of the medium σ_{ik} . It is stated that if the wave vector of excited waves and the constant gradient of the temperature are directed at an angle, i.e. $(\vec{k}\vec{\nabla}T = k\nabla T \cos \alpha, [\vec{k}\vec{\nabla}T] = k\nabla T \sin \alpha)$ theoretical calculation of the oscillation frequency and the increment of growth fails due to the high degree of the dispersion equation relative to the oscillation frequency. This theory does not consider the electric field created by the redistribution of charge carriers. The theory takes into account that the constant temperature T_0 , external field E_0 , and the mean free path of charge carriers satisfy the relation $k_0 T_0 \ll eE_0 l$, k_0 is a constant. At $k_0 T_0 \sim eE_0 l$ and $k_0 T_0 > eE_0 l$ a very high temperature is required, i.e. melting of the medium begins.

Keywords: excitation, frequency, increment, thermomagnetic, dispersion equation, temperature gradient, wave, wave vector

✉Corresponding author: Khalilova, Sh., shahlaganbarova@gmail.com

Introduction

In the work of L.E. Gurevich [1] it was shown that hydrodynamic movements in a nonequilibrium plasma, in which there is a temperature gradient, lead to the emergence of magnetic fields.

In the same work it was found that plasma with gradient of the temperature $\vec{\nabla}T$ has oscillatory properties that are noticeably different from the properties of ordinary plasma. Even in the absence of an external magnetic field and hydrodynamic motions, transverse thermomagnetic waves are possible in it (i.e., $\vec{k} \perp \vec{\nabla}T$, \vec{k} — wave vector), in which only the magnetic field oscillates. If there is a constant external magnetic field \vec{H}_0 , then the wave vector of thermomagnetic waves should be perpendicular to it and lie in the plane $(\vec{H}_0, \vec{\nabla}T)$. In addition, the usual Alphen wave splits into two hydrothermomagnetic waves, in which the vectors \vec{V} and are perpendicular to \vec{H}' . The spectrum of magnetosonic waves can change noticeably if the propagation speed of thermomagnetic waves is comparable to the speed of sound and the speed of Alphen waves.

If there is a uniform magnetic field in a plasma with gradient of the temperature, then under the influence of thermomagnetic fields it gradually turns in the direction of the temperature gradient.

Research of thermomagnetic waves in homogeneous conducting media (in semiconductors and metals) was carried out in works [2–11]. However, there is no excitation of thermomagnetic waves in anisotropic conducting media. In this theoretical work we will analyze some conditions for the excitation of stable thermomagnetic waves in anisotropic conducting media without an external magnetic field $\vec{H}_0 = 0$ and in the presence of a constant temperature gradient.

Theory

In the presence of an electric field \vec{E} , gradient of electron concentration ∇n , temperature $\vec{\nabla} T = \text{const}$ and hydrodynamic movements $\vec{V}(\vec{r}, t)$, the electric current density in a homogeneous medium has the form:

$$\vec{j} = \sigma \vec{E}^* + \sigma' [\vec{E}^* \vec{H}] - \alpha \vec{\nabla} T - \alpha' [\vec{\nabla} T \vec{H}]; \quad (1)$$

$$\vec{E}^* = \vec{E} + \frac{[\vec{V} \vec{H}]}{c} + \frac{T}{e} \frac{\vec{\nabla} n}{n} (e > 0). \quad (2)$$

In (2), \vec{E} is the external electric field, $\frac{[\vec{V} \vec{H}]}{c}$ is the electric field created by hydrodynamic motion, $\frac{T}{e} \frac{\vec{\nabla} n}{n}$ is the electric field created by the electron concentration gradient. Substituting (2) into (1), we obtain an equation of the form

$$\vec{x} = \vec{a} [\vec{b} \vec{x}]; \quad (3)$$

$$\vec{x} = \vec{E}.$$

From (3) we obtain:

$$\vec{E} = -\frac{[\vec{V} \vec{H}]}{c} - \Lambda' [\vec{\nabla} T \vec{H}] + \frac{c}{4\pi\sigma} \text{rot } \vec{H} - \frac{c\sigma'}{4\pi\sigma^2} [\text{rot } \vec{H}, \vec{H}] + \frac{T}{e} \frac{\vec{\nabla} n}{n} + \Lambda \vec{\nabla} T. \quad (4)$$

Here $\Lambda = \frac{\alpha}{\sigma}$, $\Lambda' = \frac{\alpha'\sigma - \alpha\sigma'}{\sigma^2}$, $\text{rot } \vec{H} = \frac{4\pi}{c} \vec{j}$, $\frac{\partial H'}{\partial t} = -c \text{rot } \vec{E}'$, σ —conductivity coefficient, Λ —differential thermoelectric power, Λ' —coefficient of the Nernst-Ettinghausen effect.

We will investigate some conditions of thermomagnetic waves in anisotropic conducting media and therefore we will write the electric field in isotropic media

$$\vec{E} = \eta \vec{j} + \eta' [\vec{j} \vec{H}] + \eta'' (\vec{j} \vec{H}) \vec{H} + \Lambda \frac{\partial T}{\partial x} + \Lambda' [\nabla T, H] + \Lambda'' (\nabla T, H) \vec{H}; \quad (5)$$

in anisotropic media

$$E_{ik} = \eta_{ik} E_k + \eta'_{ik} [\vec{j} \vec{H}]_k + \eta''_{ik} (\vec{j} \vec{H}) H_k + \Lambda_{ik} \frac{\partial T}{\partial x_k} + \Lambda'_{ik} [\nabla T, H]_k + \Lambda''_{ik} (\nabla T, H) \vec{H}_k. \quad (6)$$

Here η_{ik} is the tensor of the inverse value of the ohmic resistance, Λ_{ik} is the tensor of the differential thermoelectric power, Λ'_{ik} is the tensor of the Nernst-Ettinghausen coefficient, we will consider in an anisotropic body an external magnetic field \vec{H}_0 . Then in (6) the terms containing of $\eta'_{ik}, \eta''_{ik}, \Lambda''_{ik}$ are equal to zero. Then for our problem we obtain the following system of equations

$$E'_i = \eta_{ik} j'_k + \Lambda'_{ik} [\vec{\nabla} T \vec{H}]_k; \quad (7)$$

$$\text{rot } \vec{E}' = -\frac{1}{c} \frac{\partial \vec{H}'}{\partial t};$$

$$\text{rot } \vec{H}' = \frac{4\pi}{c} \vec{j}' + \frac{1}{c} \frac{\partial \vec{E}'}{\partial t}.$$

Let us assume that all variables have the form of a monochromatic wave

$$(E', H', j') \sim e^{i(\vec{k}\vec{r} - \omega t)}. \quad (8)$$

Considering (8) from (7) we obtain:

$$E'_i = \frac{ic^2}{4\pi w} \eta_{ik} (\vec{k}\vec{E}') K_k + \frac{iw^2 - ic^2 k^2}{4\pi w} \eta_{ik} E'_k + \frac{c\Lambda'_{ik}}{w} (\vec{\nabla} T \vec{E}') K_k - \frac{c\Lambda'_{ik}}{w} (\vec{k}\vec{\nabla} T) K'_k. \quad (9)$$

Here \vec{k} — wave vector, $(i, k = 1, 2, 3)$.

Let's write

$$E'_i = \delta_{ik} E'_k, \delta_{ik} = \begin{cases} 1, & i = k; \\ 0, & i \neq k. \end{cases} \quad (10)$$

Substituting (10) into (9) we obtain:

$$\delta_{ik} E'_k = \left(A \eta_{ik} K_l K_k + B \eta_{ik} + \frac{c\Lambda'_{il}}{w} K_l \frac{\partial T}{\partial x_k} \right) E'_k; \quad (11)$$

$$A = \frac{ic^2}{4\pi w}; \quad B = \frac{i(w^2 - c^2 k^2)}{4\pi w}.$$

From (11) next dispersion equation is obtained:

$$|\Phi_{ik} - \delta_{ik}| = 0; \quad (12)$$

$$\Phi_{ik} = A \eta_{ik} K_l K_k + B \eta_{ik} + \frac{c\Lambda'_{il}}{w} K_l \frac{\partial T}{\partial x_k}. \quad (13)$$

Transverse thermomagnetic waves $\vec{k} \perp \vec{\nabla} T$

At the condition $\vec{k} \perp \vec{\nabla} T$, a coordinate system can be chosen

$$k_1 \neq 0, k_2 = k_3 = 0, k_1 \frac{\partial T}{\partial x_1} = 0, \frac{\partial T}{\partial x_2} \neq 0, \frac{\partial T}{\partial x_3} = 0.$$

Having written out (13) by components and expanding the determinant (12), we obtain the following dispersion equation in the case $\vec{k} \perp \vec{\nabla} T$.

$$\begin{aligned} & i(a-b)w^5 + 4\pi(a_1 - b_1)w^4 + [2ic^2k^2(b-a) + i16\pi^2\eta + 4\pi\tilde{w}\eta_1^2]w^3 + \\ & + [4\pi c^2k^2\eta_2^2 + i16\pi^2(w_{11}\eta_{21} - w'_{21}\eta_{33} + w_{31}\eta_{23}) - 64\pi^3]w^2 + \\ & + [ic^4k^4(a-b) + 4\pi c^2k^2(w_{11}\eta_{23}\eta_{31} - w_{11}\eta_{21}\eta_{33} + w_{21}\eta_{11}\eta_{33} + w_{31}\eta_{21}\eta_{13} - \\ & - w_{31}\eta_{11}\eta_{33} - w_{21}\eta_{13}\eta_{31}) - i16\pi^2c^2k^2(\eta_{22} + \eta_{33} + 64\pi^3w_{21})]w + \\ & + 4\pi c^4k^4(\eta_{22}\eta_{33} - \eta_{32}\eta_{23}) + i16\pi^2c^2k^2(w_{21}\eta_{33} - w_{31}\eta_{23}) = 0. \end{aligned} \quad (14)$$

$$\eta = \eta_{11} + \eta_{22} + \eta_{33}.$$

From (14) it is easy to see that the general solution is very complicated and therefore we assume the following conditions

$$\begin{aligned} w_{21}\eta_{33} &= w_{31}\eta_{23}; \\ \eta_{22}\eta_{33} &= \eta_{32}\eta_{23}; \\ \eta &= \eta_{21} = \sigma_{21}. \end{aligned} \quad (15)$$

Condition (15) is the choice of the environment.

Substituting (15) into (14) we obtain the following distance equation

$$w^2 + \left(w_{11} + i \frac{4\pi}{\eta} \right) w - \frac{c^2 k^2 (\eta - \eta_{11})}{\eta} = 0. \quad (16)$$

From (16)

$$w_{1,2} = -\frac{w_{11}}{2} - i2\pi\sigma_{21} \pm \frac{w_{11}}{2} \left[1 - \frac{16\pi^2\sigma_{21}^2}{w_{11}^2} + \frac{4c^2k^2 \left(\frac{1}{\sigma_{21}} - \frac{1}{\sigma_{11}} \right) \sigma_{21}}{w_{11}^2} + i \frac{16\pi\sigma_{21}}{w_{11}} \right]^{1/2} \quad (17)$$

is obtained.

From (17) it is clear that if $\frac{ck}{\sigma_{21}} = 2\pi$, $\frac{\sigma_{11}w_{11}}{2c^2k^2} = 1$

$$\begin{aligned} w_{1,2} &= -\frac{w_{11}}{2} - i2\pi\sigma_{21} \pm w_{11} \left(\frac{\pi\sigma_{21}}{w_{11}} \right)^{1/2} (1+i); \\ w_1 &= -\frac{w_{11}}{2} - i2\pi\sigma_{21} + w_{11} \left(\frac{\pi\sigma_{21}}{w_{11}} \right)^{1/2} (1+i); \\ w_2 &= -\frac{w_{11}}{2} - i2\pi\sigma_{21} - w_{11} \left(\frac{\pi\sigma_{21}}{w_{11}} \right)^{1/2} (1+i). \end{aligned} \quad (18)$$

From (18) it is clear that w_2 is decaying wave. A wave with frequency $w_0 = -\frac{w_{11}}{2} + w_{11} \left(\frac{\pi\sigma_{21}}{w_{11}} \right)^{1/2}$ can be growing if $w_{11} \left(\frac{\pi\sigma_{21}}{w_{11}} \right)^{1/2} > 2\pi\sigma_{21}$ or $w_{11}^{1/2} > 2\pi^{1/2}\sigma_{21}^{1/2}$, $\left(\frac{w_{11}}{\sigma_{21}} \right)^{1/2} > 2\pi^{1/2}$,

$$w_{11} > 4\pi\sigma_{21}. \quad (19)$$

Conditions (19) are satisfied in a certain anisotropic medium. Thus, at $\vec{k} \perp \vec{\nabla}T$ with a frequency

$$w_0 = w_{11} \left[\left(\frac{\pi\sigma_{21}}{w_{11}} \right)^2 - \frac{1}{2} \right] \approx -\frac{w_{11}}{2} = -\frac{ck\nabla_2 T \Lambda'_{11}}{2}$$

in an anisotropic crystal a purely thermomagnetic wave is excited.

Longitudinal thermomagnetic waves $\vec{k} \parallel \vec{\nabla}T$

Given the condition, one can choose the axes so that

$$\begin{aligned} k_1 = k, k_2 = k_3 = 0, \frac{\partial T}{\partial x} = \frac{\partial T}{\partial x_1} \neq 0, \frac{\partial T}{\partial x_2} = \frac{\partial T}{\partial x_3} = 0; \\ i(a-b)w^5 + 4\pi(a_1 - b_1)w^4 + [2ic^2k^2(a-b) + i16\pi^2\eta + 4\pi\tilde{w}\eta_1^2]w^3 + \\ + [4\pi c^2k^2(a_1 - b_1) + i16\pi^2\tilde{w}\eta_2 - 64\pi^3]w^2 + \\ + [ic^4k^4(a-b) + 4\pi c^2k^2\tilde{w}_2\eta_3^2 + i16\pi^2w_3^2\eta_4 - i16\pi^2(\eta_{22} + \eta_{33}) - \\ - 64\pi^3(w_{22} + w_{33})]w + 4\pi c^4k^4(\eta_{22}\eta_{33} - \eta_{23}\eta_{32}) + 64\pi^3(w_{23}w_{32} - w_{22}w_{33}) + \\ + i16\pi^2c^2k^2(w_{23}\eta_{32} + w_{32}\eta_{23} - w_{33}\eta_{22} + w_{22}\eta_{33}) = 0. \end{aligned} \quad (20)$$

$$\begin{aligned}\eta_{22}\eta_{33} &= \eta_{23}\eta_{32}; \\ w_{32}\eta_{23} &= w_{33}\eta_{22}; \\ w_{22}\eta_{33} &= w_{23}\eta_{32}.\end{aligned}\tag{21}$$

Substituting (21) into (20):

$$-64\pi^3 w^2 - [i16\pi^2 \eta c^2 k^2 + 64\pi^3 (w_{22} + w_{33})] w + 64\pi^3 (w_{23}w_{32} - w_{22}w_{33}) = 0\tag{22}$$

is obtained.

From solution (22):

$$w_{1,2} = -\frac{w_{22} + w_{33}}{2} - i\frac{c^2 k^2 \eta}{8\pi} \pm \left[\left(\frac{w_{22} + w_{33}}{2} + i\frac{c^2 k^2 \eta}{8\pi} \right)^2 + w_{22}w_{33} - w_{23}w_{32} \right]\tag{23}$$

is obtained

is $\eta c^2 k^2 = 4\pi(w_{22} + w_{33})$

$$w = \frac{w_{22} + w_{33}}{2} \left[-1 + \frac{1}{\sqrt{2}} \left(\sqrt{\alpha^2 + \beta^2} + \alpha \right) \right]^{1/2} + \frac{w_{22} + w_{33}}{2} \left[-1 + \frac{1}{\sqrt{2}} \left(\sqrt{\alpha^2 + \beta^2} - \alpha \right) \right]^{1/2};\tag{24}$$

$$\alpha = \left(\frac{w_{22} + w_{33}}{\Omega} \right)^2; \beta = \frac{1}{16\pi}, \Omega^2 = w_{22}w_{33} - w_{23}w_{32}.\tag{25}$$

Considering (25), analysis of (24) shows that when

$$\left(\sqrt{\alpha^2 + \beta^2} - \alpha \right)^{1/2} > 1\tag{26}$$

with a frequency

$$w_0 = \frac{w_{22} + w_{33}}{2} \left[-1 + \frac{1}{\sqrt{2}} \left(\sqrt{\alpha^2 + \beta^2} + \alpha \right) \right]^{1/2}$$

an unstable wave is excited and when performing (26) it is required

$$\left(\frac{1}{16\pi} \right)^2 > \frac{2(w_{22}w_{33} - w_{23}w_{32})}{(w_{22} + w_{33})^2} + 1.\tag{27}$$

Inequality (27) is satisfied if $w_{23}w_{32} > w_{22}w_{33}$. Then

$$\left(\frac{1}{16\pi} \right)^2 > 1 - \frac{2w_{23}w_{32}}{(w_{22} + w_{33})^2}.$$

If $w_{22} = w_{33}$

$$\left(\frac{1}{16\pi} \right)^2 > 1 - \frac{w_{23}w_{32}}{2w_{22}^2}$$

or

$$\frac{w_{23}w_{32}}{2w_{22}^2} > 1.$$

Then the frequency of the thermomagnetic wave

$$w_0 = w_{22} \left[-1 + \frac{1}{\sqrt{2}} \left(\sqrt{\alpha^2 + \beta^2} + \alpha \right) \right]^{1/2}\tag{28}$$

and the growth increment

$$w_1 = w_{22} \left[-1 + \frac{1}{\sqrt{2}} \left(\sqrt{\alpha^2 + \beta^2} - \alpha \right)^{1/2} \right]. \quad (29)$$

From (28–29) it is clear that $w_1 < w_0$.

Conclusion

Thus, in anisotropic conducting media, a transverse $\vec{k} \perp \vec{\nabla}T$ and longitudinal $\vec{k} \parallel \vec{\nabla}T$ growing thermomagnetic wave is excited. The frequencies of these waves $w_0(\vec{k} \perp \vec{\nabla}T)$ and $w_0(\vec{k} \parallel \vec{\nabla}T)$ are determined by the conductivities in different directions.

$w_0(\vec{k} \parallel \vec{\nabla}T)$ depends only on the frequency $w_{22} = c\Lambda'_{22}k\nabla_2T$, and $w_0(\vec{k} \perp \vec{\nabla}T)$ depends only on the frequency $w_{11} = c\Lambda'_{11}k\nabla_2T$ and therefore the values of these frequencies are different. The increment of growing $w_1(\vec{k} \parallel \vec{\nabla}T)$ and $w_1(\vec{k} \perp \vec{\nabla}T)$ also depend on different values of the frequency of thermomagnetic waves. The Nernst-Ettinghausen coefficient Λ'_{ik} is different in different directions. Of course, studies of thermomagnetic waves in the presence of an external magnetic field certainly lead to different dependencies $w_0(\vec{k} \perp \vec{\nabla}T)$ and $w_0(\vec{k} \parallel \vec{\nabla}T)$.

The obtained expressions for frequency, expressions for increment in this theoretical work, are valid for waves propagating perpendicular to the temperature gradient, when parallel to the temperature gradient the conditions of excitation of waves in the medium will be different. It is possible to conduct corresponding experiments based on the results of this theoretical work and apply them to GaAs-type semiconductors. As for the application of the obtained results, it is necessary to experimentally measure The Nernst-Ettinghausen coefficient Λ'_{ik} in anisotropic conducting media. After measuring this coefficient, it is possible to control significantly the frequencies ω_0 and ω_1 . This can lead to an improvement in the preparation of generators based on these thermomagnetic waves.

References

- 1 Gurevich, L.E. (1963). Thermomagnetic waves and excitation of the magnetic field in nonequilibrium plasmas. *JETP*, 44, 548–555.
- 2 Aliev, S.A., & Zulfigarov, E.I. (2009). *Thermomagnetic and thermoelectric phenomena in science and technology*. BAKU — “ELM”, 325 p.
- 3 Tailanov, N.A., & Yakhshiev, U.T. (2001). Stationary thermomagnetic waves in superconductors. *Technical Physics*, 46, 1060–1062.
- 4 Hasanov, E.R., Khalilova, Sh.G., Mammadova, G.M., & Mansurova, E.O. (2023). Excitation of unstable waves in semiconductors such as GaAs magnetic fields ($\mu H \gg c$), *IJTPE*, 15(2), 302–306 (The IJTPE is indexed in Scopus / Elsevier since 2019 Impact factor 4.54).
- 5 Hasanov, E.R., Khalilova, Sh.G., & Mustafayeva, R.K. (2023). Excitation of unstable waves of electromagnetic and thermomagnetic nature in conducting media with two types of charge carriers in the presence of a constant temperature gradient. *Amorphous and microcrystalline semiconductors, Proceedings of the International Conference*, July 3–5, St. Petersburg, pp. 237–238.
- 6 Maharramova, A.A., & Hasanov, E.R. (2023). Frequency of transverse and longitudinal thermomagnetic waves in certain anisotropic conducting media, “*Modern Trends in Physics*” — the 8th International Conference, November 30 – December 1 2023, Baku State University, p. 30–31/
- 7 Hideya Nishiyama, Hiromichi Tsukada, Yukio Matsushima & Shinichi Kamiyama (1997). The effect of an applied magnetic field on non-equilibrium plasma flow along a biased flat plate. *J. Phys. D: Appl. Phys.* 30, 2804.
- 8 Gianpiero Colonna, Carlos D. Pintassilgo, & Francesco Pegoraro, et al. (2021). Theoretical and experimental aspects of non-equilibrium plasmas in different regimes: fundamentals and selected applications. *The European Physical Journal D*, 75, art. 183.
- 9 Gafel, H.S. (2022). Fractional order study of the impact of a photo thermal wave on a semiconducting medium under magnetic field and thermoplastic theories. *Information Science Letter*, 11, 629–638.
- 10 Abouelregal, A.E., Sedighi, H.M., & Eremeyev V.A. (2023). Thermomagnetic behavior of a semiconductor material heated by pulsed excitation based on the fourth-order MGT photothermal model. *Continuum Mech. Therm.*, 35(1), 81–102.
- 11 Petrov, A.S., & Svintsov, D. (2024). High-Frequency Hall Effect and Transverse Electric Galvanomagnetic Waves in Current-Biased 2D Electron Systems. *JETP Letters*, 119(10), 800–806.

Э.Р. Гасанов, Ш.Г. Халилова, Р.К. Мустафаева

Өткізгіш орталардағы көлденең және бойлық термомагниттік толқындар

Температура градиентінің $\vec{\nabla}T$ толқындық векторға \vec{k} қатысты әртүрлі бағыттарында анизотропты өткізгіш ортада қоздырылатын термомагниттік толқынға теориялық талдау жүргізіледі. $\vec{k} \perp \vec{\nabla}T$ (көлденең толқын) және $\vec{k} \parallel \vec{\nabla}T$ (бойлық толқын) жағдайларында тербеліс жиілігі әртүрлі мәнге ие болатыны көрсетілген. Бұл екі жағдайда да қоздырылатын термомагниттік толқындар арттырушы сипатқа ие. Әрбір жағдайда толқынның күшею инкременті әртүрлі болады. Термомагниттік толқындардың қозуы мен күшеюіне анизотропты ортаның әртүрлі бағыттарындағы электрөткізгіштік σ_{ik} мәндері басты рөл атқаратыны дәлелденген. Таңдалған шарттарға байланысты термомагниттік толқынның жиілігі елеулі түрде өзгереді. Екі жағдайда да (яғни, $\vec{k} \perp \vec{\nabla}T$ и $\vec{k} \parallel \vec{\nabla}T$), координаттар жүйесін таңдау теориялық есептеулерге әсер етпейді. Термомагниттік толқындардың жиілігі мен күшею инкременті координаттар жүйесіне тәуелді емес. Алайда, координаттар жүйесін таңдау магнит өрісі мен температура градиенті бағытын таңдауға елеулі әсер етеді. Гидродинамикалық қозғалыс жылдамдығы температура градиенті бағытына қарай бағытталады. Заряд тасымалдаушылар (электрондар) қоздырылған кезде пайда болатын магнит өрісі температура градиенті бағытына қатты тәуелді. Термомагниттік толқындардың қозу тербеліс жиілігі температура градиентінің шамасына сызықты түрде тәуелді. Қоздырылатын термомагниттік толқындардың күшею инкременті ортаның электрөткізгіштік σ_{ik} тензорының әртүрлі мәндерінде түрліше болады. Қоздырылатын толқынның толқындық векторы мен тұрақты температура градиенті $\left(\vec{k} \vec{\nabla}T = k \nabla T \cos \alpha, \left[\vec{k} \vec{\nabla}T \right] = k \nabla T \sin \alpha \right)$ бір-біріне белгілі бір бұрышпен бағытталған жағдайда, тербеліс жиілігіне қатысты дисперсиялық теңдеудің дәрежесі болуына байланысты тербеліс жиілігі мен күшею инкрементінің теориялық есептеулері орындалмайтындығы дәлелденген. Бұл теорияда заряд тасымалдаушылардың қайта таралуы нәтижесінде пайда болатын электр өрісі есепке алынбаған. Теорияда температураның тұрақты мәні T_0 , сыртқы өріс E_0 , және заряд тасымалдаушылардың еркін жүріс ұзындығы $k_0 T_0 \ll e E_0 l$, k_0 мына шартқа сәйкес келетіні қарастырылған. Егер $k_0 T_0 \sim e E_0 l$ және $k_0 T_0 > e E_0 l$ жағдайында болса, ортаның балқу процесі басталатындай өте жоғары температура қажет етіледі.

Кілт сөздер: қозу, жиілік, инкремент, термомагнит, дисперсиялық теңдеу, температура градиенті, толқын, толқындық вектор

Э.Р. Гасанов, Ш.Г. Халилова, Р.К. Мустафаева

Поперечные и продольные термомагнитные волны в проводящих средах

Теоретически анализируется возбуждаемая термомагнитная волна в анизотропных проводящих средах при различном направлении градиента температуры $\vec{\nabla}T$, относительно волнового вектора \vec{k} . Показано, что при $\vec{k} \perp \vec{\nabla}T$ (поперечная волна) и при $\vec{k} \parallel \vec{\nabla}T$ (продольная волна) частоты колебаний имеют разные значения. В этих двух случаях возбуждаемые термомагнитные волны являются нарастающими. Инкремент нарастания в каждом случае имеют разные значения. Показано, что значения в разных направлениях электропроводности σ_{ik} для возбуждения и для нарастания термомагнитных волн играют основной роль. В зависимости от выбранных условий значения частоты термомагнитных волн существенно меняется. В обоих случаях (т.е. $\vec{k} \perp \vec{\nabla}T$ и $\vec{k} \parallel \vec{\nabla}T$) выбор координатных систем совсем не влияет на теоретический расчёт. Частота и инкремент термомагнитных волн не зависят от выбора координатных систем. Однако выбор координатной системы существенно влияет на выбор направления магнитного поля и градиента температуры. Скорость гидродинамических движений носителей заряда поворачивается в сторону градиента температуры. Возбуждаемое магнитное поле при возбуждении носителей заряда (электронов) очень сильно зависит от направления градиента температуры. Частота колебания возбуждения термомагнитных волн линейно зависит от значения градиента температуры. Инкремент нарастания возбуждаемых термомагнитных волн имеет разные значения при разных значениях тензора электропроводности среды σ_{ik} . Утверждено, что если волновой вектор возбуждаемых волн и постоянный градиент температуры направлен под углом, т.е. $\left(\vec{k} \vec{\nabla}T = k \nabla T \cos \alpha, \left[\vec{k} \vec{\nabla}T \right] = k \nabla T \sin \alpha \right)$ теоретический расчёт частоты колебания и инкремент нарастания не удаётся из-за высокой степени дисперсионного уравнения относительно частоты колебания. В этой теории не учтены электрическое поле, создаваемое перераспределением носителей заряда. В теории учтены, что постоянная температура T_0 , внешнее поле E_0 , длина свободного пробега носителей

заряда удовлетворяют соотношению $k_0 T_0 \ll eE_0 l$, k_0 - постоянная. При $k_0 T_0 \sim eE_0 l$ и $k_0 T_0 > eE_0 l$ требуется очень высокая температура, т.е. начинается плавление среды.

Ключевые слова: возбуждение, частота, инкремент, термомагнит, дисперсионное уравнение, градиент температуры, волна, волновой вектор

Information about the authors

Hasanov, Eldar — PhD, Associate Professor, Department of Solid State Physics, Baku State University Physics, Leader of Department of Encyclopedia and Terminology, Institute of Physics, Baku, Azerbaijan; e-mail: egasanov065@gmail.com; ORCID ID: <https://orcid.org/0009-0009-6900-6148>.

Khalilova, Shahla (*contact person*) — PhD, Leading researcher of Department of Encyclopedia and Terminology, Institute of Physics, Teacher of Department of Structure of Matter, Baku State University Physics, Baku, Azerbaijan; e-mail: shahlaganbarova@gmail.com; ORCID ID: <https://orcid.org/0000-0003-4302-9674>.

Mustafayeva, Ruhiyye — PhD, Teacher, Department of Solid State Physics, Baku State University Physics, Baku, Azerbaijan; e-mail: ruhi-qrk@mail.ru; ORCID ID: <https://orcid.org/0009-0005-2342-5399>.

B.K. Rakhadilov^{1,2}, D.B. Buitkenov³, A.K. Apsezhanova²✉,
N.M. Magazov², M.B. Bayandinova²

¹PlasmaScience LLP, Ust-Kamenogorsk, Kazakhstan;

²D. Serikbayev East Kazakhstan Technical University, Ust-Kamenogorsk, Kazakhstan;

³S. Amanzholov East Kazakhstan University, Ust-Kamenogorsk, Kazakhstan

Influence of Wire Type on the Structure and Properties of Coatings Obtained by Electric Arc Metallization

Electric arc metallization (EAM) is one of the most effective and widely used thermal spraying methods, in which a protective coating is formed by melting a metal wire with an electric arc and atomising the molten material with a stream of compressed air. This technology is characterised by high productivity, adjustable layer thickness, and the versatility of applicable materials. This study presents a comparative analysis of protective coatings applied to 65G steel using electric arc metallization with both powder and cast wires made of 30KhGSA and 51KhFA alloys. The microstructure of the coatings was examined using a scanning electron microscope, and the elemental composition was determined using energy dispersive spectroscopy (EDS). The thickness and porosity of the coating were evaluated using an optical microscope. Microhardness was measured using Vickers, and surface roughness was evaluated using contact profilometry. Microstructural and EDS analyses revealed that coatings produced with cored wires exhibit a more homogeneous distribution of alloying elements, resulting in improved microhardness, reduced porosity. In contrast, coatings obtained with cast wires showed structural inhomogeneity, leading to increased porosity and decreased mechanical performance. Surface roughness measurements indicated that cored wire coatings had higher roughness values, particularly for 51KhFA. The findings analyzed that powder (cored) wire offers superior coating quality.

Keywords: electric arc metallization, cast and powder wire, porosity, steel coating, elemental composition

✉Corresponding author: Apsezhanova Akbota, akbotaapsezanova@mail.com

Introduction

Under the operating conditions of agricultural machinery in Kazakhstan, where machine components are subjected to intense abrasive wear, the task of improving the wear resistance of working elements is of particular relevance. One of the promising solutions is the formation of protective layers using the electric arc metallization (EAM) method, which enhances wear resistance and extends the service life of components [1].

Electric arc metallization (EAM) is one of the most effective and widely used thermal spraying methods, in which a protective coating is formed by melting a metal wire with an electric arc and atomising the molten material with a stream of compressed air [2]. This technology is characterised by high productivity, adjustable layer thickness, and the versatility of applicable materials, making it particularly relevant in mechanical engineering, aviation, shipbuilding, and the oil and gas industries [3, 4]. The process involves the formation of an arc between two wire electrodes, causing the metal to melt and be deposited onto a pre-prepared surface in the form of fine particles.

One of the key factors determining the structure and operational characteristics of coatings obtained by EAM is the choice of wire material [5–7]. The wire used in the EAM process can be made in the form of a solid (cast) metal rod or in the form of a powder (tubular) shell filled with alloying or hardening powders. These differences in wire design directly affect the melting characteristics, melt transfer, microstructure formation, and, ultimately, the physical and mechanical properties of the protective layer [8].

Cast wire is a solid metal wire with a uniform chemical composition, suitable for rolling and drawing. However, its alloying capabilities are limited, which reduces the potential for optimizing the properties of the coating [9, 10]. In addition, the heterogeneity of melting during spraying can contribute to the formation of agglomerates, local areas with a deficiency of alloying elements and, as a result, increased porosity and im-

paired adhesion of the coating to the substrate [11–14]. Powder (tubular) wire, on the other hand, provides much greater flexibility in forming the required composition [15, 16]. A metal shell filled with a powder mixture of elements and compounds (including carbides, borides, oxides, etc.) allows coatings with specially specified properties to be obtained, including increased hardness, wear resistance, and corrosion resistance [17–19]. The use of powder wires is particularly effective when it is necessary to use difficult-to-form alloying systems that are not suitable for the manufacture of cast wire.

The chemical composition of the wire plays a decisive role in the formation of the coating structure. Alloying elements influence the formation of carbide, boride, and intermetallic phases, which increase hardness, wear resistance, and resistance to stress corrosion cracking. However, to achieve the positive effect of alloying, it is important not only to have the nominal concentration of elements, but also their uniform distribution throughout the coating. With EAM, coatings obtained from cast wire often show zoning and uneven distribution of elements, while tubular wire allows for greater chemical uniformity, which is directly related to improved microhardness, density, and adhesion properties [7].

This study presents a comparative analysis of protective coatings applied to 65G steel using electric arc metallization with both powder and cast wires made of 30KhGSA and 51KhFA alloys. The scientific novelty of this work lies in the fact that, for the first time, a systematic and direct comparative analysis was conducted between cast and powder-filled wires of the same steel grades (30KhGSA and 51KhFA) in terms of their influence on coating structure and performance. The findings are particularly relevant for improving the durability of components used in the harsh, abrasive conditions of Kazakhstan's agricultural environment.

Materials and methods

65G steel, a high-carbon steel characterized by high hardness and wear resistance, was used as the substrate material for spraying. It is widely used in the manufacture of parts operating under conditions of increased loads and wear, such as cultivator tines, plow blades, and other agricultural machinery components. The chemical composition of the material is presented in Table 1.

Table 1

Chemical composition of 65G steel substrate, %

Element	C	Si	Mn	Ni	S	P	Cr	Cu	Fe
Content	0.62–0.70	0.17–0.37	0.9–1.2	≤0.25	≤0.035	≤0.035	≤0.25	≤0.20	basis

The substrate samples were cut from sheet metal measuring 25×10×4 mm. The surface was mechanically sanded (grain size from P100 to P360) and sandblasted with electrocorundum to create the required roughness and improve coating adhesion.

Steel wires with a diameter of 1.6 mm of two types—cast and cored—were used as the feedstock material for thermal spraying. The chemical composition of the wires corresponds to the steel grades 30KhGSA and 51KhFA. The selection of wires was based on differences in alloying composition. Detailed chemical composition data are presented in Table 2. For each composition, both cast and cored wire types were utilized. The wires were procured in ready-made form.

Cast wires were produced using the conventional method of metal melting followed by forming, whereas cored wires consisted of composite fillers enclosed in a metallic sheath. Figure 1 illustrates the elemental distribution in the composition of the 51KhFA wire used in this study. This selection enabled an objective comparative analysis of the influence of wire type and chemical composition on the structure and performance properties of the resulting coatings.

Table 2

Main grades and chemical composition of sprayed wires, %

Wire name	Fe %	C %	Si %	Mn %	Ni %	S %	P %	Cr %	Cu %	Mo %	As %
30KhGSA	basis	0.28–0.34	0.9–1.2	0.8–1.1	to 0.3	to 0.025	to 0.025	0.8–1.1	to 0.3	–	–
51KhFA	basis	0.47–0.55	0.15–0.3	0.3–0.6	to 0.25	to 0.025	to 0.025	0.75–1.1	to 0.2	–	–

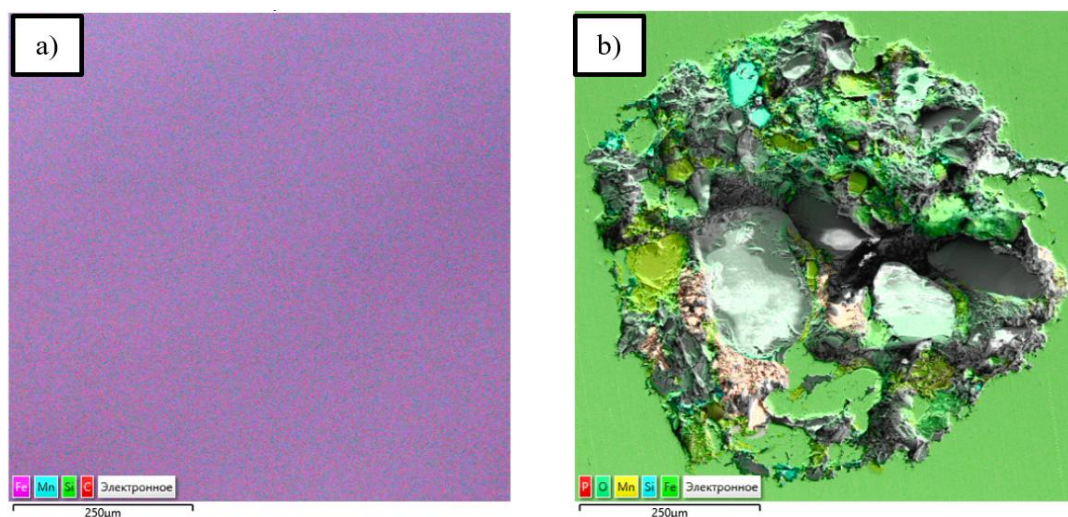


Figure 1. Cross-sectional view and distribution of elements in cast (a) and powder (b) 51KhFA wires

Electric arc metallization was carried out on a supersonic arc metallization unit SX-600, which included the following main components: a sprayer, a power source, and a compressor. The process was carried out under the following technological parameters: the power source voltage was 40 V, which ensured the stability of the electric arc and sufficient energy for melting the material. The current was set at 250 A. The wire feed rate was maintained at 12 cm/s, which ensured a stable supply of material and uniformity of the applied layer. The distance between the sprayer and the sample surface was 200 mm, which allowed for uniform distribution of the melt and reduced the thermal impact on the substrate. The working gas (compressed air) pressure was maintained at 0.7 MPa, ensuring effective particle acceleration and the formation of a dense coating structure [10]. Spraying was carried out at room temperature for both the samples and the environment, which minimized thermal impact and maintained the stability of the material structure.

Table 3

Electric arc metallization modes

Parameter	Value
Voltage (U), B	40
Current (I), A	250
Wire feed speed, cm/s	12
Distance from nozzle, mm	200
Compressed air pressure, MPa	0.7
Ambient temperature, °C	26

For a comparative analysis of coatings deposited by electric arc metallization using different wires, modern methods were used to study their structural and phase composition, microstructure, and mechanical properties [11].

The microstructure of the coatings was studied using a Tescan Vega 4 scanning electron microscope. The elemental composition was determined using Xplore 30 energy dispersive analysis. The thickness and porosity of the coatings were measured using an Olympus BX53M optical microscope, and the porosity was calculated using Metallographic Analysis Software in accordance with ASTM E2109. Microhardness was measured using the Vickers method (GOST 9450-76, ASTM E384-11) at a load of 0.025 N. Surface roughness was evaluated using a model 130 profilometer (GOST 25142-82).

Results and discussion

Figure 2 shows the typical microstructure of 30KhGSA wire obtained using scanning electron microscopy (SEM). This microstructure is typical for coatings obtained by electric arc metallization. Microstructural analysis showed that coatings formed by electric arc metallization have a characteristic layered (lamellar) structure. This morphology is typical for thermally sprayed coatings and is formed as a result of the sequential deposition of molten metal particles. During spraying, the particles, upon reaching the substrate surface,

instantly cool and solidify, forming dense and thin layers. Rapid cooling caused by the contact of hot particles with a cold base or previously applied layers leads to instant crystallization and contributes to the formation of a strong, homogeneous microstructure. This structure ensures reliable adhesion between layers due to partial thermal fusion at the melt boundaries. The lamellar structure significantly increases the mechanical strength of the coating, its resistance to cracking and abrasive wear, and reduces permeability to moisture and aggressive environments. Thus, the microstructure shown in Figure 1 indicates the high quality of the coating and confirms the effectiveness of the technological parameters used to form reliable protective coatings based on 30KhGSA wire.

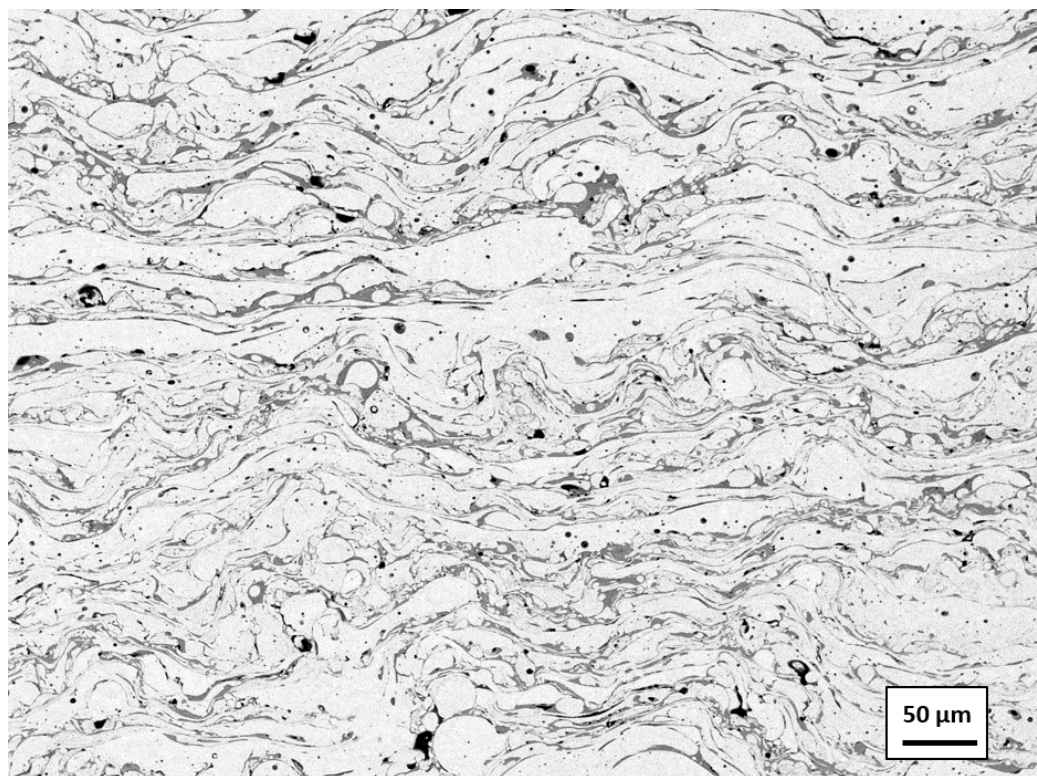
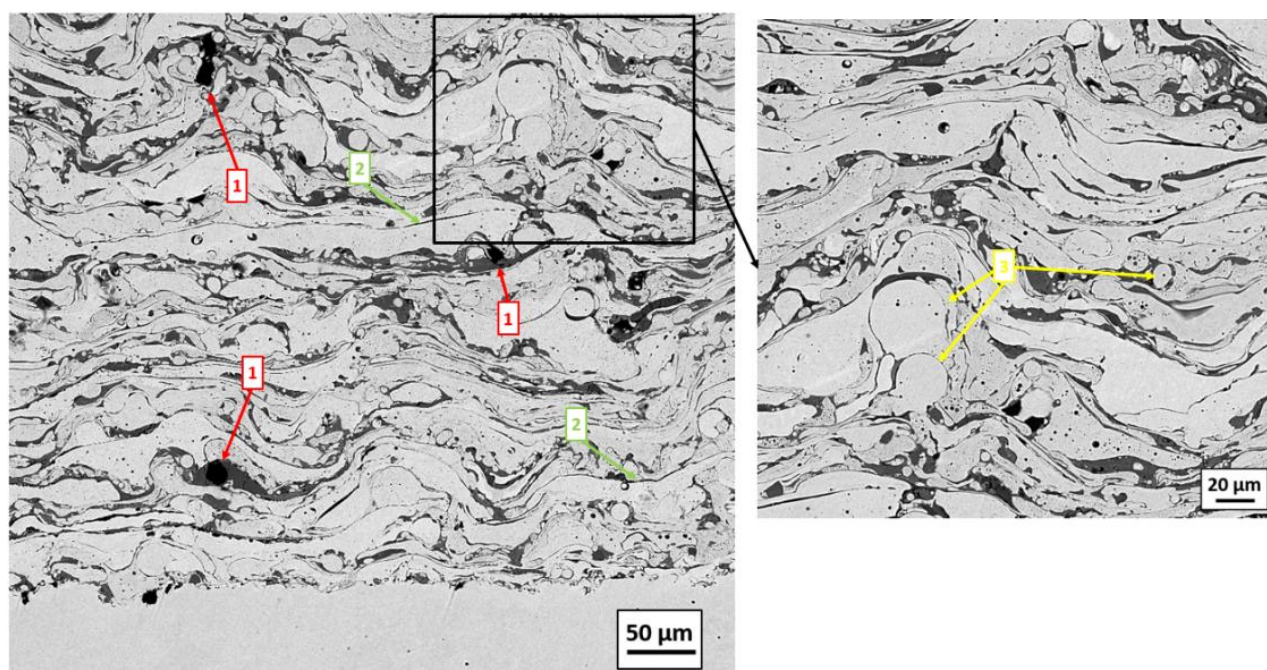


Figure 2. Layered microstructure of the coating cross section

However, characteristic defects were also identified in the coating structure, including pores, delaminations, and unmelted particles (Fig. 3), the presence of which can significantly affect the performance characteristics of the coatings. Pores typically formed due to air entrapment during spraying or incomplete sintering of the sprayed particles, especially when the particle temperature or velocity is insufficient. These porous regions may serve as pathways for the ingress of aggressive media, promoting corrosion and reducing the sealing properties of the coating [13].

Delaminations were mainly observed at interlayer boundaries and at the coating—substrate interface. Their presence may indicate violations in the surface pre-treatment process (e.g., inadequate cleaning or insufficient surface roughness), as well as insufficient kinetic energy of the sprayed particles, which fails to ensure reliable adhesion to the substrate. Such defects significantly reduce coating adhesion and may lead to its premature failure under mechanical loading.

Unmelted particles present in the structure are typically fragments of wire that did not fully melt during the arc metallization process. These inclusions can act as stress concentrators and potential initiation sites for microcracks. Under abrasive or impact loads, they contribute to accelerated wear of the coating, reducing its strength, hardness, and resistance to failure.



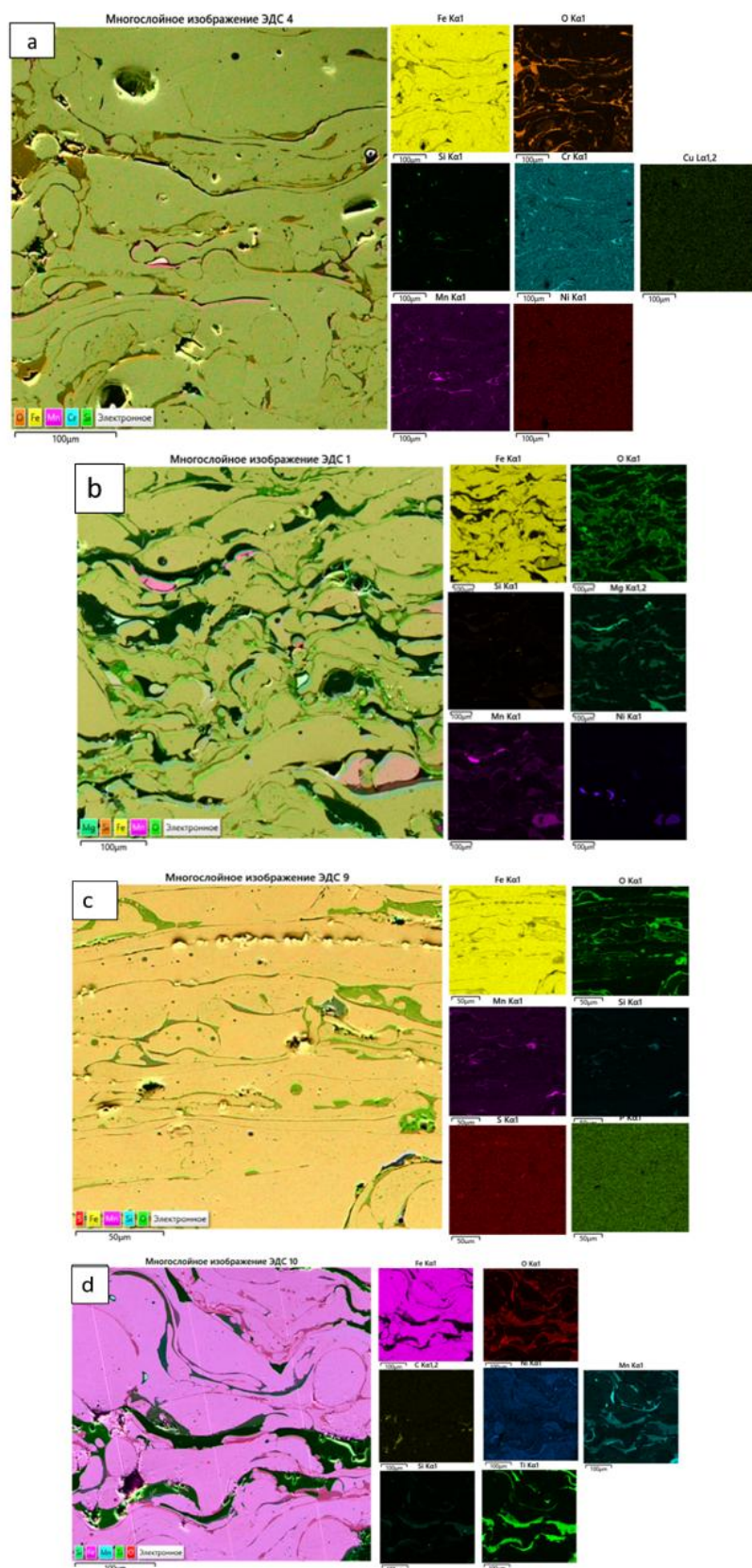
1 — pores; 2 — delamination; 3 — unmelted particles

Figure 3. Microstructural analysis of the coating with identification of defect areas in the form of pores, delamination, and unfused particles

To gain a deeper understanding of the influence of wire type on the chemical distribution within the coating, EDS analysis was performed on cross-sections of samples produced using both cored and cast wires of 30KhGSA and 51KhFA (Fig. 4). The results of EDS mapping for elements Fe, O, Si, and Mn help explain the observed differences in microstructure and, consequently, in the performance characteristics of the coatings. Coatings obtained from cored wires of 30KhGSA and 51KhFA exhibit relatively uniform distribution of alloying elements (Fig. 4*b–d*); however, the 30KhGSA coating shows a slightly coarser and more heterogeneous distribution pattern, whereas the 51KhFA coating demonstrates a more stable and homogeneous profile.

This partial distinction is reflected in the functional properties: both coatings are characterized by high microhardness (up to 720 HV), low porosity (4.3–5.0 %), and good adhesion strength (up to 19.2 MPa), with the values for 51KhFA appearing slightly more balanced. In contrast, cast wires of 30KhGSA and 51KhFA exhibit pronounced chemical heterogeneity, including localized depletions, agglomerations and “hot spots”, indicating non-uniform delivery of alloying elements during spraying. This inhomogeneity results in the formation of structural defects—such as pores, voids, and delaminations—which is further supported by SEM images showing that void-rich regions coincide with Cr- or Si-depleted areas identified through EDS analysis. Thus, the chemical inhomogeneity characteristic of cast wires is directly linked to increased porosity (up to 8.2 %), reduced hardness, and weakened adhesion to the substrate, whereas the more uniform (albeit not perfectly smooth) elemental distribution in cored wires contributes to improved performance characteristics.

An analysis of the coating characteristics shows the influence of the type and composition of the wire on the operational characteristics (Table 4). Among the samples studied, powder wire, in particular 51KhFA and 30KhGSA, demonstrated clear advantages in terms of coating density and microstructure uniformity. Although cast wires produce slightly thicker layers, coatings applied using powder wires have lower porosity (4.3–5.0 %) and more favorable surface morphology. According to roughness data, powder 51KhFA showed higher roughness values, which may be due to particle distribution characteristics or localized defects, while cast wire demonstrated a smoother surface. However, in terms of mechanical strength, Vickers microhardness tests confirmed that powder wire coatings achieve higher hardness (up to 720 HV), especially powder 30KhGSA. These results confirm that, despite minor changes in roughness, powder wire provides superior coating quality in terms of structural integrity, hardness, and defect reduction, making it more suitable for applications requiring increased wear resistance.



a — 30KhGSA cast wire; *b* — 30KhGSA cored wire; *c* — 51KhFA cast wire; *d* — 51KhFA cored wire

Figure 4. EDS mapping of coating cross-sections obtained by arc metallization using different wire types

Table 4

Comparison of key properties of coatings obtained using different types of wires

Wire	Thickness, μm	Porosity, %	Roughness Ra, μm	Microhardness, HV
30KhGSA (cored)	111.26	4.3	6.03	720
30KhGSA (cast)	158.92	7.8	6.02	620
51KhFA (cored)	160.84	5.0	7.9	700
51KhFA (cast)	148.83	8.2	6.1	650

In general, differences in the structure and properties of coatings are related to both the chemical composition and the method of wire production: powder wire technologies allow for precise dosing of components and uniform spraying, while cast wire often contains defects that disrupt the uniformity of the coating.

Conclusion

The studies conducted demonstrated a significant influence of the wire type on the quality of coatings obtained by the electric arc metallization method. It has been established that 30KhGSA and 51KhFA powder wires provide more uniform coatings with high microhardness (up to 720 HV), reduced porosity (4.3–5.0 %), and strong adhesion to the substrate (up to 19.2 MPa). This is due to the uniform distribution of alloying elements, confirmed by EDS mapping results, as well as the minimization of structural defects—pores, unfused inclusions, and delamination. At the same time, coatings applied using cast wire were characterized by higher porosity (up to 8.2 %), chemical and structural heterogeneity, and reduced adhesion, which reduces their performance characteristics.

Thus, powder wires with an optimal chemical composition have a significant advantage in the formation of steel coatings. The data obtained emphasize the importance of rational selection of wire material and process parameters. In the future, it is planned to expand the range of wire materials under investigation, optimize spraying modes using mathematical modeling methods, and test coatings under various types of wear conditions.

Acknowledgments

This research is funded by the Committee of Science of the Ministry of Science and Higher Education of the Republic of Kazakhstan (Grant No. BR21882370).

References

- 1 Rakhadilov, B., Zhurero, L., Sagdoldina, Z., Kenesbekov, A., & Bayatanova, L. (2021). Morphological Changes in the Dislocation Structure of Structural Steel 20GL after Electrolytic-Plasma Hardening of the Surface. *Journal of Surface Investigation: X-ray, Synchrotron and Neutron Techniques*, 15, 408–413.
- 2 Wielage, B., Wank, A., & Rupprecht, C. (2006). Tailoring of Wire Feedstock and Processing Conditions in High Velocity Combustion Wire Spraying. *Proc. ITSC2006–ASM International*. Seattle, WA, USA, 15–18 May, 1009–1014.
- 3 Gornik, M., Jonda, E., Latka, L., Nowakowska, M., & Godzisz, M. (2021). Influence of spray distance on mechanical and tribological properties of HVOF sprayed WC-Co-Cr coatings. *Materials Science-Poland*, 39, 545–554.
- 4 Boinovich, L.B., Domantovsky, A.G., Emelyanenko, A.M., & Emelyanenko, K.A. (2024). Synergism of Arc metallization, Laser Processing, and Hydrophobization for Long-Lasting Corrosion Protection of MA8 Magnesium Alloy. *Advanced Engineering Materials. Early View*, 27(2), 2401708. DOI: 10.1002/adem.202401708.
- 5 Qiang, W., Kang, M., Liu, J., & Ndumia, J.N. (2024). Microstructure and Wear Performance of High-Velocity Arc Sprayed FeMnCrNiBNbAl Coating. *Coatings*, 14, Art. 428. DOI: 10.3390/coatings14040428.
- 6 Guzmán-Pardo, M.A. (2023). Effect of the Surface Chemical Composition on the Corrosion Resistance in the Mixture of FeCrMoNbB (140MXC) and FeCrMnSi (530AS) Coatings Produced with the Electric Wire Arc Spraying Technique: *Part I. Materials*, 16.
- 7 Wielage, B., Pokhmurska, H., Student, M., Gvozdeckii, V., Stupnykyj, T., & Pokhmurskii, V. (2013). Iron-Based Coatings Arc-Sprayed with Cored Wires for Applications at Elevated Temperatures. *Surface and Coatings Technology*, 220, 27–35.
- 8 Romankov, S.E., Sagdoldina, Z.B., Kaloshkin, S.D., & Kaevitser, E.V. (2008). Fabrication of Ti-Al composite coatings by the mechanical alloying method. *Physics of Metals and Metallography*, 106, 67–75.
- 9 Tsyganov, I. & Moskalev, D.N. (2022). Chemical composition of brass coating for steel cord. *Izvestiya. Ferrous Metallurgy*, 65(9), 662–670.

- 10 Kakimzhanov, D.N., Rakhadilov, B.K., Tyurin, Y.N., Kolisnichenko, O.V., Zhurero, L.G., & Dautbekov, M.K. (2021). Influence of pulsed plasma treatment on phase composition and hardness of $C_{13}C_2$ -NiCr coatings. *Eurasian Journal of Physics and Functional Materials*, 5, 45–51.
- 11 Ramezani, M., Mohd Ripin, Z., Pasang, T., & Jiang, C.P. (2023). Surface engineering of metals: Techniques, characterizations and applications. *Metals*, 13, Art. 1299.
- 12 Kengesbekov, A., Rakhadilov, B., Sagdoldina, Z., Buitkenov, D., Dosymov, Y., & Kylyshkanov, M. (2022). Improving the efficiency of air plasma spraying of titanium nitride powder. *Coatings*, 12, Art. 1644.
- 13 Rakhadilov, B. et al. (2024). Influence of Spraying Process Parameters on the Characteristics of Steel Coatings Produced by Arc Spraying Method. *Coatings*, 14, No 9, 1145.
- 14 Pawlowski, L. (2008). *The Science and Engineering of Thermal Spray Coatings*. Wiley.
- 15 (2025). Karpenko Physico-Mechanical Institute of the National Academy of Sciences of Ukraine et al. Surface Topography of Arc-Sprayed Coatings by Cored Wires of Different Compositions and Its Influence on the Wear Mechanism. *CUSBTS*, 1, 11(42), 115–120.
- 16 Yu, H.L., Zhang, W., Wang, H.M., Ji, X.C., Song, Z.Y., Li, X.Y., & Xu, B.S. (2017). In-situ synthesis of TiC/Ti composite coating by high frequency induction cladding. *Journal of Alloys and Compounds*, 701, 244–255.
- 17 Dzyubyk, L. et al. (2018). Influence of the Composition of Charge of Powder Wires on the Structure and Properties of Electric-Arc Coatings. *Materials Science*, 53, 868–874.
- 18 Kim, J.H. et al. (2024). Fabrication of high-entropy alloy superconducting wires by powder-in-tube method. *Journal of Alloys and Compounds*, 995, 174816.
- 19 Korzhuk, V. et al. (2024). Properties of Powders Produced by Plasma-Arc Spheroidization of Current-Carrying Fe–Al Flux-Cored Wire. *Powder Metallurgy and Metal Ceramics*, 63(1), 12–23.

Б.К. Рахадиллов, Д.Б. Буйткенов, А.Қ. Әпсежанова, Н.М. Магазов, М.Б. Баяндинова

Электр доғалы металдандыру әдісімен алынған жабындардың құрылымы мен қасиеттеріне сым түрінің әсері

Электр доғалы металдандыру (ЭДМ) — бұл қорғаныш жабындарын алу үшін метал сымын электр доғасымен ерітіп, алынған балқыманы сығылған ауа ағынымен шашырату арқылы жүзеге асатын, кеңінен қолданылатын және тиімді термиялық бүрку әдістерінің бірі. Бұл технология жоғары өнімділікпен, қабат қалыңдығын реттеу мүмкіндігімен және қолданылатын материалдардың әмбебаптығымен ерекшеленеді. Мақалада 65Г болатқа 30ХГСА және 51ХФА қорытпаларынан жасалған ұнтақты және құйма сымдарды қолдану арқылы алынған жабындардың салыстырмалы талдауы ұсынылған. Жабынның микроқұрылымы сканерлік электронды микроскоппен зерттелді, ал элементтік құрамы энергодисперсиялық спектроскопия (EDS) әдісімен анықталды. Қаптаманың қалыңдығы мен кеуектілігі оптикалық микроскоппен өлшенді. Микроберіктік Виккерс әдісімен, ал беткі кедір-бұдырлық контактілі профилометрмен бағаланды. Микроқұрылым және EDS талдауы ұнтақты сыммен алынған жабындардың қоспалау элементтері біркелкі таралғанын, бұл өз кезегінде микроберіктікті арттырып, кеуектілікті азайтатынын көрсетті. Құйма сыммен алынған жабындарда құрылымдық біркелкі еместік байқалып, кеуектілік артты және механикалық қасиеттері нашарлады. Зерттеу нәтижелері ұнтақты сымның жоғары сапалы жабындар алуға артықшылықтарын көрсетті.

Кілт сөздер: электр доғалы металдандыру, құйма және ұнтақ сымды, кеуектілік, болат жабын, элементтік құрам

Б.К. Рахадиллов, Д.Б. Буйткенов, А.Қ. Әпсежанова, Н.М. Магазов, М.Б. Баяндинова

Влияние типа проволоки на структуру и свойства покрытий, полученных методом электродуговой металлизации

Электродуговая металлизация (ЭДМ) является одним из наиболее эффективных и широко применяемых методов термического напыления, при котором защитное покрытие формируется за счёт плавления металлической проволоки электрической дугой и распыления расплава сжатым воздухом. Технология отличается высокой производительностью, регулируемой толщиной слоя и универсальностью применяемых материалов. В статье представлена сравнительная оценка защитных покрытий, нанесённых на сталь 65Г методом дуговой металлизации с использованием порошковой и литой проволоки из сплавов 30ХГСА и 51ХФА. Микроструктура покрытий исследовалась с использованием сканирующего электронного микроскопа, а элементный состав — методом энергодисперсионной спектроскопии (EDS). Толщина и пористость покрытия определялись с помощью оптического микроскопа. Микротвёрдость измерялась по Виккерсу, шероховатость поверхности — с использованием контак-

ного профилометра. Анализ микроструктуры и EDS показал, что покрытия, полученные из порошковой проволоки, характеризуются более равномерным распределением легирующих элементов, что обеспечивает повышенную твёрдость и снижает пористость. Покрытия из литой проволоки, напротив, демонстрируют структурную неоднородность, повышенную пористость и ухудшенные механические характеристики. Установлено, что порошковая проволока обеспечивает более высокое качество покрытий.

Ключевые слова: дуговая металлизация, литая и порошковая проволока, пористость, стальное покрытие, элементный состав

Information about the authors

Rakhadilov, Bauirzhan — Doctor of Philosophy (PhD) in Science, Associate professor, LLP “PlasmaScience”, Leading Researcher, Ust-Kamenogorsk, Kazakhstan; e-mail: rakhadilovb@gmail.com, ORCID: <https://orcid.org/0000-0001-5990-7123>;

Buitkenov, Dastan — PhD, Leading Researcher of Scientific Research Center “Surface Engineering and Tribology”, S. Amanzholov East Kazakhstan University, Ust-Kamenogorsk, Kazakhstan; e-mail: buitkenov@gmail.com; ORCID ID: <https://orcid.org/0000-0002-0239-5849>;

Apsezhanova, Akbota (*contact person*) — PhD student in the specialty 8D05301 — Technical Physics, D. Serikbayev East Kazakhstan Technical University (EKTU), Researcher at the Research Center “Protective and Functional Coatings”, Ust-Kamenogorsk, Kazakhstan; e-mail: akbotaapsezanova@mail.com; ORCID: <https://orcid.org/0009-0001-7778-7767>

Magazov, Nurtoleu — PhD student in the specialty 8D05301 — Technical Physics, D. Serikbayev East Kazakhstan Technical University (EKTU), Researcher at the Research Center “Protective and Functional Coatings”, Ust-Kamenogorsk, Kazakhstan; e-mail: magazovn@gmail.com; ORCID: <https://orcid.org/0000-0002-9941-9199>

Bayandinova, Moldir — PhD student in the specialty 8D05301 — Technical Physics, at S. Amanzholov East Kazakhstan University, Kazakhstan; e-mail: shohmanovamb@gmail.com, ORCID: <https://orcid.org/0000-0001-6699-9097>

Article

UDC 536.24; 004.94

 <https://doi.org/10.31489/2025PH3/68-76>

Received: 28.04.2025

Accepted: 07.06.2025

A.S. Zhumanbayeva, N.Zh. Jaichibekov[✉], D.Y. Kurmanova

L.N. Gumilyov Eurasian National University, Astana, Kazakhstan

**Study of the Influence of Turbulence Models on Hydrodynamic
and Thermal Parameters of Heat Carriers in Calculations of Heat Exchangers**

In this paper, the heat exchange processes between a cold (oil) and a highly heated (water) heat carrier in a “tube-in-tube” type heat exchanger with a parallel flow scheme are studied using semi-empirical turbulence models: $k-\omega$ SST, $k-\varepsilon$, and Transition SST. The analysis of the obtained results showed that the $k-\omega$ SST turbulence model was more preferable for the calculation of a heat exchanger with a sufficiently small tube diameter, because of the effect of the boundary layer in the tube. This turbulence model more pronouncedly reproduces the laminar-turbulent transition, which is carried out in these processes, where the viscosity of oil strongly depends on temperature. Finite difference and finite volume methods were chosen for numerical modelling and calculation of heat exchange processes. The calculations were carried out on the basis of Computational Fluid Dynamics, using the Ansys Fluent. The RANS equations closed by means of the gamma-Retheta turbulence model, which takes into account the laminar-turbulent transition and the $k-\omega$ SST model equations, were used for numerical modelling of coolant hydrodynamics. Based on the proposed turbulence model, the distributions of hydrodynamic and thermal parameters and similarity criteria (Re, Pr, Nu) of the process along the length of the tube are obtained.

Keywords: heat transfer, numerical calculation, heat exchanger, oil, hydrodynamics, cooling fluids, heat flow, laminar-turbulent transition, intermittency, heat exchange intensity, viscosity

[✉]Corresponding author: Jaichibekov, Nurbolat, jaich@mail.ru

Introduction

Fluid dynamics in the innertube space of a heat exchanger is defined by the process’s complexity and is determined by numerous parameters. Research in works [1, 2] focus on numerical modeling of heat exchange in different types of HE. The findings of heat exchanger calculations are utilized to optimize and intensify heat exchange processes [3–5]. In particular, it has been demonstrated that when turbulence develops, the influence of injected oil viscosity on the hydraulic resistance of the pipeline is greatly reduced.

Unsteady three-dimensional Navier-Stokes equations expressed regarding instantaneous (direct numerical modelling), average (solution of Reynolds equations), or space-filtered (modeling of massive vortices) functions explain the unsteady spatial flow of a viscous incompressible fluid. To close the averaged Reynolds or filtered Navier-Stokes equations, the eddy viscosity hypothesis is used.

Works in [6–9] investigate the accuracy of various turbulence models used to close the Reynolds equations. A comparison of the accuracy of various turbulence models used to close the Reynolds equations is the subject of further research. Basically, the available calculations use the $k-\varepsilon$, $k-\omega$ SST (Shear Stress

Transport) and Transition SST models. The calculations make it possible to achieve a satisfactory agreement between the results of numerical modeling and the data from industrial experiments. At the same time, the calculations performed using two-parameter turbulence models do not take into account the laminar-turbulent transition, which affects the determination of the effective length of the HE [10–13].

This paper presents the results of numerical calculations using various turbulence models: the $k-\varepsilon$ model, including models, that take into account the laminar-turbulent transition ($k-\omega$ SST, Transition SST). The calculation results are compared with the results of the distribution of the average mass temperature of oil and water (cold and hot coolants) along the length of the heat exchanger [10], obtained using the Log-Mean Temperature Difference (LMTD) method and they are consistent with the literature data [14; p. 4.1]. A comparative analysis of the obtained results based on these models with data from a physical experiment and calculations based on semi-empirical dependencies allows us to select an effective turbulence model for use in calculations of direct-flow HE.

Calculation method

Numerical modelling of heat transfer processes was based on finite difference and finite volume methods. To solve this problem, computational fluid dynamics (CFD) methods were used using the Ansys Fluent software package, which allows taking into account the effects of turbulence and heat transfer in fluid flows. The use of CFD methods in the design of HE allows not only to improve the main indicators of their performance while ensuring acceptable mechanical reliability, but also to create designs that practically do not need modification. Thermal and hydrodynamic calculations make it possible to analyze temperature distribution in various conditions of heat exchange with diffusion and convection processes, to optimize the geometry of heat exchangers and to calculate hydraulic resistances.

Closing equations for determining turbulent viscosity, which is calculated using the kinetic energy of turbulence, the dissipation of turbulence energy, and the intermittency parameter for the above turbulence models, are commonly used in computational fluid dynamics and in various engineering and scientific applications. These equations for the above three models are given below. All empirical coefficients used in these equations are defined in [13].

$k-\varepsilon$ model: the turbulence kinetic energy k and the dissipation energy of turbulence ε are determined from the following system of equations (1):

$$\begin{aligned}\frac{\partial}{\partial t}(\rho k) + \frac{\partial}{\partial x_i}(\rho k u_i) &= \frac{\partial}{\partial x_j} \left[\left(\mu + \frac{\mu_t}{\sigma_k} \right) \frac{\partial k}{\partial x_j} \right] + G_k + G_b - \rho \varepsilon - Y_M + S_k \\ \frac{\partial}{\partial t}(\rho \varepsilon) + \frac{\partial}{\partial x_i}(\rho \varepsilon u_i) &= \frac{\partial}{\partial x_j} \left[\left(\mu + \frac{\mu_t}{\sigma_\varepsilon} \right) \frac{\partial \varepsilon}{\partial x_j} \right] + C_{1\varepsilon} \frac{\varepsilon}{k} (G_k + C_{3\varepsilon} G_b) - C_{2\varepsilon} \rho \frac{\varepsilon^2}{k} + S_\varepsilon\end{aligned}\quad (1)$$

$k-\omega$ SST (Shear Stress Transport) model (2):

$$\begin{aligned}v_j \frac{\partial \text{Re}_{\theta t}}{\partial x_j} &= P_{\theta t} + \frac{\partial}{\partial x_j} \left[\sigma_{\theta t} (v + v_t) \frac{\partial \text{Re}_{\theta t}}{\partial x_j} \right], \\ v_j \frac{\partial \gamma}{\partial x_j} &= P_\gamma - E_\gamma + \frac{\partial}{\partial x_j} \left[\left(v + \frac{v_t}{\sigma_\gamma} \right) \frac{\partial \gamma}{\partial x_j} \right].\end{aligned}\quad (2)$$

Here $P_{\theta t}$ represents the production term for the momentum thickness Reynolds number; P_γ and E_γ are output and dispersal terms of the intermittency; $\sigma_{\theta t}$ and σ_γ are model constants.

Transition SST model (also known as $\gamma-\tilde{\text{Re}}_{\theta t}$), equation (3):

$$\begin{aligned}\frac{\partial(\rho \gamma)}{\partial t} + \frac{\partial(\rho U_j \gamma)}{\partial x_j} &= P_{\gamma 1} - E_{\gamma 1} + P_{\gamma 2} - E_{\gamma 2} + \frac{\partial}{\partial x_j} \left[\left(\mu + \frac{\mu_t}{\sigma_\gamma} \right) \frac{\partial \gamma}{\partial x_j} \right], \\ \frac{\partial(\rho \tilde{\text{Re}}_{\theta t})}{\partial t} + \frac{\partial(\rho U_j \tilde{\text{Re}}_{\theta t})}{\partial x_j} &= P_{\theta t} + \frac{\partial}{\partial x_j} \left[\sigma_{\theta t} (\mu + \mu_t) \frac{\partial \tilde{\text{Re}}_{\theta t}}{\partial x_j} \right].\end{aligned}\quad (3)$$

The given equations of the corresponding turbulence models are used to calculate the heat exchanger of direct flow type. For example, Figure 1 demonstrates a diagram of an externally insulated Thermal insulation straight tube-in-tube heat exchanger where two heat transfer fluids flow in parallel in the same direction. The cold coolant, oil, flows through the inner pipe, while the highly heated heat carrier in the outer pipe is water.



Figure 1. Schematic diagram of a heat exchanger of direct flow type (parallel flow)

When solving this problem, the following initial parameters for thermal calculation are used. The inner diameter of the pipe through which the cool heat carrier flows is 12 mm, and its outer diameter is 14 mm. The inner diameter of the pipe through which the highly heated heat carrier flows is 20 mm. Temperatures of cool and highly heated heat carriers in the inlet section are 303 K and 423 K. Mass flow rates of cool and highly heated heat carriers are equal to 0.3814 kg/s and 0.6386 kg/s (the velocity in the inlet section is assumed to be 4 m/s).

The results of calculations agree with the data of numerical modeling and with the results of distribution of the average mass temperature of oil and water (cold and hot coolants) along the length of the heat exchanger, obtained using the finite difference method and based on numerical modeling [11].

Results and Discussion

Figure 2 demonstrates comparative graphs of the change in the temperature of coolants along the tube of the heat exchanger for three models of turbulence for the direct flow of coolants. Here in the figure and further for all figures the following designations are introduced: 1 — $k-\omega$ SST model; 2 — $k-\varepsilon$ model; 3 — Transition SST model. The figure demonstrates that the temperature change curves of the coolants for all three models are alike, in that the temperature of the highly heated heat carrier declines while the temperature of the cool heat carrier arise throughout the tube.

It can also be noted that for all three turbulence models the temperature differences for both coolants are more noticeable and closer to the exit from the HE tubes. An analysis of the temperature change graphs also demonstrates that the graph of the heating temperature of the cold coolant (oil) along the tube for the $k-\varepsilon$ model is lower compared to the other two models, and the graph of the cooling temperature of the hot coolant is lower for the Transition SST model, while the intensity of oil heating is higher for the $k-\omega$ SST model.

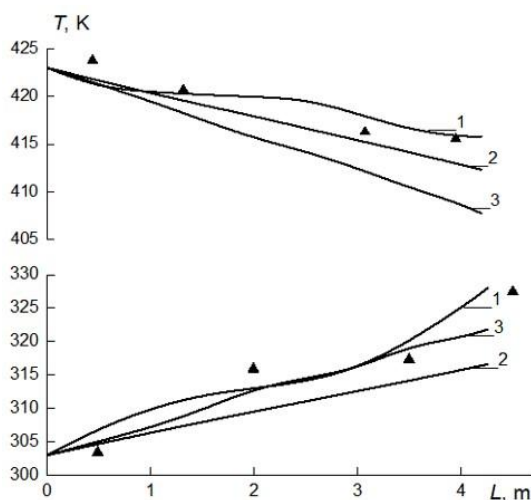


Figure 2. Variation of water (hot) and oil (cold) temperature along the length of the tube in parallel flow for all three models, the triangular icons correspond to the results of calculations using the LMTD method

This figure also demonstrates that for the $k-\varepsilon$ model, the temperature change for both coolants is linear along the length of the HE tubes.

The differences between the models are explained by sensitivity to viscosity profiles and turbulent energy distribution.

Figure 3 demonstrates the dissemination of the axial component of the oil velocity in the radial direction in the cross sections of the pipeline during straight flow for given turbulence models, namely the $k-\omega$ SST, $k-\varepsilon$ and Transition SST models. Velocity profiles are given at two cross sections of the HE tubes, namely at 1.5 m from the tube inlet and at the outlet, where these cross sections are shown in the figures. For all considered turbulence models, the velocity profiles have the form of logarithmic distribution. For the flow patterns of heat carriers in direct flow, the velocity profiles closest to the turbulent flow correspond to the $k-\omega$ SST and Transition SST models, which is natural, since the $k-\varepsilon$ turbulence model more accurately represents the movement outside the boundary layer, and heat exchange between the heat carriers occurs mainly in the boundary layer. Moreover, such profiles are pronounced in the cross-sections at the outlet of the tube.

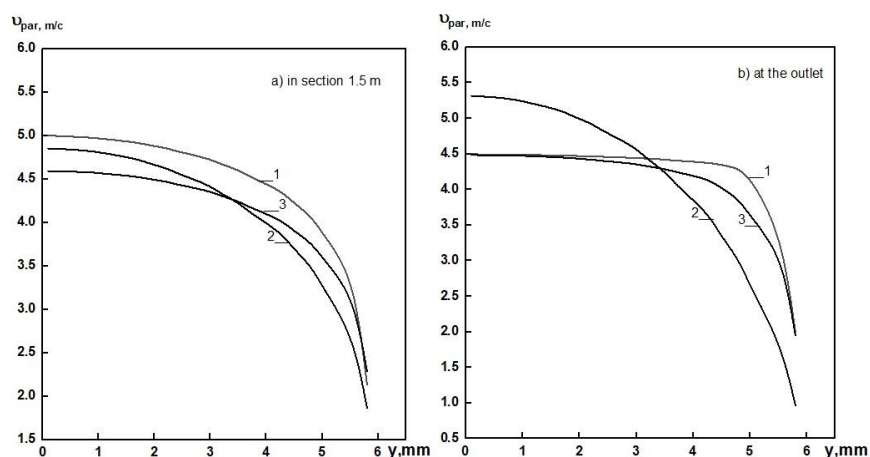


Figure 3. Dissemination of the axial component of oil velocity in different cross sections of the pipeline in the radial direction

The axial velocity component grows from center to wall depending on the model. The $k-\omega$ SST model gives smoother dissemination.

Figure 4a demonstrates a plot of the dependence of the Reynolds number Re on the tube length L in the case of straight flow for different turbulence models. It can be seen from this figure that the laminar-turbulent transition is clearly observed also in the straight stream within a distance $x = 3-3.2$ m for the case of $k-\omega$ SST model, and this transition for this model starts at numbers around $Re = 2300$ in the straight stream. For the other two turbulence models, this effect is weakly pronounced in the straight flow case.

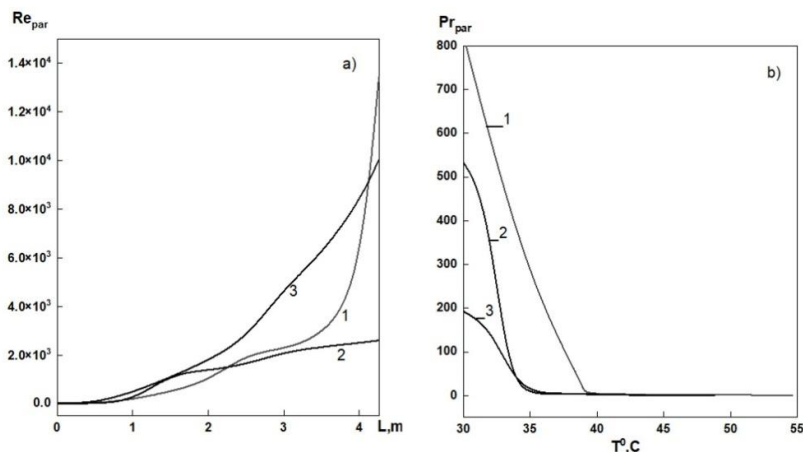


Figure 4. Distribution of Reynolds numbers for a smooth tube along the tube length (a) and dependence of the oil Prandtl number on temperature (b)

Figure 4b demonstrates the dependence of the Prandtl number for oil on temperature in cases of straight flow for turbulence models $k-\omega$ SST, $k-\varepsilon$, and Transition SST. From the figures it is clearly seen that for the scheme of straight flow of coolants, the movement of coolants at moderate temperatures (from 30 to 40 degrees Celsius) the value of Prandtl number has the highest value for the turbulence model $k-\omega$ SST and the lowest value for the Transition SST model, and for the model $k-\varepsilon$ values in between. Taking into account that the Prandtl number is defined as the ratio of the kinematic viscosity coefficient to the diffusivity of the medium, we can conclude that near the solid boundary of the tube the viscosity of the medium plays a significant role, which is expressed in the $k-\omega$ SST model.

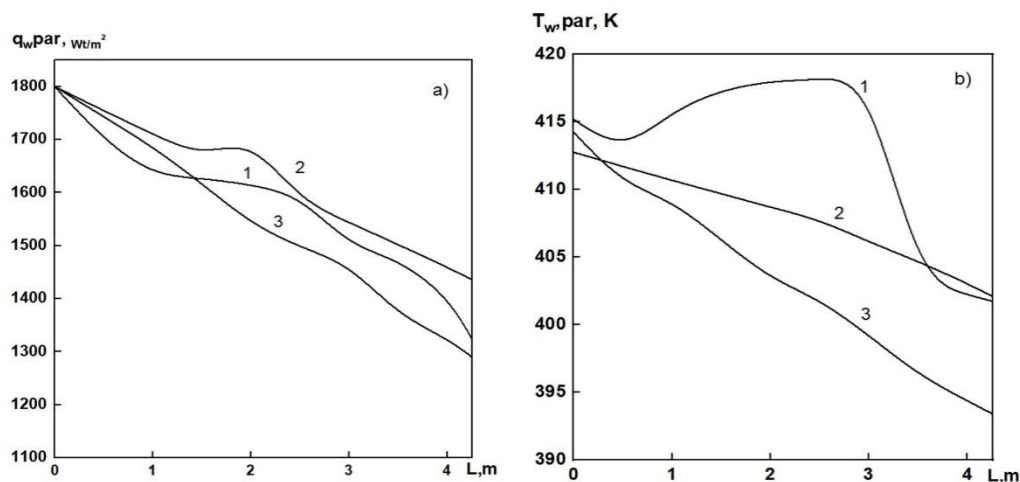


Figure 5. Variation of heat flux q_w along the length of the heat transfer wall (a) and wall temperature T_w along the length of the heat transfer wall on the oil side (b)

Figure 5a demonstrates the plots of heat flux q_w variation along the length of the heat transfer wall of the coolant motion for the three turbulence regimes. It can be seen from the plots that the behavior of the heat flux curves is identical for both schemes and for all turbulence models.

At high turbulence (curve 1) the wall temperature is higher along the entire length, which is due to improved heat transfer, while at lower turbulence (curve 3) the wall temperature is lower, indicating less efficient heat transfer. The temperature curves have a smoother and decreasing character along the length of the tube.

Figure 5b demonstrates modification in the temperature of the T_w wall along the length of the heat transfer wall from the oil side, where a laminar-turbulent transition is distinguished, this effect is not distinguished in the other two turbulence models.

In the case of strong dependence of viscosity on temperature as the coolant is heated, the flow regime changes from laminar to developed turbulent. In this case, using the local heat transfer coefficient α , the relationship for the local Nusselt number is valid: $Nu = \alpha d_g / \lambda$.

Figure 6a demonstrates that the Nusselt number for the $k-\omega$ SST model is larger at the inlet of the HE tube; this can be explained by the fact that the Nusselt number characterizes the intensity of heat transfer due to convection, expressed through the heat transfer coefficient of the medium.

Figure 6b demonstrates the distribution of the heat transfer coefficient along the tube length for all three turbulence models considered. The heat transfer coefficient α was calculated by the known formula through the heat flux through the wall and the temperature difference between the liquid medium and the solid wall by the formula $\alpha = q_w / (T_w - T)$.

It can be seen from the figure that the laminar-turbulent transition for both flow patterns, i.e., also in the direct flow, is observed only for the $k-\omega$ SST model.

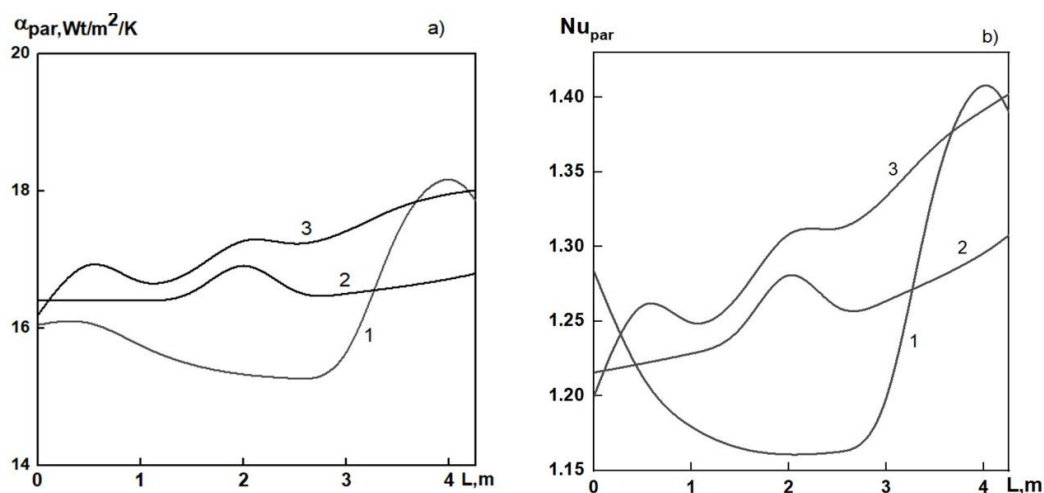


Figure 6. Dissemination of heat transfer coefficient along the length of the tube and difference of number Nu along the length of the tube

From the given figure it is also possible to notice that in the region of the tube length $x = 3$ m, for both cases the laminar-turbulent transition of the oil flow regime is visible, while for other two turbulence regimes the change of Nu number along the tube length is more uniform. The results are compared with laminar regime (Poiseuille formula) and turbulent regime (Blasius and Nikuradze formulae).

Figure 7a demonstrates the curves of variation of overpressure values P_g along the length of the tube for the three turbulence regimes. Here, for all three turbulence modes, there is a drop in the overpressure (hence, and absolute) pressure along the entire length of the tube. At the exit of the tube, the overpressure approaches zero, i.e., the absolute pressure approaches the atmospheric pressure value. Here we also observe a significant increased pressure for the $k-\varepsilon$ turbulence model, which is probably explained by the failure to take into account the influence of the boundary layer in this turbulence model.

The pressure distribution along the tube steadily decreases as expected for steady flow. Figure 7b demonstrates the variation of the friction coefficient λ along the length of the tube for straight flow and counterflow for the three turbulence regimes.

The figure demonstrates that the values of the friction coefficient for the $k-\varepsilon$ turbulence are much higher than the corresponding values for the two turbulence regimes along the length of the tube, which is most likely a consequence of not taking into account the effect of the boundary layer on the tube wall.

At the same time, the values of λ for the $k-\varepsilon$ and Transition SST models in the graph lie higher in both shape and values. It should also be noted here that it is for the $k-\omega$ SST turbulence model that the laminar-turbulent transition is pronounced for both schemes and that occurs at a distance of 3–3.5 m from the beginning of the tube.

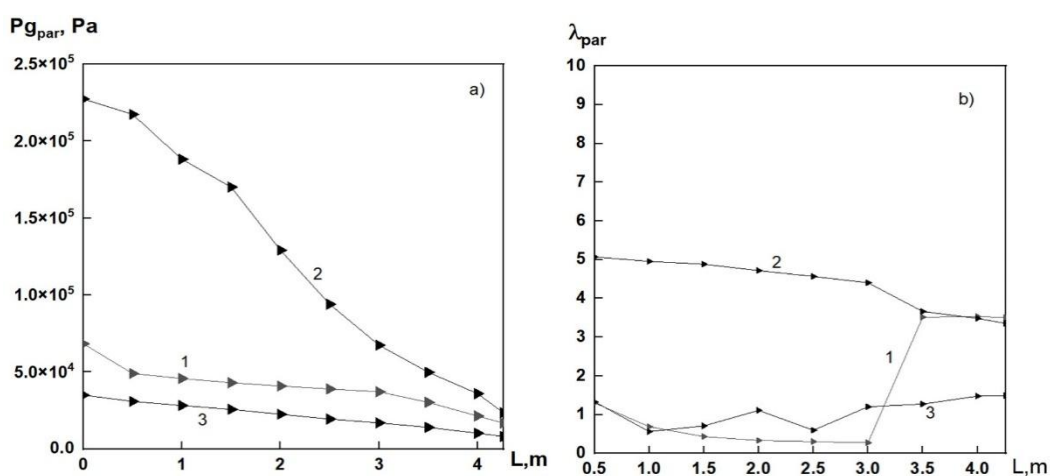


Figure 7. Variation of overpressure P_g and friction coefficient λ along the length of the tubing

Conclusion

Based on a numerical analysis of the heat exchanger of the type “tube-in-tube” using $k-\omega$ SST, $k-\varepsilon$ and Transition SST various turbulence models the following major results are obtained. For all turbulence models, a characteristic behavior of the temperature curves is observed: the temperature of the highly heated heat carrier declines while the temperature of the cool heat carrier rises along the length of the tube. The $k-\omega$ SST model demonstrates the greatest heating of the cool heat carrier, while the $k-\varepsilon$ model demonstrates a smoother and more linear behavior of the temperature profile. It follows from Figures 2 and 5b that the numerical values of the distribution of the mass average temperature of oil along the HE tube and its distribution along the tube surface are higher for the $k-\omega$ SST model, which indicates the effectiveness of using this model for numerical calculation.

The oil axial velocity profiles have a logarithmic shape for all models and are more pronounced for the $k-\omega$ SST and Transition SST models, especially in the outlet sections, indicating a more reliable modelling of turbulent processes near the wall. The $k-\varepsilon$ model reflects the boundary layer effect worse, which limits its applicability in problems with active heat transfer near the wall. The laminar-turbulent transition is most clearly recorded when using the $k-\omega$ SST model, in the range of 3–3.5 m from the tube inlet, which is confirmed by changes in the Reynolds number, heat transfer coefficient and friction coefficient.

For all models, the expected decrease in overpressure along the tube is observed. However, the $k-\varepsilon$ model demonstrates higher pressure values, probably due to insufficient consideration of boundary effects. Numerical values of heat flux through the tube wall appear to be higher for straight flow and heat transfer efficiency (in terms of Nusselt number) at the tube outlet. The Prandtl number for oil is maximized in the $k-\omega$ SST model, which is due to the largest contribution of the viscosity of the medium near the tube wall. This emphasizes the advantage of this model in modelling heat transfer with strong temperature dependence of viscosity.

Taking into account more accurate description of transient modes, correspondence of numerical simulation results to physical processes in the boundary layer and satisfactory representations of temperature and hydrodynamic profiles, the $k-\omega$ SST turbulence model can be considered as the most acceptable in calculations of heat exchangers with smooth tube surface in HE. These studies also emphasize the importance of a properly chosen mesh and the need to calibrate the models depending on specific heat transfer conditions or other processes.

References

- 1 Yogesh S.S. et al. Heat transfer and pressure drop characteristics of inclined elliptical fin tube heat exchanger of varying ellipticity ratio using CFD code / S.S. Yogesh, A.S. Selvaraj, D.K. Ravi et al. // International Journal of Heat and Mass Transfer. — 2018. — Vol. 119. — P. 26–39. <https://doi.org/10.1016/j.ijheatmasstransfer.2017.11.094>
- 2 Chen K. et al. Effects of non-uniform fin arrangement and size on the thermal response of a vertical latent heat triple-tube heat exchanger / K. Chen, H. I. Mohammed, J. M. Mahdi et al. // Journal of Energy Storage. — 2022. — Vol. 45. — P. 103723. <https://doi.org/10.1016/j.est.2021.103723>
- 3 Osley W.G. CFD investigation of heat transfer and flow patterns in tube side laminar flow and the potential for enhancement / W.G. Osley, P. Droegemueller, P. Ellerby // Chemical Engineering Transactions. — 2013. — Vol. 35. — P. 997–1002. <https://doi.org/10.3303/CET1335166>
- 4 Karar O. et al. Experimental and numerical investigation on convective heat transfer in actively heated bundle-pipe / O. Karar, S. Emani, S.M. Gounder et al. // Engineering Applications of Computational Fluid Mechanics. — 2021. — Vol. 15, Issue 1. — P. 848–864. DOI: 10.1080/19942060.2021.1920466
- 5 Rana S. CFD approach for the enhancement of thermal energy storage in phase change material charged heat exchanger / S. Rana, M. Zunaid, R. Kumar // Case Studies in Thermal Engineering. — 2022. — Vol. 33. — P. 101921. <https://doi.org/10.1016/j.csite.2022.101921>
- 6 Allouche Y. et al. Validation of a CFD model for the simulation of heat transfer in a tubes-in-tank PCM storage unit / Y. Allouche, S. Varga, C. Bouden et al. // Renew. Energy. — 2016. — Vol. 89. — P. 371–379. <https://doi.org/10.1016/j.renene.2015.12.038>
- 7 Balaji D. CFD analysis of a pressure drop in a staggered tube bundle for a turbulent cross flow / D. Balaji, L. S. S. Prakash // Int. Adv. Res. J. Sci. Eng. Technol. — 2016. — Vol. 3. — P. 35–40. <https://doi.org/10.17148/IARJSET.2016.3209>
- 8 Czarnota T. Turbulent convection and thermal radiation in a cuboidal Rayleigh–Benard cell with conductive plates / T. Czarnota, C. Wagner // Int. J. Heat Fluid Flow. — 2016. — Vol. 57. — P. 150–172. <https://doi.org/10.1016/j.ijheatfluidflow.2015.10.006>
- 9 Mohanan A.K. Flow and heat transfer characteristics of a cross-flow heat exchanger with elliptical tubes / A.K. Mohanan, B.V. Prasad, S. Vengadesan // Heat Transf. Eng. — 2020. — Vol. 42. — P. 1846–1860. <https://doi.org/10.1080/01457632.2020.1826742>

- 10 Kurmanova D. et al. Modelling and Simulation of Heat Exchanger with Strong Dependence of Oil Viscosity on Temperature / D. Kurmanova, N. Jaichibekov, A. Karpenko, et al. // Fluids. — 2023. — Vol. 8, Issue 95. — P. 1–18. <https://doi.org/10.3390/fluids8030095>
- 11 Kurmanova D. Control of heat transfer characteristics in helicoidal heat exchangers with strong dependence of oil viscosity on temperature / D. Kurmanova, N. Jaichibekov, K. Volkov, A. Zhumanbayeva // 9th International Symposium on Advances in Computational Heat Transfer, CHT-24. — 2024. — P. 97–101. <https://www.dl.begellhouse.com/references/1bb331655c289a0a,3ecc9d403d74976a,52bf5fc425678078>.
- 12 Kurmanova D.E. Numerical modeling and calculation of heat transfer between heat carriers in heat exchangers / D.E. Kurmanova, N.J. Jaichibekov, A.G. Karpenko, K.N. Volkov // Bulletin of the Karaganda University. Physics Series. — 2023. — № 1(109). — P. 59–70. DOI: https://doi.org/10.31489/2024ph2_72-81
- 13 ANSYS Theory Guide / ANSYS, Inc. Southpointe. — Canonsburg, PA, 2019. — 988 p.
- 14 Лушник В.Г. Теплообменник «труба в трубе» с диффузорными каналами с газовыми и жидкими теплоносителями / В.Г. Лушник, А.И. Решмин, К.С. Егоров // Физико-химическая кинетика в газовой динамике. — 2024. — Том. 25, Вып. 4. — С. 1–21. <http://chemphys.edu.ru/issues/2024-25-4/articles/1115/>

А.С. Жұманбаева, Н.Ж. Жәйшібеков, Д.Е. Құрманова

Турбуленттік модельдердің жылу алмастырғыш аппараттарды есептеудегі жылу тасымалдағыштардың гидродинамикалық және жылулық параметрлеріне әсерін зерттеу

Мақалада $k-\omega$ SST, $k-\varepsilon$ және transition SST турбуленттілігінің жартылай эмпирикалық модельдерін пайдалана отырып, тікелей ағындар схемасы үшін «құбырдағы құбыр» типті жылу алмастырғыштағы (ЖАА) суық (мұнай) және ыстық (су) жылу алмастырғыш арасында болатын жылу алмасу процестері зерттелді. Талдау нәтижелері көрсеткендей, түтіктің диаметрі өте аз жылу алмастырғышты есептеу кезінде түтіктегі шекаралық қабаттың әсерін ескере отырып, $k-\omega$ SST турбуленттілік моделі қолайлы болды. Бұл турбуленттілік моделі ламинарлы-турбулентті ауысуды айқынырақ көрсетеді, ол осы процестерде жүзеге асырылады, мұнда мұнайдың тұтқырлығы температураға өте тәуелді. Жылу алмасу процестерін сандық модельдеу және есептеу үшін ақырлы айырымды мен ақырлы көлем әдістері таңдалды. Есептеулер ANSYS Fluent бағдарламалық кешенін пайдалана отырып, есептеу гидродинамикасы (Computational Fluid Dynamics, CFD) құралдарының негізінде жүргізілді. Жылу алмастырғыштардың гидродинамикасын сандық модельдеу үшін ламинарлы — турбулентті ауысуды және модельдің $k-\omega$ SST теңдеулерін ескеретін gamma-Retheta турбуленттілік моделімен тұйықталған Рейнольдс бойынша орташа Навье-Стокс теңдеулері (RANS, Reynolds-averaged Navier — Stokes) қолданылды. Ұсынылған турбуленттілік моделі негізінде гидродинамикалық және жылу параметрлерінің таралуы, сондай-ақ ЖАА түтігінің ұзындығы бойынша процестің ұқсастық критерийлері (Re, Pr, Nu) алынды.

Кілт сөздер: жылу беру, сандық есептеу, жылу алмастырғыш, мұнай, гидродинамика, салқындатқыш сұйықтар, жылу ағыны, ламинарлы-турбулентті ауысу, үзіліссіздік, жылу алмасу қарқындылығы, тұтқырлық

А.С. Жуманбаева, Н.Ж. Джайчибеков, Д.Е. Курманова

Исследование влияния моделей турбулентности на гидродинамические и тепловые параметры теплоносителей в расчетах теплообменных аппаратов

В статье проведено исследование теплообменных процессов, происходящих между холодным (нефть) и горячим (вода) теплоносителями в теплообменном аппарате (ТОА) типа «труба в трубе» для схемы прямоток, с использованием полуэмпирических моделей турбулентности $k-\omega$ SST, $k-\varepsilon$ и Transition SST. Анализ полученных результатов показал, что при расчете теплообменного аппарата с достаточно малым диаметром трубки более предпочтительной оказалась модель турбулентности $k-\omega$ SST, из-за учета влияния пограничного слоя в трубке. Данная модель турбулентности более выражено воспроизводит ламинарно-турбулентный переход, который осуществляется в данных процессах, где вязкость нефти сильно зависит от температуры. Для численного моделирования и расчета теплообменных процессов были выбраны методы конечных разностей и конечных объемов. Расчеты проводились на основе средств вычислительной гидродинамики (Computational Fluid Dynamics, CFD), с использованием программного комплекса Ansys Fluent. Для численного моделирования гидродинамики теплоносителей применялись осредненные по Рейнольдсу уравнения Навье-Стокса (RANS, Reynolds-averaged Navier-Stokes), замкнутые при помощи модели турбулентности gamma-Retheta, учитывающей лами-

нарно-турбулентный переход и уравнения k - ω SST модели. На основе предложенной модели турбулентности получены распределения гидродинамических и тепловых параметров, а также критериев подобия (Re, Pr, Nu) процесса по длине трубы ТОА.

Ключевые слова: теплопередача, численный расчет, теплообменник, нефть, гидродинамика, охлаждающие жидкости, тепловой поток, ламинарно-турбулентный переход, перемежаемость, интенсивность теплообмена, вязкость

References

- 1 Yogesh, S.S., Selvaraj, A.S., Ravi, D.K., & Rajagopal, T.K.R. (2018). Heat transfer and pressure drop characteristics of inclined elliptical fin tube heat exchanger of varying ellipticity ratio using CFD code. *International Journal of Heat and Mass Transfer*, 119, 26–39. <https://doi.org/10.1016/j.ijheatmasstransfer.2017.11.094>
- 2 Chen, K., Mohammed, H.I., Mahdi, J.M., Rahbari, A., Cairns, A., & Talebizadehsardari, P. (2022). Effects of non-uniform fin arrangement and size on the thermal response of a vertical latent heat triple-tube heat exchanger. *Journal of Energy Storage*, 45, 103723. <https://doi.org/10.1016/j.est.2021.103723>
- 3 Osley, W.G., Droegemueller, P., & Ellerby, P. (2013). CFD investigation of heat transfer and flow patterns in tube side laminar flow and the potential for enhancement. *Chemical Engineering Transactions*, 35, 997–1002. DOI: 10.3303/CET1335166
- 4 Karar, O., Emani, S., Gounder, S.M., Myo Thant, M.M., Mukhtar, H., Sharifpur, M., & Sadeghzadeh, M. (2021). Experimental and numerical investigation on convective heat transfer in actively heated bundle-pipe. *Engineering Applications of Computational Fluid Mechanics*, 15(1), 848–864. DOI: 10.1080/19942060.2021.1920466
- 5 Rana, S., Zunaid, M., & Kumar, R. (2022). CFD approach for the enhancement of thermal energy storage in phase change material charged heat exchanger. *Case Studies in Thermal Engineering*, 33, 101921. <https://doi.org/10.1016/j.csite.2022.101921>
- 6 Allouche, Y., Varga, S., Bouden, C., & Oliveira, A.C. (2016). Validation of a CFD model for the simulation of heat transfer in a tubes-in-tank PCM storage unit. *Renewable Energy*, 89, 371–379. <https://doi.org/10.1016/j.renene.2015.12.038>
- 7 Balaji, D., & Prakash, L.S.S. (2016). CFD analysis of a pressure drop in a staggered tube bundle for a turbulent cross flow. *International Advanced Research Journal in Science, Engineering and Technology*, 3(2), 35–40. <https://doi.org/10.17148/IARJSET.2016.3209>
- 8 Czarnota, T., & Wagner, C. (2016). Turbulent convection and thermal radiation in a cuboidal Rayleigh-Binard cell with conductive plates. *International Journal of Heat and Fluid Flow*, 57, 150–172. <https://doi.org/10.1016/j.ijheatfluidflow.2015.10.006>
- 9 Mohanan, A.K., Prasad, B.V., & Vengadesan, S. (2021). Flow and heat transfer characteristics of a cross-flow heat exchanger with elliptical tubes. *Heat Transfer Engineering*, 42(21), 1846–1860. <https://doi.org/10.1080/01457632.2020.1826742>
- 10 Kurmanova, D., Jaichibekov, N., Karpenko, A., & Volkov, K. (2023). Modelling and Simulation of Heat Exchanger with Strong Dependence of Oil Viscosity on Temperature. *Fluids*, 8(95), 1–18. <https://doi.org/10.3390/fluids8030095>
- 11 Kurmanova, D., Jaichibekov, N., Volkov, K., & Zhumanbayeva, A. (2024). Control of heat transfer characteristics in helicoidal heat exchangers with strong dependence of oil viscosity on temperature. *9th International Symposium on Advances in Computational Heat Transfer*, CHT-24, 97–101. <https://www.dl.begellhouse.com/references/1bb331655c289a0a,3ecc9d403d74976a,52bf5fc425678078>
- 12 Kurmanova, D.E., Jaichibekov, N.J., Karpenko, A.G., & Volkov, K.N. (2023). Numerical modeling and calculation of heat transfer between heat carriers in heat exchangers. *Bulletin of the University of Karaganda-Physics*, 1(109), 59–70. DOI: <https://doi.org/10.31489/2023ph1/59-70>
- 13 ANSYS Fluent Theory Guide. (2019). ANSYS, Inc. Southpointe. — Canonsburg, PA, 988.
- 14 Lushchik, V.G., Reshmin, A.I., & Egorov, K.S. (2024). Teploobmennik «truba v trube» s diffuzornymi kanalami s gazovymi i zhidkimi teplonositeliami [Double-Pipe Heat Exchanger with Diffuser Channels with Gas and Liquid Coolants]. *Fiziko-khimicheskaya kinetika v gazovoi dinamike — Physical-Chemical Kinetics in Gas Dynamics*, 25(4), 1–21 [in Russian].

Information about the authors

Zhumanbayeva, Aizhan — Doctoral student, Department of Mechanics, L.N. Gumilyov Eurasian National University, Astana, Kazakhstan; e-mail: aizhanzhumanbayeva347@gmail.com; ORCID ID: <https://orcid.org/0009-0007-2725-3672>

Jaichibekov, Nurbolat (contact person) — Doctor of Physical and Mathematical Sciences, Professor, Department of Mechanics, L.N. Gumilyov Eurasian National University, Astana, Kazakhstan; e-mail: jaich@mail.ru; ORCID ID: <https://orcid.org/0000-0002-3053-8288>

Kurmanova, Dinara — PhD, Department of Mechanics, L.N. Gumilyov Eurasian National University, Astana, Kazakhstan; e-mail: dikonya89_29@mail.ru; ORCID ID: <https://orcid.org/0009-0009-9787-7426>

Adem Akkuş✉

Department of Physics, Faculty of Arts and Sciences, Gaziosmanpaşa University, Tokat, Turkey

On the Analytical Determination of the Seebeck Coefficient Using the Fermi–Dirac Approximation

The Seebeck coefficient, or thermoelectric power, is a key physical parameter that quantifies the voltage generated in response to a temperature gradient across a material. Accurate evaluation of this coefficient is essential in order to optimize the performance of thermoelectric devices. This study proposes a theoretical approach to the analytical determination of the Seebeck coefficient in semiconductors, based on the Fermi–Dirac statistical approximation. The model incorporates the temperature dependence of the Fermi level, which introduces an intrinsic gradient along the thermoelectric structure under non-equilibrium thermal conditions. This framework enables a more precise understanding of the interplay between the carrier distribution, energy levels, and temperature variation. The analytical expressions obtained here show good agreement with the results of numerical methods, and offer significant advantages in terms of modeling and designing high-performance thermoelectric materials. The proposed approach proves to be an efficient and insightful tool for theoretical investigations and optimization studies in semiconductor thermoelectrics.

Keywords: Seebeck coefficient; thermoelectric power; semiconductor; Fermi–Dirac method

✉ *Corresponding author:* Adem Akkuş, ademakkus76@gmail.com

Introduction

Thermoelectric effects, which are primarily quantified by the Seebeck coefficient, involve direct inter-conversion between thermal and electrical energy in a material system. The Seebeck effect refers to a phenomenon where a temperature gradient established along a thermoelectric material induces an electric potential difference, and vice versa, and this forms the foundational principle behind thermoelectric generators and coolers [1–7]. The efficiency of these energy conversion processes is strongly governed by the magnitude and behavior of the Seebeck coefficient indifferent materials and temperature regimes.

In semiconductors and complex materials, the Seebeck coefficient is particularly sensitive to microscopic interactions involving charge carriers. These include carrier–carrier, carrier–phonon, and in the case of magnetic semiconductors, carrier–localized magnetic moment interactions. Such interactions can significantly alter the distribution function of carriers, leading to notable changes in the thermoelectric response. For example, scattering mechanisms impose constraints on the final states that carriers can occupy, often resulting in a reduction of the Seebeck coefficient due to the suppression of entropy transport per carrier [8, 9].

The Seebeck coefficient is not solely a material constant, and is closely associated with the carrier concentration, effective mass, and temperature, all of which affect the position and dynamics of the Fermi level. In degenerate or heavily doped semiconductors in particular, where classical (Boltzmann) statistics become insufficient, a quantum-statistical approach becomes necessary. The Fermi–Dirac distribution provides a more accurate description of carrier occupancy in such systems, and is essential in order to capture realistic transport behavior [10, 11]. The Gaussian density of states (DOS) approximation is also widely used to model disordered or amorphous semiconductors and organic materials, in which the electronic states are not sharply defined due to substantial energetic disorder. Unlike crystalline semiconductors, which have well-defined band structures derived from periodic Bloch states, disordered systems lack long-range structural order. This absence of periodicity results in localized electronic states with broadened energy levels, due to variations in the local environment such as structural distortions or fluctuations in molecular orientation [12–14].

In this study, we present an analytical approach for evaluating the Seebeck coefficient in semiconducting materials within the framework of a Gaussian DOS and the Fermi–Dirac statistical approximation. The use of the Gaussian approximation for the DOS is physically justified in systems where energetic disorder

dominates, such as amorphous and organic semiconductors. In these materials, the absence of long-range order leads to a broadening of the electronic energy levels, which can be effectively modeled by a Gaussian distribution. This approximation is commonly accepted for disordered systems, including amorphous silicon, disordered metal oxides, and organic semiconductors, where localized states and site-to-site energy fluctuations govern the charge transport [15–18]. To incorporate the temperature dependence of the chemical potential (Fermi level), we used a numerical method in Mathematica 10.0 that is valid across both non-degenerate and degenerate regimes. This theoretical framework enables improved insight into the thermoelectric properties of materials without relying solely on numerical simulations. The analytical results obtained here demonstrate the reliability and applicability of the proposed method for thermoelectric modeling.

Proposed Method and Formulae

An analytical formula was proposed in [19–23] for the calculation of the Seebeck coefficient, as presented below:

$$S = -\frac{eL^2}{\tau T \sigma} \int_{-\infty}^{\infty} \frac{E - E_f}{kT} f(E, T) (1 - f(E, T)) N(E) dE, \quad (1)$$

where σ is the electrical conductivity, τ is the scattering time, $L^2 = \frac{1}{3}(\tau v)^2$ is the scattering distance (mean free path), $N(E)$ is the DOS, which can be represented by a Gaussian function, and $f(E)$ is the Fermi–Dirac distribution function. These quantities are defined as follows [20]:

$$N(E) = \frac{N_0}{\sqrt{2\pi}\delta} e^{-\frac{1}{2}\left(\frac{E-E_0}{\delta}\right)^2} \quad (2)$$

and

$$f(E) = \frac{1}{1 + e^{\frac{E-E_f}{kT}}}, \quad (3)$$

where the energy E_0 is defined as the center of the Gaussian distribution, N_0 is the total concentration of energetic states, and δ is the width of the distribution. Substituting Eqs. (2) and (3) into Eq. (1) gives the following expression:

$$S = -\frac{eL^2}{\sigma \tau k T^2} \frac{N_0}{\sqrt{2\pi}\delta} \int_{-\infty}^{\infty} \frac{1}{1 + e^{\frac{E-E_f}{kT}}} \left(1 - \frac{1}{1 + e^{\frac{E-E_f}{kT}}} \right) (E - E_f) e^{-\frac{1}{2}\left(\frac{E-E_0}{\delta}\right)^2} dE, \quad (4)$$

where σ is the conductivity of the material. Eq. (4) can be expressed in the following form:

$$S = -\frac{eL^2}{\sigma \tau k T^2} \frac{N_0}{\sqrt{2\pi}\delta} Q(k, \delta, T, E_f, E_0), \quad (5)$$

where

$$Q(k, \delta, T, E_f, E_0) = \int_{-\infty}^{\infty} \frac{1}{1 + e^{\frac{E-E_f}{kT}}} \left(1 - \frac{1}{1 + e^{\frac{E-E_f}{kT}}} \right) (E - E_f) e^{-\frac{1}{2}\left(\frac{E-E_0}{\delta}\right)^2} dE. \quad (6)$$

Due to the complexity of Eq. (6), the derivation of a closed-form analytical expression is highly challenging; it is therefore expressed as a sum of simpler integrals, in the following form:

$$Q(k, \delta, T, E_f, E_0) = L(k, \delta, T, E_f, E_0) + M(k, \delta, T, E_f, E_0) - R(k, \delta, T, E_f, E_0) - K(k, \delta, T, E_f, E_0), \quad (7)$$

where

$$L(k, \delta, T, E_f, E_0) = \int_0^{E_f} \frac{(E - E_f)}{1 + e^{\frac{E-E_f}{kT}}} e^{-\frac{1}{2}\left(\frac{E-E_0}{\delta}\right)^2} dE, \quad (8)$$

$$M(k, \delta, T, E_f, E_0) = \int_{E_f}^{\infty} \frac{(E - E_f)}{1 + e^{\frac{E - E_f}{kT}}} e^{-\frac{1}{2} \left(\frac{E - E_0}{\delta} \right)^2} dE, \quad (9)$$

$$R(k, \delta, T, E_f, E_0) = \int_0^{\infty} \frac{(E + E_f)}{1 + e^{\frac{E + E_f}{kT}}} e^{-\frac{1}{2} \left(\frac{E + E_0}{\delta} \right)^2} dE, \quad (10)$$

$$K(k, \delta, T, E_f, E_0) = \int_{-\infty}^{\infty} \frac{(E - E_f)}{\left(1 + e^{\frac{E - E_f}{kT}} \right)^2} e^{-\frac{1}{2} \left(\frac{E - E_0}{\delta} \right)^2} dE. \quad (11)$$

As can be seen from Eq. (5), the determination of the Seebeck coefficient depends on the accurate evaluation of Eqs. (8)–(11). To derive an analytical expression from Eqs. (8)–(11), the binomial expansion theorem and the exponential series expansion are employed, as follows [24, 25]:

$$e^{\pm x} = \sum_{i=0}^{\infty} (\pm 1)^i \frac{x^i}{i!} \quad (12)$$

and

$$(x \pm y)^n = \begin{cases} \lim_{N \rightarrow \infty} \sum_{m=0}^N (\pm 1)^m f_m(n) x^{n-m} y^m & \text{for noninteger } n \text{ and } x \geq y \\ \sum_{m=0}^n (\pm 1)^m f_m(n) x^{n-m} y^m & \text{for integer } n \end{cases} \quad (13)$$

where $f_m(n)$ are binomial coefficients defined by:

$$f_m(n) = \frac{1}{m!} \prod_{i=0}^{m-1} (n - i). \quad (14)$$

By substituting Eqs. (12) and (13) into Eqs. (8)–(10), a general analytical expression for $L(k, \delta, T, E_f, E_0)$, $M(k, \delta, T, E_f, E_0)$ and $R(k, \delta, T, E_f, E_0)$ can be derived as follows:

$$L(k, \delta, T, E_f, E_0) = \lim_{N \rightarrow \infty} \sum_{i=0}^N \frac{(-1)^i}{(2\delta^2)^i i!} \sum_{j=0}^{2i} (-1)^j f_j(2i) E_0^j H_{2i-j}(k, T, E_f); \quad (15)$$

$$M(k, \delta, T, E_f, E_0) = \lim_{N' \rightarrow \infty} \sum_{i=0}^{N'} f_i(-1) \text{Exp} \left(\frac{E_f(i+1)}{kT} - \frac{E_0^2}{2\delta^2} \right) T \left(E_f, \frac{1}{2\delta^2}, -\frac{E_0^2}{\delta^2} + \frac{i+1}{kT} \right) \quad (16)$$

$$R(k, \delta, T, E_f, E_0) = \lim_{N \rightarrow \infty} \sum_{i=0}^{N'} f_i(-1) \text{Exp} \left(-\frac{E_f i}{kT} - \frac{E_0^2}{2\delta^2} \right) S_i \left(E_f, \frac{1}{2\delta^2}, \frac{E_0}{\delta^2} \right) \quad (17)$$

$$H_n(k, T, E_f) = \int_0^{E_f} \frac{(E - E_f) E^n}{1 + e^{\frac{E - E_f}{kT}}} dE \quad (18)$$

$$T(p, q, b) = \frac{e^{-p(b+pq)}}{4\sqrt{q^3}} \left(2\sqrt{q} - e^{\frac{(b+2pq)^2}{4q}} \sqrt{\pi(b+2pq)} \text{Erfc} \left(\frac{b+2pq}{2\sqrt{q}} \right) \right) \quad (19)$$

$$S_i(p, q, b) = \begin{cases} \frac{2\sqrt{q} - \sqrt{\pi} e^{\frac{b^2}{4q}} (b - 2pq) \operatorname{Erfc}\left(\frac{b}{2\sqrt{q}}\right)}{4\sqrt{q^3}} & \text{for } i = 0 \\ \frac{1}{4} \lim_{N \rightarrow \infty} \sum_{j=1}^N \frac{(-1)^j}{j!} \left(\frac{i}{kT}\right)^j q^{-\frac{1}{2}(3+j)} \left(2\sqrt{q} \Gamma(j/2 + 1) \left({}_1F_1\left(\frac{2+j}{2}, \frac{1}{2}, \frac{b^2}{4q}\right) - \right. \right. \\ \left. \left. - bp {}_1F_1\left(\frac{2+j}{2}, \frac{3}{2}, \frac{b^2}{4q}\right) \right) + \Gamma\left(\frac{j+1}{2}\right) \left(2pq {}_1F_1\left(\frac{1+j}{2}, \frac{1}{2}, \frac{b^2}{4q}\right) - b(j+1) \times \right. \right. \\ \left. \left. \times {}_1F_1\left(\frac{3+j}{2}, \frac{3}{2}, \frac{b^2}{4q}\right) \right) \right) & \text{for } i \neq 0 \end{cases} \quad (20)$$

where the parameters N and N' are the upper limits of the summations. The quantities $\Gamma(x)$ and $\operatorname{Erfc}(x)$ are defined as follows:

$$\Gamma(x) = \int_0^{\infty} t^{x-1} e^{-t} dt, \quad (21)$$

$$\operatorname{Erfc}(x) = \frac{2}{\sqrt{\pi}} \int_x^{\infty} e^{-t^2} dt. \quad (22)$$

Note that the functions $K(k, \delta, T, E_f, E_0)$ and $H_n(k, T, E_f)$ are computed using numerical integration techniques.

Numerical Results and Discussion

As can be seen from the preceding equations, accurate determination of the Seebeck coefficient S requires evaluation of the integral given in Eq. (5). However, due to the mathematical complexity introduced by the Gaussian distribution and Fermi–Dirac statistics, obtaining a general closed-form analytical solution for the integral in Eq. (5) remains a significant challenge. In the present study, Eq. (5) was evaluated both analytically, using the derived expression in Eq. (7), and numerically, using the Mathematica 10.0 software package. A numerical integration technique was employed to compute the Seebeck coefficient accurately over a wide temperature range. Figure shows a graph of the Seebeck coefficient as a function of temperature. The results obtained from both the analytical formula in Eq. (5) and the numerical calculations are shown on the graph, which clearly illustrates the temperature-dependent behavior of the Seebeck coefficient; there is consistency between the two methods, thus validating the reliability of the proposed approach. In Figure, the black dashed curve represents the numerically calculated Seebeck coefficient, whereas the red solid curve depicts the values derived analytically using Eq. (5), and it can be seen that there is good agreement between them. The calculations were performed based on the parameters in Eq. (6) with values of $e = 1.602 \times 10^{-19} \text{ C}$, $L^2 \sim 0.864 \times 10^{-19} \frac{\text{m}^2}{\text{s}}$, $\tau \sim 10^{-15} \text{ s}$ [24], $\sigma \sim 10^{-9} \Omega \text{m}$ and $N_0 = 10^{27} \text{ m}^{-3}$ [15]. As shown in

Figure, the desired level of precision was achieved when the series was truncated at values for the upper limit of $N = N' = 30$.

Table presents the partial sums corresponding to progressively increasing upper summation limits N in Eq. (8). Higher accuracy can be readily achieved by increasing the upper-term limits in the series expansions of Eqs. (10)–(12). The dependence of the Seebeck coefficient on temperature, which arises from the thermal broadening of the Fermi–Dirac distribution and the temperature-dependent behavior of the density of states, was systematically analyzed. The results of the numerical simulations show good agreement with the analytical expression given in Eq. (5), thus validating the accuracy of the proposed approach. These results not only validate the applicability of the numerical method but also demonstrate that the proposed approach captures the essential physics governing thermoelectric transport. It also provides a practical framework for further theoretical studies or the experimental design of semiconductor-based thermoelectric devices.

Conclusion

In this study, a novel analytical expression for the Seebeck coefficient was derived using the binomial expansion theorem and the exponential series expansion. As can be seen from Figure and Table, the general analytical expressions for the Seebeck functions obtained through the applied method exhibit strong consistency with the theoretical framework of the proposed approach. This agreement confirms the validity and accuracy of the analytical methodology used to derive the Seebeck coefficients.

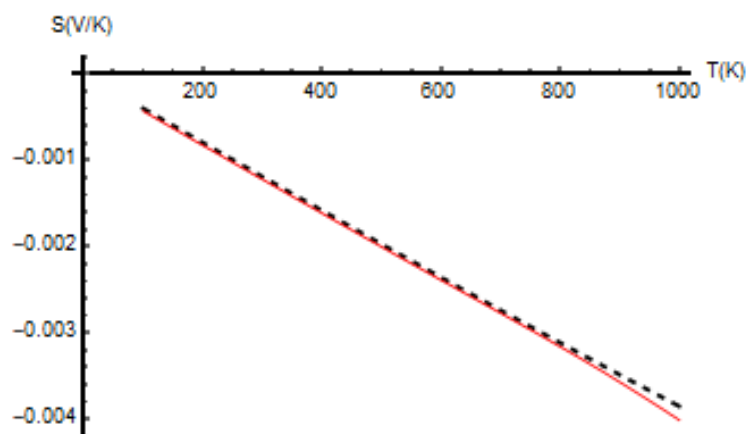


Figure. Variation in the S Seebeck coefficient with respect to T temperature
(where $E_f = 2.5$ eV, $E_0 = 3.2$ eV, $k = 8.617 \times 10^{-5}$ eV \cdot K $^{-1}$, $\delta = 1.2$ eV)

T a b l e

Convergence of the derived expression for $Q(k, \delta, T, E_f, E_0)$ as a function of summation limits $N = N'$
(for $E_f = 8.2$ eV, $E_0 = 4.63$ eV, $k = 8.617 \times 10^{-5}$ eV \cdot K $^{-1}$, $\delta = 1.5$ eV)

N	Eq. (5)
10	-0.000100960026019
20	-0.000101693247456
30	-0.0001018524517281
40	-0.0001019115964974
50	-0.0001019398713466
60	-0.0001019554937334
70	-0.0001019565058798

References

- 1 Singh, S., Poudel, B., Nozariasbmarz, A., Takeuchi, T., & Priya, S. (2023). Constructive approach towards design of high – performance thermoelectrics, thermal diodes, and thermomagnetic devices for energy generation applications. In *Energy Harvesting and Storage Devices* (pp. 80–107). CRC Press.
- 2 Kubenova, M. M., Kuterbekov, K. A., Balapanov, M. K., Ishembetov, R. K., Kabdrakhimova, G. D., Alina, R. A., ... & Ildos, R. (2024). Investigation of thermoelectric properties of nanocrystalline copper chalcogenides. *Bulletin of the University of Karaganda–Physics*, 29, 1(113), 59–65.
- 3 Han, H., Zhao, L., Wu, X., Zuo, B., Bian, S., Li, T., ... & Yu, L. (2024). Advancements in thermoelectric materials: optimization strategies for enhancing energy conversion. *Journal of Materials Chemistry A*, 12(36), 24041–24083.
- 4 Apertet, Y., Ouerdane, H., Goupil, C., & Lecoq, P. (2016). A note on the electrochemical nature of the thermoelectric power. *The European Physical Journal Plus*, 131, 1–8.
- 5 Park, J., Xia, Y., Ozoliņš, V., & Jain, A. (2021). Optimal band structure for thermoelectrics with realistic scattering and bands. *npj Computational Materials*, 7(1), 43.

- 6 Kokalj, J., & McKenzie, R. H. (2015). Enhancement of the thermoelectric power by electronic correlations in bad metals: A study of the Kelvin formula. *Physical Review B*, 91(12), 125143.
- 7 Lafuente-Bartolome, J., Lian, C., Sio, W. H., Gurtubay, I. G., Eiguren, A., & Giustino, F. (2022). Unified approach to polarons and phonon-induced band structure normalization. *Physical Review Letters*, 129(7), 076402.
- 8 Portavoce, A., Assaf, E., Bertoglio, M., Narducci, D., & Bertaina, S. (2023). Magnetic moment impact on spin dependent Seebeck coefficient of ferromagnetic thin films. *Scientific Reports*, 13(1), 172.
- 9 Snyder, G. J., Pereyra, A., & Gurunathan, R. (2022). Effective mass from Seebeck coefficient. *Advanced Functional Materials*, 32(20), 2112772.
- 10 Mamedov, B. A., & Copuroglu, E. (2016). Unified analytical treatments of the two-parameter Fermi functions using binomial expansion theorem and incomplete gamma functions. *Solid State Communications*, 245, 42–49.
- 11 Justice, P., Marshman, E., & Singh, C. (2019). Student understanding of Fermi energy, the Fermi–Dirac distribution and total electronic energy of a free electron gas. *European Journal of Physics*, 41(1), 015704.
- 12 Qin, D., Chen, J., & Lu, N. (2023). A Novel Density of States (DOS) for Disordered Organic Semiconductors. *Micromachines*, 14(7), 1361.
- 13 Nenashev, A. V., Oelerich, J. O., & Baranovskii, S. D. (2015). Theoretical tools for the description of charge transport in disordered organic semiconductors. *Journal of Physics: Condensed Matter*, 27(9), 093201.
- 14 Xiao-Hong, S., Jiu-Xun, S., & Chun-Hua, X. (2016). Dependence of general Einstein relation on density of state for organic semiconductors. *Organic Electronics*, 35, 65–73.
- 15 Mendels, D., & Tessler, N. (2014). Thermoelectricity in disordered organic semiconductors under the premise of the Gaussian disorder model and its variants. *The Journal of Physical Chemistry Letters*, 5(18), 3247–3253.
- 16 Scheinert, S., & Paasch, G. (2014). Influence of the carrier density in disordered organics with Gaussian density of states on organic field-effect transistors. *Journal of Applied Physics*, 115(4), 044507.
- 17 Selvaggi, J. P. (2018). Analytical evaluation of the charge carrier density of organic materials with a Gaussian density of states revisited. *Journal of Computational Electronics*, 17, 61–67.
- 18 Maddalena, F., de Falco, C., Caironi, M., & Natali, D. (2015). Assessing the width of Gaussian density of states in organic semiconductors. *Organic Electronics*, 17, 304–318.
- 19 Skipetrov, S. E., & Page, J. H. (2016). Red light for Anderson localization. *New Journal of Physics*, 18(2), 021001.
- 20 Paasch, G., & Scheinert, S. (2010). Charge carrier density of organics with Gaussian density of states: analytical approximation for the Gauss–Fermi integral. *Journal of Applied Physics*, 107(10), 104501.
- 21 Wang, Y., Hu, Y. J., Bocklund, B., Shang, S. L., Zhou, B. C., Liu, Z. K., & Chen, L. Q. (2018). First principles thermodynamic theory of Seebeck coefficients. *Physical Review B*, 98(22), 224101.
- 22 Mott, N. F. (1971). Conduction in non-crystalline systems. *Philosophical Magazine*, 24(187).
- 23 Selvaggi, J. P. (2019). Modeling the Seebeck coefficient for organic materials with the Kubo–Greenwood integral and a Gaussian density of states. *Journal of Computational Electronics*, 18(2), 473–481.
- 24 Gradshteyn, I. S., & Ryzhik, I. M. *Tables of Integrals, Sums, Series and Products*, 4th ed., Academic Press, New York, 1980.
- 25 Guseinov, I. I., Mamedov, B. A., Kara, M., & Orbay, M. E. T. İ. N. (2001). On the computation of molecular auxiliary functions A n and B n. *Pramana Journal of Physics*, 56, 691–696.

Адам Аккуш

Ферми-Дирак жуықтауын пайдаланып Зеебек коэффициентін аналитикалық анықтауы

Зеебек коэффициенті немесе термоэлектрлік қуат — бұл материал бойынша температура градиентіне жауап ретінде пайда болатын кернеуді сандық түрде анықтайтын негізгі физикалық параметр. Бұл коэффициентті дәл анықтау термоэлектрлік құрылғылардың өнімділігін оңтайландыру үшін қажет. Зерттеуде шамамен Ферми-Дирак әдісіне негізделген жартылай өткізгіштердегі Зеебек коэффициентін аналитикалық анықтауға теориялық тәсілді ұсынады. Модель Ферми деңгейінің температураға тәуелділігін ескереді, бұл тепе-теңдіксіз жылу жағдайында термоэлектрлік құрылым бойымен ішкі градиенттің пайда болуына әкеледі. Бұл модель тасымалдаушының таралуы, энергия деңгейлері мен температураның өзгеруі арасындағы өзара байланысты дәлірек түсінуге мүмкіндік береді. Алынған аналитикалық өрнектер сандық әдістердің нәтижелерімен жақсы сәйкес келеді және өнімділігі жоғары термоэлектрлік материалдарды модельдеумен жобалауда артықшылықтар береді. Ұсынылған тәсіл жартылай өткізгіш термоэлектрика саласындағы теориялық зерттеулер мен оңтайландырудың тиімді және ақпараттық құралы.

Кілт сөздер: Зеебек коэффициенті, термоэлектрлік қуат, жартылай өткізгіш, Ферми-Дирак тәсілі

Адам Аккуш


Об аналитическом определении коэффициента Зеебека с использованием приближения Ферми–Дирака

Коэффициент Зеебека или термоэлектродвижущая сила, является важным физическим параметром, который количественно описывает напряжение, возникающее в ответ на температурный градиент в материале. Точное определение этого коэффициента необходимо для оптимизации характеристик термоэлектрических устройств. В настоящем исследовании предлагается теоретический подход к аналитическому определению коэффициента Зеебека в полупроводниках на основе приближённого метода Ферми–Дирака. Модель учитывает температурную зависимость уровня Ферми, что приводит к возникновению внутреннего градиента вдоль термоэлектрической структуры в неравновесных тепловых условиях. Эта модель позволяет более точно понять взаимосвязь между распределением носителей, энергетическими уровнями и температурными изменениями. Полученные аналитические выражения хорошо согласуются с результатами численных методов и предоставляют значительные преимущества при моделировании и проектировании высокоэффективных термоэлектрических материалов. Предложенный подход является эффективным и информативным инструментом для теоретических исследований и оптимизации в области термоэлектрики полупроводников.

Ключевые слова: коэффициента Зеебека, термоэлектродвижущая сила, полупроводник, метод Ферми–Дирака

Information about the author

Adem Akkuş — Department of Physics, Research Assistant, Faculty of Arts and Sciences, Gazi-osmanpaşa University, Taşlıçiftlik Campus, 60000, Tokat, Turkey; e-mail: ademakkus76@gmail.com; ORCID ID: <https://orcid.org/0009-0007-2638-7433>

L.G. Sulyubayeva¹, D.R. Baizhan¹, S.D. Bolatov¹,
N.Ye. Berdimuratov¹, N.Ye. Bazarov²

¹Research Center “Surface Engineering and Tribology”,
Sarsen Amanzholov East Kazakhstan University, Ust-Kamenogorsk, Kazakhstan;

²LLP “PlasmaScience”, Ust-Kamenogorsk, Kazakhstan

Investigation of the Influence of Technological Regimes of Thermocyclic Electrolyte-Plasma Treatment On The Structural-Phase State and Tribocorrosion Properties of 12Kh1MF Steel

This paper presents the results of a detailed study on the influence of thermocyclic electrolyte-plasma treatment on the structural-phase state, microhardness, and tribocorrosion properties of heat-resistant steel 12Kh1MF. The treatment was carried out using a 10 % Na₂CO₃ aqueous solution and a voltage of 300/150 V. It resulted in the formation of a zonal microstructure with a martensitic surface layer up to 600 μm thick. The structure was divided into zones: hardened, thermal influence, and base material. Microhardness increased by 1.5 times due to martensitic transformation. X-ray analysis confirmed the formation of α'Fe and Fe₃C phases. Tribological tests showed a 10 % reduction in the friction coefficient and a 1.5–2-fold increase in wear resistance. Corrosion tests in a salt fog chamber revealed enhanced protective properties, with mass loss reduced and corrosion resistance improved by 10–30 %, depending on the treatment mode. Based on a comprehensive analysis, the most effective thermocyclic treatment mode was identified, ensuring an optimal balance of mechanical strength and corrosion resistance. The findings highlight the high potential of thermocyclic electrolyte-plasma treatment as a promising method for enhancing the surface properties of steel components operating in aggressive environments.

Keywords: electrolytic-plasma treatment, heat-resistant structural steel, thermocyclic electrolytic-plasma treatment, microhardness, low-alloy steel, microstructure, surface strengthening, corrosion testing

 *Corresponding author:* Bolatov Sanzhar Daurenuly, sanzharbolatov94@gmail.com

Introduction

Structural steels are materials widely used in power engineering and other industries. They have a number of characteristics that make them suitable for use in high temperature and pressure environments. In thermal power plants, they are used to manufacture steam pipes, turbines and other types of parts. However, with prolonged service life, degradation of the structure occurs, which leads to unstrengthening of the steel [1]. In such cases for steel hardening the traditional heat treatment is carried out, which is carried out with volumetric treatment of the entire working surface of the part, but as it is known in working mechanisms the core of the part must remain plastic for proper operation of the entire unit [2]. Therefore, scientists and engineers develop various methods of hardening, including not only classical heat treatment, but also additional methods that can modify only the near-surface area of parts without changing its plastic characteristics. Technologies based on electro-discharge machining processes, such as electrolyte-plasma technologies for material modification, can be considered as an example of such machining methods [3]. Combining these methods can increase the strength, wear resistance and heat resistance of structural steels, providing longer service life in extreme conditions.

Modern research in the field of electrolyte-plasma processing is actively developing, covering both theoretical and practical aspects of electrodischarge phenomena, contributing to the creation of highly efficient and cost-effective methods of materials processing such as electrical discharge machining (EDM) [4, 5], electrospark machining (ESM) [6], electrolyte-plasma hardening (EPH) [7], and electrolyte-plasma anodic treatment (EPAT) [7, 5], electrospark machining (ESM) [6], electrolyte-plasma hardening (EPH) [7], electrolyte-plasma anodic treatment (EPAO) [8], electrolyte-plasma chemical heat treatment (EPChT) [9] expanding their application in various industrial sectors, including power and mining engineering.

The study by Garba E., Abdul-Rani A.M., Yunus N.A. [10] and co-authors demonstrates the wide possibilities of electrical discharge machining (EDM), which is used in such industries as mold and die manufacturing, as well as in mechanical engineering, nuclear, aerospace and biomedical industries. According to the authors' conclusions, the main advantage of this technology is the high accuracy of manufacturing complex parts. However, EDM has a number of significant disadvantages, including low material removal rate, poor surface quality, long processing time, high cost, as well as being limited to processing only electrically conductive materials. These factors limit its application in production.

In the monograph by Korzhyk V., Tyurin Yu. and Kolisnichenko O. [11] the results of theoretical and experimental studies of dynamic processes of modification of metal surfaces by means of electric current regulated by means of an electrode with liquid electrolyte were presented. Based on the conducted studies, integrated hardening technologies were developed and specialized equipment was created, allowing for oxidation, alloying and structural transformation of the surface without affecting the entire volume of the product. The use of these technologies significantly improves the physical and mechanical characteristics of materials, increasing their strength, wear resistance and resistance to fatigue loads under friction and wear conditions.

The studies by Berladir K. and her co-authors consider the process of nitrocarburizing with cyclic heating in comparison with isothermal nitrocarburizing [12]. The authors found that the use of thermocyclic nitrocarburizing in comparison with isothermal nitrocarburizing allows for an increase in resistance to cavitation destruction by 0.6–1.5 times. In addition, the use of chemical-thermocyclic treatment helps to reduce processing time, reveal the grain structure and improve the mechanical properties of structural steel.

One of the promising technologies in this area is thermocycling electrolytic-plasma treatment (TEPT). This method combines thermal, electrical and plasma effects on the material in an electrolytic environment, where active elements contribute to its modification due to the flow of electric current through the environment to the surface of the material. This approach allows to significantly increase the hardness of the surface layers. The TEPT process includes cyclic alternation of heating and cooling, which causes significant structural changes in the material and improves its mechanical properties, facilitating wide application in production. Thus, according to the analysis, it was established that technologies based on the processes of electric discharge phenomena are applicable as an alternative to traditional heat treatment in order to improve the performance characteristics of a wide class of steels, however, the definition of technological regimes of cathodic electrolytic-plasma treatment with thermocycling has not been studied in detail. Therefore, the aim of this work is to study the influence of technological regimes of thermocyclic electrolytic-plasma treatment on the structural-phase state and tribocorrosion properties of 12Kh1MF structural steel.

Materials and methods of research

In this work, 12Kh1MF steel was used as the material for TEPT. This steel is widely used in the power industry, in particular, it is used to manufacture pipelines, boilers and other elements operating in aggressive environments. The chemical composition of 12Kh1MF steel according to GOST 20072-74 is given in Table.

T a b l e

Chemical composition of steel grade 12Kh1MF, %

C	Si	Mn	Cr	Mo	V	P	S
0.1–0.15	0.17–0.37	0.4–0.7	0.9–1.2	0.25–0.35	0.15–0.03	>0.035	>0.03

Thermocyclic hardening of 12Kh1MF steel samples was performed using an electrolytic plasma treatment unit at the Surface Engineering and Tribology Research Center of the Sarsen Amanzholov East Kazakhstan University. The EPO unit schematically consists of an electrolytic cell and a power source (Figure 1 *a, b*).

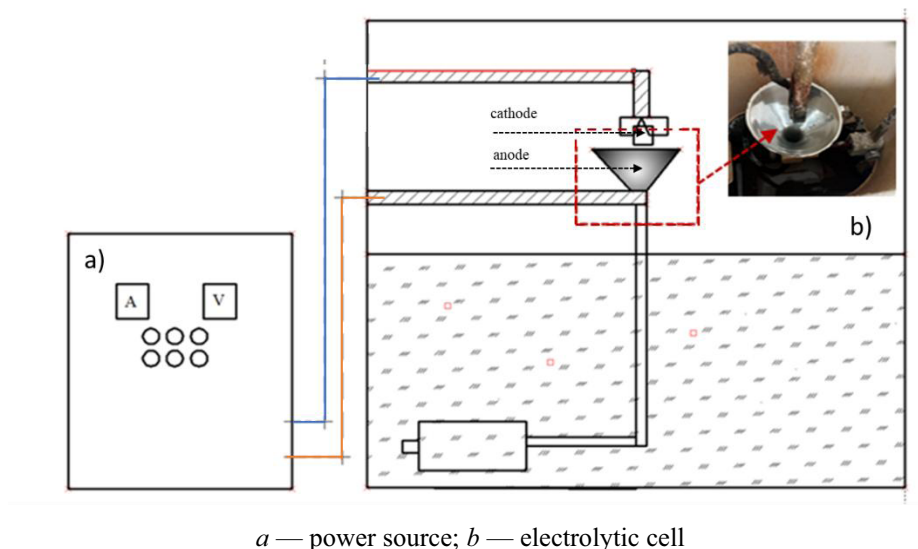


Figure 1. Schematic representation of the unit for thermocycling electrolytic-plasma treatment

The essence of the process of thermocycling hardening by the method of electrolytic-plasma treatment is as follows. At low voltage (about 150 V) in the electrolytic cell with an aqueous solution of electrolyte, a standard electrochemical process occurs. With an increase in voltage to 300 V, intensive gas evolution begins on the electrodes, which leads to the formation of a vapor-gas shell (VGS) near the electrode surface.

The electric field strength in the VGS reaches 10^4 – 10^5 V/cm. At a temperature of about 100 °C, such a field initiates the ionization of vapors, as well as the emission of ions and electrons necessary to maintain a stable electric discharge. As a result, electrolyte plasma is formed. In this process, an aqueous solution of sodium carbonate (Na_2CO_3) acts as a medium for heating and cooling.

For thermocyclic electrolytic-plasma heating of 12Kh1MF steel, an aqueous solution of sodium carbonate (Na_2CO_3) with a concentration of 10 % and 15 % (wt. %) was used. Our previous studies have established [13, 14] that at higher concentrations of Na_2CO_3 , the electrical conductivity of the electrolyte increases, which leads to intense heating and high current density. A 10 % aqueous solution of Na_2CO_3 has a low current density compared to 15 % Na_2CO_3 , which ensures smoother heating without the risk of melting the steel surface, and also ensures effective control of the heating process for various technological tasks. Therefore, in further experiments, we will use an electrolyte composition with 10 % sodium carbonate and 90 % distilled water.

During thermocycling (Table 2), when an electric potential of 300 V is applied, the sample surface rapidly heats up. When periodically switching between high electric potential (300 V) and low (150 V), a cyclic change in the heating rate is observed. This regime allows controlling the intensity of the thermal effect, which helps to increase the duration of heating and form a thick heated layer on the surface of the material. By alternating supply at a voltage of 300 V and a current of 30 A for 5 seconds, with a decrease to 150 V and a current of 8 A for 5 seconds, the electrolyte temperature increases to 37 °C. This allows controlling the heating process, providing different temperature profiles and intensity of thermal effect on the samples.

Table 2

Results of corrosion tests of samples before and after TEPT

Sample	Mass before testing, g	Mass after testing, g	Loss of mass, g	Loss of mass per unit area Δm , kg/m ²
Initial	9.5391	9.5299	0.0092	0.0191
Cycle No.1	11.2293	11.2198	0.0095	0.0129
Cycle No.2	8.4946	8.4883	0.0063	0.0109
Cycle No.3	7.0022	6.9941	0.0081	0.0152

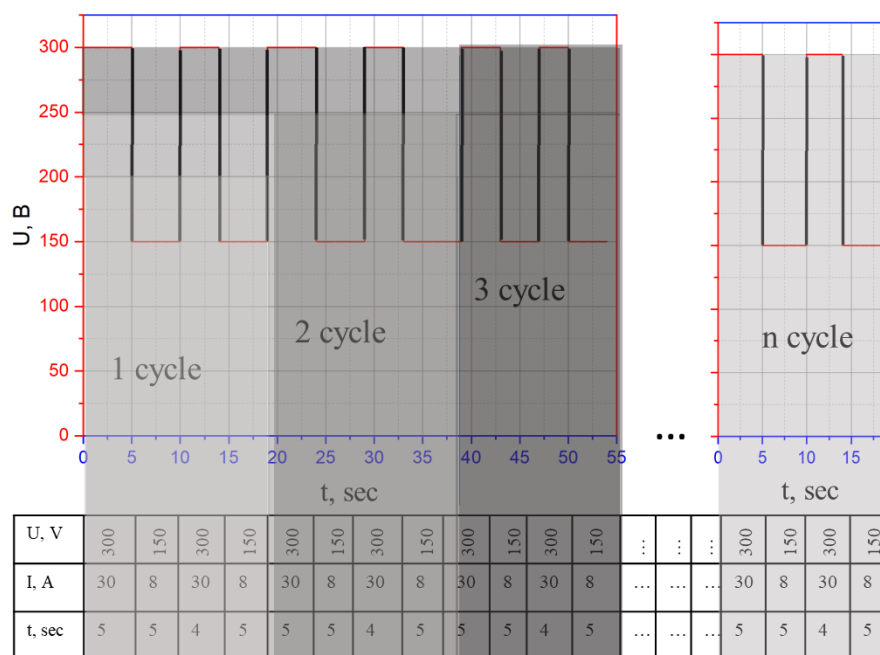


Figure 2. Parameters of the thermocycling electrolytic plasma treatment regime

The maximum steel surface temperature reaches 900 °C in the third cycle, with an increase in the electrolyte temperature to 39 °C. In cycles № 1 and № 3, the steel surface temperature reaches 800 °C and 850 °C, respectively, with the electrolyte temperature increasing to 36 °C and 37 °C, respectively.

The samples for processing were ground and polished on the Metapol-2000P unit. The microstructure of the samples was revealed by chemical etching using a 4 % solution of nitric acid (HNO₃) in ethyl alcohol. The microstructure of the original and processed steels was studied on a TESCAN MIRA scanning electron microscope with a magnification of ×60 and ×1000.

X-ray phase analysis of the samples to determine the phase composition before and after TEPT was carried out on an Expert Pro unit. Surface analysis was carried out from 10° to 90° with a delay of 0.02 s, in 2θ mode.

To determine the hardness of the cross-section of the samples, a METOLAB 502 microhardness tester was used, equipped with a tetrahedral Vickers diamond pyramid with a square base and an angle of $\alpha = 136^\circ$ between the opposite faces at the apex in strict compliance with the requirements of GOST 9450-76, imposed on the Vickers method. The diamond indenter under a load of $F = 1$ N was pressed perpendicularly and maintained under load for 10 s.

Tribological tests were carried out on a TRB3 tribometer. At a load of 6 N over a distance of 60 m using the ball-on-disk method and a speed of 2 cm/s. The radius of the trace was 3 mm ($D = 6$ mm). A ball with a diameter of 6 mm made of 100Cr6 (analogous to ShKh15) was used as a counterbody.

Corrosion resistance tests were carried out in a HUD-E808 salt fog chamber according to GOST 34388-2023. The neutral salt medium was 5 % sodium chloride (NaCl). The study was conducted at a temperature of 35 °C for 8 hours. Although the actual working conditions of 12Kh1MF steel in steam pipelines typically involve temperatures of 400–550 °C in a water vapor medium, such laboratory conditions are commonly used for accelerated corrosion testing. These parameters allow the simulation of long-term surface degradation processes under controlled and reproducible conditions, providing a comparative evaluation of corrosion resistance before and after surface treatment.

Quantitative assessment of corrosion was carried out according to GOST 9.908-85. The mass loss per unit surface area Δm , g/m², was calculated using formula (1):

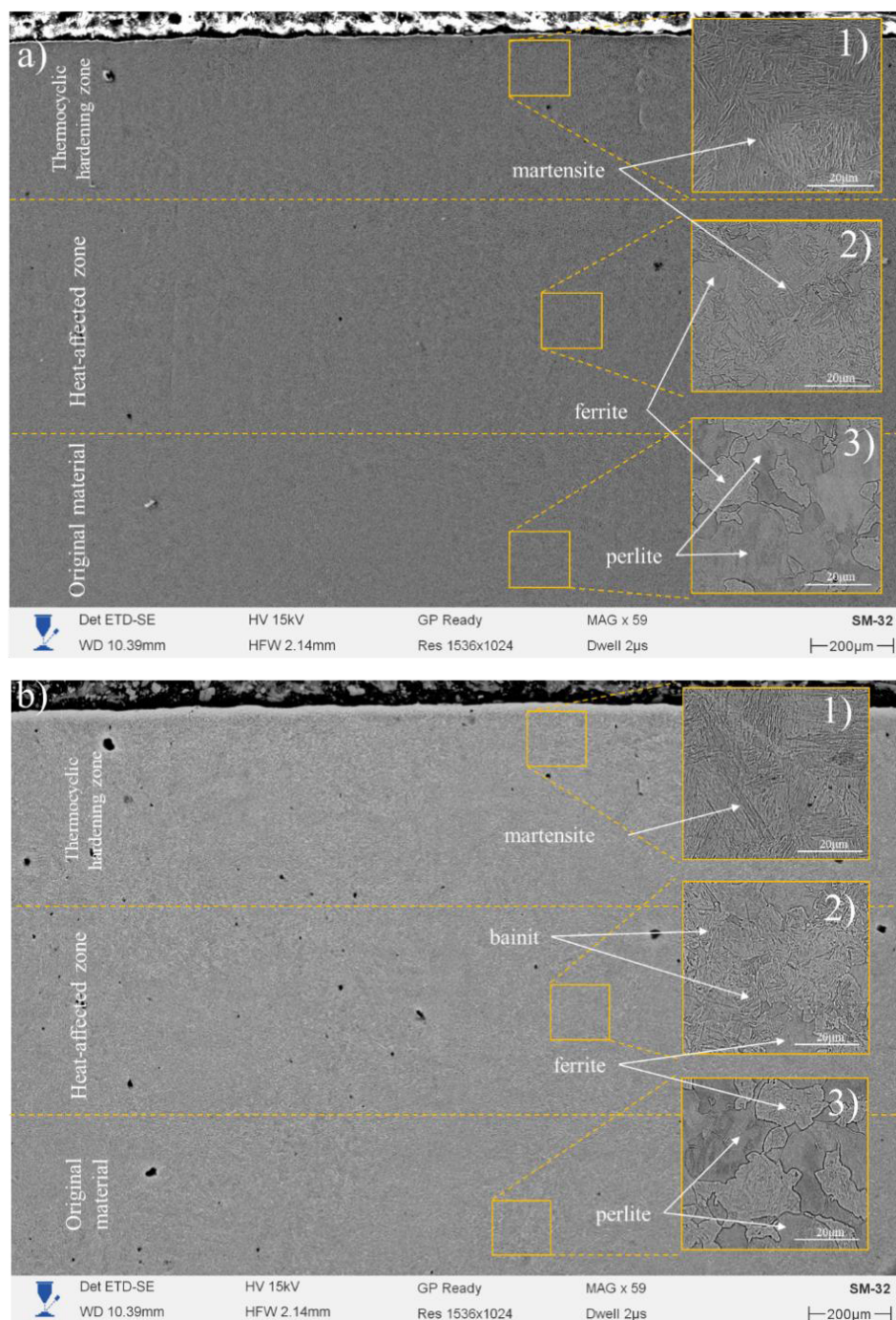
$$\Delta m = \frac{m_0 - m_1}{S}, \quad (1)$$

where m_0 is the mass of the sample before testing, g; m_1 is the mass of the sample after testing and removal of corrosion products, g; S is the surface area of the sample, m².

Results and discussion

Figure 3 shows the SEM results of the microstructure of the cross section of 12Kh1MF steel after treatment in an electrolyte containing an aqueous solution of 10 % Na_2CO_3 in three different cycles (No. 1, No. 2, No. 3), which allows us to draw conclusions about the influence of thermal conditions on the formation of the structure and tribomechanical properties of materials. In the initial state, 12Kh1MF steel has a ferrite-pearlite structure. After TEPT in different cycles, the structure of 12Kh1MF steel mainly consists of the martensite phase, which is associated with rapid cooling, which leads to an increase in microhardness and an improvement in tribocorrosion properties (Table 2, 3).

After TEPT under different conditions, zonal structures are formed in 12Kh1MF steel, which differ in microstructure and hardness, and are distinguished as the zone of thermocycling quenching, the heat-affected zone and the original material (Fig. 3).



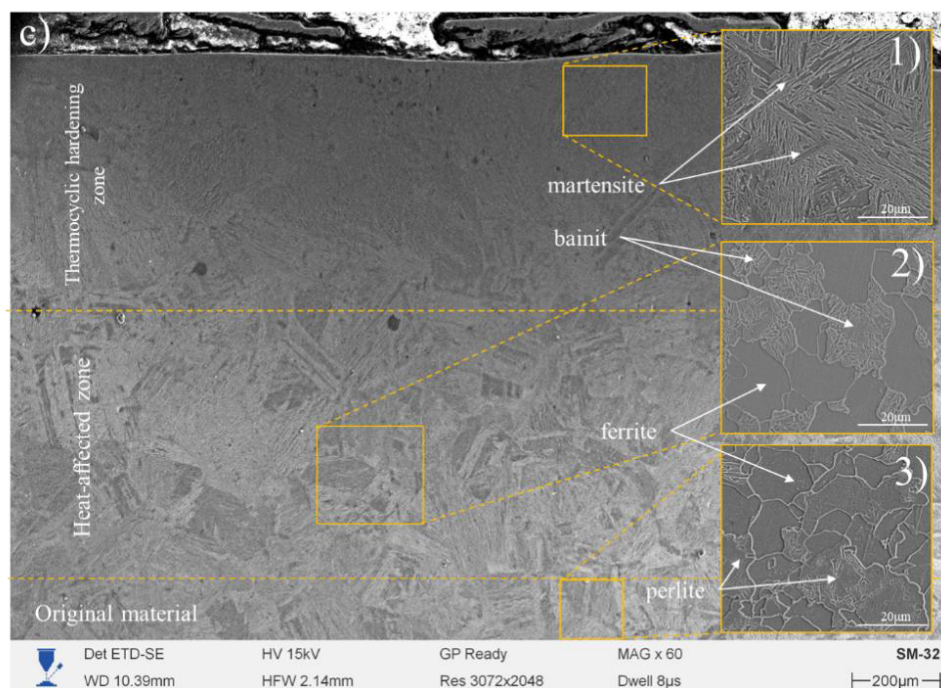


Figure 3. SEM image of the cross-section of 12Kh1MF steel after TEPT in cycles No. 1 (a), No. 2 (b) and No. 3 (c): 1) thermocyclic hardening zone; 2) heat-affected zone; 3) original material

As shown in Figure 3a, the microstructure of 12Kh1MF steel obtained after TEPT in cycle No. 1 is obvious that the zone of thermocycling quenching is characterized by the presence of a martensite microstructure with a thickness of $\sim 400\ \mu\text{m}$ (Fig. 3, a, 1), while the heat-affected zone demonstrates the transition from martensite to the original state (ferrite-pearlite) (Fig. 3, a, 2, 3). In cycle No. 2, a zone with a thickness of $\sim 500\ \mu\text{m}$ is also visible (Fig. 3, b, 1). The formation of martensite is a consequence of rapid cooling. In the zone of thermocycling quenching, the martensite structure predominates, and in the heat-affected zone, bainite and ferrite (Fig. 3, b, 2, 3). In cycle No. 3, the martensite microstructure with a thickness of $\sim 600\ \mu\text{m}$ in the zone of thermocycling quenching transforms into bainite, thereby entering the heat-affected zone with a thickness of $\sim 600\ \mu\text{m}$ (Fig. 3, c, 1, 2, 3). Thus, the zone of thermocycling quenching under different cyclic conditions has a thickness of up to $600\ \mu\text{m}$ with a martensitic structure that contributes to the improvement of the surface microhardness of the material.

Table 3 shows the results of measuring the surface microhardness of steel samples before and after TEPT. According to the results, it was found that after TEPT, the microhardness increased by ~ 1.5 times, which is associated with the formation of a martensitic structure.

Table 3

Results of corrosion tests of samples before and after TEPT

Sample	Phasecomposition	Microhardness, $\text{HV}_{0.1}$	TRB ³		Corrosionrate, mm/year
			μ	Wear intensity, $\text{mm}^3/\text{N} \times \text{m}$	
Initial	αFe	205 ± 30	0.627	0.0004706	0.0024
Cycle No.1	$\alpha'\text{Fe}, \text{Fe}_3\text{C}$	345 ± 30	0.617	0.0004391	0.0016
Cycle No.2	$\alpha'\text{Fe}, \text{Fe}_3\text{C}$	365 ± 34	0.596	0.0003047	0.0013
Cycle No.3	$\alpha'\text{Fe}, \text{Fe}_3\text{C}$	373 ± 31	0.613	0.0002672	0.0019

In order to identify changes in the structural and phase state, X-ray phase analysis of the surface of 12Kh1MF steel samples was carried out before and after TEPT under different conditions (Fig. 4). According to the presented results of X-ray phase analysis, it was found that in the initial state, the steel has a ferrite-pearlite structure (αFe phase) (Fig. 4), and after TEPT, the formation of a martensite phase ($\alpha'\text{Fe}$) with a strengthening cementite phase (Fe_3C) is observed in all samples, which is consistent with the results of SEM analysis.

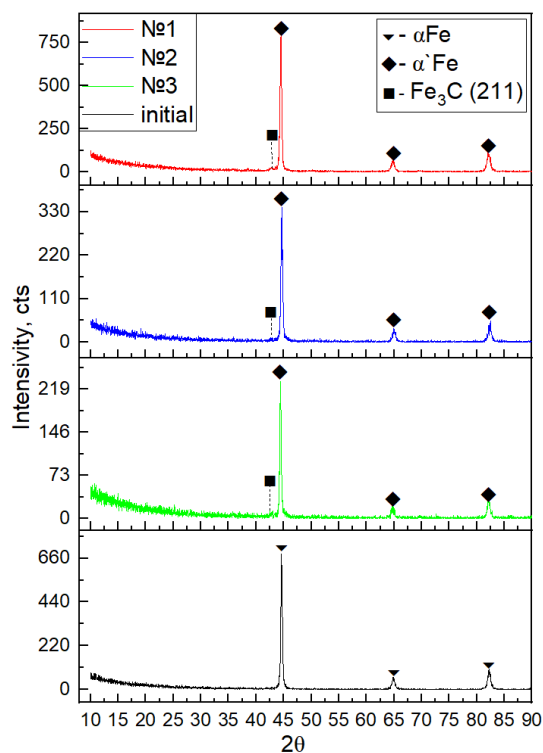


Figure 4. Results of X-ray phase analysis of steel before and after TEPT in different cycles

Figure 5 shows the results of tribological tests of steel samples before and after TEPT, according to which it was revealed that, compared to the initial state with a value of 0.627, the friction coefficient decreased by an average of 10 %, and the wear resistance of 12Kh1MF steels increased by ~1.5–2 times (Table 3).

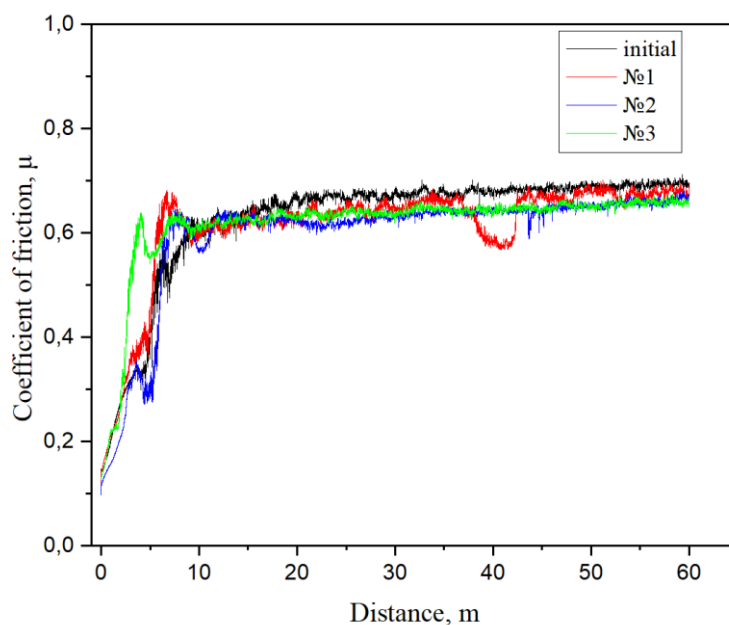


Figure 5. Tribology results before and after TEPT

The results of corrosion tests of steel before and after treatment are presented in Table 2. According to the analysis of the mass loss of samples using formula (1), it was found that after testing, the corrosion resistance improved by 10–30 % compared to the original sample. A reduction in mass loss is observed in cy-

cle № 2 when compared to cycles № 1 and № 3. It is evident that the more moderate regime of cycle № 2, in comparison to cycle № 3, serves to reduce the likelihood of residual stresses that have the potential to accelerate localised corrosion.

Thus, the results of the studies show that the concentration of the electrolyte and the selected heating cycles have a significant effect on the properties and structure of steels. The results of the studies and their analysis are correlated in Table 3.

It has been established that the electrolyte concentration (10 % Na₂CO₃) in combination with optimal heating cycles (e.g. No. 2 and No. 3) contributes to an increase in microhardness and improvement of tribo-corrosion properties due to stable energy density and controlled heating during TEPT.

Conclusion

On the basis of the obtained results the following deductions and conclusions were made:

– the microstructure of the cross section of steel 12Kh1MF after TEPT has a zonal structure, it was found that in the electrolyte containing 10 % Na₂CO₃ + 90 % distilled water, is formed thermocyclic hardened layer with a thickness of up to 600 microns, which varies depending on the cycle, structurally consisting of the main phases of martensite (α' Fe) and cementite (Fe₃C), the formation of which contributes to an increase in microhardness in ~1.5 times.

– According to the results of tribo-corrosion tests of samples before and after TEPT it was revealed that wear resistance of the samples was increased by ~10 % on average, and corrosion resistance improved by 10–30 % compared to the original sample.

On the basis of the obtained results the optimal technological regime of thermocyclic electrolyte-plasma treatment of steel 12Kh1MF was established: electrolyte composition aqueous solution of 10 % sodium carbonate at a temperature of 900 °C, 2-3 cycles of treatment at a voltage of 300 V – 150 V and a current of 30 A – 8 A for 5–60 seconds.

Acknowledgments

This research is funded by the Science Committee of the Ministry of Science and Higher Education of the Republic of Kazakhstan (Grant No. BR24992879).

References

- 1 Шахабов М.М. Эксплуатационные характеристики стальных конструкций длительного срока эксплуатации / М.М. Шахабов, А.Б. Сивенков, Д.А. Корольченко. — Вестник МГСУ. — 2023. — Т. 18. — Вып. № 6. — С. 864–879. — DOI: <http://dx.doi.org/10.22227/1997-0935.2023.6.864-879>.
- 2 Захарова І. Вплив процесів термообробки на характеристики зварних з'єднань у виробництві труб за для важливих середовищ / І. Захарова, Д. Студенікін // Наука та виробництво. — 2024. — Vol. 28. — P. 79–85.
- 3 Goyal N. An analysis of effect of machining parameters on non-conducting materials using electro chemical discharge machining / N. Goyal // Materials Today: Proceedings. — 2020. — Vol. 37. — DOI: <http://dx.doi.org/10.1016/j.matpr.2020.09.596>.
- 4 Юриков Ю.В. Повышение эффективности электроэрозионного восстановления шеек валов. Автореф. дис. ... канд. техн. наук. — / Ю.В. Юриков. — Воронеж, 2000.
- 5 Такунцов К.В. Электроэрозионно-электрохимическая обработка: современное состояние, проблемы, перспективы / К.В. Такунцов, А.Н. Зайцев // Перспективные технологии физико-химической размерной обработки и формирования эксплуатационных свойств металлов и сплавов. — Уфа, 2001. — С. 9–13.
- 6 Koch O. Recent progress in micro-electro discharge machining. Part 1: Technology / O. Koch, W. Ehrfeld, F. Michel // Proc. Intern. Symp. Electrical machining. — Bilbao, Spain, 2001. — P. 117–127.
- 7 Fujino M. Development of Multi-Purpose Microprocessing Machine / M. Fujino, N. Okamoto, T. Masuzawa // Proc. Intern. Symp. Electrical Machining. — Lausanne, Switzerland, 1995. — P. 613–620.
- 8 Сайфуллин Р.Н. Влияние режимов электроискровой обработки на износостойкость закалённых лезвий ножей / Р.Н. Сайфуллин, Р.Ф. Арбузов, А.Л. Бирюков // Технический сервис машин. — 2023. — Т. 3, № 61. — С. 87–93. — DOI: <http://dx.doi.org/10.22314/2618-8287-2023-61-3-87-93>.
- 9 Baizhan D. Investigation of Changes in the Structural-Phase State and the Efficiency of Hardening of 30CrMnSiA Steel by the Method of Electrolytic Plasma Thermocyclic Surface Treatment / D. Baizhan, B. Rakhadilov, L. Zhurerova, Y. Tyurin, Zh. Sagdoldina, M. Adilkanova, R. Kozhanova // Coatings. — 2022. — Vol. 12. — P. 1696. — DOI: <http://dx.doi.org/10.3390/coatings12111696>.
- 10 Garba E. A Review of Electrode Manufacturing Methods for Electrical Discharge Machining: Current Status and Future Perspectives for Surface Alloying / E. Garba, A.M. Abdul-Rani, N.A. Yunus, A.A. Aliyu, I.A. Gul, M. Al-Amin, R. Aliyu // Machines. — 2023. — Vol. 11. — P. 906. — DOI: <http://dx.doi.org/10.3390/machines11090906>.

11 Korzhyk V. Surface modification of metal products by electrolyte plasma: monograph / V. Korzhyk, Yu. Tyurin, O. Kolisnichenko. — Kharkiv: PC TECHNOLOGY CENTER, 2021. — P. 180.

12 Berladir K. Strengthening of the NKV Type Centrifugal Pump's Shaft by Chemical-Thermocycling Treatment. In Advanced Manufacturing Processes; Tonkonogyi, V., Ivanov, V., Trojanowska, J., Eds. / K. Berladir, T. Hovorun, O. Gusak // Springer: Cham, Switzerland. — 2021. — P. 525–535. — DOI: http://dx.doi.org/10.1007/978-3-030-77719-7_52.

13 Sulyubayeva L.G. Influence of Thermocyclic Electrolyte-Plasma Treatment on Mechanical Properties of U9 Tool Steel / L.G. Sulyubayeva, D.B. Buitkenov, D.R. Baizhan, N.E. Berdimuratov, N.S. Raisov, A.Zh. Zhumabekov // Bulletin of the University of Karaganda–Physics. — 2024. — Vol. 107. — P. 77–88. — DOI: <https://doi.org/10.31489/2025ph1/77-88>.

14 Попова Н.А. Фазовые превращения в сталях 30ХГС под действием электролитно-плазменной нитроцементации / Н.А. Попова, Л.Г. Журикова, Е.Л. Никоненко, М.К. Скаков // Вестник Томского государственного университета. — 2016. — № 1. — С. 60–70.

Л.Г. Сулюбаева, Д.Р. Байжан, С.Д. Болатов, Н.Е. Бердімуратов, Н.Е. Базаров

Термоциклдік электролитті-плазмалық өңдеу технологиялық режимдерінің 12Х1МФ болатының құрылымдық-фазалық күйіне және трибокоррозиялық қасиеттеріне әсерін зерттеу

Жұмыста 12Х1МФ маркалы ыстыққа төзімді болаттың құрылымдық-фазалық күйіне, микроқаттылығына және трибокоррозиялық қасиеттеріне термоциклдік электролиттік-плазмалық өңдеудің әсері жан-жақты зерттелді. Өңдеу 300/150 В кернеуде натрий карбонатының (Na_2CO_3) 10 % сулы ерітіндісінде жүргізілді. Нәтижесінде қалыңдығы 600 мкм-ге дейін жететін мартенситтік құрылымды зоналық микроқұрылым қалыптасты. Микроқұрылым ұшы мынадай аймақтарға бөлінді: термиялық циклді катаяту, жылу әсер ететін аймақ және бастапқы материал. Мартенситтік құрылымның түзілуіне байланысты болаттың микроқаттылық қабілеті бастапқы материалмен салыстырғанда 1,5 есе өсті. Рентгендік фазалық талдау αFe және Fe_3C фазаларының түзілуін анықтады. Трибологиялық сынақтар үйкеліс коэффициентінің 10% төмендегенін және тозуға төзімділігінің 1,5-2 есе артқанын көрсетті. Тұзды тұман камерасындағы коррозиялық сынақтар материалдың қорғаныс қасиеттерінің жақсарғанын көрсетті: масса жоғалту азайды және өңдеу режиміне байланысты коррозияға төзімділік 10–30 %-ға артты. Жүргізілген талдау нәтижесінде әдістің 12Х1МФ конструкциялық болатының беріктік пен коррозияға төзімділіктің оңтайлы теңгерімін қамтамасыз ететін ең тиімді термоциклдік өңдеу режимі анықталды. Алынған нәтижелер термоциклдік электролиттік-плазмалық өңдеудің агрессивті ортада жұмыс істейтін болат бөлшектерінің беткі қасиеттерін жақсартуда тиімді әдіс екенін дәлелдейді.

Кілт сөздер: электролиттік-плазмалық өңдеу, ыстыққа төзімді құрылымдық болат, термоциклдік электролиттік-плазмалық өңдеу, микроқаттылық, төмен қоспаланған болат, микроқұрылым, бетті беріктендіру, коррозияға сынау

Л.Г. Сулюбаева, Д.Р. Байжан, С.Д. Болатов, Н.Е. Бердімуратов, Н.Е. Базаров

Исследование влияния технологических режимов термоциклической электролитно-плазменной обработки на структурно-фазовое состояние и трибокоррозионные свойства стали 12Х1МФ

В данной работе всесторонне исследовано влияние термоциклической электролитно-плазменной обработки на структурно-фазовое состояние, микротвердость и трибокоррозионные свойства жаропрочной стали марки 12Х1МФ. Обработку проводили в 10 % водном растворе карбоната натрия (Na_2CO_3) при напряжении 300/150 В. В результате образовалась зональная мартенситная микроструктура толщиной до 600 мкм. Микроструктура была разделена на зоны наконечника: разделена на зону термоциклического упрочнения, зону термического воздействия и исходный материал. За счет образования мартенситной структуры микротвердость стали увеличилась в 1,5 раза по сравнению с исходным материалом. Рентгенофазный анализ выявил образование фаз αFe и Fe_3C . Трибологические испытания показали снижение коэффициента трения на 10 % и увеличение износостойкости в 1,5–2 раза. Коррозионные испытания в камере солевого тумана показали улучшение защитных свойств материала: уменьшение потери массы и повышение коррозионной стойкости на 10–30 % в зависимости от режима обработки. В результате проведенного анализа был определен наиболее эффективный режим термоциклической обработки конструкционной стали 12Х1МФ, обеспечивающий оптимальный баланс прочности и коррозионной стойкости. Полученные результаты доказывают, что термоциклическая электролитно-плазменная обработка является эффективным методом улучшения поверхностных свойств стальных деталей, работающих в агрессивных средах.

Ключевые слова: электролитно-плазменная обработка, жаропрочная конструкционная сталь, термоциклическая электролитно-плазменная обработка, микротвёрдость, низколегированная сталь, микроструктура, упрочнение поверхности, коррозионные испытания

References

- 1 Shakhabov, M.M., Sivenkov, A.B., & Korolchenko, D.A. (2023). Eksploatatsionnye kharakteristiki stalnykh konstrukttsii dlitel'nogo sroka eksploatatsii [Operational characteristics of steel structures of long term service life]. *Vestnik Moskovskogo gosudarstvennogo stroitel'nogo universiteta — Bulletin of the Moscow State University of Civil Engineering*, 18(6), 864–879 [in Russian].
- 2 Захарова І. Студенікін Д. (2024). Вплив процесів термообробки на характеристики зварних з'єднань у виробництві труб за для важливих середовищ [Influence of heat treatment processes on the characteristics of welded joints in the production of pipes for Important Media]. *Наука та виробництво — Science and production*, 28, 79–85 [in Ukrainian].
- 3 Goyal N. (2020). An analysis of effect of machining parameters on non-conducting materials using electrochemical discharge machining. *Materials Today: Proceedings*, 37.
- 4 Yurikov Yu.V. (2000). Povyshenie effektivnosti elektroerozionnogo vosstanovleniia sheek valov [Improving the efficiency of electrical discharge restoration of shaft]. *Candidate's thesis*. Voronezh [in Russian].
- 5 Takuntsov K.V., & Zaitsev A.N. (2001). Elektroerozionno-elektrokhimicheskaia obrabotka: sovremennoe sostoianie, problemy, perspektivy [Electrical discharge-electrochemical machining: current state, problems, prospects]. *Perspektivnye tekhnologii fiziko-khimicheskoi razmernoi obrabotki i formirovaniia eksploatatsionnykh svoistv metallov i splavov — Advanced technologies of physicochemical dimensional machining and formation of operational properties of metals and alloys*, 9–13. Ufa [in Russian].
- 6 Koch O., Ehrfeld W., & Michel F. (2001). Recent progress in micro-electro discharge machining. Part 1: Technology. *Proc. Intern. Symp. Electrical machining*, 117–127. Bilbao, Spain.
- 7 Fujino M., Okamoto N., & Masuzawa T. (1995). Development of Multi-Purpose Microprocessing Machine. *Proc. Intern. Symp. Electrical Machining*, 613–620. Lausanne, Switzerland.
- 8 Sayfullin R.N., Arbuzov R.F., & Biryukov A.L. (2023). Vlianie rezhimov elektroiskrovoi obrabotki na iznosostoikost zakalennykh lezviy nozhei [Influence of electric spark treatment modes on the wear resistance of hardened knife blades]. *Tekhnicheskii servis mashin — Technical Service of Machines*, 3(61), 87–93 [in Russian].
- 9 Baizhan D., Rakhadilov B., Zhurero L., Tyurin Y., Sagdoldina Zh., Adilkanova M., & Kozhanova R. (2022). Investigation of Changes in the Structural-Phase State and the Efficiency of Hardening of 30CrMnSiA Steel by the Method of Electrolytic Plasma Thermocyclic Surface Treatment. *Coatings*, 12, 1696.
- 10 Garba E., Abdul-Rani A.M., Yunus N.A., Aliyu A.A., Gul I.A., Al-Amin M., & Aliyu R. (2023). A Review of Electrode Manufacturing Methods for Electrical Discharge Machining: Current Status and Future Perspectives for Surface Alloying. *Machines*, 11, 906.
- 11 Korzhyk V., Tyurin Yu., & Kolisnichenko O. (2021). Surface modification of metal products by electrolyte plasma: monograph. *Kharkiv: PC TECHNOLOGY CENTER*, 180.
- 12 Berladir, K., Hovorun, T., & Gusak, O. (2021). Strengthening of the NKV Type Centrifugal Pump's Shaft by Chemical-Thermocycling Treatment. In *Advanced Manufacturing Processes*; Tonkonogiy, V., Ivanov, V., Trojanowska, J. (Eds.). *Springer: Cham, Switzerland*, 525–535.
- 13 Sulyubayeva L.G., Buitkenov D.B., Baizhan D.R., Berdimuratov N.Ye., Raisov N.S., & Zhumabekov A.Zh. (2024). Influence of Thermocyclic Electrolyte-Plasma Treatment on Mechanical Properties of U9 Tool Steel. *Bulletin of the University of Karaganda—Physics*, 107, 77–88.
- 14 Popova N.A., Zhurero L.G., Nikonenko E.L., & Skakov M.K. (2016). Phase transformations in 30KhGS steel under the action of electrolyte-plasma nitrocarburizing. *Bulletin of Tomsk State University*, 1, 60–70 [in Russian].

Information about the authors

Sulyubayeva, Laila — PhD, Associate professor, Senior Researcher of Research Center “Surface Engineering and Tribology”, S. Amanzholov East Kazakhstan University, Ust-Kamenogorsk, Kazakhstan; e-mail: lsulyubayeva@gmail.com; ORCID ID: <https://orcid.org/0000-0002-1924-1459>;

Baizhan, Daryn — Senior Researcher of Research Center “Surface Engineering and Tribology”, S. Amanzholov East Kazakhstan University, Ust-Kamenogorsk, Kazakhstan; e-mail: daryn.baizhan1@gmail.com, ORCID ID: <https://orcid.org/0000-0002-9105-3129>;

Bolatov, Sanzhar (contact person) — Young Researcher of Research Center “Surface Engineering and Tribology”, S. Amanzholov East Kazakhstan University, Ust-Kamenogorsk, Kazakhstan; e-mail: sanzharbolatov94@gmail.com, ORCID ID: <https://orcid.org/0009-0003-3136-0535>;

Berdimuratov, Nurbol — Leading researcher of Research Center “Surface engineering and tribology”, Sarsen Amanzholov East Kazakhstan University, Ust-Kamenogorsk, Kazakhstan; e-mail: nurbol.ber@gmail.com; ORCID ID: <https://orcid.org/0009-0000-6880-6439>;

Bazarov, Nuraly — Researcher LLP “PlasmaScience”, Ust-Kamenogorsk, Kazakhstan; e-mail: bazarov.nuraly@gmail.com, ORCID ID: <https://orcid.org/0009-0001-9182-7016>.

S.N. Hosseinimotlagh¹, M.A. Zarei², A. Shakeri¹✉¹Department of Physics, Shi. C., Islamic Azad University, Shiraz, Iran;²Department of Physics, Payame Noor University, Tehran, Iran

Control Method of Plasma Burning in Tokamak Fusion Reactor with Neutron-Free $p^{11}B$ Fuel via Alpha-Proton-Alpha Avalanche Reaction Mechanism

This article deals with the problems of neutronic fuels. The characteristic features of plasma burning control in tokamak fusion reactor with neutron-free $p^{11}B$ fuel via alpha-proton-alpha avalanche reaction are analyzed. On the basis of the study the author suggests, a model with no dimensions for plasma ignition, where equations for particle and energy equilibrium are utilized. In this framework $p^{11}B$ fuel are considered. In fact, this work presents a novel method to control the burning plasma such that we can control the system variations, the rate of fueling and supplementary power. Applying the simulation equations and we calculate quality factor for $p^{11}B$ fuel. The neutronic fuels come with two main drawbacks: (i) they generate neutrons that necessitate protection and can harm and activate the reactor's structure, (ii) the production of tritium involves added complexity, expense, and the need for radial space for a lithium blanket. It has been demonstrated that the neutron-free $p^{11}B$ reaction is often regarded as a potential remedy for these issues.

Keywords: plasma, fusion, dynamics, neutron-free, energy, control, avalanche, alpha, proton, fuel

✉Corresponding author: Abuzar Shakeri, Abuzar.Shakeri@gmail.com

Introduction

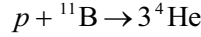
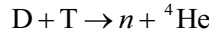
Managing plasma density and temperature within fusion reactors constitutes one of the key challenges in advancing this technology. The source of instability arises from the fact that, with lower temperatures, fusion heating enhances as plasma temperature rises. To maintain stability at such operational levels in fusion reactors, a dynamic control system will be crucial. Throughout the years, various techniques for managing the burn conditions have been explored. Among these studies, three specific forms of actuation have been identified: (i) deliberate impurities injection, (ii) fueling rate adjustment, and (iii) power of supplementary [1–3]. Control systems that rely on altering the supplementary power function necessitate functioning at sub-ignition levels where the supplementary power is active [4–6]. When the plasma temperature increases due to a positive initial temperature fluctuation, the control system decreases the supplementary power output. Conversely, managing negative initial temperature fluctuations is less complex, primarily depending on having sufficient heating capacity. Control systems that adjust the fueling rates enable functioning at ignition levels where supplementary power remains inactive [7–11].

Despite their capability to manage disruptions in starting conditions that result in thermal excursions, they struggle with disturbances in starting conditions that cause quenching. Intentionally introducing impurities can effectively amplify radiation losses within the plasma, serving to avert thermal excursions. When faced with significant positive shifts in the initial temperature, this strategy necessitates a substantial quantity of impurities. Consequently, once the thermal excursion is regulated, extra supplementary power must be supplied, which leads to a decrease in Q , to counteract the radiation losses brought about by the impurities until they are entirely eliminated from the reactor. Previous studies have studied the control of plasma burning in a tokamak fusion reactor with D^3He and DT fuel. However, the innovative design of this work is that we study the method of controlling the burning of neutron-free $p^{11}B$ plasma through the alpha-proton-alpha avalanche reaction mechanism.

The main objective of the article is checking the burning plasma stability conditions in fusion reactor for $p^{11}B$ fuel. Therefore, the paper is organized as follows. In Section.2 fuel selection consideration is introduced. Section.3, indicates a zero-dimensional burning plasma model. Section.4, indicates the control meth-

ods. In section.5, we discuss on the simulation parameters and results, for selected fuels ($p^{11}\text{B}$). Section.6, summarizes the conclusions.

Two different fuel combinations, DT and $p^{11}\text{B}$, are viewed as the most promising options for achieving functional fusion reactors in the near future.



Although DT is the most common fuel used for fusion reactor but $p^{11}\text{B}$ fuel is considered in this work due to the advantages of reduced radioactivity, reduced radiation damage, increased safety and efficiency, lower cost of electricity and potentially shorter path to commercialization $p^{11}\text{B}$ fuel.

Managed fusion with sophisticated fuels, especially hydrogen-boron-11, stands out as an incredibly promising energy source. This hydrogen-boron fuel mainly generates energy as charged particles rather than neutrons, which greatly lowers or could even eradicate induced radioactivity. The principal reaction, $p + {}^{11}\text{B} \rightarrow 3 {}^4\text{He}$, results solely in charged particles. In addition, a secondary reaction, ${}^4\text{He} + {}^{11}\text{B} \rightarrow {}^{14}\text{N} + n$, generates neutrons as the alpha particles created by the principal reaction decelerate within the plasma; however, these neutrons account for just about 0.2 % of the overall fusion energy, with an average energy of only 2.5 MeV.

Zero-dimensional burning plasma model using alpha-proton-alpha avalanche reaction mechanism

As illustrated in Figure 1, the processes involved in the $p^{11}\text{B}$ avalanche reaction that generates a surge of alpha particles include: [19] (i): an alpha particle produced from the fusion of $p^{11}\text{B}$ strikes a proton that is stationary in the laboratory setting. (ii): This alpha particle subsequently collides with a second proton in the surrounding medium, which is also at rest. The resulting energetic proton then engages with one ${}^{11}\text{B}$ atom in the environment, which remains stationary. (iii): This leads to the formation of three additional alpha particles. So that:

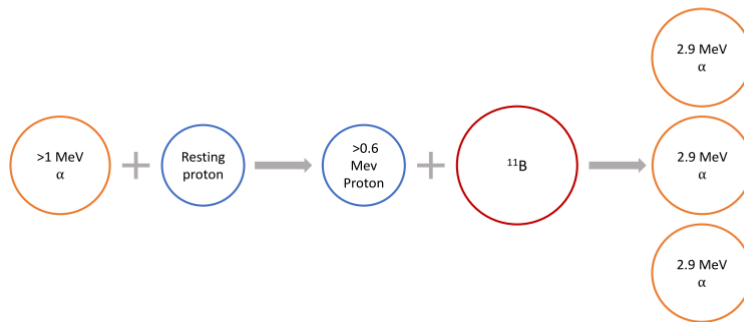
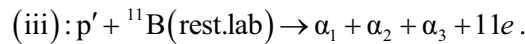
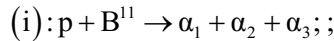


Figure 1. Exploring the mechanism of the α -p- α avalanche reaction. When an α particle strikes a resting proton, this proton gains sufficient energy to engage with ${}^{11}\text{B}$, resulting in the generation of three α particles

These three α particles can once more generate accelerated protons, leading to an avalanche of α particles. The equations that describe the coupled nonlinear point kinetics of the $p^{11}\text{B}$ fusion reaction, taking into account the alpha-proton-alpha avalanche process, can be expressed as follows:

In this work, a model with zero dimensions is utilized for the process of plasma ignition, employing the equations for particle and energy equilibrium [12, 13]. Within this framework, the characteristics of $p^{11}\text{B}$ fuel and its density are evaluated independently, enabling us to identify appropriate isotopic fuels suitable for use as an actuator. The representation of the model can be illustrated through these equations:

$$\frac{dn_\alpha}{dt} = -\frac{n_\alpha}{\tau_\alpha} + 3n_p n_{11\text{B}} \langle \sigma v \rangle \quad (1)$$

$$\frac{dn_p}{dt} = -\frac{n_p}{\tau_p} - n_p n_{11B} \langle \sigma v \rangle + n_p n_\alpha \sigma_{el} v_\alpha + S_p, \quad (2)$$

$$\frac{dn_{11B}}{dt} = -\frac{n_{11B}}{\tau_{11B}} - n_p n_{11B} \langle \sigma v \rangle + S_{11B}, \quad (3)$$

$$\frac{dE}{dt} = -\frac{E}{\tau_E} + Q_\alpha n_p n_{11B} \langle \sigma v \rangle - P_{rad} + P_{aux} + P_{ohmic}, \quad (4)$$

here σ_{el} denotes the elastic cross-section and v_α is the proton-alpha relative velocity before the elastic collision. In the above equations, n_α , n_p , n_{11B} are the alpha, hydrogen, and boron 11 particle densities respectively, and E signifies energy. τ_{11B} , τ_p , τ_α , τ_E are boron 11, hydrogen, alpha, particles along with energy confinement duration, respectively, that are connected by relationships: $\tau_\alpha = k_\alpha \tau_E$, $\tau_p = k_p \tau_E$, $\tau_{11B} = k_{11B} \tau_E$ parameters of which k_α , k_p and k_{11B} are listed in the Table 1. The energy confinement duration scaling referenced in this research focuses on ITER90H-P [14]. The design of the controller does not rely on this scaling, and the scaling applied is:

$$\tau_E = f 0.082 I^{1.02} R^{1.6} B^{0.15} A_i^{0.5} \kappa_x^{-0.19} P^{-0.47}, \quad (5)$$

f is scaling factor and established by evaluating the relationship between the power required for the L-H transition and the overall plasma heating power P . In this work, the system operates continuously in H-mode, and we set f to 0.85 for our simulation purposes. The quantities R , I , κ_x , and B remain fixed and are given in Table 1.

The isotopic number $A_i = 3\gamma + 2(1-\gamma) = \gamma + 2$ ($\gamma = \frac{n_{11B}}{n_p + n_{11B}}$ is boron 11 densities fraction which is equal to 2.5 for the 50:50 $p^{11}B$ mixture). P_{rad} is radiation loss which approximated as:

$$P_{rad} = P_{brem} = A_b Z_{eff}^2 n_e^2 \sqrt{T}. \quad (6)$$

Where $A_{b(p^{11}B)} = 5.35 \times 10^{-37} \frac{Wm^3}{\sqrt{KeV}}$, $Z_{eff} = \sum_i \frac{n_i Z_i^2}{n_e} = \frac{n_p + n_{11B} + 4n_\alpha}{n_e}$ and $n_e = n_p + n_{11B} + 2n_\alpha$ refers to the coefficients associated with bremsstrahlung radiation [15], the effective atomic number, and the density of electrons respectively. Also, Z_i denotes the atomic number of different ions. $\langle \sigma v \rangle$ is known as fusion reactivity which is temperature dependent and calculated by:

$$\begin{aligned} \langle \sigma v \rangle &= C_1 \zeta^{-5/6} \xi^2 \exp\left(-3\zeta^{1/3} \xi\right) + 5.41 \times 10^{-15} T^{-3/2} \times \exp\left(-\frac{148}{T}\right), \\ \zeta &= 1 - \frac{C_2 T + C_4 T^2 + C_6 T^3}{1 + C_3 T + C_5 T^2 + C_7 T^3}, \\ \xi &= C_0 / T^{1/3}. \end{aligned} \quad (7)$$

Where the parameter C_i is found in [16]. S_{11B} and S_p are boron 11 and the hydrogen fueling injection rates as control inputs, and P_{aux} is supplementary heating in the fuel of $p^{11}B$.

Q_α denotes α -particles energy, where $Q_\alpha(p^{11}B) = 2.9 \text{ MeV}$ for $p^{11}B$ fusion reaction [17]. P_{ohmic} (Ohmic power) is given by:

$$P_{ohmic} = \eta j^2 \quad (8)$$

Here:

$$\eta = \ln\left(\frac{T^{3/2}}{\sqrt{\pi} Z_{eff} e^3 \sqrt{n}}\right) \times 1.03 \times 10^{-4} \times T^{-3/2} Z_{eff}, \quad (9)$$

η is referred to as Spitzer resistivity while j denotes the current density of plasma. In the equation (9), T is measured in Kelvin [18]. The temperature, the total power of plasma heating P , and the density plasma are expressed as follows:

$$T = \frac{2}{3} \frac{E}{n} \quad (10)$$

$$P = P_{fusion} - P_{rad} + P_{aux} + P_{ohmic} \quad (11)$$

$$n = 2n_p + 2n_{11B} + 3n_\alpha \quad (12)$$

Where fusion power for $p^{11}B$ fuel is given by:

$$P_{fusion} = Q_\alpha n_p n_{11B} \langle \sigma v \rangle = Q_\alpha \gamma (1 - \gamma) n_{p^{11}B}^2 \langle \sigma v \rangle \quad (13)$$

Such that: $n_{p^{11}B} = n_p + n_{11B}$ is the summation of first and second fuel densities.

Table 1

Parameters of reactor

1)	Plasma volume (m ³)	$V = 1500$
2)	Plasma current (MA)	$I = 24$
3)	Minor radius (m)	$a = 3.8$
4)	Major radius (m)	$R = 14$
5)	Boron 11 (Helium 3) particle confinement constant	$k_{11B} = 2.6$
6)	Hydrogen particle confinement	$k_p = 3.6$
7)	Alpha particle confinement constant	$k_\alpha = 7$
8)	Magnetic field (T)	$B = 3.5$
9)	Elongation at χ (κ_x)	$\kappa_x = 2.2$

The equilibrium numerical values for various densities, \bar{n}_{11B} , \bar{n}_α , \bar{n}_p , energy, \bar{E} , along with the source of fueling terms \bar{S}_{11B} , \bar{S}_p and the auxiliary (supplementary) heating \bar{P}_{aux} , are established by solving a set of nonlinear equations obtained by setting the left side of equations 1–4 to zero. It is important to mention that in these equations, the variables $\bar{\beta} = \frac{knT}{B^2 / 2\mu_0}$, $\bar{\gamma}$, and \bar{T} are selected randomly [19].

$$0 = -\frac{\bar{n}_\alpha}{\bar{\tau}_\alpha} + \bar{n}_p \bar{n}_{11B} \langle \overline{\sigma v} \rangle \quad (14)$$

$$0 = -\frac{\bar{n}_p}{\bar{\tau}_p} - \bar{n}_p \bar{n}_{11B} \langle \overline{\sigma v} \rangle + \bar{S}_p \quad (15)$$

$$0 = -\frac{\bar{n}_{11B}}{\bar{\tau}_{11B}} - \bar{n}_p \bar{n}_{11B} \langle \overline{\sigma v} \rangle + \bar{S}_{11B} \quad (16)$$

$$0 = -\frac{\bar{E}}{\bar{\tau}_E} + Q_\alpha \bar{n}_p \bar{n}_{11B} \langle \overline{\sigma v} \rangle - \bar{P}_{rad} + \bar{P}_{aux} + P_{ohmic} \quad (17)$$

For arbitrarily values of $\bar{\beta}$, $\bar{\gamma}$, \bar{T} , equilibrium values \bar{n}_α , \bar{n}_p , \bar{n}_{11B} , \bar{E} , \bar{S}_p , \bar{S}_{11B} , \bar{P}_{aux} calculated from equations 14–17 are shown in Table 2 [20]. Defining the difference from the average values as: $n_{11B} - \bar{n}_{11B}$, $\tilde{n}_\alpha = n_\alpha - \bar{n}_\alpha$, $\tilde{n}_p = n_p - \bar{n}_p$, $\tilde{E} = E - \bar{E}$, therefore, the equations describing the changes can be formulated as:

$$\frac{d\tilde{n}_\alpha}{dt} = -\frac{\tilde{n}_\alpha}{\tau_\alpha} - \frac{\bar{n}_\alpha}{\tau_\alpha} + S_\alpha \quad (18)$$

$$\frac{d\tilde{n}_p}{dt} = -\frac{\tilde{n}_p}{\tau_p} - \frac{\bar{n}_p}{\tau_p} - S_\alpha + S_D \quad (19)$$

$$\frac{d\tilde{n}_{11B}}{dt} = -\frac{\tilde{n}_{11B}}{\tau_{11B}} - \frac{\bar{n}_{11B}}{\tau_{11B}} - S_\alpha + S_{11B} \quad (20)$$

$$\frac{d\tilde{E}}{dt} = -\frac{\tilde{E}}{\tau_E} - \frac{\bar{E}}{\tau_E} + Q_\alpha S_\alpha - P_{rad} + P_{aux} + P_{ohmic} \quad (21)$$

To simplify S_α is written as follows:

$$S_\alpha(E, n_\alpha, n_p, n_{11B}) = n_p n_{11B} \sigma v = \gamma(1-\gamma) n_{p11B}^2 \sigma v \quad (22)$$

Notice that, $\langle \sigma v \rangle$ is a function of $n_{11B}, n_p, n_\alpha, E$. The starting fluctuations $\tilde{n}_{11B}, \tilde{n}_p, \tilde{n}_\alpha, \tilde{E}$ are compelled to become zero, and this research is accomplished through the adjustment of the fuel sources (S_{11B} and S_p) and the supplemental energy (P_{aux}).

Table 2

Equilibrium point

\bar{T}	Temperature	250 keV
$\bar{\beta}$	Plasma Beta	93 %
\bar{n}_p	Density of Hydrogen Density	$1.2 \times 10^{19} \text{ m}^{-3}$
\bar{n}	Total Density	$9.44 \times 10^{19} \text{ m}^{-3}$
\bar{n}_α	Density of Alpha particle Density	$1.53 \times 10^{19} \text{ m}^{-3}$
\bar{S}_p	Hydrogen Fueling Rate	$1.30 \times 10^{17} \text{ m}^{-3} \text{ s}^{-1}$
\bar{S}_{11B}	Boron 11 Fueling Rate	$1.60 \times 10^{17} \text{ m}^{-3} \text{ s}^{-1}$
\bar{P}_{aux}	Supplementary Power	$1.80 \times 10^5 \text{ W / m}^3$
\bar{P}	Net plasma power	$1.59 \times 10^5 \text{ W / m}^3$
\bar{E}	Energy Density	$6.7 \times 10^6 \text{ J / m}^{-3}$
$\bar{\gamma}$	Boron 11 Fraction	0.5

Control methods

The controllers operate at sub-ignition and ignition points. Controllers that rely on the modulation of supplementary power must function at sub-ignition levels, where the supplementary power is not zero. In contrast, when the controllers adjusted by the fueling rate are utilized, they can operate at ignition points where the supplementary power is zero. In the following both cases can be considered. First, to stabilize the energy the following conditions put in equation (21):

$$Q_\alpha S_\alpha - P_{rad} + P_{aux} + P_{ohmic} = \frac{\bar{E}}{\tau_E} \quad (23)$$

The equation (21) is satisfied and written as follows:

$$\frac{d\tilde{E}}{dt} = -\frac{\tilde{E}}{\tau_E} \quad (24)$$

\tilde{E} demonstrates exponential stability as τ_E is greater than zero. Condition (23) is satisfied by adjusting the α -heating component $Q_\alpha S_\alpha$ and the supplementary heating. We can manipulate the α -heating term by

changing the ratio $\gamma = \frac{n_{11B}}{n_p + n_{11B}}$ in the plasma. Stabilization control is performed in according to the following steps:

1) Beginning in equation (23), we set $P_{aux} = 0$, $\gamma = \gamma^*$ and to solve this equation for γ^* :

$$Q_\alpha \gamma^* (1 - \gamma^*) - P_{rad} + P_{ohmic} = \frac{\bar{E}}{\tau_E} \quad (25)$$

$$\gamma^* (1 - \gamma^*) = \frac{\frac{\bar{E}}{\tau_E} + P_{rad} - P_{ohmic}}{Q_\alpha n_{p^{11B}}^2 \langle \sigma v \rangle} = C \quad (26)$$

$$\gamma^* = \frac{1 \pm \sqrt{1 - 4C}}{2} \quad (27)$$

If $C \leq 0.25$, the two resulting solutions for γ^* are real and less than 0.5 and would be acceptable. If $C > 0.25$, there is no real answer and we are moving on to the second step.

2) If $\gamma^* = 0.5$, simply adjusting the γ ratio will not satisfy condition (23), thus requiring changes through heating. To achieve this, the supplementary power is determined as follows:

$$P_{aux} = \frac{\bar{E}}{\tau_E} - n_{p^{11B}}^2 \sigma v Q_\alpha \gamma^* (1 - \gamma^*) - P_{ohmic} + P_{rad} \quad (28)$$

In accordance with the control aims and prior stages, ideal benchmark values for the energy \bar{E} and the fraction of fuel particles γ^* are established.

According to obtained dynamical equations in above, we choose Lyapunov function as follows:

$$V = \frac{k_1^2 \tilde{E}^2 + k_2^2 \hat{\gamma}^2 + \tilde{n}_{p^{11B}}^2}{2} \quad (29)$$

Where $k_1 = 10^{15}$, $k_2 = 10^{20}$ and the derivative of Lyapunov function \dot{V} with simplification is as follows:

$$\begin{aligned} \dot{V} = & -\frac{k_1^2 \tilde{E}^2}{\tau_E} + \frac{k_2^2 \hat{\gamma}}{n_{p^{11B}}} \left[\frac{k_1^2 n_{p^{11B}} \tilde{E} \phi}{k_2^2} - \frac{n_{11B}}{\tau_{11B}} - S_\alpha + S_{11B} - n_{p^{11B}} \dot{\gamma}^* - \gamma \left(-\frac{n_{11B}}{\tau_{11B}} - \frac{n_p}{\tau_p} - 2S_\alpha + S_D + S_{11B} \right) \right] + \\ & + \tilde{n}_{p^{11B}} \left[-\frac{n_{11B}}{\tau_{11B}} - \frac{n_p}{\tau_p} - 2S_\alpha + S_p + S_{11B} \right] \end{aligned} \quad (30)$$

By stabilizing of equation (30):

$$S_p = \frac{n_{11B}}{\tau_{11B}} + \frac{n_p}{\tau_p} + 2S_\alpha - S_{11B} - K_p \tilde{n}_{p^{11B}} \quad (31)$$

Where $K_D > 0$. This selection reduces equation (30) to:

$$\dot{V} = \frac{k_2^2 \hat{\gamma}}{n_{p^{11B}}} \left[\frac{k_1^2 n_{p^{11B}} \tilde{E} \phi}{k_2^2} - \frac{n_{11B}}{\tau_{11B}} - S_\alpha + S_{11B} - n_{p^{11B}} \dot{\gamma}^* + K_p \tilde{n}_{p^{11B}} \gamma \right] - \frac{k_1^2 \tilde{E}^2}{\tau_E} - K_p \tilde{n}_{p^{11B}}^2 \quad (32)$$

Finally, we take:

$$S_{11B} = -\frac{k_1^2 n_{p^{11B}} \tilde{E} \phi}{k_2^2} + \frac{n_{11B}}{\tau_{11B}} + S_\alpha + n_{p^{11B}} \dot{\gamma}^* - K_p \tilde{n}_{p^{11B}} \gamma - K_{11B} \hat{\gamma} \quad (33)$$

$$S_p = \frac{k_1^2 n_{p^{11B}} \tilde{E} \phi}{k_2^2} + \frac{n_p}{\tau_p} + S_\alpha - n_{p^{11B}} \dot{\gamma}^* - K_p \tilde{n}_{p^{11B}} (1 - \gamma) + K_{11B} \hat{\gamma} \quad (34)$$

The results of the calculations are shown in the next section.

Results and Discussion

In the study of nuclear fusion, the Lawson criterion, initially formulated for fusion reactors, serves as a crucial standard for assessing the circumstances required for a fusion reactor to ignite. Achieving this condition means that the energy produced from the fusion reactions can effectively heat the plasma enough to keep its temperature stable despite any losses, all without the need for external energy sources. This criterion can be expressed as follows:

$$n\tau_E \geq \frac{12T(\text{keV})}{Q_\alpha \langle \sigma v \rangle} \quad (35)$$

The results of Lawson criterion calculation for $p^{11}\text{B}$ fuel are shown in Figure 2. As seen in Figure 2, Lawson criterion is true for $p^{11}\text{B}$ fuel.

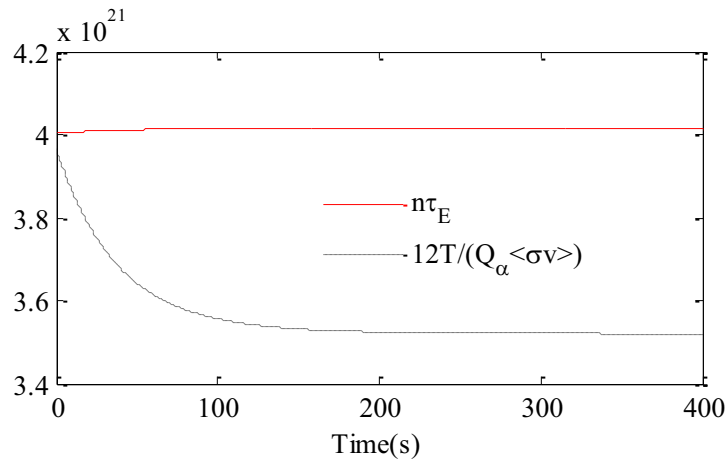


Figure 2. Lawson criterion for $p^{11}\text{B}$ fuel

The simulation in this work is performed for the initial values $E(0)=1.2\bar{E}$, $n_\alpha(0)=1.2\bar{n}_\alpha$, $\gamma(0)=.88\bar{\gamma}$, $n_{p^{11}\text{B}}(0)=.8\bar{n}_{p^{11}\text{B}}$. It has been observed that a controller is capable of adjusting its inputs to achieve the intended result on the system's output. A specific kind of control system, where the output does not affect the input signal's control actions, is known as an open loop system (Fig. 3). This type of system is characterized by the absence of measurement or feedback of the output signal or condition for evaluating against the input signal. Thus, these systems are often labeled as non-feedback systems. Moreover, since an open loop system lacks feedback to verify if the intended output was reached, it operates on the assumption that the input's target was met, as it is unable to rectify any potential errors and cannot adjust for any external influences on the system.



Figure 3. Open loop state

In the simulation of open loop, the system is first fluctuated, while the actuators (S_{n_B} , P_{aux} , S_p) maintain their steady-state values (Table 2) as equations (1–4) are resolved. The results of the simulation indicate that in the absence of active control, a thermal deviation arises, causing the system to stray from the intended equilibrium point. Figure 5 (dotted-black) illustrates the changes in the states over time.

In the open-loop state (Fig. 4), the densities of alpha particles, energy, hydrogen, and boron-11 particles decrease. The behaviors of total particles density, temperature and β for these states (open loop) are shown in Figures 6(d, e, f). A control system that incorporates one or more feedback paths is known as a Closed

Loop System. Closed Loop Control Systems are commonly used in managing processes as well as in electronic control applications. Feedback systems have part of their output signal fed back to the input for comparison with the desired set point condition. The kind of feedback signal may lead to either constructive feedback or detrimental feedback. Within a closed-loop system, a controller is employed to assess the system's output against the target condition and transform any discrepancies into control actions aimed at minimizing the error and restoring the system's output to the intended response. Subsequently, closed-loop control systems utilize feedback to assess the real input to the system and may incorporate multiple feedback loops.

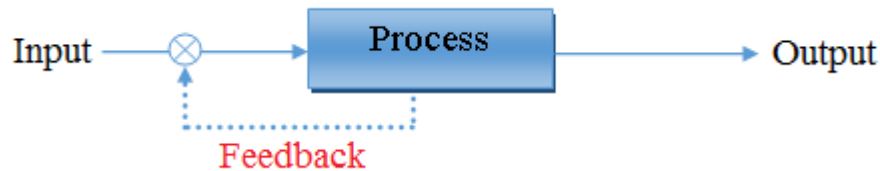
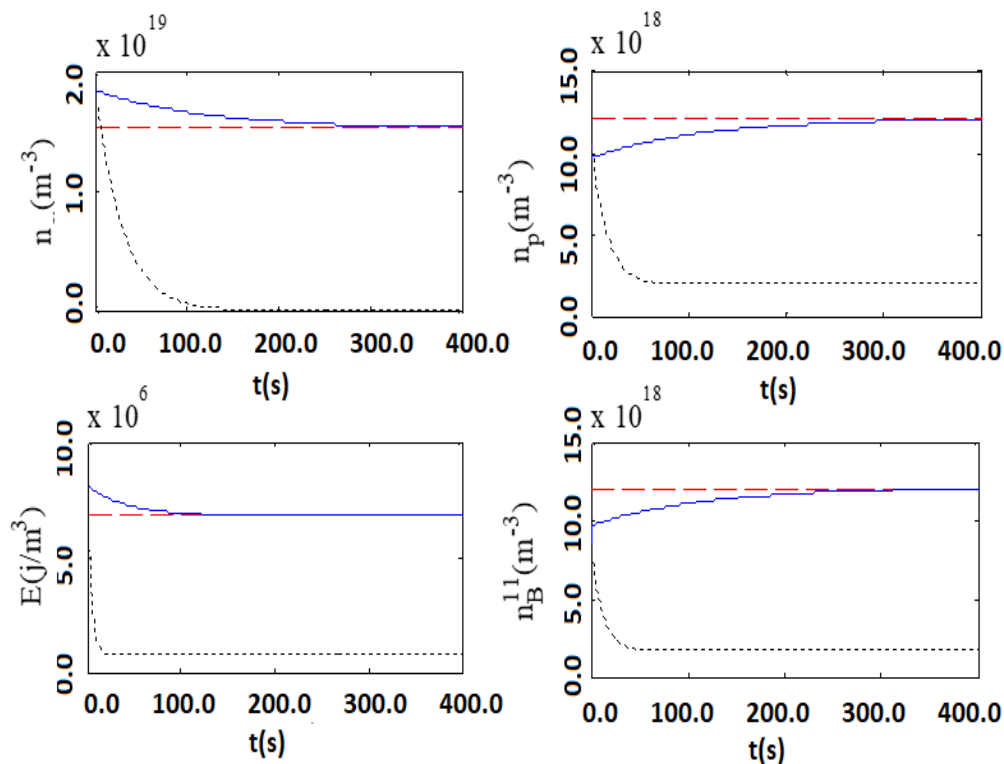


Figure 4. Close loop state

In a simulation of closed loop, the regulator must adjust fuel and thermal levels to achieve the ideal equilibrium of the system. Figure 5 (solid-blue) illustrates the progression of the states regarding densities and energy throughout the simulation, while Figures 6(a, b, c) depict the temporal changes in overall particle density, temperature, and β for the closed loop condition. Following a thermal fluctuation, the progression of densities and energy successfully converges to their target equilibrium levels.

Figure 7 illustrates how the actuator and fuel ratios change over time in a closed-loop state. These Figures demonstrate the variations in supplementary power, fuel injection rates, and fuel fractions over time to manage the system's energy. As shown in Figure 7, in this system supplementary power is nonzero at first and so system is controlled based on modulation of fueling rate and change of supplementary power (sub-ignition point).

Figure 5. Time evolution of $p^{11}\text{B}$ fuel in open loop states (black-dotted), close loop states (blue-solid) and equilibrium value (red-dashed)

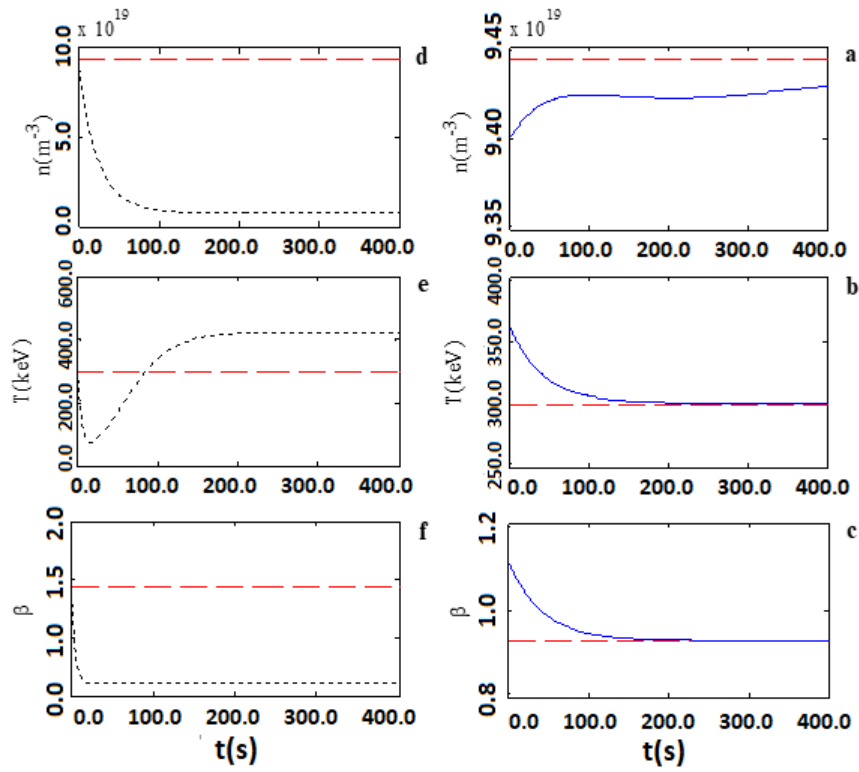


Figure 6. Time Evolution of T , n , β for $p^{11}\text{B}$ fuel, open loop (black-dotted — d, e, f), close loop (blue-solid — a, b, c) and equilibrium values (red-dashed)

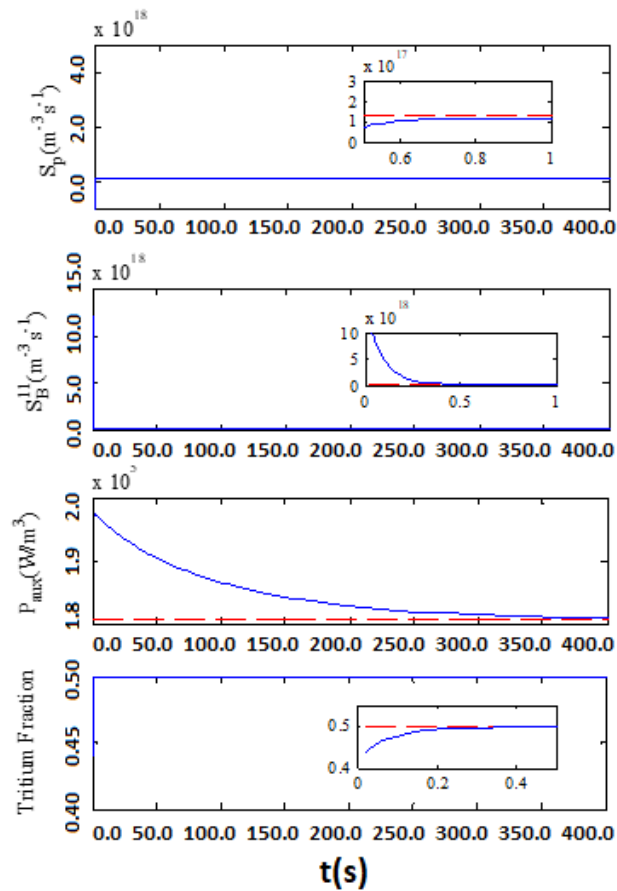


Figure 7. Actuation (blue-solid), equilibrium value (red-dashed) and Boron 11 Fraction for $p^{11}\text{B}$ fuel

Figure 8 shows the time evolutions of the fusion, radiation, ohmic and net plasma heating power which compared with equilibrium values. Fusion and ohmic heating power increases and radiation heating power decreases over time that as a result the net plasma heating power is close to the equilibrium value after time .04 s. The quality factor in fusion reactors is defined as:

$$Q = \frac{P_{fusion}}{P_{auxiliary}} \quad (36)$$

This factor is shown in Figure 9 and as be seen after time 300 s is close to .13.

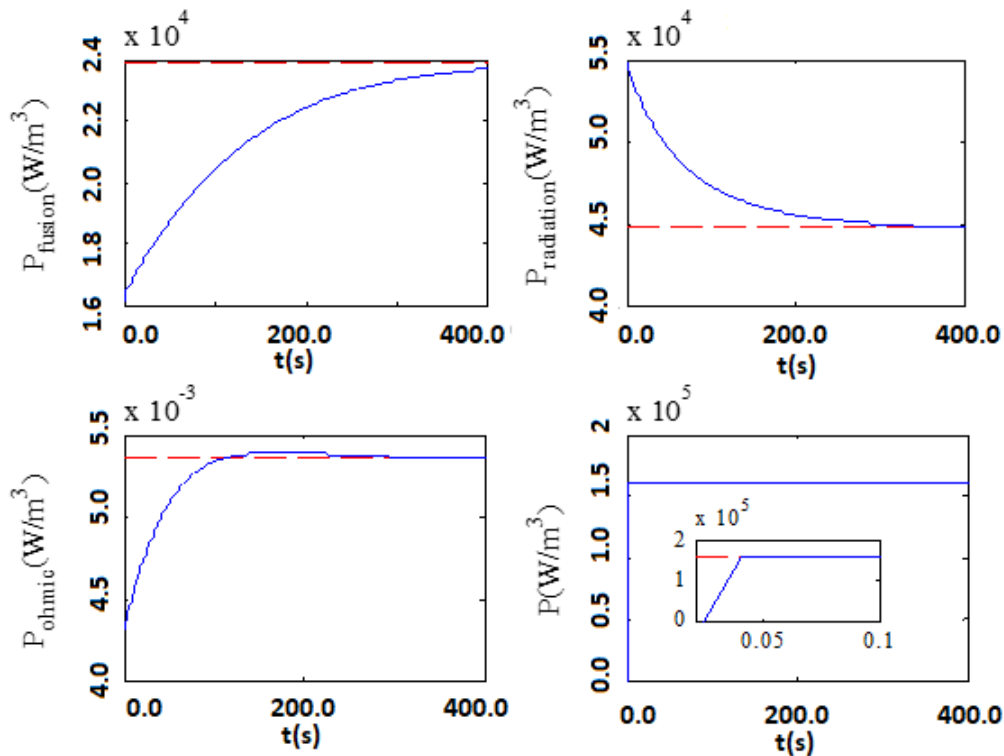


Figure 8. Fusion, radiation, ohmic, and overall Plasma heating power (shown in blue and solid) as opposed to their steady-state values (represented in red and dashed).

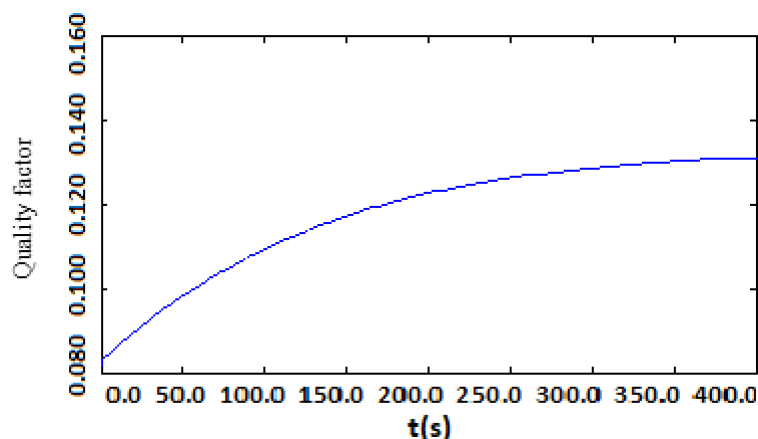


Figure 9. Time evolution of quality factor

Conclusions

In order to burning control, the supplementary power is put to zero initially and by changing the fueling rate and boron 11 fraction, system approaches to control values. Since the supplementary power is zero, system operates in ignition point and when the fueling rate approaches to its equilibrium value and the bo-

ron 11 – hydrogen ratio 50:50 the supplementary power should be added to control the system so this system operates in sub-ignition point and the system (energy and particles density) is controlled. In the case of $p^{11}\text{B}$ fuel the system is controlled by adding the supplementary power and since the supplementary power is non-zero the system operates in sub-ignition point and hydrogen – boron 11 ratio in primary times is equal to 50:50 (Fig. 6) and as a result system (energy and particles density) approaches to its equilibrium values.

Compared to a deuterium-tritium (DT) reactor, the lower neutron flux in a $p^{11}\text{B}$ reactor provides significant advantages in engineering, safety, and environmental impact, including:

1. There is no risk of structural melting during a loss-of-coolant incident.
2. The first wall does not need to be replaced frequently, which results in increased reactor uptime and greatly diminished radiation exposure for workers.
3. There is a significant decrease in tritium emissions and concerns regarding radioactive waste.
4. Tritium breeding is unnecessary, eliminating the need for a large lithium blanket and avoiding issues related to liquid metals.

References

- 1 Anand, H., Coda, S., Felici, F., Galperti, C., & Moret, J.-M. (2017). A novel plasma position and shape controller for advanced configuration development on the TCV tokamak. *Nucl. Fusion*, 57, 126026. DOI: 10.1088/1741-4326/aa7f4d
- 2 Mele, A. et al. (2019). MIMO shape control at the EAST tokamak: simulations and experiments. *Fusion Eng. Des.*, 146, 1282–1285. DOI:10.1016/j.fusengdes.2019.02.058
- 3 Anand, H. et al. (2020). Plasma flux expansion control on the DIII-D tokamak. *Plasma Phys. Control Fusion*, 63, 015006. DOI:10.1088/1361-6587/abc457
- 4 De Tommasi, G. (2019). Plasma magnetic control in tokamak devices, *J. Fusion Energy*, 38, 406–436. DOI: 10.1007/s10894-018-0162-5
- 5 Blum, J., Heumann, H., Nardon, E., & Song, X. (2019). Automating the design of tokamak experiment scenarios. *J. Comput. Phys.*, 394, 594–614. DOI: 10.1016/j.jcp.2019.05.046
- 6 Moret, J.-M. et al. (2015). Tokamak equilibrium reconstruction code LIUQE and its real time implementation. *Fusion Eng. Des.*, 91, 1–15. DOI:10.1016/j.fusengdes.2014.09.019
- 7 Xie, Z., Berse, G., Clary, P., Hurst, J. & van de Panne, M. (2018). Feedback control for Cassie with deep reinforcement learning. In *2018 IEEE/RSJ International Conference on Intelligent Robots and Systems (IROS) IEEE*, 1241–1246. DOI: 10.1109/IROS.2018.8593722
- 8 Jardin, S. (2010). *Computational Methods in Plasma Physics*, CRC Press. DOI: 10.1201/EBK1439810958
- 9 Bellemare, M. G. et al. (2020). Autonomous navigation of stratospheric balloons using reinforcement learning. *Nature*, 588, 77–82. DOI: 10.1038/s41586-020-2939-8
- 10 Humphreys, D. et al. (2020). Advancing fusion with machine learning research needs workshop report. *J. Fusion Energy*, 39, 123–155. DOI: 10.1007/s10894-020-00258-1
- 11 Joung, S. et al. (2019). Deep neural network Grad-Shafranov solver constrained with measured magnetic signals. *Nucl. Fusion*, 60, 16034. DOI: 10.1088/1741-4326/ab555f
- 12 van de Plassche, K. L. et al. (2020). Fast modeling of turbulent transport in fusion plasmas using neural networks. *Phys. Plasmas*, 27, 022310. DOI: 10.1063/1.5134126
- 13 Abbate, J., Conlin, R., & Kolemen, E. (2020). Data-driven profile prediction for DIII-D. *Nucl. Fusion*, 61, 046027. DOI:10.1088/1741-4326/abe08d
- 14 Kates-Harbeck, J., Svyatkovskiy, A., & Tang, W. (2019). Predicting disruptive instabilities in controlled fusion plasmas through deep learning. *Nature*, 568, 526–531. DOI:10.1038/s41586-019-1116-4
- 15 Walker, M. L., & Humphreys, D.A. (2006). Valid coordinate systems for linearized plasma shape response models in tokamaks. *Fusion Sci. Technol.*, 50, 473–489. DOI:10.13182/FST06-A1271
- 16 Austin, M. E. et al. (2019). Achievement of reactor-relevant performance in negative triangularity shape in the DIII-D tokamak. *Phys. Rev. Lett.*, 122, 115001. DOI:10.1103/PhysRevLett.122.115001
- 17 Kolemen, E. et al. (2018). Initial development of the DIII-D snowflake divertor control. *Nucl. Fusion*, 58, 066007. DOI: 10.1088/1741-4326/aab0d3
- 18 Anand, H. et al. (2019). Real time magnetic control of the snowflake plasma configuration in the TCV tokamak. *Nucl. Fusion*, 59, 126032. DOI: 10.1088/1741-4326/ab4440
- 19 Wabersich, K. P., Hewing, L., Carron, A., & Zeilinger, M.N. (2021). Probabilistic model predictive safety certification for learning-based control. *IEEE Tran. Automat. Control*, 67, 176–188. DOI: 10.1109/TAC.2021.3049335
- 20 Abdolmaleki, A. et al. (2021). On multi-objective policy optimization as a tool for reinforcement learning. Preprint at <https://arxiv.org/abs/2106.08199>

С.Н. Хоссейнимотлаг, М.А. Зарей, А. Шакери

Альфа-протон-альфа көшкіні реакциясы механизмі арқылы нейтронсыз $p^{11}B$ отыны бар токамак термоядролық реакторында плазманы жағуды бақылау әдісі

Мақала нейтрондық отын проблемаларына арналған. Альфа-протон-альфа көшкіні реакциясы арқылы нейтронсыз $p^{11}B$ отыны бар токамак термоядролық реакторында плазманың жануын бақылаудың сипаттамалық ерекшеліктері талданған. Зерттеу негізінде авторлар бөлшектер мен энергия тепе-теңдігінің теңдеулері қолданылатын плазмалық тұтану өлшемдері жоқ модельді ұсынады. Осы модель шеңберінде $p^{11}B$ отыны қарастырылған. Шын мәнінде, бұл жұмыс жанып жатқан плазманы басқарудың жаңа әдісін ұсынады, осылайша жүйенің өзгеруін, жанармай құю жылдамдығын және қосымша қуатты басқаруға болады. Модельдеу теңдеулерін қолдана отырып, $p^{11}B$ отынының сапа коэффициенті есептелді. Нейтрондық отынның екі негізгі кемшілігі бар: (i) олар қорғауды қажет ететін және реактордың құрылымына зиян келтіретін және белсендіретін нейтрондарды шығарады, (ii) тритий өндірісі қосымша күрделілікті, шығындарды және литий жабыны үшін радиалды кеңістіктің қажеттілігін қамтиды. Нейтронсыз $p^{11}B$ реакциясы көбінесе осы мәселелерді шешудің әлеуетті құралы ретінде қарастырылатыны көрсетілген.

Кілт сөздер: плазма, термоядролық синтез, динамика, нейтронсыз, энергия, бақылау, көшкін, альфа, протон, отын

С.Н. Хоссейнимотлаг, М.А. Зарей, А. Шакери

Способ управления горением плазмы в термоядерном реакторе токамак на безнейтронном топливе $p^{11}B$ по механизму альфа-протон-альфа лавинной реакции

Статья посвящена проблемам нейтронного топлива. Проанализированы характерные особенности управления горением плазмы в термоядерном реакторе токамак с использованием безнейтронного топлива $p^{11}B$ посредством лавинной реакции альфа-протон-альфа. На основе проведенного исследования авторы предлагают безразмерную модель зажигания плазмы, в которой используются уравнения равновесия частиц и энергии. В рамках этой модели рассматривается топливо $p^{11}B$. В работе представлен новый метод управления горячей плазмой, позволяющий контролировать изменения в системе, скорость заправки топливом и дополнительную мощность. Применяя уравнения моделирования, был рассчитан коэффициент качества топлива $p^{11}B$. У нейтронного топлива есть два основных недостатка: (i) оно генерирует нейтроны, которые требуют защиты и могут повредить конструкцию реактора и активировать ее, (ii) производство трития сопряжено с дополнительной сложностью, расходами и необходимостью в радиальном пространстве для литиевого покрытия. Показано, что безнейтронная реакция $p^{11}B$ часто рассматривается как потенциальное решение этих проблем.

Ключевые слова: плазма, термоядерный синтез, динамика, без нейтронов, энергия, управление, лавина, альфа, протон, топливо

Information about the authors

Seyede Nasrin Hosseini-motlagh — Doctor of Physics, Leading Researcher, Department of Physics, Shi.C., Islamic Azad University, Shiraz, Iran; e-mail: nasrinhosseini_motlagh@iau.ir; <https://orcid.org/0000-0001-5381-2449>;

Mohammad Ali Zarei — Doctor of Physics, Senior Researcher, Department of Physics, Payame Noor University, Tehran, Iran; e-mail: M.Zarei2345@gmail.com;

Abuzar Shakeri (contact person) — Doctor of Technical Sciences, Senior Researcher, Department of Physics, Shi. C., Islamic Azad University, Shiraz, Iran e-mail: Abuzar.Shakeri6845@gmail.com; <https://orcid.org/0009-0007-8075-6711>